Model Based and Robust Control Techniques for Internal Combustion Engine Throttle Valves

Jacob Lykke Pedersen

A thesis submitted in partial fulfilment of the
requirements of the University of East London
for the degree of

Doctor of Philosophy

October 2013

Revision: 2.0.0

Acknowledgments

I am greatly thankful to my supervisor, Professor Stephen Dodds, whose valuable technical support, knowledge and experience enabled me to finish this work. On a personal level I would like to thank, Professor Stephen Dodds and his wife, Margaret, for the many talks and lunches ☺.

I thank Dr W. Hosny for being my Director of studies since Professor Dodds became Emeritus.

I would also like to thank my colleagues at Delphi for the support and in particular Johan Dufberg for reviewing the work. Also, I would like to take this opportunity to thank my managers, Anthony Potter and Gary Forwards, for supporting this work.

I owe many thanks to my wife, Inger Lise, for all the support and help she has given me through the years of this research.

Summary

The performances of position controllers for a throttle valve used with internal combustion engines of heavy goods vehicles is investigated using different control techniques.

The throttle valve is modelled including the hard stops and static friction (stick-slip friction), which are nonlinear components. This includes a new simple approach to the modelling of static friction. This nonlinear model was validated in the time domain using experimental results, parameterised by experimental data using a Matlab based parameter estimation tool. The resulting state space model was linearised for the purpose of designing various linear model based controllers. This linearised model was validated using experimental data in the frequency domain.

The correct design of each model based controller is first confirmed by simulation using the linear throttle valve model, the specified step response being expected. Then the robustness is assessed in the frequency domain using the Matlab® Control System Design Toolbox and in the time domain by simulation using Monte Carlo based plant parameter mismatching between the simulated real plant and its model used for the control system design. Once satisfactory performance of a specific controller is predicted by simulation using the linear model, this is replaced by the nonlinear model to ascertain any deterioration in performance. Controllers exhibiting satisfactory performance in simulation with the nonlinear plant model are then investigated experimentally.

The set of controllers investigated in this work includes types that are not currently employed commercially, as well as traditional ones, consisting of the IPD, PID, DPI controllers and the linear state feedback controller with and without an integrated observer. The other controllers are the sliding mode

controller, observer based robust controller (OBRC) and the polynomial controller. The traditional controllers are designed using partial pole placement with the derived linear plant model. The other controllers have structures permitting full pole placement, of which robust pole placement is an important option. In the pole placement design, the locations of the closed loop poles are determined using the settling time formula.

Despite the use of robust pole placement, the static friction caused a limit cycle, which led to the use of an anti-friction measure known as dither.

The 14 different controllers were investigated for their ability to control the throttle valve position with nonlinear friction, parameter variations and external disturbances. This information was gathered, together with qualitative information regarding ease of design and practicability to form a performance comparison table.

The original contributions emanating from the research programme are as follows:

- The successful application of new control techniques for throttle valves subject to significant static friction
- The first time investigation of partial and robust pole placement for throttle valve servo systems.
- A simplified static friction model which can be used for other applications.

Contents

List of Figures

List of Symbols

L	Inductance [Henry - H]
L_a	DC motor armature inductance [Henry - H]
R	Resistance [Ohm - Ω]
R_a	DC motor armature resistance [Ohm - Ω]
I	Current [Ampere - A]
V	Voltage [Volt]
k_e	DC motor voltage constant [V/(rad/sec)]
k_t	DC motor torque constant [Nm/A]
J	Moment of inertia [kg m^2]
J_x	Throttle system inertia (lumped)
θ	Angle [rad]
ω	Angle speed [rad/sec]
k_{spring}	Coiled spring constant [Nm/rad]
N	Gear size [m]
r	Gear radius [m]
$k_{kinetic}$	Kinetic (viscos) friction constant [Nm sec/rad]
n	System order, if nothing else is stated
T_s	Control settling time [sec]
T_{so}	Observer settling time [sec]
ν	Volume [m^3]
p	Pressure [N / m^2]
$\dot{m}$	Mass flow [kg/sec]
Sec	Seconds
$S(\ )$	Switching function
r_{pp}	Pole-to-pole ratio [-]
$r_{pp\min}$	Minimum pole-to-pole ratio [-]
h	Sampling time interval [sec]
σ	Sigma

s	Laplace variable
Γ	Torque [Newton Meter - Nm]
⊠	Closed loop poles
×	Open loop poles
⊙	zeros

List of Acronyms

ADC	Analogy-to-Digital Converter
DAC	Digital-to-Analogy Converter
DC	Direct Current
DPF	Diesel Particulate Filter
DPI	Derivative Proportional Integral controller
e.m.f.	Electromotive force
ECU	Electronic controller unit
EGR	Exhaust Gas Recirculation
FFT	Fast Fourier Transform
HGV	Heavy Goods Vehicle
I/O	Input / Output
IPD	Integral Proportional Derivative controller
LCR	Inductance (L), capacitance (C) and resistance (R)
LSF	Linear State Feedback
LTI	Linear Time Invariant
Matlab®	Mathematical tool from Mathworks, Inc.
MAXB	Micro Auto Box
NO_x	Nitrogen Oxides
OBRC	Observer Based Robust Control
PID	Proportional Integral Derivative controller
PRBS	Pseudo random binary sequence
PWM	Pulse Width Modulation
SCR	Selective Catalytic Reduction
Simulink®	Diagram simulation tool from Mathworks, Inc.
SISO	Single Input – Single Output
SMC	Sliding Mode Control
VGT	Variable Geometry Turbine
VSC	Variable Structure Control

1 Introduction

1.1 Engine System

Figure 1.1 shows an overview of the engine system that this research programme supports, a detailed description of which is given in Appendix A.1.

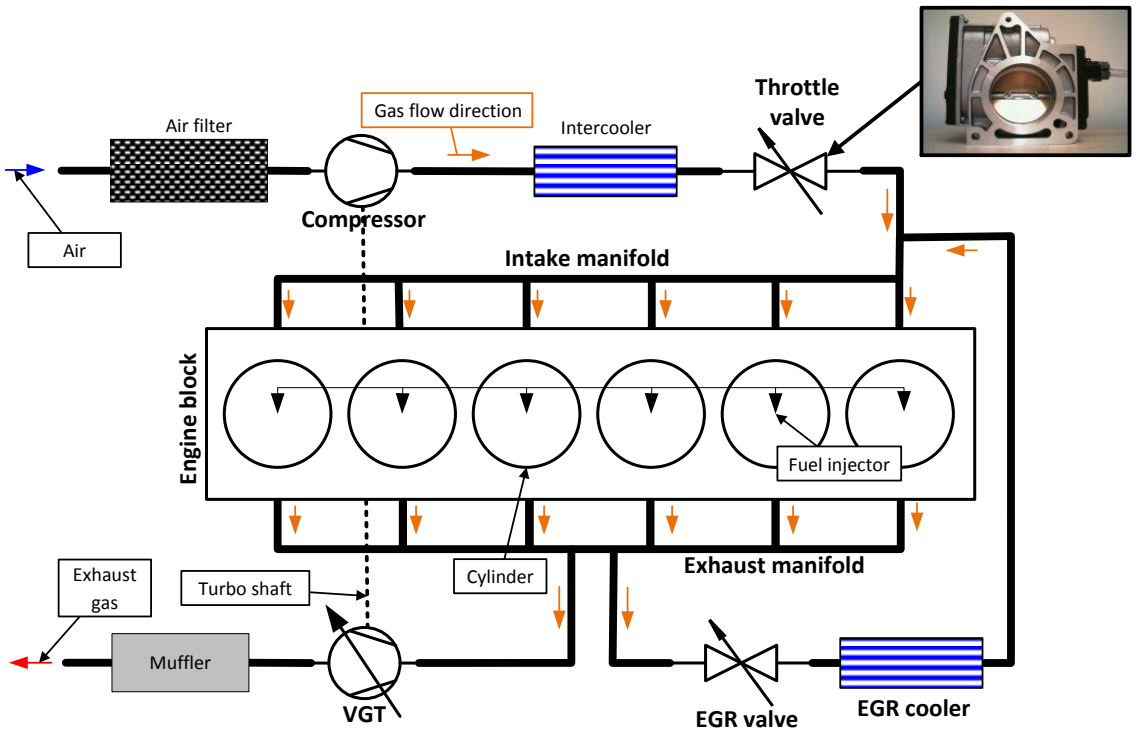

Figure 1.1: An example of a schematic for a turbocharged Euro VI engine configuration with high pressure EGR and throttle valve

The throttle valve, described in more detail in the following section, is the focus of this research programme but this will be equally useful for the other valves employed in the system as each of these has similar characteristics.

1.2 Throttle Valve

On a petrol engine the throttle valve is used to control the air-to-fuel ratio by applying a variable constraint to the air path, which will reduce the air flow. On Diesel engines (Figure 1.1) the throttle valve is used as a means to increase the EGR rate and reduce the air-to-fuel ratio, in a low power operating range. In this range, the operation of the VGT vanes has no effect and therefore the throttle has to be used. The amount of air into the engine can be controlled by closing the throttle valve, creating a lower pressure in the intake manifold. This lower pressure can also be used to induce more EGR flow through its high pressure path, assuming that the exhaust manifold pressure stays constant.

For the EURO VI regulation, a high EGR_{rate} is needed in the low power range making use of the throttle valve. During the DPF regeneration, the air-to-fuel ratio needs to be controlled to within a specific range, which will require the use of the throttle valve. Furthermore, the throttle valve can be used to damp engine shaking following key off by closing it.

Throttle valves suffer from considerable nonlinear friction in their mechanisms that makes it difficult to control accurately, particularly as it is subject to significant variations due to changes in temperature and wear over the engine lifetime. The static (stick-slip) friction component is particularly troublesome and can cause controller limit cycling (Townsend and Salisbury, 1987) which can compromise the engines emission performance. This also presents a challenge for the control system designer when it is important to obtain a prescribed dynamic response to reference input position changes.

1.2.1 Hardware Description

The throttle system (Figure 1.2) consists of a spring loaded throttle plate which is driven by a *direct current* (DC) motor through a gear system. A pre-windup coil spring applies a residual torque which makes the valve open in the case of an electrical failure. The throttle plate position is measured by a potentiometer type sensor attached to the plate, where fully open = 0 [rad] and fully closed = 1.57 [rad].

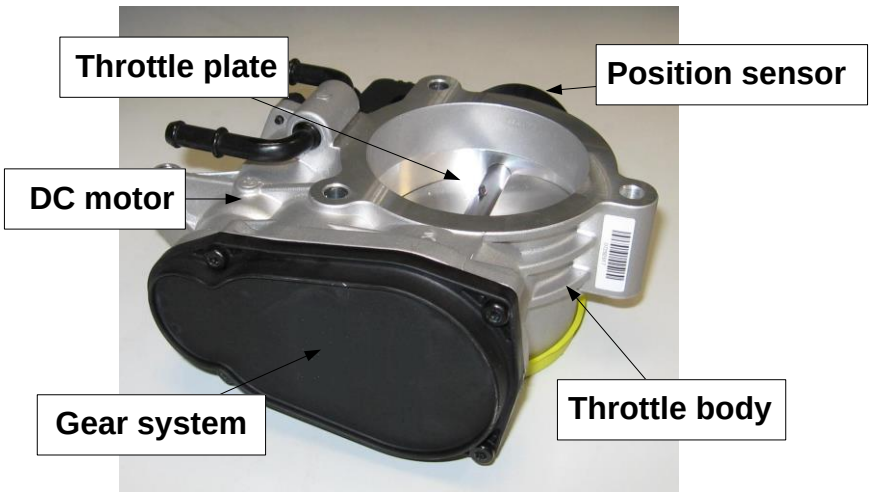

Figure 1.2: A throttle valve

The air flow through the throttle valve is a function of the air-to-fuel ratio, EGR rate and after-treatment demands. In the normal operation mode, the throttle reference position is calculated by using the desired throttle air flow, pressures and the temperatures.

The mass flow passing the throttle valve illustrated in Figure 1.3 can be modelled by the isentropic (constant entropy) flow equation for a converging-diverging nozzle (Wallance et al., 1999, Schöppe et al., 2005).

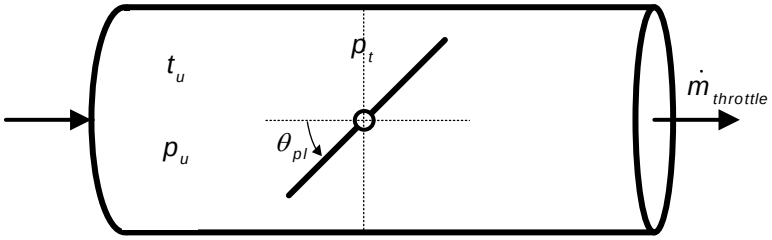

Figure 1.3: Schematic of a throttle valve

For the gas mass flow through the throttle valve:

$$\dot{m}_{throttle} = A_{throttle}\left(\theta_{pl}\right) \cdot C \cdot \frac{p_u}{\sqrt{R \cdot T_u}} \Phi\left(\frac{p_t}{p_u}\right) \tag{1.1}$$

For the non-choked flow (sub-sonic):

$$\Phi\left(\frac{p_t}{p_u}\right) = \left(\frac{p_t}{p_u}\right)^{\frac{1}{\kappa}} \sqrt{\frac{2\kappa}{\kappa-1} \cdot \left[1 - \left(\frac{p_t}{p_u}\right)^{\frac{\kappa-1}{\kappa}}\right]} \quad , \quad \left(\frac{p_t}{p_u}\right) \geq \left(\frac{\kappa+1}{2}\right)^{\frac{\kappa}{1-\kappa}} \tag{1.2}$$

For the choked flow (sonic):

$$\Phi\left(\frac{p_t}{p_u}\right) = \sqrt{\kappa}\left(\frac{2}{\kappa+1}\right)^{\frac{\kappa+1}{2(\kappa-1)}}, \qquad \left(\frac{p_t}{p_u}\right) < \left(\frac{\kappa+1}{2}\right)^{\frac{\kappa}{1-\kappa}} \tag{1.3}$$

where

R: Gas constant

$\kappa = c_p / c_v$ (1.4 for air)

C: Throttle valve flow coefficient (dimensionless)

$A_{throttle}$: Geometrical effective valve area

p_u: Upstream pressure

p_t: Throat pressure

$\dot{m}_{throttle}$: Mass flow through the throttle valve

θ_{pl}: Throttle plate position

The geometrical area for flow passage of an elliptical throttle plate:

$$A_{throttle}\left(\theta_{pl}\right) = \pi r^2 \left(1 - \frac{r}{r_1}\cos\left(\theta_{pl}\right)\right) \tag{1.4}$$

where

r : Pipe radius

r_1: Maximum throttle plate radius

In theory, equation (1.1) to (1.4) could be rearranged to get the desired throttle position, using the desired gas flow, the gas temperature and its pressures. In practice, however, it is difficult to get an accurate throttle position by this means due to model parametric errors. This could be circumvented by creating two functions, one based on the physics of the system and a second one based on empirical data, as follows.

$$f_1\left(\dot{m}_{throttle}, T_u, p_u, p_t\right) = \frac{\dot{m}_{throttle}}{\frac{p_u}{\sqrt{R \cdot T_u}}\Phi\left(\frac{p_t}{p_u}\right)} \tag{1.5}$$

$$\theta_{pl_{desired}} = f_2\left(f_1\left(\dot{m}_{throttle}, T_u, p_u, p_t\right)\right) \tag{1.6}$$

where

f_2: A function which converts the corrected flow f_1 into a throttle position demand

The aim of the throttle valve position control system (Figure 1.4) is to control the position (i.e., the angle) of the plate inside the throttle valve. In the normal mode, the desired throttle position demand from equation (1.6) is fed into the throttle position controller, but in special circumstances this can be overridden by other demands such as the DPF regeneration mode or engine shut down (key off). The controller measures the throttle plate position and adjusts this to achieve the desired position demand. The throttle plate position is adjusted using the torque produced by the DC motor and gear system.

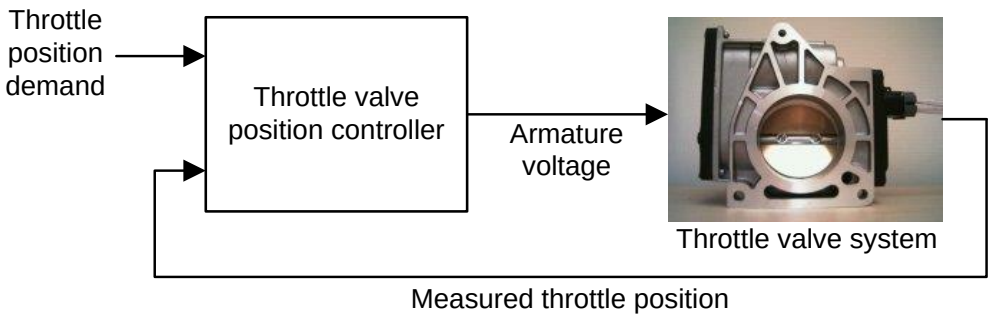

Figure 1.4: Throttle valve position control system

The torque is proportional to the DC motor armature current. The current is controlled by the throttle valve position controller's output driver.

1.2.2 Ideal Control System Specification

The aim of the throttle valve position control system design is to achieve the following:

1. The position reference must be followed with a minimum delay and steady state error.
2. The control system must exhibit robustness to minimise the impact of the static (stick-slip) friction, change in friction parameters due to wear & tear.
3. The control system must be able to compensate for failure of the retention spring (pre-windup coil spring).

Figure 1.5 shows an example of a desired throttle valve position demand (0 = fully open, 1.57 = fully closed) for a typical drive cycle during DPF regeneration (source: Delphi Diesel Systems). In the DPF regeneration mode the valve is used to control the narrow air/fuel ratio operation range for the DPF to heat up and stay in the regeneration mode. If the air-to-fuel ratio exceeds the

boundaries it can cause the DPF to stop regenerating or in the worst case damage the DPFs ceramic structure due to the generated heat.

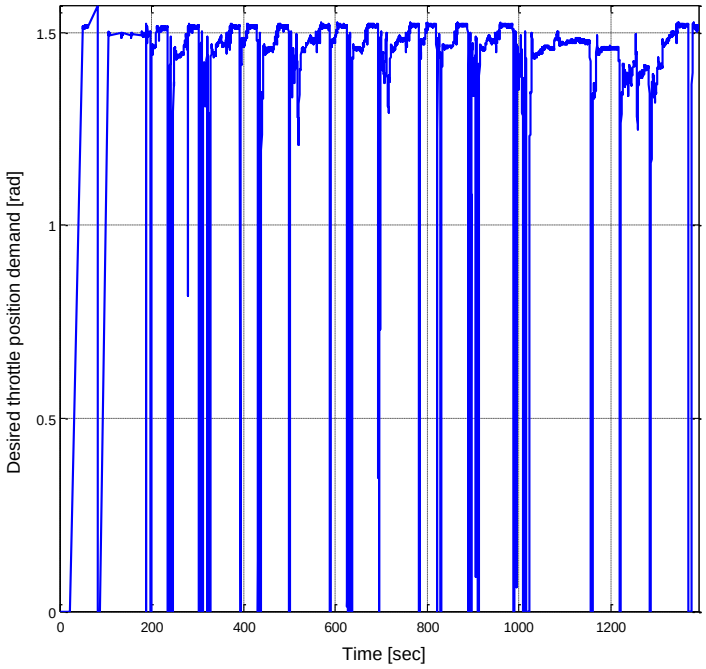

Figure 1.5: Desired throttle position demand for a typical drive cycle during DPF regeneration

The dynamics of the desired closed loop system response has to be chosen in such a way that it tracks the demand without too much lag. The lag can cause the air flow to differ from that demanded for significant periods and impact the engine output emission. Choosing too fast a desired closed loop system response can, however, wear down the actuator, in this case the DC motor and gear system in the throttle valve. In addition the speed of response is restricted by the DC motor voltage supply.

Figure 1.6 shows a classic definition of the system settling time T_s (Franklin et al., 2002). This is defined as the time it takes from applying an ideal instantaneous step input to the time at which the systems output has entered

and remained within a specified range of the expected steady state value. In this case the range has been chosen to +/- 5%.

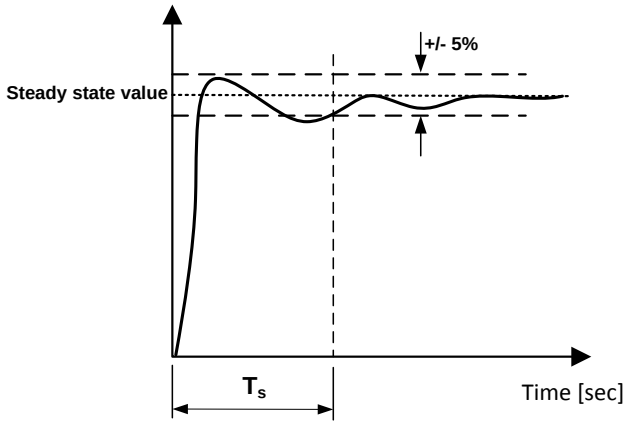

Figure 1.6: System settling time definition

Figure 1.7 shows the minimum and maximum peak values of the controller output during a simulation of a closed loop pulse response (pulse duration 1 second). The simulation is done on a nonlinear throttle valve plant model, with various desired closed loop settling times. The controller is in this case implemented as a state space controller with an integrator in the outer loop to remove the steady state offset. This will be described in more detail in Chapter 4.

The saturation level for the throttle actuator used for this project is +/- 12 volt. Figure 1.7 indicates that peak control effort needed to achieve a desired settling time of 0.1 seconds for a position demand change nearly at the maximum value. This will bring the control system into saturation, but only at the maximum level. The control saturation resulting from attempting to reduce this further would seriously deteriorate the control system performance.

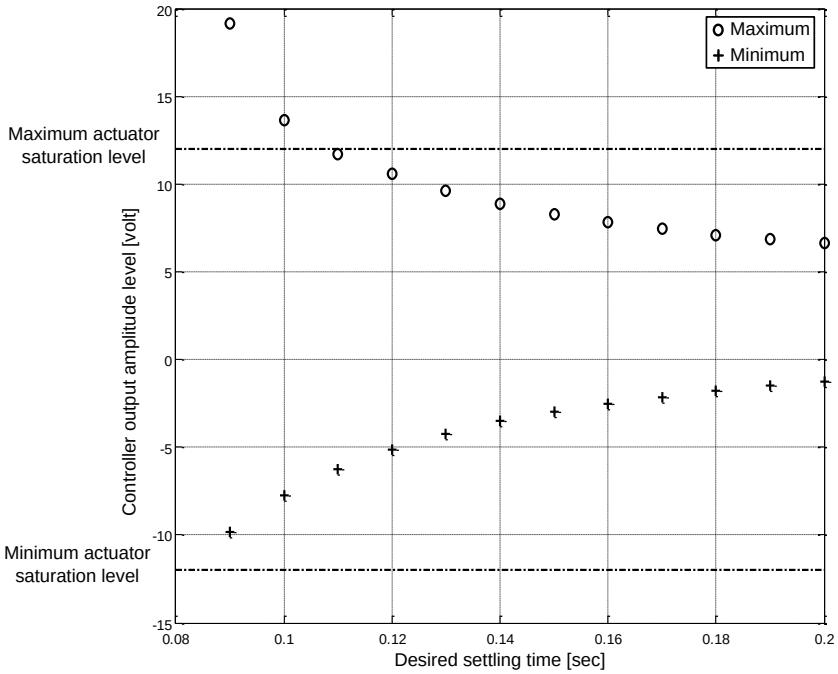

Figure 1.7: Maximum / minimum control effort as function of desired settling time

Figure 1.8 is a sample of the desired throttle valve position demand from the DPF regeneration cycle. It shows the simulated impact of the settling time on the system response during the regeneration cycle. When the settling time increases the lag between the desired response (throttle position demand) and the simulated closed loop system response has an increased dynamic lag, as expected.

As stated before, too much lag can cause the emission output level to increase, while controller saturation indicates too fast a response which can prematurely wear the throttle system. The desired closed loop settling time should be chosen as a compromise between lag and saturation of the control system, in this case 0.1 second.

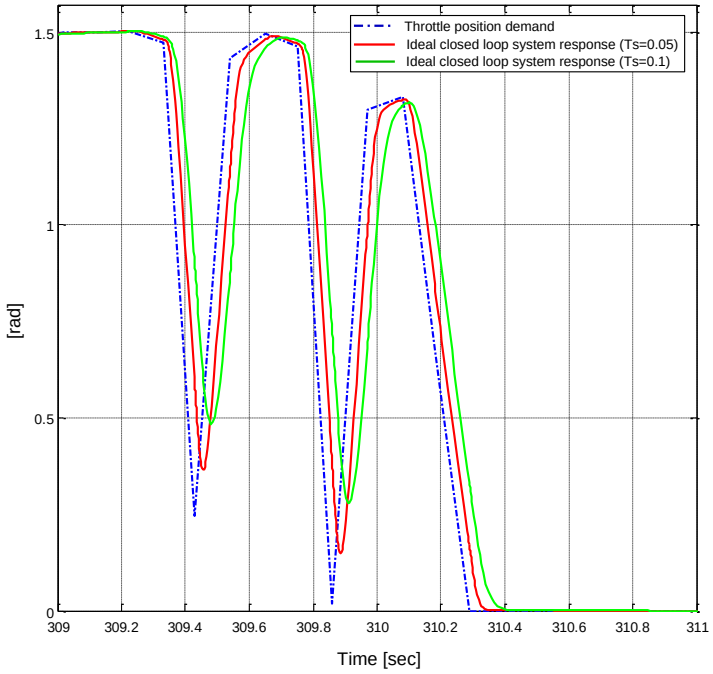

Figure 1.8: A section of the generation DPF cycle with different settling times

1.2.3 Current Control Techniques

The throttle valve position is currently governed by a PID/DPI controller with feed forward and measures to overcome the static friction. Despite the presence of the integral term, the feed forward is used to counteract the coil spring torque, which also avoids prolonged transient behaviour due to relying solely on the integral action for this. To minimise the effects of the static friction an additional oscillatory signal can be added to the control variable that produces a corresponding torque just sufficient to overcome the static friction. This is known as control dither (Leonard and Krishnaprasad, 1992). The amplitude and frequency of this signal are adjusted at the commissioning stage. This, however, is quite difficult and time consuming.

In most cases the traditional controllers, i.e., PID/DPI controllers and their variants are employed and tuned by certain procedures, such as Zeigler-Nichols (Meshram and Kanojiya, 2012) or trial and error.

1.3 Motivation

The aim of this research is to study the control techniques used in vehicle power trains for the position control of the throttle valve and to seek new control techniques taking advantage of the flexibility of modern processing technology to achieve an improved performance and reduce the commissioning time. The adoption of model based control techniques and increased robustness against parametric uncertainties and external disturbances are expected to play major roles in reaching this goal.

Model based control system design means the derivation of design formulae for the adjustable parameters of a controller based on a mathematical model of the plant (in this case the throttle valve) and a design specification. Major benefits of this approach are as follows.

a) The control system design can be validated by comparing the response of a simulation of the control system with the expected response set by the design specification.
b) The robustness can be assessed by introducing external disturbances and parametric mismatches in the simulation and observing the resulting deviation of the control system response from the nominal response determined in (a).

Model based control system design, is adopted throughout this thesis, as it forms a firm basis for comparison of the different control techniques.

1.4 Contribution

The original contributions emanating from the research programme, that entailed the comparison of fourteen different controllers, are as follows:

- The successful application of new control techniques for throttle valves subject to significant static friction
- The first time investigation of partial and robust pole placement for throttle valve servo systems.
- A simplified static friction model which can be used for other applications.

1.5 Structure of the thesis

As the research focuses on control techniques used for the intake throttle valve in *heavy duty* (HD) vehicle power trains, chapter 1 gives a general engine system overview and a more detailed description of the intake throttle valve. The first task in the development of a model based control algorithm is the establishment of a mathematical model of the particular plant to be controlled. So Chapter 2 presents a detailed electrical and mechanical nonlinear model of the intake throttle valve. Then a linear model is derived on the basis of the nonlinear one. In chapter 3 the nonlinear model is parameterised by the use of measurements, calculations and a parameter estimation tool from Mathworks®. An introduction to the PID controller is given in the beginning of chapter 4. Then the methodology of the controller performance assessment is introduced. This is followed by explanations of the common features of the controllers under investigation, comprising pole placement, control dither and integrator anti-windup. The different control strategies are then introduced and the corresponding control laws for the throttle valve are derived. Then the performance of each is assessed. In Chapter 5 the performances of all 14 different controllers are compared. Finally, Chapter 6 presents the overall conclusions and recommendations for further research.

2 Modelling

2.1 Introduction

The throttle system (Figure 2.1) consists of a spring loaded throttle plate which is mechanically connected to a brushed DC motor through a gear system (Scattolini et al., 1997). The pre-stressed coil spring is a safety measure preventing the engine stalling in case of an electric fault, in which the motor is not energised by making the plate go to its open position. The plate's position is measured by a potentiometer with an output range between 0.5 and 4.5 [V] with total position accuracy of +/- 2%. The non-zero output range is to insure that the control system can detect if the position signal wire breaks.

A pictorial view of the throttle valve components is shown in Figure 2.1. A more detailed exploded view of the throttle valve may be found in appendix A.5.

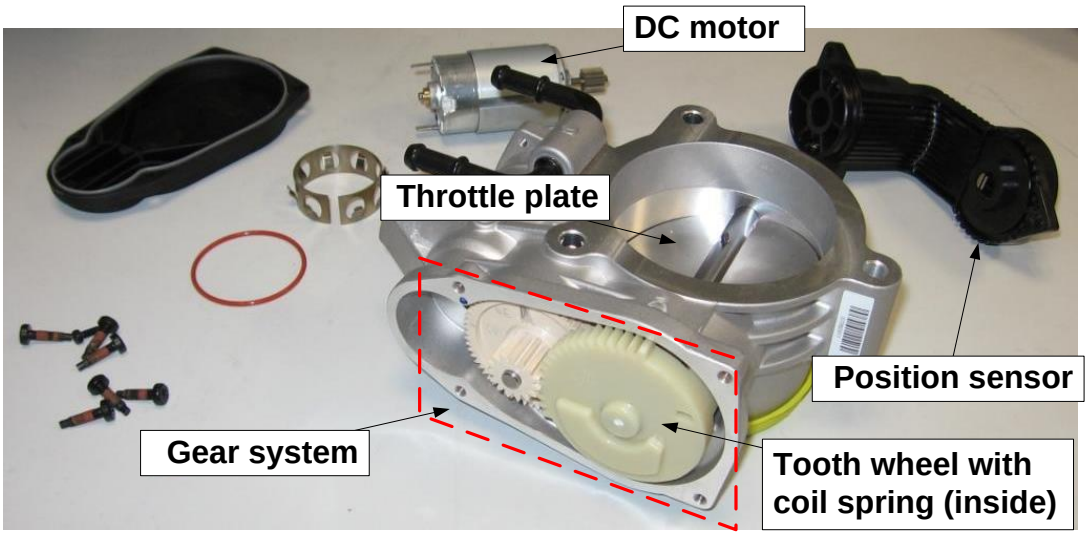

Figure 2.1: A disassembled throttle valve

The throttle valve system model comprises two parts: an electrical and mechanical model. The electrical model consists of the equations of the

armature circuit of the DC motor while the mechanical model consists of the equations modelling the mechanical load, including the moment of inertia, the gear system, the spring and friction.

Figure 2.2 shows a schematic diagram of the throttle valve system, starting from the left with DC motor. The DC motor is modelled as an electric load (resistance R_a and inductance L_a) and back electromotive force (e.m.f.) which depends on the shaft speed. The output torque from the DC motor is proportional to the current. The mechanical system is modelled as a gear system with a moment of inertia and kinetic friction components on both sides. The gear is used to amplify the DC motor torque.

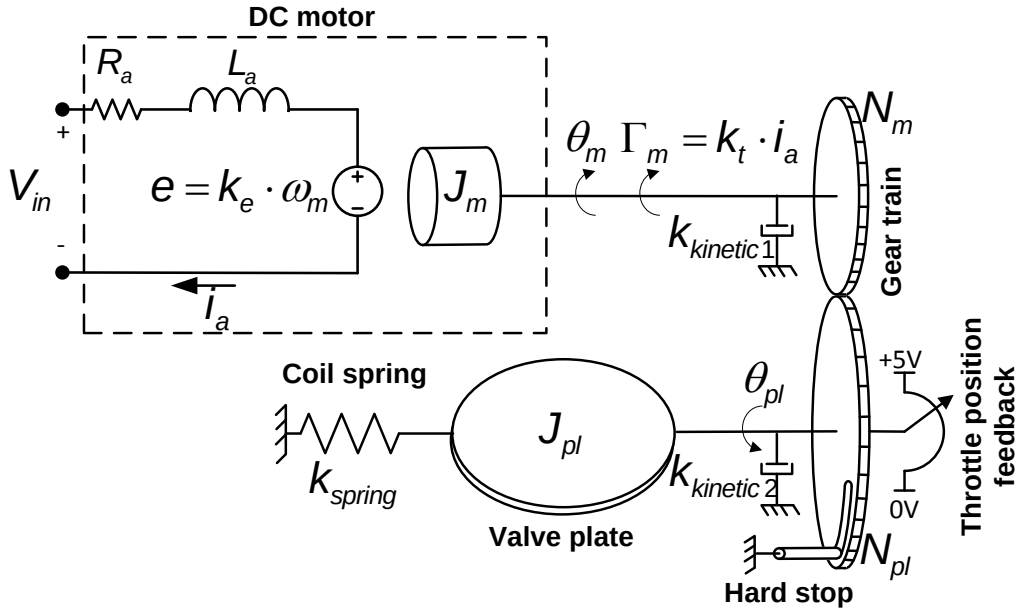

Figure 2.2: Throttle valve schematic diagram

Table 2.1 defines all the parameters of the model.

Table 2.1: Parameters of throttle valve model

Quantity	Description	Units
V_{in}	DC motor input voltage	V
i_a	DC motor armature current	A
R_a	DC motor armature resistance	Ohm
L_a	DC motor armature inductance	H
k_t	DC motor torque constant	Nm/A
k_e	DC motor voltage constant	V/(rad/sec)
e	DC motor back e.m.f. generated voltage	V
Γ_m	Torque generated by the DC motor	Nm
θ_m	DC motor position	rad
ω_m	DC motor speed	rad/sec
θ_{pl}	Throttle valve plate position	rad
J_{pl}	Moment of inertia for the valve plate	kg*m^2
J_m	Moment of inertia for the DC motor	kg*m^2
k_{spring}	Coiled spring constant	Nm/rad
$k_{kinetic1}$	The lumped kinetic (viscos) friction constant including the DC motors bearings and half of the gear train friction	Nm sec/rad
$k_{kinetic2}$	The lumped kinetic (viscos) friction constant including the throttle plate bearings and half of the gear train friction	Nm sec/rad
N_m	DC motor wheel diameter	m
N_{pl}	Throttle plate wheel diameter	m
N_{pl} / N_m	Gear ratio	-

The throttle valve is a butterfly valve type, which means that air flow passing through the throttle valve will not create a load torque and this is therefore not included in the model. The main load torque comes from a linear coiled spring which increases its torque in proportion with the closing angle of the throttle valve.

The mechanical and electrical models of the throttle valve are combined in subsection 2.4 to form a complete linear state space model and the corresponding transfer function model. The linear state space model is used for the controller and observer designs in Chapter 4.

The linear model is extended to form a more comprehensive model in subsection 2.5 that includes hard stops, static and Coulomb friction, making the model nonlinear. The nonlinear model is used to develop the control strategies and to validate them before they are tested on the experimental setup.

In subsection 3 the model is parameterised by using measurements, experiments and a parameter estimation tool from Mathworks®. The parameterised model is then validated in the time and frequency domains.

2.2 The Electrical Model

The DC motor in the throttle valve is mechanically commutated (brushed) with permanent stator magnets (Figure 2.3). The electric current, i_a, which runs through the armature windings, with the resistance R_a and inductance L_a, generates a torque Γ_m equal to the current amplitude multiplied by the constant k_t

$$\Gamma_m = k_t \cdot i_a \tag{2.1}$$

The armature voltage, V_{in}, supplied by a DC voltage source, drives the armature current, i_a, through the motor. In this case the input voltage source is the throttle valve position controller. The torque is generated by the current through the armature windings interacting with the magnetic field from the stator magnets. The maximum torque is generated when the angle between the conducting windings and magnetic field is 90°. This angle is maintained by the commutator that switches the different sets of armature windings on and off as they rotate under the magnets.

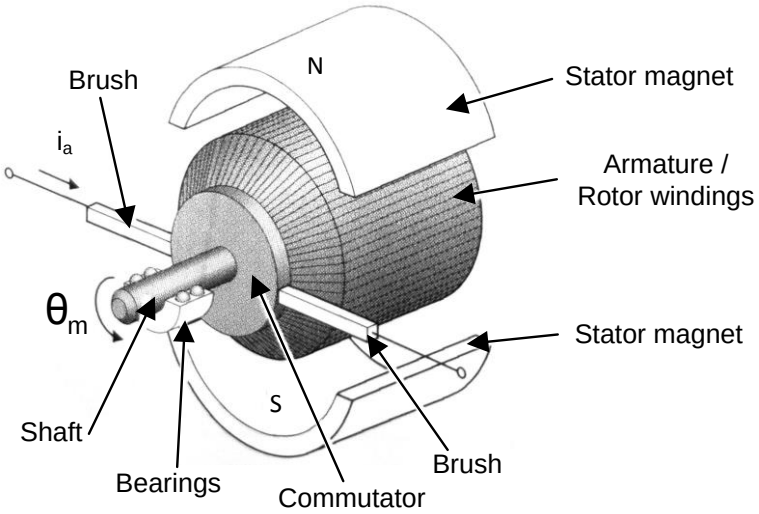

Figure 2.3: Model of a brush DC motor

The torque forces the armature/shaft to spin. The speed of the DC motor, ω_m, generates a back e.m.f. proportional to the speed via the constant k_e. Thus

$$e = k_e \cdot \omega_m \tag{2.2}$$

The faster the DC motor spins the larger the armature voltage needed to maintain the required armature current, as shown in Figure 2.4.

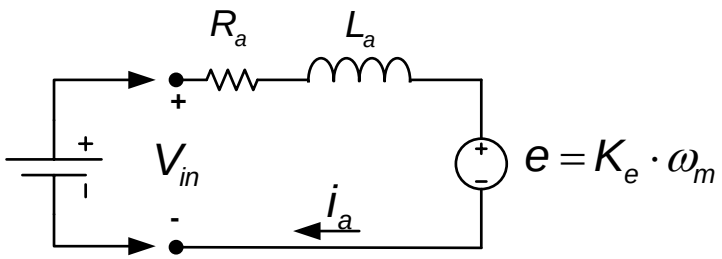

Figure 2.4: Electrical schematic of the DC motor

If the DC motor is supplied by a constant voltage, the motor speed will settle to a constant equilibrium value. The armature current will be limited by the back e.m.f. and the resulting electromagnetic torque will be just enough to drive the mechanical friction and load at the constant equilibrium speed. With reference to Figure 2.4, the differential equation modelling the electrical part is as follows.

$$\begin{aligned} V_{in}(t) &= L_a \frac{dI_a(t)}{dt} + R_a \cdot i_a(t) + k_e \cdot \frac{d\theta_m(t)}{dt} \Rightarrow \\ \frac{di_a(t)}{dt} &= \frac{1}{L_a}\left(V_{in}(t) - i_a(t) \cdot R_a - k_e \cdot \frac{d\theta_m(t)}{dt} \right) \end{aligned} \tag{2.3}$$

The armature current generating the electromagnetic torque, i_a, is found by integrating (2.3). Figure 2.5 shows the state variable block diagram model of the electrical part of the DC motor corresponding to (2.3).

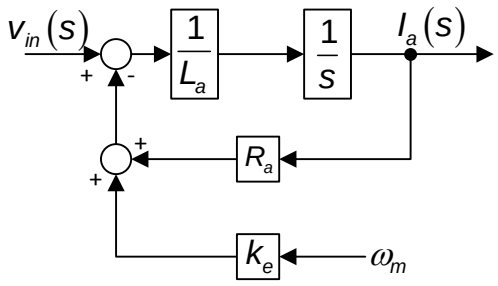

Figure 2.5: State space representation of equation (2.3)

2.3 Mechanical Model

The mechanical model of the throttle valve is split into three sections: the dynamic model, the friction model and the hard stops. The dynamic model comprises the moments of inertia of the mechanical components, the gear train and the friction.

Initially, a linear model will be developed for the model based linear control system design. This includes the kinetic friction, sometimes called the viscous friction, in which the friction torque is directly proportional to the relative velocity between the moving surfaces. A more detailed friction model, however, is needed later, that includes nonlinear friction which is significant in this application. This is developed in subsection 2.3.4, by adding static and Coulomb friction components to the kinetic friction.

Another system nonlinearity consists of the two hard stops of the butterfly valve that limit the movement of the throttle valve plate position. This is modelled using a high gain linear feedback loop approximation explained in subsection 2.3.5.

2.3.1 Linear Dynamic Model

The dynamic model, depicted in Figure 2.6, contains the linear parts of the mechanical throttle model consisting of the load spring, the moments of inertia, the gear train and the kinetic friction.

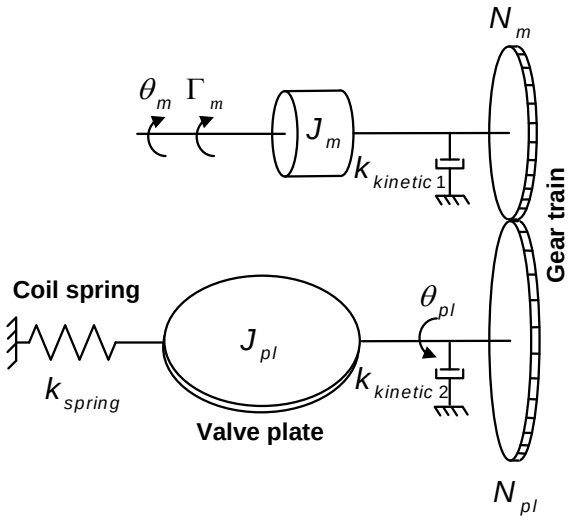

Figure 2.6: Throttle body schematic without the DC motor

The gear system in the throttle valve consists of three parts (Figure 2.1), a tooth wheel directly mounted on the DC motors shaft, a middle wheel with two different tooth wheel diameters and a tooth wheel mounted on the valve plate shaft. The model, however, is simplified to just two wheels with a single gear ratio as shown in Figure 2.7.

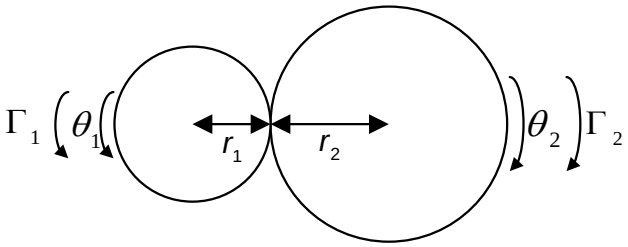

Figure 2.7: Gear system

Here, $r_{1,2}$ are the radii of the toothed wheels, $\Gamma_{1,2}$ are the tooth wheel torques and $\theta_{1,2}$ are the tooth wheel angles of rotation.

The following relationships hold for this gear system

$$r_1 \cdot \theta_1 = r_2 \cdot \theta_2 \tag{2.4}$$

$$\frac{\Gamma_2}{\Gamma_1} = \frac{\theta_1}{\theta_2} = \frac{N_2}{N_1} = \frac{r_2}{r_1} \tag{2.5}$$

The mechanical model for Figure 2.6 (disregarding the gear train moment of inertia) is based on the following torque balance equation.

$$\Gamma_m = \Gamma_{i,m} + \Gamma_{f,m} + \Gamma_{i,pl} + \Gamma_{f,pl} + \Gamma_{sping,pl} \tag{2.6}$$

where the terms are defined in Table 2.2.

Table 2.2: Torque components of mechanical model

$\Gamma_{i,m} = J_m \cdot \ddot{\theta}_m$	Torque from the DC motors moment of inertial
$\Gamma_{f,m} = k_{kinectic1} \cdot \dot{\theta}_m$	Kinetic friction torque for the DC motor side
$\Gamma_{i,pl} = J_{pl} \cdot \ddot{\theta}_{pl}$	Torque from valve plate moment of inertial
$\Gamma_{f,pl} = k_{kinectic2} \cdot \dot{\theta}_{pl}$	Kinetic friction torque for valve plate side
$\Gamma_{sping,pl} = k_{spring} \cdot \theta_{pl}$	Spring torque (valve plate side)

Relationship (2.5) is used to simplify the mechanical model by referring the moment of inertia and kinetic friction from the DC motor to the valve plate side. Also the lumped moment of inertia J_1 (DC motor, J_m, and half of the gear train) and the kinetic friction constant, $k_{kinetic1}$, are referred to the other side of the gear by using relationship (2.5), as shown in Figure 2.8.

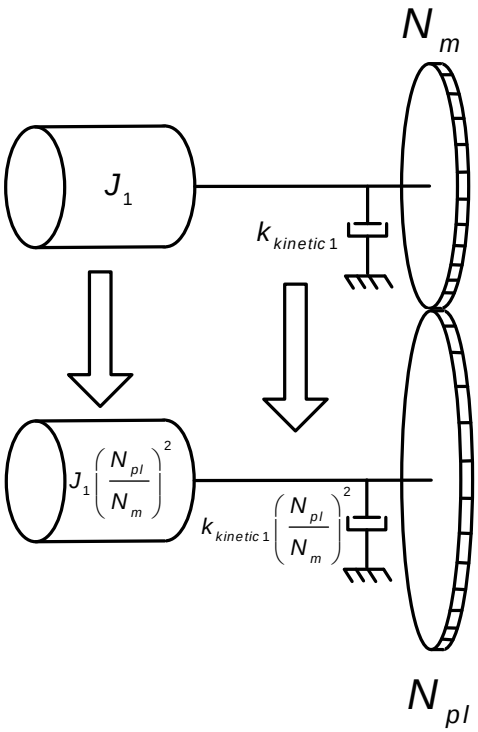

Figure 2.8: Transfer the moment of inertia and friction to the other side of the gear

Figure 2.9 shows a schematic of the plate side of the gear system.

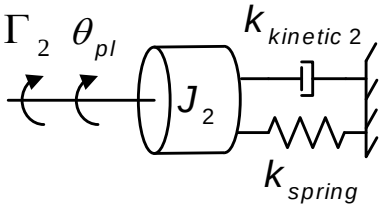

Figure 2.9: Throttle plate side of the gear system

Here, J_2 is the lumped moment of inertia including the valve plate, J_{pl}, and half of the gear train. On the valve plate side Γ_2 is the torque acting on the plate shaft from the gear system. The load on this subsystem is the linear spring

torque which is a function of the valve plate position, the kinetic friction torque and the inertial torque due to the moment of inertia. Thus

$$\Gamma_2 = J_2 \cdot \frac{d^2\theta_{pl}}{dt^2} + k_{kinetic\,2} \cdot \frac{d\theta_{pl}}{dt} + \theta_{pl} \cdot k_{spring} \tag{2.7}$$

The DC motor torque is transferred to the valve plate side by using (2.5). Thus

$$\Gamma_2 = \Gamma_m \frac{N_{pl}}{N_m} \tag{2.8}$$

Then (2.7) can be rewritten as

$$\Gamma_m \frac{N_{pl}}{N_m} = J_2 \cdot \frac{d^2\theta_{pl}}{dt^2} + k_{kinectic\,2} \cdot \frac{d\theta_{pl}}{dt} + \theta_{pl} \cdot k_{spring} \tag{2.9}$$

Combining the two parts, i.e., the DC motor part which has been transferred to the valve plate side (Figure 2.8) and the mechanical load represented by equation (2.9), yields

$$\Gamma_m \frac{N_2}{N_1} = J_x \cdot \frac{d^2\theta_{pl}}{dt^2} + k_{kinetic} \cdot \frac{d\theta_{pl}}{dt} + \theta_{pl} \cdot k_{spring} \tag{2.10}$$

where the lumped moment of inertia is

$$J_x = J_1 \left(\frac{N_{pl}}{N_m} \right)^2 + J_2$$

and the lumped kinetic friction is

$$k_{kinetic} = k_{kinetic\,1} \left(\frac{N_{pl}}{N_m} \right)^2 + k_{kinetic\,2}\,.$$

Figure 2.10 shows the lumped system on the throttle plate side.

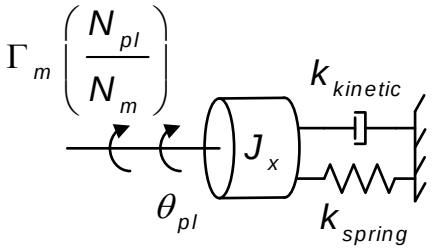

Figure 2.10: Representation of lumped system

As stated previously, the coil spring is pre-stressed in the factory to keep the throttle open in the case of an electrical failure. To model this, an offset torque is added by means of an angle offset, $\theta_{Initial\ spring}$, as follows:

$$\Gamma_{pl} = \left(\theta_{pl} + \theta_{Initial\ spring} \right) \cdot k_{spring} \tag{2.11}$$

It should be noted that this initial spring torque is only to be included in the nonlinear model including the end stops.

2.3.2 The Mechanism of Friction

To move a mechanical part that has close contact with another mechanical part requires a level of force (Figure 2.11). This force level is known as the mechanical friction force. This friction comes from the interaction between the roughness on the two surfaces, where smoother surfaces will decrease the friction force (Popov, 2010).

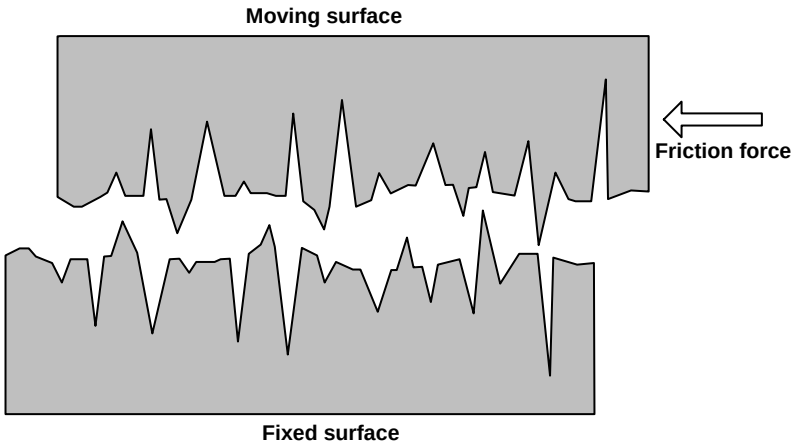

Figure 2.11: Surface interaction

Through time, the throttle valve on a vehicle will be exposed to moisture and dirt that infiltrates the mechanical system. This will result in an increase in the friction between relatively moving components. The amount of friction will change during the day due to temperature change of the mechanical components, but also throughout the lifetime of the throttle valve due to wear. As mentioned before, the friction can cause problems for the controller and even make it limit cycle (Townsend and Salisbury, 1987) (Sanjuan and Hess, 1999) (Radcliffe and Southward, 1990). This points out how important it is to simulate a control system design with a friction model included, prior to implementation.

2.3.3 Preliminary Experiments to Assess the Randomness of the Friction

It would appear from the description in subsection 2.3.2 that the stochastic frictions force is a function of the displacement between the two mechanical surfaces, giving friction force repeatability if the mechanical motion is repeated. Random friction force variations would, however, be produced by quasi-freely moving foreign bodies (dirt). To test the repeatability of the friction effects in the

throttle valve application, a set of preliminary experiments was carried out using a standard throttle valve and an existing *proportional-integral* (PI) position controller with a low amplitude dither. Dither is used as an anti-friction measure which is explained in a later chapter. Essentially good repeatability would indicate that the final control system could be designed to directly compensate for the friction forces. On the other hand, bad repeatability would indicate the need for the final control system to exhibit robustness against unknown friction effects. The system was tested using a ramp function as the position reference input to the controller. A slow ramp is particularly good for testing friction due to its low relative velocity, which exaggerates the effects of static friction, to be explained shortly. The same experiment was repeated firstly four times on one day to detect relatively short term friction variations and then on two different days to detect any longer term friction variations. These experiments are represented in Table 2.3.

Table 2.3: Preliminary friction experiments

Day 1	Day 2
$\theta_{\text{pl11}}(t)$	$\theta_{\text{pl21}}(t)$
$\theta_{\text{pl12}}(t)$	$\theta_{\text{pl22}}(t)$
$\theta_{\text{pl13}}(t)$	-
$\theta_{\text{pl14}}(t)$	-

Note: On day 2 only two experiments were performed.

Figure 2.12 shows the superimposed results for day 1.

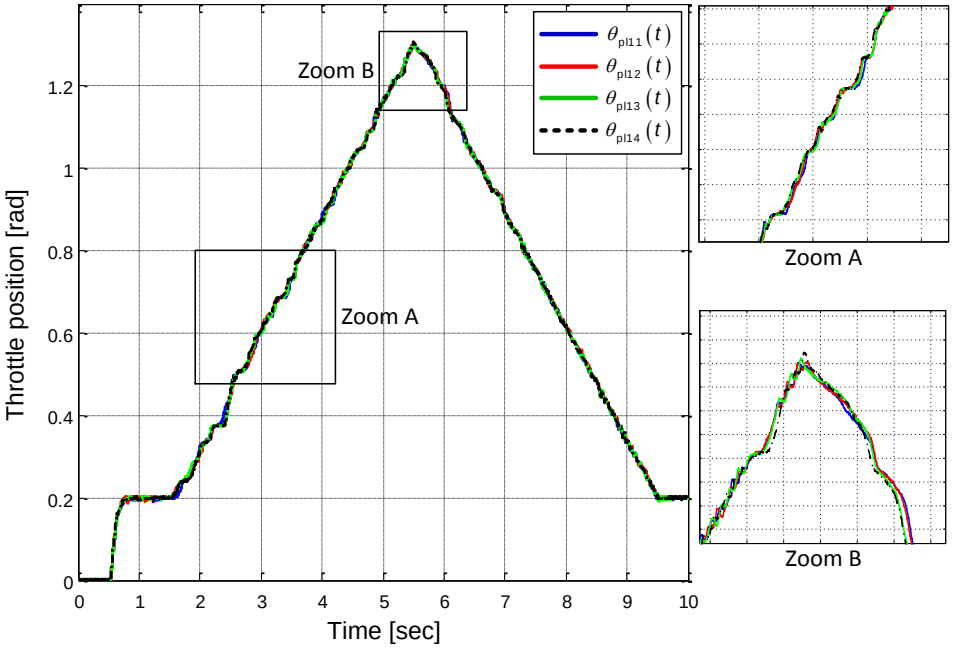

Figure 2.12: The same day friction repeatability experiment

This indicates very little experiment-to-experiment variations (Zoom A-B).

Figure 2.13 shows the superimposed results of two experiments carried out on two separate days.

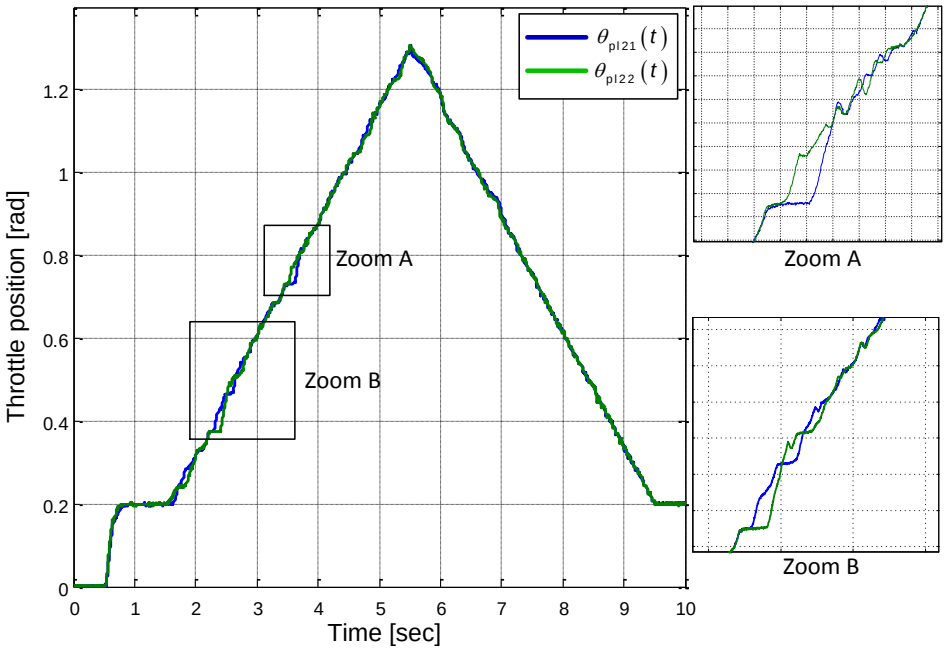

Figure 2.13: Different days friction repeatability experiment

This indicates more variation than in Figure 2.12. This experiment was repeated with a higher level of dither but this indicated no improvement.

To examine the ensemble variations in errors from one experimental run to the next, i.e., the randomness of the errors, accumulative errors for the above experiments were calculated. These are defined as

$$e_{a\,i,j}(t) = \int_0^t \left|\theta_{pl,i}(\tau) - \theta_{pl,j}(\tau)\right| d\tau,\ j = 1,2,\ k = 1,2,\ i \neq j \qquad (2.12)$$

Note that τ is the relative time in the sense that data from several data experimental runs, taken at different absolute times, are compared on the same time scale starting at $\tau = 0$. The rationale behind this is that the larger the ensemble variations between experimental run, *i,* and experimental run, *j*, the larger the mean slope of $e_{a\,i,j}(t)$ has to be, which must be positive. Only the first two experiments are included here, since four experiments have six associated

accumulative errors, which are considered sufficient. Figure 2.14 shows the results.

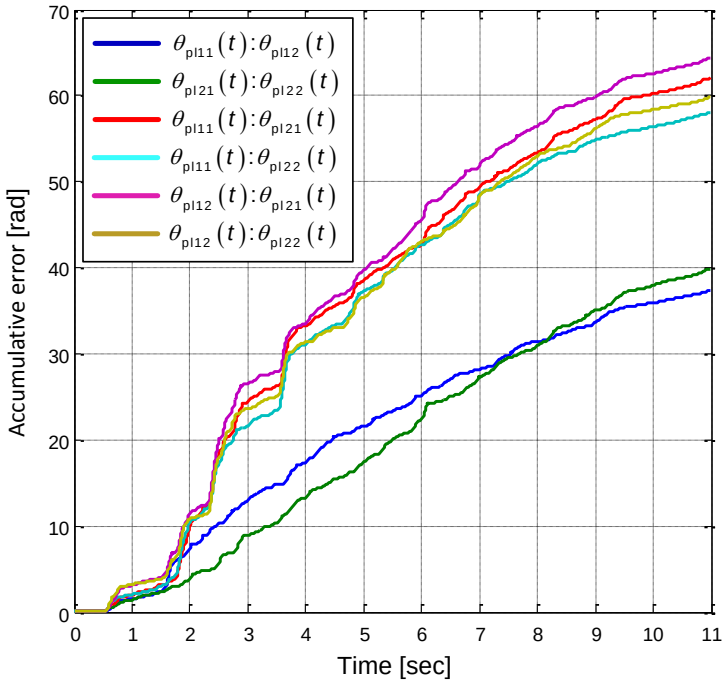

Figure 2.14: The experiments accumulated differences

The figure reflects the observation made by comparing Figure 2.12 with Figure 2.13 that the day-to-day experimental errors are greater than those for experiments performed on the same day. All the graphs of Figure 2.14 indicate considerable ensemble variations from one run to another, in all six combinations. This confirms the randomness of the friction in the throttle valve which makes it difficult to produce an accurate friction model for the purpose of direct compensation in the controller. The conclusion is that controller robustness must be relied upon to counteract the effects of friction in conjunction with added control dither. The control dither is explained in more details in a later chapter.

2.3.4 The Friction Model

Friction is considered to have three different components: the kinetic, Coulomb and static friction (Hensen, 2002)

- The kinetic friction is linear and dependent on the velocity, which is in many cases caused by the roughness of the surfaces.
- The Coulomb friction (steady friction) is constant but direction dependent.
- The static friction (stick-slip friction) is the measure of the friction force required to just start the relative motion commencing at zero velocity. This nonlinear friction can be substantial compared to the other friction components. The static friction can, in some cases, be dependent on the position of the mechanical components due to the randomness of the asperities on the surface (Hensen, 2002), but the modelling of this has not been included in this work.

The classical friction model of a bi-directional mechanical system, such as the throttle valve, illustrated by the velocity to torque transfer characteristic shown in Figure 2.15.

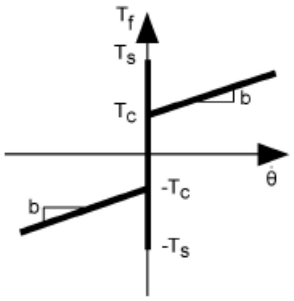

Figure 2.15: Classic friction model (Papadopoulos and Chasparis, 2002)

It comprises the three components already introduced:

i) Kinetic friction torque

$$\Gamma_{kinetic} = \omega \cdot k_{kinetic} \tag{2.13}$$

ii) Coulomb friction torque

$$\Gamma_{coulomb} = sign(\omega) \cdot k_{coulomb} \tag{2.14}$$

iii) Static (stick-slip) friction torque

$$\Gamma_{static} = \begin{cases} \Gamma_e, & |\Gamma_e| < \Gamma_s,\ \omega = 0,\ \dot{\omega} = 0 \\ \Gamma_s \cdot sign(\Gamma_e), & |\Gamma_e| > \Gamma_s,\ \omega = 0,\ \dot{\omega} \neq 0 \end{cases} \tag{2.15}$$

where Γ_e is the externally applied torque and Γ_s is the breakaway torque.

The proposed static friction model (Papadopoulos and Chasparis, 2002), has the drawback of inaccuracy around zero velocity. A generic friction model was proposed by (Haessig and Friedland, 1990) (Majd and Simaan, 1995) which includes a more realistic continuous transition between the breakaway torque and the sum of the kinetic and Coulomb torque. The nonlinear function used, however, is relatively complicated. To circumvent this, a new approach is presented by the author (Pedersen and Dodds, 2011) which is simpler and imposes a lower computational demand, as follows:

$$\Gamma_{total} = \left(\Gamma_{kinetic} + \Gamma_{Coulomb} + \Gamma_{static}\right) \cdot y_t \tag{2.16}$$

where $\Gamma_{coulomb}$, $\Gamma_{kinetic}$ are defined by equation (2.13) and (2.14). A transition section, defined by y_t, is introduced to smooth the zero crossing

$$y_t = \begin{cases} |\omega| / \omega_1, & \{\omega| - \omega_1 \leq \omega \leq \omega_1\} \\ 1, & \{\omega|\ \omega_1 \leq |\omega|\} \end{cases} \tag{2.17}$$

The static friction component has been modelled around a rectangular hyperbola function to form a similar shape to the one used in the classical friction model. Thus

$$\Gamma_{static} = \frac{A}{\dot{\theta} + |B| sign(\dot{\theta})} \tag{2.18}$$

where $A = \Gamma_1(B + \omega_1)$, $B = \dfrac{\Gamma_1\omega_1 - \Gamma_2\omega_2}{\Gamma_2 - \Gamma_1}$ and ω_1 together with ω_2 are defined in Figure 2.16.

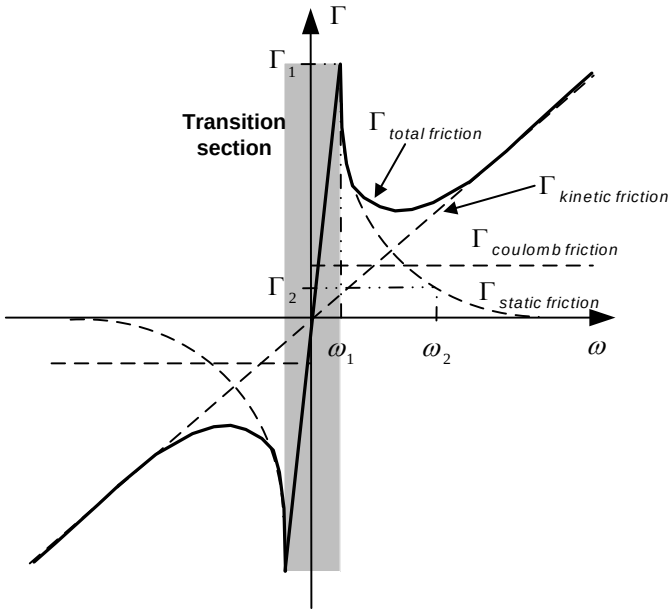

Figure 2.16: The new friction model and its components

In Figure 2.16, at zero velocity the friction is modelled as zero to increase the model stability. The slope in the transition section is large to decrease the impact on the static friction model. To simplify the parameterisation of the friction model the two parameters ω_1 and Γ_2 are set initially to constant values of 0.01 [rad/sec] and 0.001 [Nm].

Figure 2.17 shows a simplified implementation of the new friction model in block diagram form. This can be implemented in Simulink® by using standard blocks. In general it has to be emphasised that to get an accurate simulation result using Simulink® it is required to run the model in variable step mode and with zero crossing enabled.

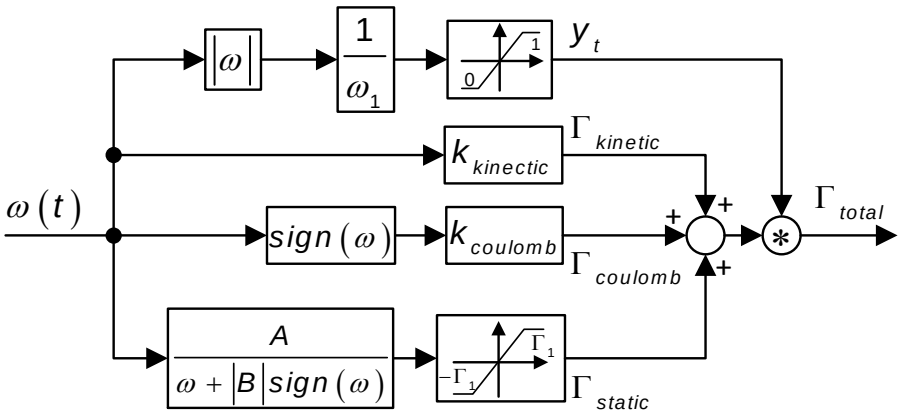

Figure 2.17: Friction model implementation

An output result from simulating the new friction model is shown in Figure 2.18. This is only an example and is not yet parameterised for the throttle valve.

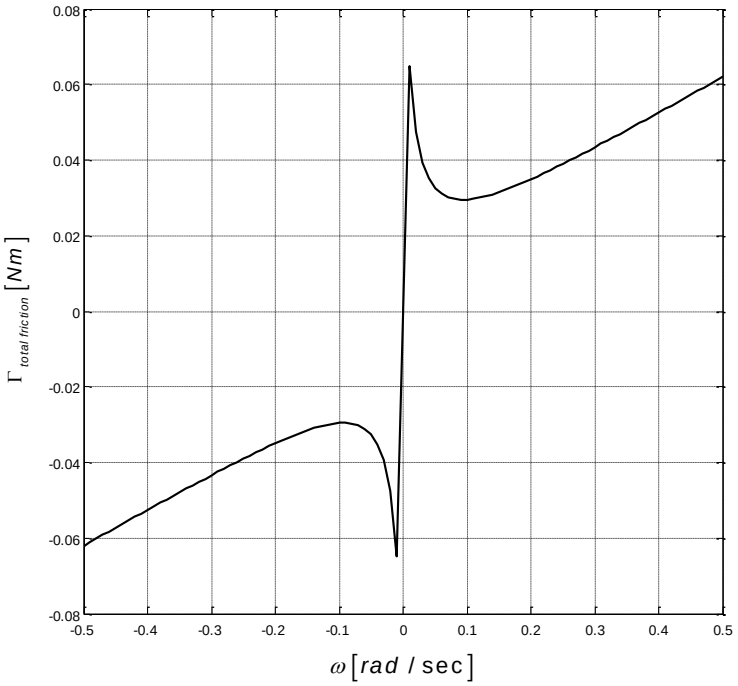

Figure 2.18: New friction model simulation

2.3.5 Hard Stops

The throttle plate has a limited operation range, normal from 0 to about 90°. These mechanical position constraints are called hard stops, see Figure 2.2. This can be modelled by a high gain control loop applying a torque sufficient to restrain the system between two fixed positions.

$$\Gamma_{hard\ stop} = \begin{cases} 0, & \theta_{pl_{\min}} \le \theta_{pl} \le \theta_{pl_{\max}} \\ k_{hard\ stop}\left(\theta_{pl} - \theta_{pl_{\max}}\right), & \theta_{pl} > \theta_{pl_{\max}} \\ k_{hard\ stop}\left(\theta_{pl} - \theta_{pl_{\min}}\right), & \theta_{pl} < \theta_{pl_{\min}} \end{cases} \tag{2.19}$$

Figure 2.19 shows how equation (2.19) can be implemented

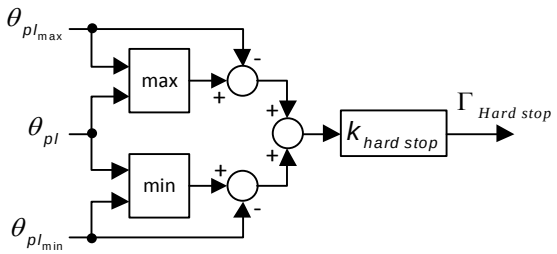

Figure 2.19: Hard stop model

This will apply a force equal to the sum for torques acting on the mechanical system. The position will obviously go beyond the minimum $\theta_{pl_{\min}}$ and maximum $\theta_{pl_{\max}}$ position but by a negligible amount for $k_{hard\ stop}$ sufficiently large (100). A similar strategy is used by Mathworks® in some of their Simulink® models.

2.4 Linear System Model

The mechanical and electrical models are combined in this subsection to form a linear state space model (subsection 2.4.1) and a transfer function (subsection 2.4.2) for the throttle system.

The linear throttle model is based on the equations of the previous sections but does not include the hard stops and the extended friction model. First, using equations (2.3) and (2.5),

$$\frac{dI_a(t)}{dt} = \frac{1}{L_a}\left(V_{in} - i_a \cdot R_a - k_e \cdot \frac{d\theta_{pl}(t)}{dt} \cdot \frac{N_{pl}}{N_m}\right) \tag{2.20}$$

when using equation (2.10)

$$\Gamma_m \frac{N_{pl}}{N_m} = J_x \cdot \frac{d^2\theta_{pl}}{dt^2} + k_{kinetic} \cdot \frac{d\theta_{pl}(t)}{dt} + \theta_{pl} \cdot k_{spring} \tag{2.21}$$

$$\frac{d^2\theta_{pl}}{dt^2} = \frac{1}{J_x}\left(\Gamma_m \frac{N_{pl}}{N_m} - k_{kinetic} \cdot \frac{d\theta_{pl}(t)}{dt} - \theta_{pl} \cdot k_{spring}\right) \tag{2.22}$$

A model of the complete system, shown in Figure 2.20, can be obtained using equation (2.1), (2.20) and (2.22)

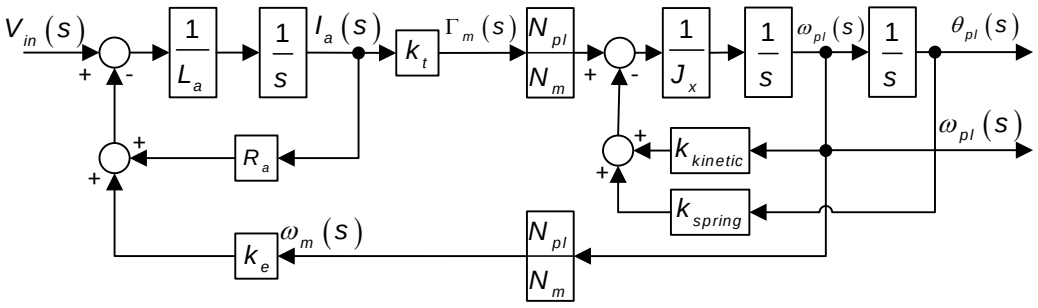

Figure 2.20: Linear throttle model

2.4.1 State Space Model

Since the block diagram model of Figure 2.20 comprises three interconnected first order subsystems, when expressed in the time domain, it becomes a state space model, the general form of which is shown in Figure 2.21.

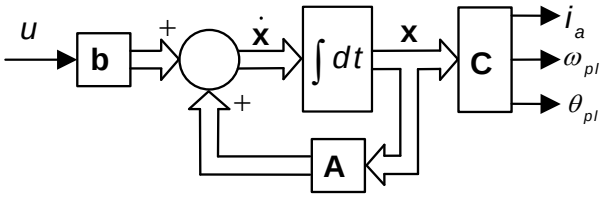

Figure 2.21: State variable block diagram

Figure 2.20 leads directly to the physical state representation in which the state variables are physical variables of the plant, i.e.,

$$x_1 = i_a \tag{2.23}$$

$$x_2 = \omega_{pl} \tag{2.24}$$

$$x_3 = \theta_{pl} \tag{2.25}$$

The state space equations corresponding to Figure 2.21 are as follows:

$$\dot{\mathbf{x}} = \mathbf{A}\mathbf{x} + \mathbf{b}u \tag{2.26}$$

$$y = \mathbf{C}\mathbf{x} \tag{2.27}$$

As shown in Figure 2.21, the measurement variables are the physical state variables, $y_i = x_1$, $y_\omega = x_2$ and $y_\theta = x_3$ and therefore $\mathbf{C} = \mathbf{I}^{(3)}$, where $\mathbf{I}^{(3)}$ is the unit matrix of dimension, 3×3.

Note that the measurement equation is often shown as $y = \mathbf{C}\mathbf{x} + \mathbf{D}u$, but in this case, $\mathbf{D} = 0$, since none of the state variables can respond instantaneously to a step change in the control input, $u(t) = v_{\text{in}}(t)$. This is true for nearly all physical plants. Substituting for i_a, ω_{pl} and θ_{pl} in equations (2.20) and (2.22) using equations (2.23), (2.24) , (2.25) and (2.1) yields

$$\dot{x}_1 = \frac{1}{L_a}\left(v_{in} - x_1 \cdot R_a - k_e \cdot x_2 \cdot \frac{N_{pl}}{N_m} \right) \tag{2.28}$$

and

$$\dot{x}_2 = \frac{1}{J_x}\left(k_t \cdot x_1 \frac{N_{pl}}{N_m} - k_{kinetic} \cdot x_2 - x_3 \cdot k_{spring} \right) \tag{2.29}$$

and the third state differential equation follows from equations (2.24) and (2.25) as

$$\dot{x}_3 = \omega_{pl} = x_2 \tag{2.30}$$

The plant matrix corresponding to the state differential equations, (2.28), (2.29) and (2.30) is

$$\mathbf{A} = \begin{bmatrix} -\frac{R_a}{L_a} & -\frac{k_e \cdot N_{pl}}{L_a \cdot N_m} & 0 \\ \frac{k_t \cdot N_{pl}}{J_x \cdot N_m} & -\frac{k_{kinetic}}{J_x} & -\frac{k_{spring}}{J_x} \\ 0 & 1 & 0 \end{bmatrix} \tag{2.31}$$

and the input matrix is

$$\mathbf{b} = \begin{bmatrix} \frac{1}{L_a} \\ 0 \\ 0 \end{bmatrix}. \tag{2.32}$$

As stated above, the output matrix is

$$\mathbf{C} = \begin{bmatrix} 1 & 0 & 0 \\ 0 & 1 & 0 \\ 0 & 0 & 1 \end{bmatrix} \tag{2.33}$$

The complete state space model is therefore as follows

$$\begin{bmatrix}\dot{x}_1\\ \dot{x}_2\\ \dot{x}_3\end{bmatrix}=\begin{bmatrix}-\frac{R_a}{L_a} & -\frac{k_e\cdot N_{pl}}{L_a\cdot N_m} & 0\\ \frac{k_t\cdot N_{pl}}{J_x\cdot N_m} & -\frac{k_{kinetic}}{J_x} & -\frac{k_{spring}}{J_x}\\ 0 & 1 & 0\end{bmatrix}\cdot\begin{bmatrix}x_1\\ x_2\\ x_3\end{bmatrix}+\begin{bmatrix}\frac{1}{L_a}\\ 0\\ 0\end{bmatrix}u \tag{2.34}$$

$$\begin{bmatrix}i_a\\ \omega_{pl}\\ \theta_{pl}\end{bmatrix}=\begin{bmatrix}1 & 0 & 0\\ 0 & 1 & 0\\ 0 & 0 & 1\end{bmatrix}\cdot\begin{bmatrix}x_1\\ x_2\\ x_3\end{bmatrix} \tag{2.35}$$

2.4.2 Transfer Function

The plant transfer function is needed for the design of some of the controllers. Mason's rule can be used to find the transfer function from the block diagram of Figure 2.20. Mason's rule states that the transfer function of the signal flow graph is (Franklin et al., 2002)

$$G(s)=\frac{Y(s)}{U(s)}=\frac{1}{\Delta}\sum_i G_i\Delta_i \tag{2.36}$$

where G_i is the forward path gain, Δ the system determinant given by

$$\Delta=1-\sum\text{loop gains}+\sum\text{products of non-touching loops taken two at a time}\ -\ldots \tag{2.37}$$

and Δ_i are the forward path determinants (due to loops that do not touch the paths). Since the block diagram conveys the same information as the signal flow graph, it will be sufficient to refer to Figure 2.20. The plant determinant may then be found as

$$\begin{aligned}\Delta=1+&\frac{R_a}{L_a}\frac{1}{s}+\frac{k_{kinetic}}{J_x}\frac{1}{s}+\frac{k_{spring}}{J_x}\frac{1}{s^2}+\frac{k_e}{L_a}\frac{k_t}{J_x}\frac{1}{s^2}\left(\frac{N_{pl}}{N_m}\right)^2+\\ &\frac{R_a}{L_a}\frac{k_{kinetic}}{J_x}\frac{1}{s^2}+\frac{R_a}{L_a}\frac{k_{spring}}{J_x}\frac{1}{s^3}\end{aligned} \tag{2.38}$$

In this case, there is only one forward path gain,

$$G_1 = \frac{1}{L_a}\frac{1}{s}k_t\frac{N_{pl}}{N_m}\frac{1}{J_x}\frac{1}{s^2} \tag{2.39}$$

and all four loops touch the forward path, giving $\Delta_1 = 1$. In this case equation (2.36) reduces to

$$G(s) = \frac{Y(s)}{U(s)} = \frac{G_1}{\Delta} \tag{2.40}$$

Substituting for G_1 and Δ in equation (2.40) using equation (2.38) and (2.39) then yields the plant's transfer function in the form,

$$\frac{Y_\theta(s)}{V_{in}(s)} = \frac{b_0}{s^3 + a_2 s^2 + a_1 s + a_0} \tag{2.41}$$

where the coefficients are given by

$a_0 = R_a k_{spring} / (L_a J_x)$

$a_1 = k_{spring} / J_x + k_e k_t / (L_a J_x)(N_{pl} / N_m)^2 + R_a k_{kinetic} / (L_a J_x)$

$a_2 = R_a / L_a + k_{kinetic} / J_x$

$b_0 = k_t N_{pl} / (L_a N_m J_x)$

Another state space model may be formed directly from the transfer function equation (2.41) with the control canonical state representation, as shown in Figure 2.22 in the Laplace domain.

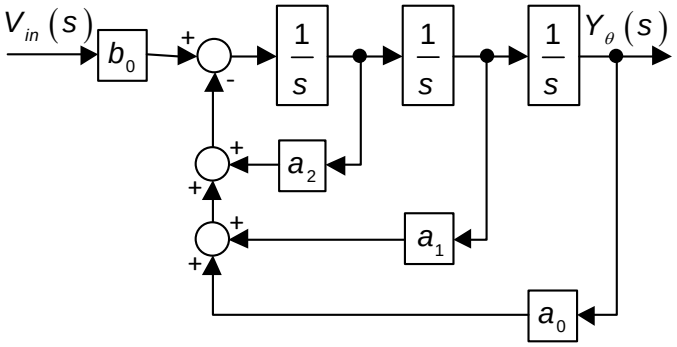

Figure 2.22: Linear throttle model in control canonical form

2.5 Nonlinear System Model

In this subsection, the linear model developed in the previous subsection is extended to include three significant mechanical nonlinearities comprising

a) the hard stops

b) the static friction

c) the Coulomb friction

While the linear model is convenient for the control system design, modelling these nonlinearities makes it possible to model throttle valve behaviour more accurately. The resulting nonlinear model is used for predicting the performances yielded by the different control strategies before they are tested on the experimental setup. A block diagram of the complete plant model including these nonlinearities is shown in Figure 2.23.

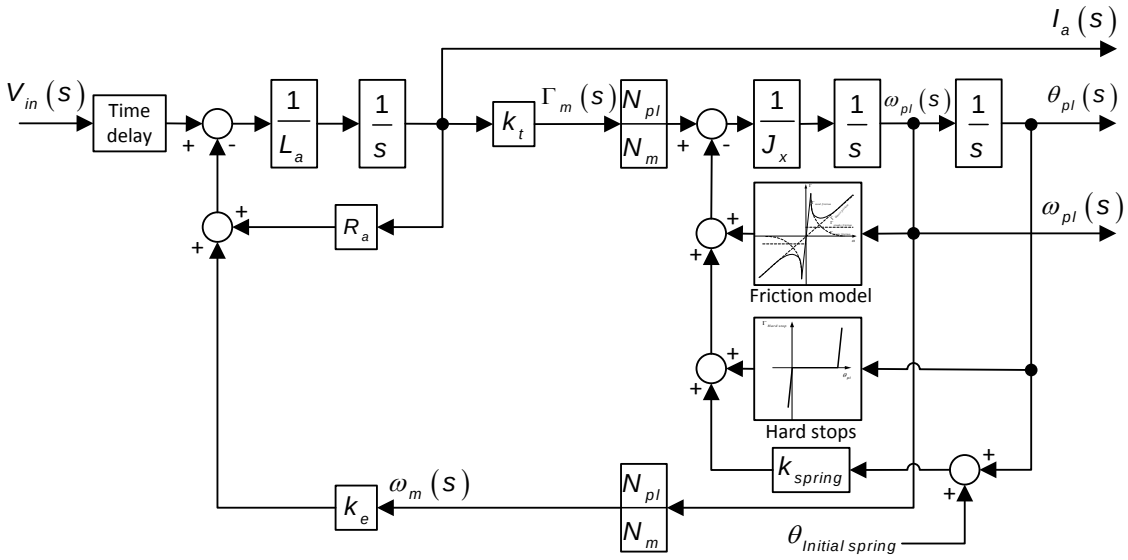

Figure 2.23: Nonlinear throttle model

The hard stop model represents the limits of the throttle plate movement imposed by the mechanical design of the throttle. As described in subsection 2.3.5, the hard stop model only introduces a restraint torque if the throttle plate position exceeds the predefined minimum and maximum positions. This feature is essential to keep the throttle plate within limits when the pre-stressed coil spring torque is applied.

In addition to the nonlinearities, two more features are introduced to make the model more realistic, as follows:

i) The pre-stressed coil spring offset torque, already introduced in subsection 2.3.1, is modelled by adding a constant angle, $\theta_{Initial\ spring}$, to the variable throttle angle, θ_{pl}, before the spring constant, k_{spring}.

ii) A pure time delay block is introduced at the input to model the delay introduced by the pulse width modulation of the H-bridge driver circuits in the armature circuit of the DC motor, and the sampling process.

Certain nonlinear phenomena have not been modelled, as the experimental work is considered sufficient to assess the effects on the control system performance. The first is the cogging torque from the gear train between the DC motor output shaft and the throttle plate. This is only predicted to have a minor effect on the system during transients and no great effect on the position control accuracy. The second is position dependent static friction. As this will vary significantly from one throttle valve to the next due to manufacturing tolerances, it is unpredictable. The approach adopted is therefore to set the parameters of the position independent friction model described above to yield friction levels at least equal to the maximum ones expected in practice.

2.6 Reduced Order Linear System Model

The third order linear throttle valve model, shown in Figure 2.20, can be reduced to a second order model by eliminating the inductance L_a. This is possible since the time constant, L_a/R_a, is relatively small. With reference to Appendix A.2, $L_a = 8.372 \cdot 10^{-4}\ [H]$ and $R_a = 2.795\ [Ohms]$, giving $L_a/R_a \cong 3 \cdot 10^{-4}$ [sec]. This is so small compared with the required control loop settling time, which is set to 0.1 [sec] in this work, that the exponential mode associated with this electrical time constant will not have a significant effect. With reference to Figure 2.20, it should be noted that the presence of the back e.m.f. loop of the model will mean that the electrical time constant will not have precisely the value, R_a/L_a, but it will be of the same order. The reduced order model is then Figure 2.20 with the inductance removed, as shown in Figure 2.24.

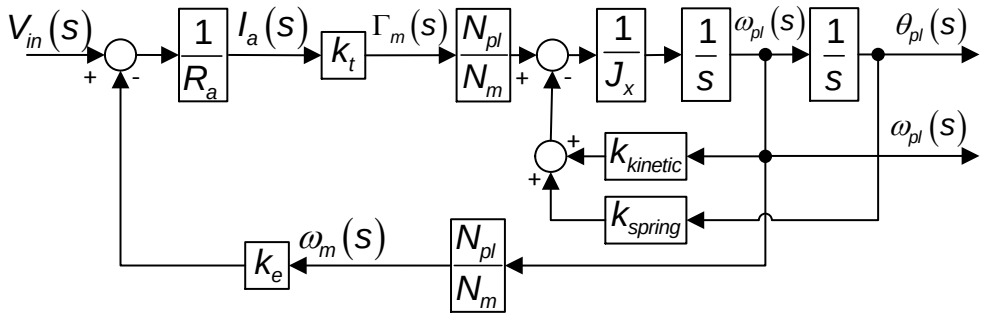

Figure 2.24: Second order throttle valve model

Using Mason's rule to find the transfer function gives

$$\frac{Y_\theta(s)}{V_{in}(s)} = \frac{b_0}{s^2 + a_1 s + a_0} \tag{2.42}$$

where the coefficients are given by

$$a_0 = k_{spring} / J_x$$

$$a_1 = k_t / R_a \cdot k_e / J_x \left(N_{pl} / N_m\right)^2 + k_{kinetic} / J_x$$

$$b_0 = k_t N_{pl} / \left(R_a N_m J_x\right)$$

3 Model Parameterisation

The lack of datasheets for the throttle valve made it necessary to measure and estimate all the parameters needed to form an accurate model. The approach taken is referred to as grey box parameter estimation. This is a cross between white box and black box parameter estimation. In white box parameter estimation, the individual components of the plant are modelled using basic physical principles. At the other extreme, black box parameter estimation completely ignores the internal physical structure of the plant and uses observations of the measured output responses to given inputs to fit a mathematical model by calculation of the constant coefficients. Grey box estimation is usually applied where white box estimation is preferred but is only applied to a subset of the physical components for which it is practicable. A set of subsystems is then identified that contains all the remaining components and the black box approach is applied to these subsystems.

In pursuance of the white box approach, the throttle valve was disassembled to measure parameters such as the diameter of the gear wheels and the DC motor voltage constant, k_e. Some parameters such as the moment of inertia and static friction could not be measured directly due to lack of appropriate equipment or lack of sufficient precision even with the best available equipment. To extract those parameter values from the plant, the parameter estimation tool was used from the *Simulink Design Optimization* toolbox from Mathworks®. The parameter estimation tool uses measurements of the real plant's inputs and outputs. The tool adjusts the model parameters such, with the same input, that the models output response follows that of the real plant within certain tolerances. A set of measurements from the assembled throttle valve was collected, each with a different input voltage waveform to improve the parameter estimation.

3.1 Parameter Measurement

The measured parameters are defined below together with the values obtained.

3.1.1 Gear Ratio

With reference to Figure 2.1, the following dimensions and ratios were determined:

- DC-motor tooth wheel: Ø 11.5 mm
- Gear link tooth wheel (1): Ø 41.5 mm
- Gear link tooth wheel (2): Ø 16 mm
- Throttle plate tooth wheel: Ø 51 mm

Ratio 1 (DC-motor / gear link 1): 41.5/11.5 ~ 3.6

Ratio 2 (gear link 2 / throttle plate): 51/16 ~ 3.2

Total gear ratio between the DC-motor and the throttle plate N_{pl} / N_m: 11.5

3.1.2 DC Motor Voltage Constant

The simplest approach to determine the constant, k_e [V/(rad/sec)], is to drive the DC motor at a constant speed (by an external electric motor), and measure the output voltage of the unloaded motor. Unfortunately this was not possible with the equipment available and a different approach had to be adopted. The DC motor is disconnected from the gear system and a DC voltage supply is connected to its terminals. Before starting the test a reflection pad is attached to the DC motors shaft to measure its speed by a light reflection speed meter. The test is done with two different voltages, 2, 2.5 and 3 [V] and the speeds recorded: (66.46, 89.4, 114.61) [rad/sec]. The value of k_e is found to be to 0.021 [V/(rad/sec)], on the assumption that the measurements lie on a straight line and the DC motor current is small. Further the kinetic friction for the DC

motor is assumed to be small. This value is used in the initiation of the parameter estimation tool.

3.1.3 DC Motor Resistance

A DC voltage is applied to the motor terminals and the current is measured. Then the resistance R_a is calculated ($R_a = 3.1$ [Ohm]) by using Ohm's law. This test has been done at zero speed to eliminate the effect of the back e.m.f. The value obtained was used in the initiation of the parameter estimation tool.

3.1.4 DC motor inductance

The inductance is measured using by a digital LCR meter (Wheatstone bridge). The measured inductance (Table 3.1) depends on the frequency used by LCR meter due to the eddy current losses in the ferromagnetic inductor core material. The LCR meter voltage is set to 1 [V] peak-to-peak.

Table 3.1 Measured DC motor inductance

Measurement frequency [kHz]	Measured inductance [mH]
1	0.76
5	0.60
10	0.52
50	0.36
100	0.31

The PWM switch frequency used in the experiments for the parameterisation was 2 kHz and therefore the value 0.72 [mH] was chosen. The value found is used as initial value for the parameter estimation tool.

3.1.5 DC Motor Torque Constant

The DC motor torque constant k_t, can be found by a load test where the DC motor is run with constant load and its current is measured. It was not possible to do this test due to the lack of equipment. Instead it was assumed to be equal to the DC motor voltage constant (Mohan et al., 1995)(Page 377-378), i.e., k_e already estimated in subsection 3.1.2.

3.1.6 DC motor moment of inertia and the kinetic friction

Due to limitations in the measurement setup it is not possible to measure the DC motors speed when disconnected from the throttle valve system. The DC motor current is the only available measurement which can be logged. It is necessary to find a way to measure/calculate the DC motor moment of inertia and the kinetic friction which only depends on the DC motor current. A simplified version of the DC motor model presented in section 2.4 is shown in Figure 3.1 in which the armature inductance has been ignored on the basis that the electrical time constant, L_a/R_a, is much smaller than the mechanical time constant, $J_m / k_{kinetic}$.

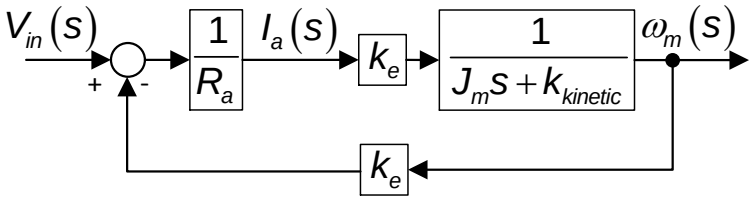

Figure 3.1: Simplified DC motor model

Here, R_a is the armature resistance, k_e is the motor constant, J_m is the armature moment of inertia and $k_{kinetic}$ the DC motor's kinetic friction constant. The parameters, k_t, R_a and k_e were found from the previous subsections.

The transfer function from $V_{in}(s)$ to $I_a(s)$ is

$$\frac{I_a(s)}{V_{in}(s)} = \frac{\frac{1}{R_a}}{1+\left(\frac{1}{R_a}k_e{}^2\frac{1}{J_m s + k_{kinetic}}\right)} = \frac{\left(\frac{J_m}{R_a}s + \frac{k_{kinetic}}{R_a}\right)\left(\frac{1}{k_{kinetic} + k_e{}^2 / R_a}\right)}{1+s\frac{J_m}{k_{kinetic} + k_m{}^2 / R_a}} \tag{3.1}$$

The DC motor kinetic friction, $k_{kinetic}$, is assumed to be the predominant load in the steady state. Using equation (3.1) in steady state ($s \to 0$) and solve for $k_{kinetic}$

$$I_{a_{ss}}(s) = \frac{\frac{k_{kinetic}}{R_a}}{k_{kinetic} + k_e{}^2 / R_a} V_{in_{ss}}(s) \Rightarrow k_{kinetic} = \frac{I_{a_{ss}}(s)\frac{k_e{}^2}{R_a}}{V_{in_{ss}}(s)/R_a - I_{a_{ss}}(s)} \tag{3.2}$$

where $I_{a_{ss}}$ and $V_{in_{ss}}$ are the DC motor current and input voltage in the steady state. The transient response of the fictional subsystem, $I_a(s)/V_{in}(s)$, without zeros is,

$$\frac{X(s)}{V_{in}(s)} = \frac{1}{1+s\frac{J_m}{k_{kinetic} + k_e{}^2 / R_a}}, \tag{3.3}$$

will be

$$x(t) = V_{in}\left[1 - e^{-t/T}\right], \tag{3.4}$$

where $T = J_m / \left[k_{kinetic} + k_e{}^2 / R_a\right]$ with unit [sec]. Using the above,

$$i_a(t) = \frac{k_{kinetic}}{R_a}\frac{1}{k_{kinetic} + k_e{}^2 / R_a}x(t) + \frac{J_m}{R_a}\frac{1}{k_{kinetic} + k_e{}^2 / R_a}\frac{d}{dt}\left[x(t)\right] \tag{3.5}$$

Using equation (3.5) and (3.4)

$$i_a(t) = \frac{V_{in}}{k_{kinetic} + k_e{}^2 / R_a}\left[\frac{k_{kinetic}}{R_a}\left(1 - e^{-t/T}\right) + \frac{J_m}{R_a T}e^{-t/T}\right] = \frac{V_{in}}{k_{kinetic} + k_e{}^2 / R_a}\left[\frac{k_{kinetic}}{R_a}\left(1 - e^{-t/T}\right) + \left(\frac{k_{kinetic} + k_e{}^2 / R_a}{R_a}\right)e^{-t/T}\right] \tag{3.6}$$

At $t = T$

$$i_a(T) = \frac{V_{in}}{k_{kinetic} + k_e{}^2 / R_a}\left[\frac{k_{kinetic}}{R_a}\left(1 - e^{-1}\right) + \left(\frac{k_{kinetic} + k_e{}^2 / R_a}{R_a}\right)e^{-1}\right] \tag{3.7}$$

The calculated value, $i_a(T)$, is used to log the point in time where the measured DC motor current, from the experiment, passes the value $i_a(T)$. The logged point in time is then used to calculate the DC motor moment of inertia by

$$T = J_m / \left[k_{kinetic} + k_e{}^2 / R_a\right] \Rightarrow$$
$$J_m = T\left(k_{kinetic} + k_e{}^2 / R_a\right) \tag{3.8}$$

The DC motor is disconnected from the gear system and a voltage step, $V_{in}(0) = 2$, is applied to its input terminals while the input current $i_a(t)$ is measured. Figure 3.2 shows the measured current, the calculated steady state current $i_{a_{ss}}(t)$ and the value of $i_a(T)$ found by equation (3.7). The ripple on the current is caused by the power electronics driving the DC motor.

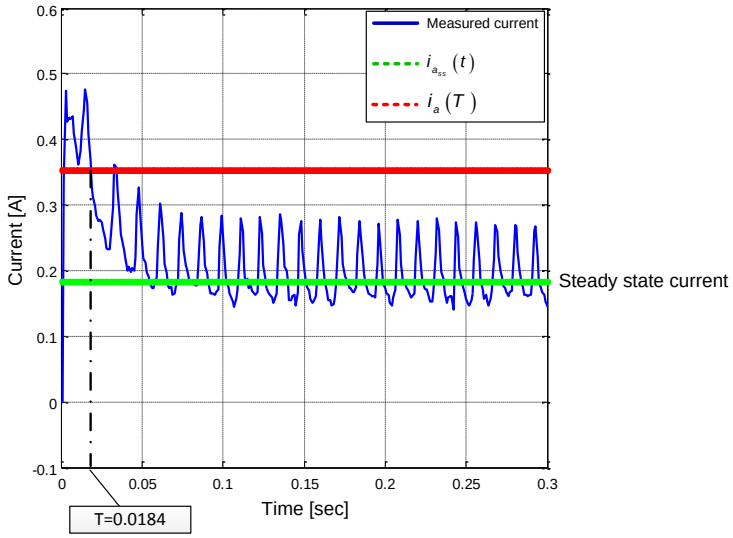

Figure 3.2: Measured current and the value $i_a(T)$

First the steady state current and the voltage is used to find the kinetic friction, $k_{kinetic} = 5.6 \cdot 10^{-5}$ $[Nm/(rad/\sec)]$ from equation (3.2). The value for $i_a(T)$ is found from equation (3.7) and the point in time where the measured current passes $i_a(T)$ is found by visual inspection in Figure 3.2, for $T = 0.0184$ [sec]. This time is inserted in equation (3.8) from which the DC motor's moment of inertia is calculated $J_m = 3.7 \cdot 10^{-6}$ $[Kg\,m^2]$.

The calculated values of $k_{kinetic}$ and J_m were then used to find a calculated value of $i_a(t)$ by using equation (3.6), and a simulated value of $i_a(t)$ by using the system in Figure 3.1. The result is shown Figure 3.3.

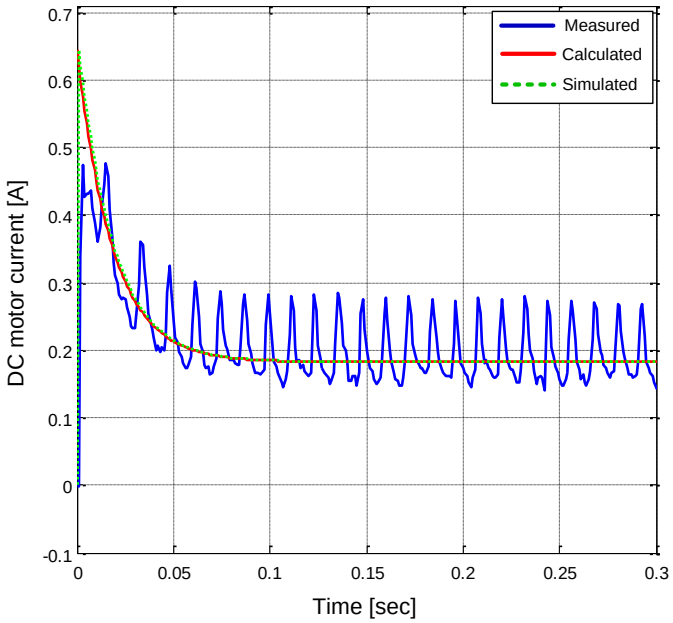

Figure 3.3: DC motor friction and moment of inertia validation

This confirms the accuracy of the method. Hence these values are used as the initial values for the parameter estimation tool.

3.1.7 Throttle Valve System Moment of Inertia

The throttle valve mechanical system contains different components such as the plate and gear wheels, which all contribute to the moment of inertia. Estimation of this part of the mechanical system is impracticable with the procedure of subsection 3.1.6, due to the systems hard stops. Instead, approximate calculations of the moment of inertia contributions of the plate, shaft and gear wheels were carried out on the basis of identifying mass elements and their radii of gyration from their centres of rotation. The net moment of inertia contribution is used in the initiation of the parameter estimation tool.

3.1.8 The Coil Spring

An estimate of the coil spring constant (k_{spring}) and the coil spring initial torque ($= \theta_{Initial\ spring} \cdot k_{spring}$) is done by using a hanging scale [kg] as a torque meter and the throttle position sensor (Figure 3.4). The DC motor is mechanically disconnected from the gear train to minimise the static friction and cogging torque. Two pieces of sheet metal with holes in the end are clamped onto the valve plate. This is used as an extension for the hanging scale to be attached. A piece of string is fastened to the extension and attached to the hanging scale in the other end. The hanging scale is used to measure the force needed to move the throttle plate away from the initial position and then from one position to another. The position is measured by attaching a voltage meter to the position sensors output.

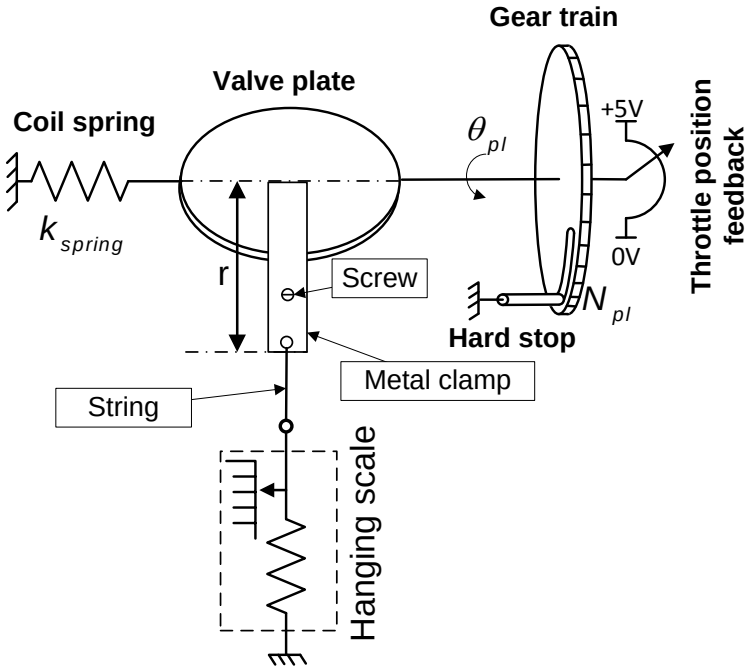

Figure 3.4: Measure of the coil spring torque

The initial torque needed to move the plate

$$\Gamma_0 = r \cdot F = r\left(m \cdot a\right) = 0.144 \cdot 0.21 \cdot 9.81 = 0.297 \tag{3.9}$$

Moving the plate to a position (= 27°) before the metal clamp extension touches the throttle body

$$\Gamma_1 = r \cdot F = r\left(m \cdot g\right) = 0.144 \cdot 0.25 \cdot 9.81 = 0.3532 \tag{3.10}$$

where F is force in the string and g the standard gravity.

The spring constant

$$k_{spring} = \frac{\Gamma_1 - \Gamma_0}{\theta_1 - \theta_0} = 0.120\left[Nm / Rad\right] \tag{3.11}$$

where $\theta_0 = 0$ and $\theta_1 = 27° / 180 \cdot \pi$

The coil spring initial torque in units of Rad

$$\theta_{Initial\ spring} = \frac{\Gamma_0}{k_{spring}} = 2.5\left[Rad\right] \tag{3.12}$$

These values are used as the initial values for the parameter estimation tool.

3.1.9 Hard Stops

The mechanical properties of the hard stops were not regarded as being in scope of this project. It was considered sufficient to set an initial value of 50 for the gain of the position restraint loop in the simulation representing the hard stops. This was used in the initiation of the parameter estimation tool.

The maximum throttle position was measured to be $\approx 90°$. The minimum has been set at $-0.1°$ to enable linear operation in the simulation around $0°$, without actuating the hard stop restraint.

3.1.10 Throttle Valve System Kinetic Friction

Estimation of the kinetic friction of the mechanical system driven by the DC motor using the method presented in subsection 3.1.6 is impracticable due to the system's hard stops. The parameter estimation tool was therefore entirely relied upon for estimation of this kinetic friction component.

3.1.11 Static and Coulomb Friction

For the reason explained in subsection 3.1.10, the static and Coulomb friction was estimated using the parameter estimation tool, noting that this is not restricted to linear systems.

3.2 Parameter Estimation

3.2.1 Introduction

The *Simulink Design Optimization* toolbox from Mathworks® was used to estimate the parameters offline and improve the accuracy of the calculated and measured parameters.

First the measured input and output data from tests done on the real plant are imported into the tool. The measured input data is automatically applied to a plant model, running in Simulink, by the tool. Before the first run an initial parameter set is loaded, which is defined by the user. After each simulation run the tool adjusts the model parameters to minimise the error between the measured real plant outputs and the model outputs as illustrated in Figure 3.5. This process is repeated a number of times until the error is lower than a specified value. The parameter estimation tool can run the model with various sets of measured data in order to include variations from different running conditions.

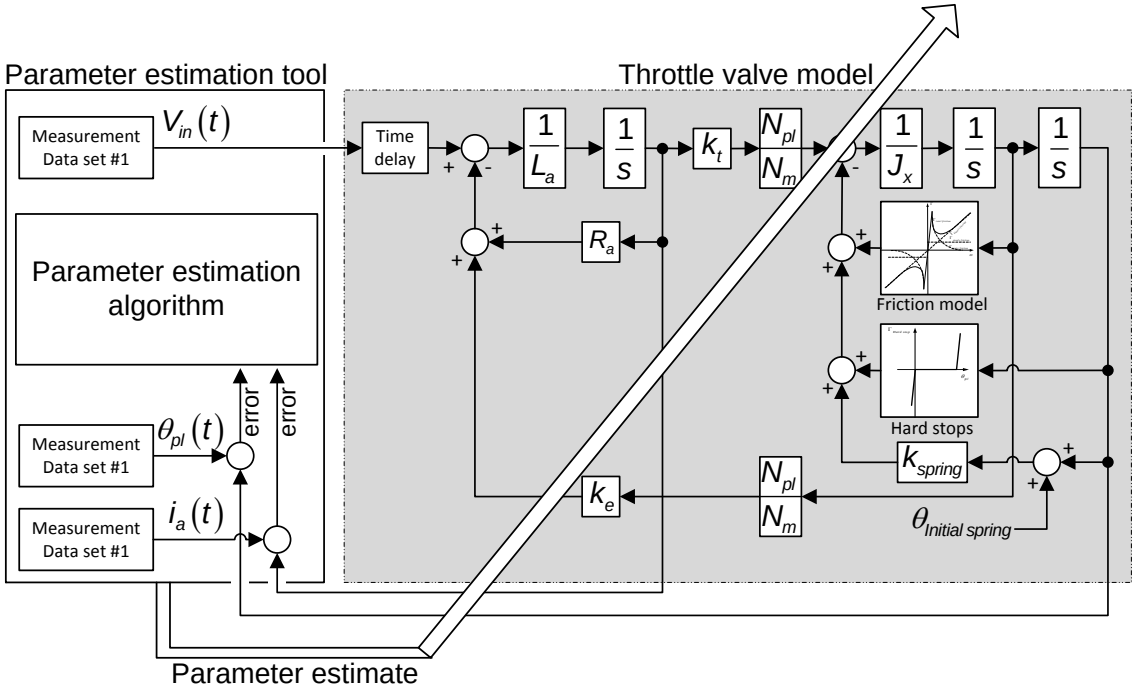

Figure 3.5: Parameter estimation using the toolbox from Mathworks®

To maximise the accuracy, the estimation was split into two parts:

1. The DC motor model parameters estimated using measurements of the DC motor current and the corresponding armature voltages. The resulting parameter estimates were used in the overall throttle valve estimation of part two.
2. The throttle valve model parameters estimated with various sets of measurements selected to make the estimation more precise and fit various running conditions.

3.2.2 DC Motor Model Parameters

The DC motor parameters were estimated using three sets of data, as shown in Figure 3.6. These were chosen to get a good estimate of k_e, L_a, R_a and the time delay. To get a good estimate of the parameter k_e (and k_t) the DC motor speed has to be greater than zero, while an input voltage step will excite the

dynamics of the current giving a better estimate of L_a. The initial parameter set used for this is specified in subsection 3.1.

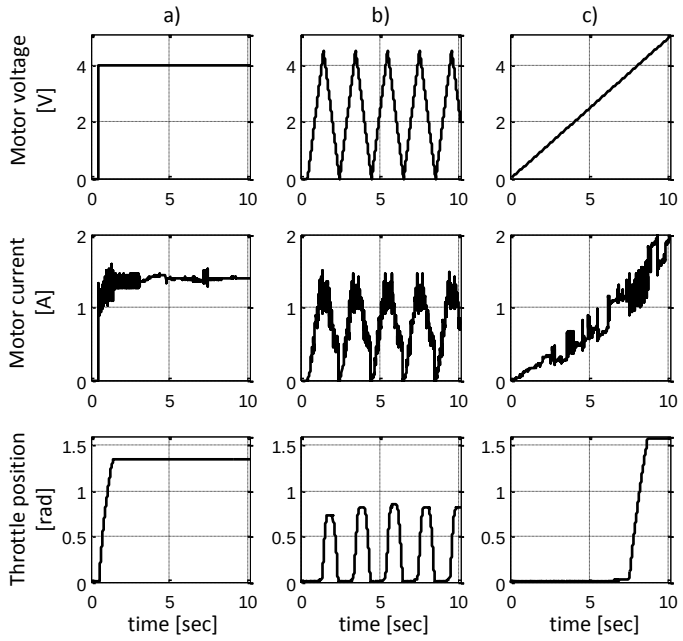

Figure 3.6: Measurement data used for the DC motor model parameter estimation

The data logged DC motor armature voltage and velocity were used as input signals to the DC motor model while the DC motor current was used as an output reference, as shown in Figure 3.7. The DC motor velocity was derived by differentiating the low pass filtered throttle position signal. The three data sets were repeatedly set to run by the parameter estimation tool to get a good estimate of k_e, L_a, R_a and the time delay.

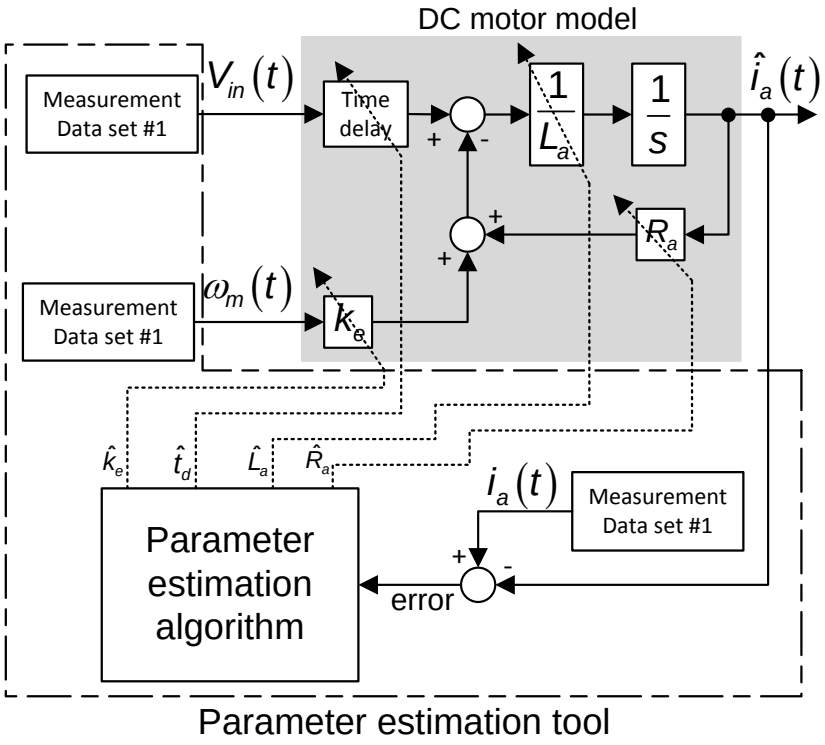

Figure 3.7: Estimation of the DC motor parameters

The result of this parameter fit was used to initiate the estimation of all the throttle valve model parameters.

3.2.3 Throttle Valve Model Parameters

Estimating all the throttle valve's parameters is accomplished using 17 different data sets with various input voltage waveforms. A subset of the data set used for this parameter estimation can be seen in Figure 3.8. The motor voltage was used as input signal to the throttle valve model while the throttle valve position and DC motor current were used as output references. The parameter estimation tool allows weighting factors to be imposed on all the data used as reference. This feature was used to down-scale the impact of the DC motor current on the estimation result. This was done to obtain a better fit with the throttle valve position, since this is the controlled output and therefore more important.

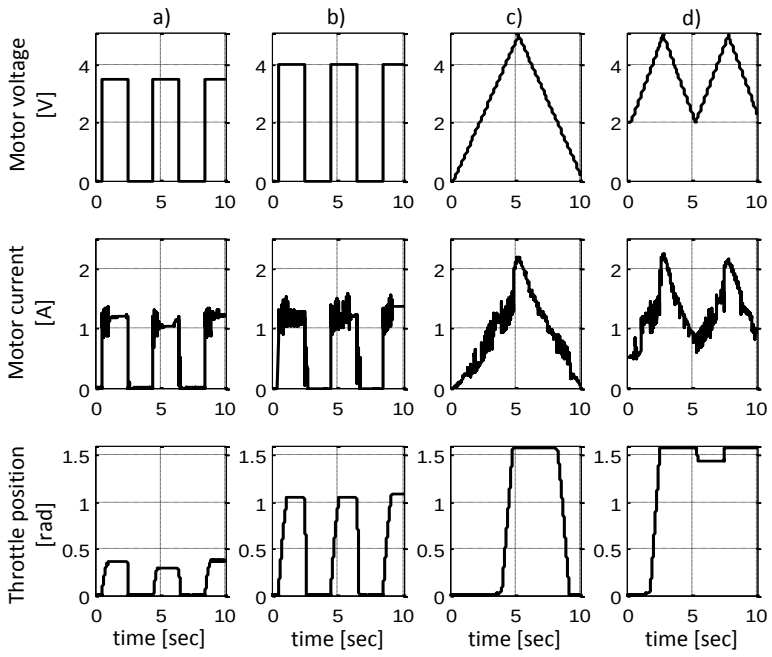

Figure 3.8: A subset of the data sets used for the throttle valve model parameter estimation

The nonlinear model is shown in Figure 3.9 together with the final parameter estimates .

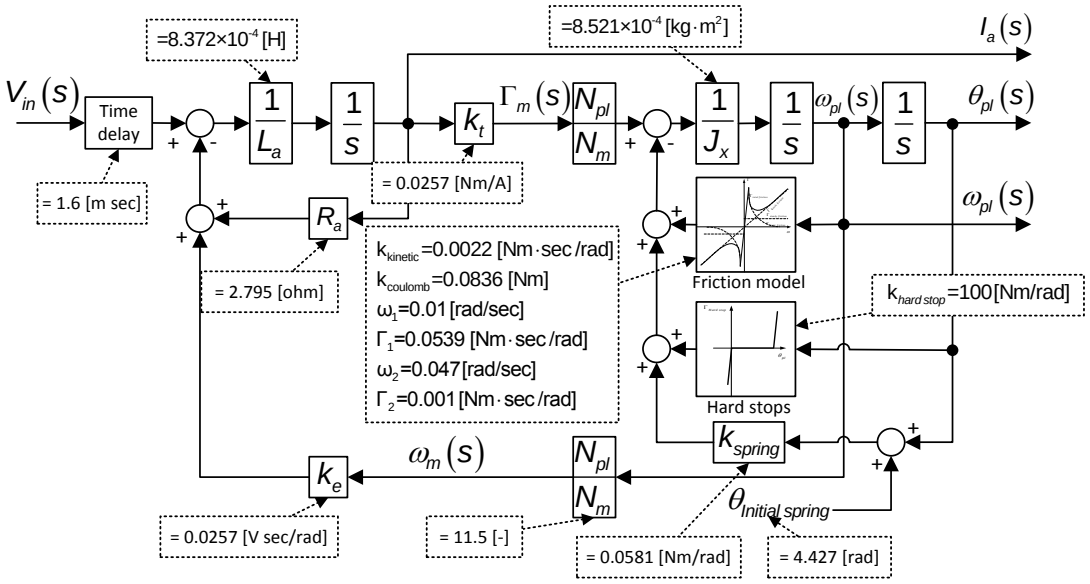

Figure 3.9: Nonlinear throttle valve model with parameter values

A full list of the parameters used for the simulation work can be found in Appendix 0.

3.3 Model Verification in the Time Domain

The validation is done by a applying the same time varying DC motor voltage to both the non-linear plant model and the real plant. The validations were done with no position controller applied (open loop). Figure 3.10 shows four of the most significant validation experiments where the blue signal is the experimental data and the green signal the data from the non-linear model. In the bottom of Figure 3.10 the difference between the real plant and simulated plant is shown.

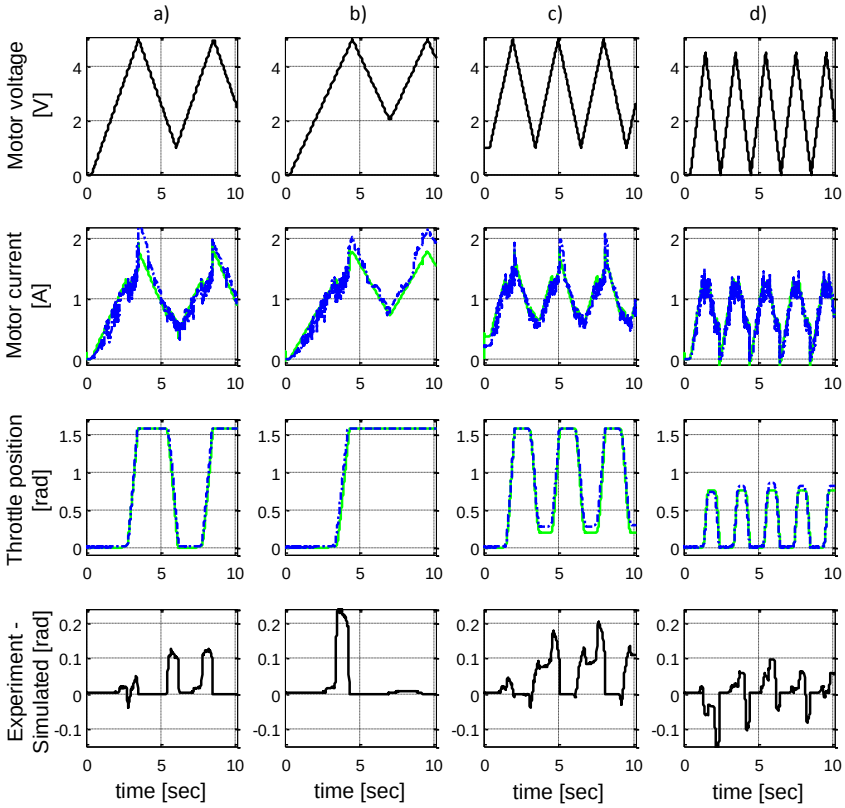

Figure 3.10: Comparison between the non-linear plant model and the plant (Blue dashed: Experimental data. Green: Simulated data)

The four experiments shown are designed to validate the friction model parameters. In Figure 3.10 b) the voltage is ramped up slowly until the throttle valve closes and then ramped down again to the point just before it will open. The static friction applies a force great enough to keep the throttle valve closed. The experiments shown in Figure 3.10 c) and d) are designed to make the throttle valve position operate over a limited range, again with focus on the friction.

3.4 Model Validation in the Frequency Domain

A known way of system identification is to create a frequency response model of the plant (Ljung, 1998). This can be used to validate the parameters found by creating a frequency response model for the real plant and the model, and then do a comparison between the two. This has been carried out on this research programme as an additional validation test, and to find the throttle valve system bandwidth. The bandwidth is needed to enable a sufficiently high throttle position sampling frequency to be set.

To estimate a frequency response model for a plant the input and output signals are sampled and processed using fast Fourier transforms. This information is then used in the System Identification Toolbox from Mathworks® to create a frequency response model.

The quality of the result obtained from the System Identification Toolbox depends on a number of factors such as the form of the input signal, the sampling period of the data acquisition and the signal-to-noise ratio. The

experiment on the real plant, to capture the input and output signals, can be intrusive or nonintrusive. In the intrusive experiment the input signal, from the controller, is replaced by a step, impulse or sinusoidal signal. In the nonintrusive experiment, a small signal is added to the controllers output before entering the input on the real plant. Common types of signals used are sinusoidal ones with different frequencies spanning the intended bandwidth of the control system to be ultimately designed. Another type is the *pseudo random binary sequence* (PRBS) shown in Figure 3.11 (Pintelon and Schoukens, 2004) with a Fourier spectrum spanning this bandwidth. Changing the types of signals used for the system identification can result in slightly different frequency response models. It is therefore a good idea to simulate the method on a known plant model of similar form to the one expected from the identification process using different input signal types and select the one that produces the closest approach to the known plant model.

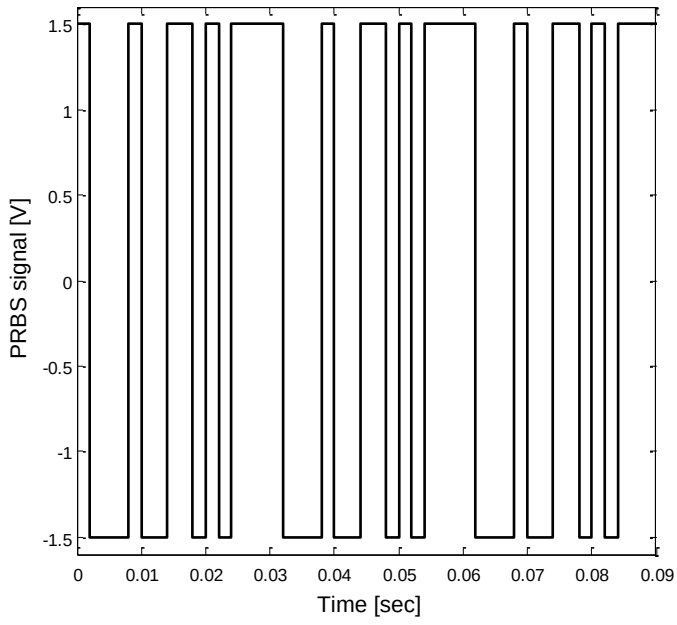

Figure 3.11: An example of a pseudo random binary sequence

The PRBS is usually a good choice and this is selected for the throttle system identification. As illustrated in Figure 3.11 the PRBS is a pulse train signal with a variable mark-space ratio which yields a relatively flat frequency spectrum over its bandwidth. Since it is generated by digital register fed by a clocked combinatorial Boolean function of the register state, producing a maximal but finite length sequence, the signal repeats with a fixed period and it is this property that gives rise to the term ‘pseudo-random’ rather than just ‘random’. This effect, however, does not seriously colour the power spectrum and therefore does not impair the system identification.

The PRBS signal is added to the output from the controller and its amplitude level should be low compared to the controller output. This will minimise the PRBS signal’s impact on the control loop. The frequency band of the PRBS can be chosen by selecting the PRBS’s update rate (sampling frequency) and its sequence length.

To summarise, the factors that are important when using the PRBS are:

- The amplitude of the signal
- The update rate
- The sequence length
- The sampling frequency of the output signal from the plant
- The number of the times the PRBS sequence is repeated
- The power electronics switch frequency (H-Bridge)

For the PRBS experiment on the throttle valve system the following parameters are set

- Data sampling frequency = 500 Hz
- PRBS update rate: $T = \frac{1}{500}[\text{sec}]$
- PRBS sequence length: $N_{seq} = 2^{10} - 1 = 1023$

- Minimum injected frequency: $f_{\min} = \frac{1}{N_{seq} \cdot T} = 0.49[Hz]$
- Maximum injected frequency: $f_{\max} = \frac{1}{2 \cdot T} = 250[Hz]$

- PRBS cycle length = 2 seconds
- PRBS amplitude = +/- 1.5 [V]
- Experiment length = 40 seconds (20 repetitions)

During the experiment, the throttle position is kept at around 45° (open loop) which is about midway between the end stops to allow the maximum amplitude of movement for nominally linear operation. From the experimental input and output data a transfer function is generated using the System Identification Toolbox from Mathworks. In fact, the same procedure is used to generate a transfer function from the nonlinear throttle valve model. Although, strictly, the transfer function is a notion applying only to linear systems, the result obtained with a nonlinear plant is, arguably, similar to that obtained analytically by the method of linearisation about the operating point. This is certainly true for continuous nonlinearities but the stick slip friction, which is significant in the throttle valve application, is discontinuous. Despite this there is no other known way to obtain a better transfer function model for control system design. The restriction of continuous nonlinearities does mean that the transfer function model cannot be heavily relied upon. This is only being used for the initial controller design with the possibility of having to make controller adjustments following the first experimental trials.

The bode plots of the real plant and the identified plant model are plotted together in Figure 3.12. The plots are similar from $\omega = 0$ to about $\omega = 0.5$ [rad/sec] but a difference between them of around -5 [dB] is evident up to $\omega = 100$ [rad/sec] and increases to about -8 [dB] at the upper limit of frequency. The throttle systems bandwidth is somewhat less than 2 [Hz].

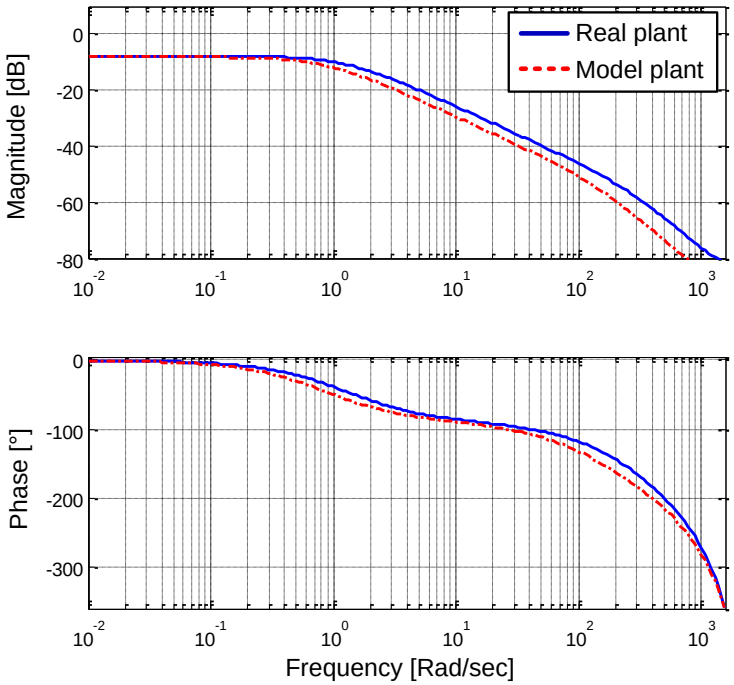

Figure 3.12: Bode plots – Comparison between the non-linear plant model and the plant

4 Control Techniques and Performance Assessment

4.1 Introduction

In this chapter, the different control techniques to be investigated are explained. The controllers are then designed. This is followed by simulations and corresponding experimental results that for a basis for the performance assessment and the comparisons of the following chapter.

The correct procedure in the establishment of any control system design is to first consider the simplest possible controller and identify any shortcomings, thereby establishing a need, if necessary, to introduce specific features. In this way, unnecessary complexity is avoided. In the case of the throttle valve application under study, this led several years ago to the PID controller, which has been employed in many systems to this date. Modern digital processors, however, permit more sophistication in the controller without increasing the complexity and cost of the hardware and therefore reducing its reliability. Under these circumstances it is very much worth considering more sophisticated control techniques that might offer advantages in performance improvement or ease of commissioning. This is the motivation of the research programme.

In subsection 4.2, the process leading to the establishment of the PID controller is briefly reviewed, starting with the simple proportional controller, so that the subsequent work of this research programme is set in context.

4.2 The Earlier Developments Leading to the PID Controller

The simplest controller that can be considered is the proportional controller as shown applied to the linear throttle valve model defined by transfer function (2.41). This is shown in Figure 4.1

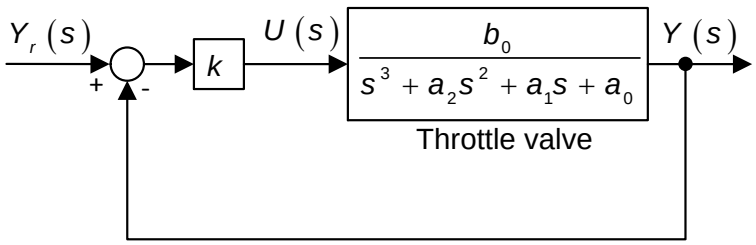

Figure 4.1: Proportional controller applied to the throttle valve

where $Y_r(s)$ is the controller reference input, $Y(s)$ is the throttle valve position output and $U(s)$ is the controller output which is a voltage driving the throttle valves DC motor.

Using the parameter values found in Chapter 3, the plant has three open loop poles at $s_{1,2,3} = \{-3301\}, \{-35.1\}, \{-2\}$, and Figure 4.2 shows the root locus.

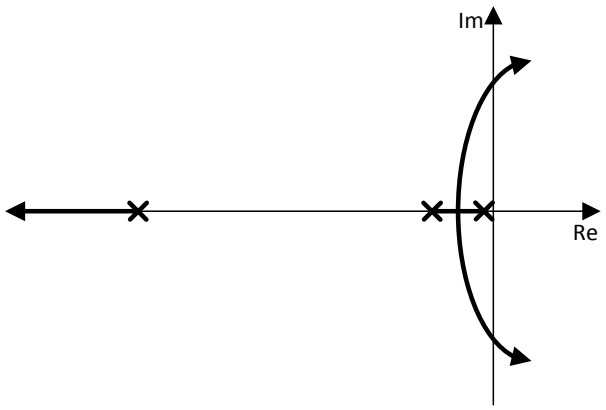

Figure 4.2: Root locus of the system with unity gain feedback control

It is evident that there is an upper limit on the gain, K, beyond which instability results, indicated by the points where the complex conjugate loci cross the imaginary axis of the *s*-plane. At lower gains for which the system is stable, the damping ratio would be too low due to the relatively small negative real part of the complex conjugate poles. At the critical value of K at the break-away point, the two dominant poles are situated at $s_{2,3} \cong \{-18\}, \{-18\}$ yielding a settling time (5% criterion) given (Dodds, 2008) by the settling time formula,

$$T_s = 1.5(1+n)T_c \tag{4.1}$$

where $n = 2$ and $T_c = 1/18$, yielding $T_s = 0.25$ [sec]. Any attempt to reduce this settling time by increasing K would cause overshooting. Also, the system is subject to a steady state error due to the plant being of type '0', i.e., containing no pure integrators, due to the presence of the retention spring described in subsection 2.1. This steady state error is evident in Figure 4.3.

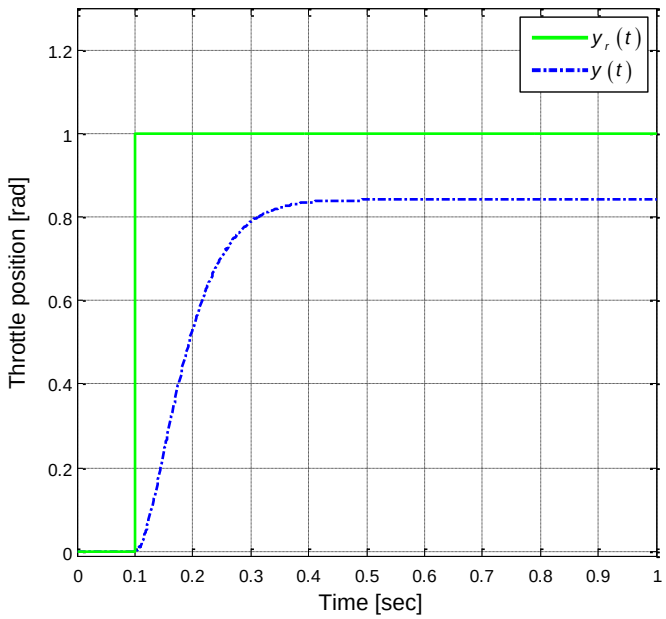

Figure 4.3: Step response with proportional controller adjusted for critical damping

This steady state error will impair the performance of an engine management system, since it has to operate in steady state for a substantial proportion of its lifetime. This necessitates the introduction of an integral term in the controller but, alone, renders difficult the task of obtaining an acceptable settling time and minimal overshoot of the step response. Hence the derivative term is called for that enables the overshooting to be reduced when increasing the proportional gain in an attempt to reduce the settling time. The result is the PID controller.

Before moving on, it should be mentioned that the PID controller applied to a third order plant model yields a closed loop system of fourth order. Since there are only three adjustable controller parameters on the PID controller, only three of the four closed loop poles can be placed as desired. This restriction is removed in some of the controllers considered in this research programme, enabling design by the method of pole placement as described in subsection 4.4.2.

4.3 Methodology

4.3.1 Simulation Details

Throughout the research the control strategies are simulated, using Matlab and Simulink, with both the linear and nonlinear throttle valve models from Chapter 2. The control strategies and throttle valve models are implemented using block diagrams as in Simulink (referred as Simulink models). The Simulink models are shown in the continuous domain using the Laplace operator to make the investigation work easier. Most of the simulations are run in variable step mode, which can make the execution faster and ensures relatively high precision. The sliding mode control, however, in its basic form, incorporates a discontinuous element that can cause variable step algorithms to become ‘stuck’ in an effort to

maintain precision by reducing the step-length. In these cases a fixed step algorithm is employed which, in any case is needed for the real time implementation using the rapid prototype hardware from company dSPACE (www.dspace.com).

It is important to note that the zero crossing detection is enabled in the nonlinear friction models, wherever possible, to maximise the accuracy.

All the control strategies to be implemented on dSPACE are first validated using Simulink to avoid issues that might damage the throttle valve.

4.3.2 Experimental Setup

The control strategies are tested by using a throttle valve system connected to the *MicroAutoBox* (MAXB) from dSPACE through a power amplifier, shown in Figure 4.4. A control strategy block diagram (model) is formed by using Simulink®. The model is compiled and downloaded into the MAXB. The MAXB is a rapid prototype system which consists of a powerful main processor and some peripheral hardware including ADC's, PWM's, DAC's and digital input/output (I/O).

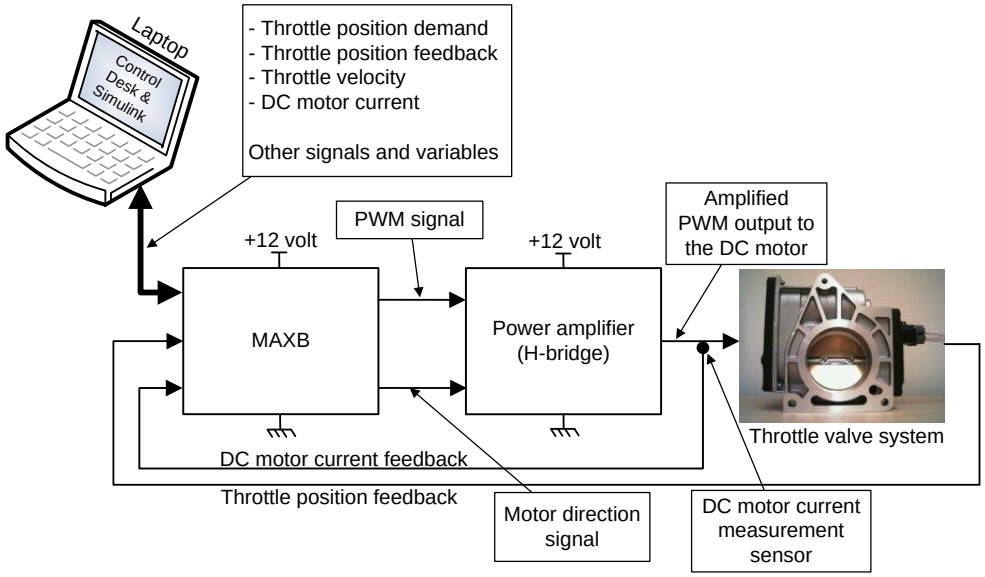

Figure 4.4: Experimental setup for testing the throttle valve position control strategies

The downloaded code runs in real time, according to the specified sampling frequency, on the main processor in the MAXB. MAXB supports the implementation of Laplace operators (s) but only with a fixed sampling time. The MAXB will measure the specified inputs like the ADC's, run the control strategy and update the outputs at each sample point, shown in Figure 4.5.

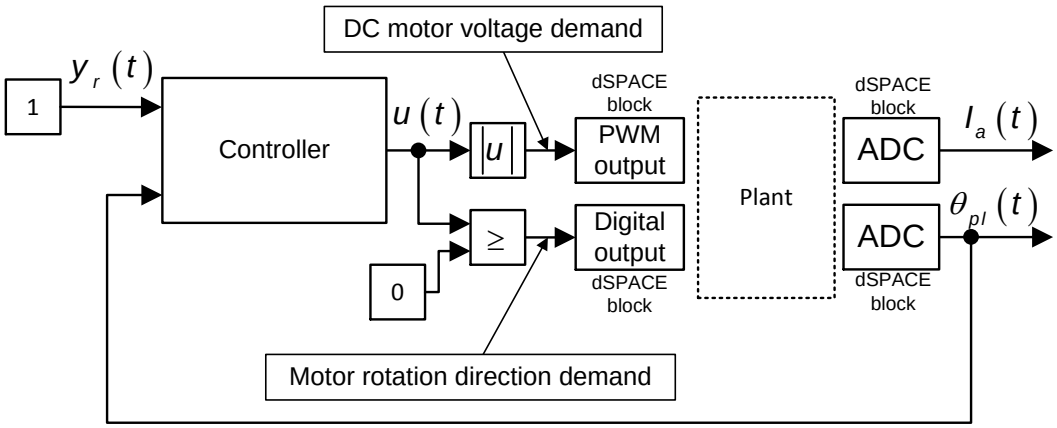

Figure 4.5: PI controller implemented in dSPACE (simplified diagram)

The measured inputs to the MAXB are the DC motor current and the throttle plate angular position. The plate angular velocity is calculated from the measured position. The outputs are a DC motor voltage demand and the motor rotational direction. The DC motor voltage is in the form of a *pulse width modulation* (PWM) signal. The motor rotational direction is a digital logic signal whose state determines the sign of the armature voltage applied to the DC motor. The MAXB outputs are connected to the power amplifier (H-Bridge) which is described in Appendix A.4. The H-Bridge output is connected to the DC motor on the throttle system. The measured DC motor current and throttle plate position are fed back to the MAXB.

When the model is running in the MAXB, all the variables can be monitored, changed and logged with the use of a program running on the attached computer called *ControlDesk* from dSPACE.

Figure 4.6 shows the experimental hardware used for the investigation. Two power supplies are used to make it possible to adjust the H-Bridge voltage level.

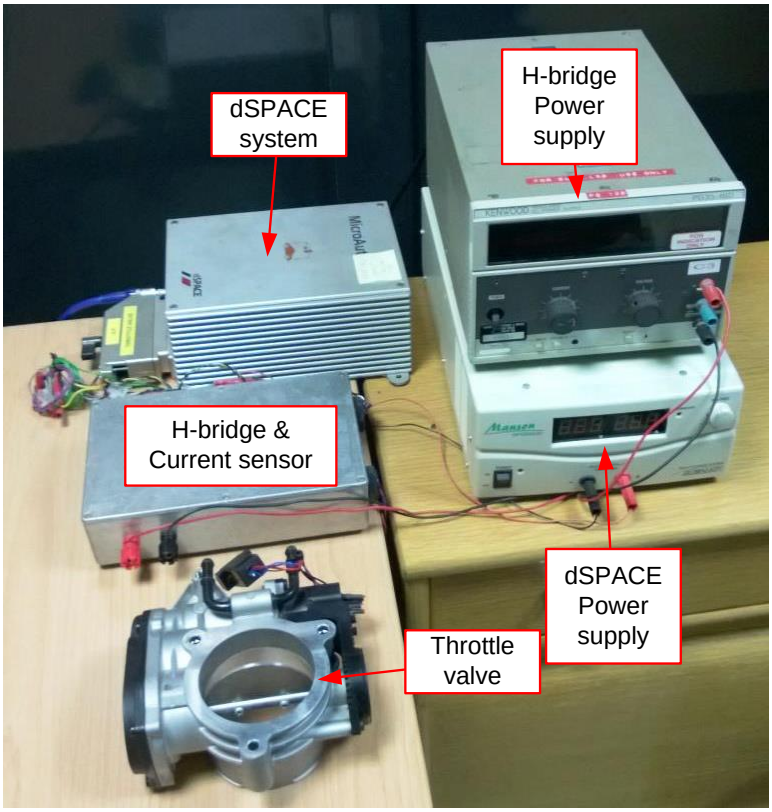

Figure 4.6: Experimental hardware

4.3.3 Simulation and Experimental validation

Three reference input functions have been chosen to test the control performance, as shown in Figure 4.7.

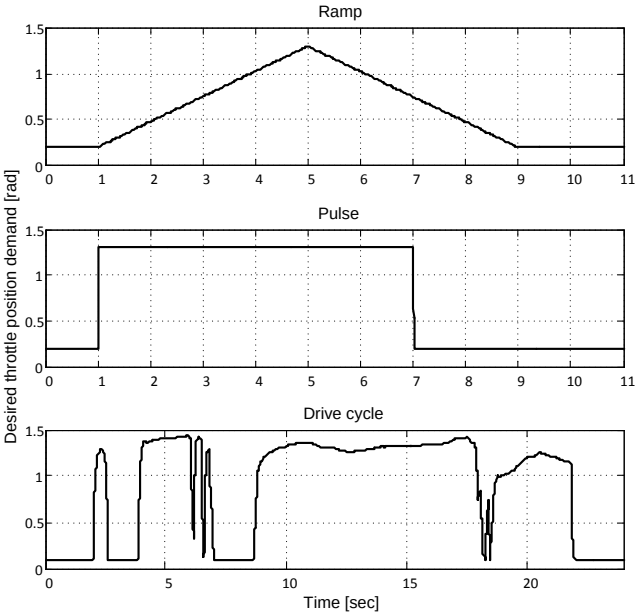

Figure 4.7: Throttle position demand waveforms for control test

Slow ramp:

- Used to test the controllers capabilities of handling static friction.

Pulse:

- This will test the dynamics of the system such as under-overshoots and the settling time.

Drive cycle:

- This is a sample of the position demand data shown in Figure 1.5 taken from an operating throttle valve control system, which enables the ability of the control system to follow fast and slow position demands to be assessed.

The normal operational range of the throttle valve is between 0 and 1.5 [rad]. The reference inputs have been scaled so as to avoid the mechanical system hard stops. This allows the system to operate in the continuous mode in which the control systems under investigation are intended to operate.

4.3.4 Sensitivity and Robustness Assessment

4.3.4.1 Sensitivity

The sensitivity is defined here as a measure of how much the transient and steady state responses differ from those specified in the presence of plant modelling uncertainties and external disturbances (Dodds, 2013). Conversely, robustness is defined as the ability of a control system to maintain its specified transient and steady state performance despite plant modelling uncertainties and external disturbances. So an additional performance aim is to minimise the sensitivity, which is equivalent to maximising the robustness.

Any linear control structure can be transformed into the standard form shown in Figure 4.8, where $D(s)$ is an external disturbance, $G(s)$ is the plant transfer function while $K(s)$ and $H(s)$ are controller transfer functions.

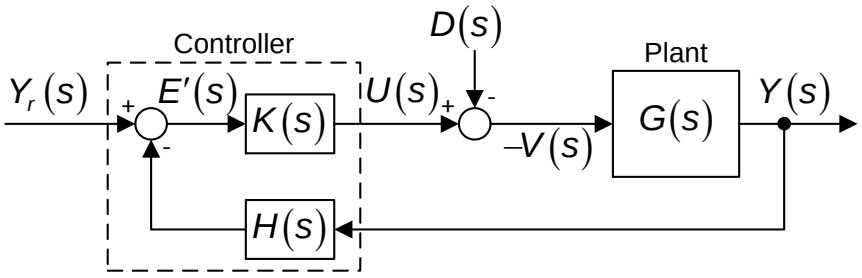

Figure 4.8: Standard linear control system structure

Note that the error is noted $E'(s)$ (not meaning a derivative!) to distinguish it from the error, $E(s) = Y_r(s) - Y(s)$, the difference being due to the feedback transfer function, $H(s)$. The closed loop transfer function is then

$$G_{cl}(s) = \frac{Y(s)}{Y_r(s)} = \frac{K(s)G(s)}{1 + K(s)H(s)G(s)} \tag{4.2}$$

Then the sensitivity of the closed loop transfer function with respect to the plant transfer function is defined as

$$S_p^C(s) = \lim_{\delta \to 0} \frac{\delta G_{cl}(s)/G_{cl}(s)}{\delta G(s)/G(s)}\bigg|_{G(s)=\tilde{G}(s)} = \frac{1}{1+K(s)H(s)\tilde{G}(s)} \tag{4.3}$$

where $G_{cl}(s)$ is the closed loop transfer function and $\tilde{G}(s) = G(s) - \delta G(s)$ is the assumed plant transfer function, i.e., the transfer function model of the plant. The robustness is then

$$R_p^C(s) = 1 - S_p^C(s) = \frac{K(s)H(s)\tilde{G}(s)}{1+K(s)H(s)\tilde{G}(s)}. \tag{4.4}$$

The *Matlab Simulink Control System Design* toolbox is used throughout this research to extract the sensitivity for various controllers by realising, with reference to Figure 4.8, that

$$\frac{V(s)}{D(s)}\bigg|_{Y_r(s)=0} = \frac{1}{1+K(s)H(s)\tilde{G}(s)} = S_p^C(s), \tag{4.5}$$

This is a measure of what proportion of the disturbance gets through to the plant while the controller is trying to cancel it. It is therefore a direct measure of sensitivity with respect to external disturbances. It is also known that deviations of the plant parameters from the nominal ones in the plant model used for the control system design may be represented by equivalent (but not physically present) external disturbances applied to the model. This further explains the use of transfer function (3.5) to represent the sensitivity derived on the basis of plant parameter variations through (4.3).

The transfer function, $E'(s)/Y_r(s)$, is also the sensitivity transfer function given by equation (4.5). The reader is warned, however, that taking $E(s)/Y_r(s)$ for any linear control system, where $E(s) \triangleq Y_r(s) - Y(s)$ is the control error, will yield the required sensitivity transfer function *only* if $H(s) = 1$ after converting the control system block diagram to the form of Figure 4.8. If $H(s) \neq 1$, then $E'(s) \neq E(s)$ and $E(s)/Y_r(s) \neq S_p^C(s)$.

The control error transfer function, $G_e(s) = E(s)/Y_r(s)$, has a meaning separate from the sensitivity, which is simply an indication of how the control error behaves. In the frequency domain, it would be possible to plot what could be termed the error frequency response, $G_e dB(\omega) = 20\log_{10}|G_e(\omega)|$, alongside $S_p^C dB(\omega) = 20\log_{10}|S_p^C(\omega)|$. In cases where $H(s) \neq 1$, it is possible that the plot of $G_e dB(\omega)$ could lie significantly above that of $S_p^C dB(\omega)$ but this would not necessarily indicate poor performance as it could result from a non-overshooting monotonic step response, while an overshooting step response, which is, arguably, less desirable, could yield a lower lying $G_e dB(\omega)$ plot. This has been confirmed from results obtained from the throttle valve control system but since the value of $G_e dB(\omega)$ in assessing the performance of a control system is doubtful, only the sensitivity results are presented.

To summarise, the sensitivity of a control system may be assessed by creating a Bode magnitude plot with input, $D(s)$, and output, $V(s)$, using a Simulink block diagram with a summing junction inserted at the plant input as shown in Figure 4.8.

The result from the toolbox is a Bode plot where the magnitude is in Decibels

$$S_p^C dB(\omega) = 20 \cdot \log_{10}|S_p^C(j\omega)| \tag{4.6}$$

To illustrate the sensitivity an example is shown of the linear throttle valve model with a proportional controller. The control structure shown in Figure 4.8 is used for this where $H(s) = 1$, $K(s) = 2.9$, $D(s) = 0$ and $G(s)$ is given by the linear throttle valve model as transfer function (2.41). Figure 4.9 shows the sensitivity plot for this using the Simulink toolbox.

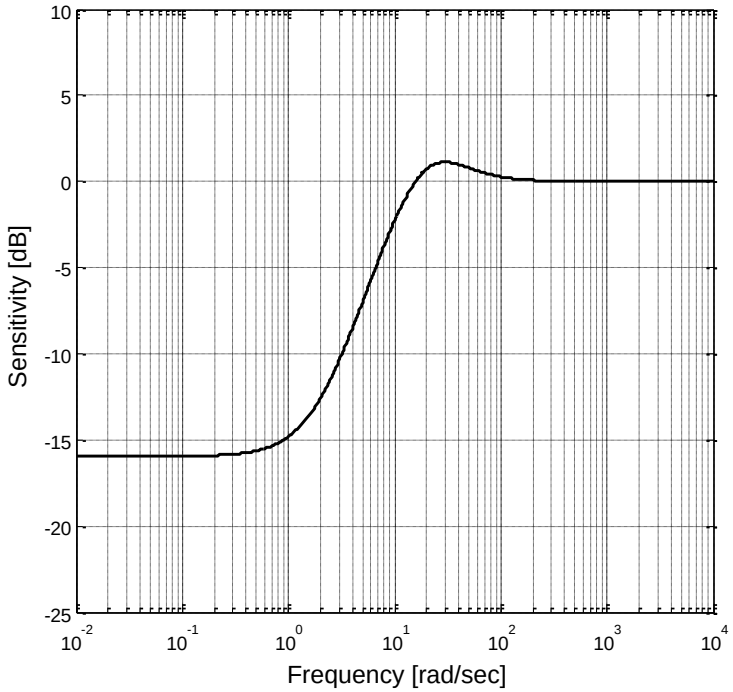

Figure 4.9: Sensitivity of the linear throttle valve control loop with a proportional controller

To check this result, equation (4.3) is applied with the throttle valve model (2.41) and the values given in Appendix 0, as follows.

$$S_p^C(s) = \frac{V(s)}{D(s)} = \frac{1}{1+K(s)H(s)\tilde{G}(s)} = \frac{s^3 + a_2 s^2 + a_1 s + a_0}{s^3 + a_2 s^2 + a_1 s + a_0 + K(s) b_0} \qquad (4.7)$$

At low frequencies $\omega \to 0 \Rightarrow s \to 0$. Hence

$$S_p^C(s) = \lim_{\omega \to 0} \frac{s^3 + a_2 s^2 + a_1 s + a_0}{s^3 + a_2 s^2 + a_1 s + a_0 + K(s) b_0} = \frac{a_0}{a_0 + K(s) b_0} \equiv -15.95[dB] \qquad (4.8)$$

At high frequencies $\omega \to \infty$

$$S_p^C(s) = \lim_{\omega \to \infty} \frac{s^3 + a_2 s^2 + a_1 s + a_0}{s^3 + a_2 s^2 + a_1 s + a_0 + K(s) b_0} = 1 \equiv 0[dB] \qquad (4.9)$$

These calculations are in agreement.

4.3.4.2 Parameter Variation using Monte Carlo Analysis

Variations in the true plant parameters with respect to those used for a controller design can cause considerable departures from the specified performance or even closed loop instability. These parametric uncertainties can come from a number of sources such as product tolerances and parameter estimation. For the throttle valve used in this research there are seven physical parameters used in the model upon which the controller designs are based, which are R_a, L_a, k_e, k_t, $k_{kinetic}$, k_{spring} and J_x, defined in Chapter 2.

To test a system sensitivity with respect to just two parameters for all possible parameter variations in (+/-5%) steps up to (+/-10%) extremes would entail 25 combinations and as many tests, as illustrated in Figure 4.10.

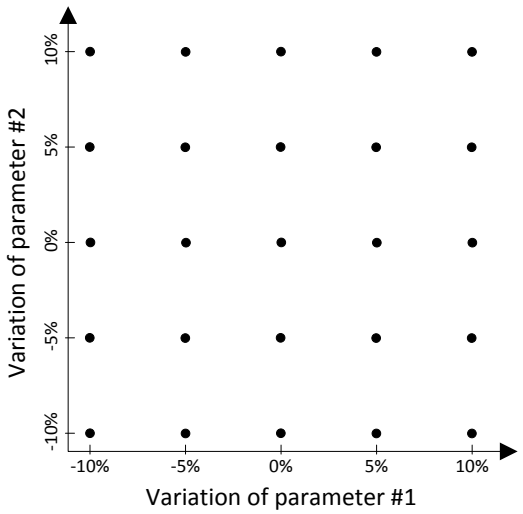

Figure 4.10: A 2D matrix for parameter variations test

The black dots indicate the different combinations of parameter variations. Instead, a Monte Carlo analysis implements a normal statistical distribution of each parameter, which is more realistic, with the maximum limits replaced by 3σ values. In this way, more tests are carried out for parameter values that are more likely to occur, thereby achieving a smaller number of test runs than would

be needed with a flat statistical distribution, which is implied by the simple scheme of Figure 4.10. The concentration of parameter combinations about the nominal values given by Monte-Carlo analysis is illustrated in Figure 4.11.

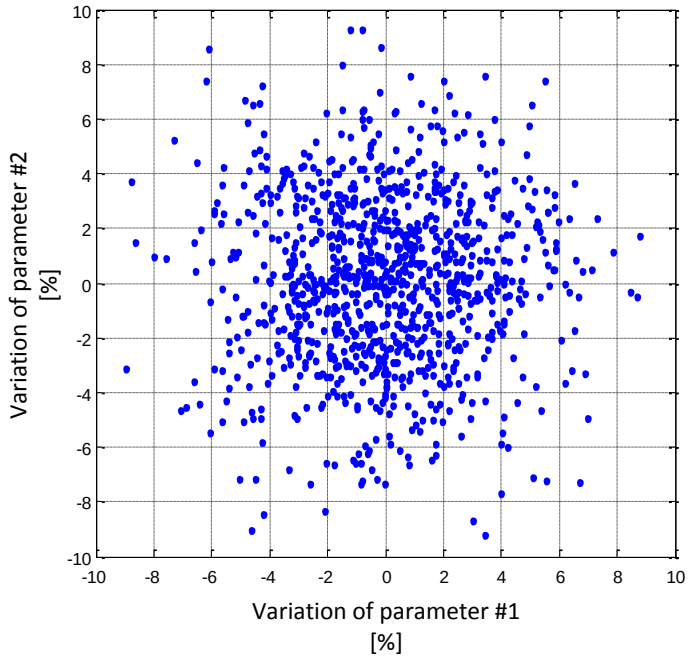

Figure 4.11: Illustration of 2D parametric variations for Monte-Carlo analysis (Standard deviation = 3 %, Mean value = 0)

A normally distributed random set of numbers (specific number of observations) with a specific standard deviation and a mean value of zero are generated for each parameter (Figure 4.12). Seven different sets are generated, one for each parameter tested, with a set length = 1000.

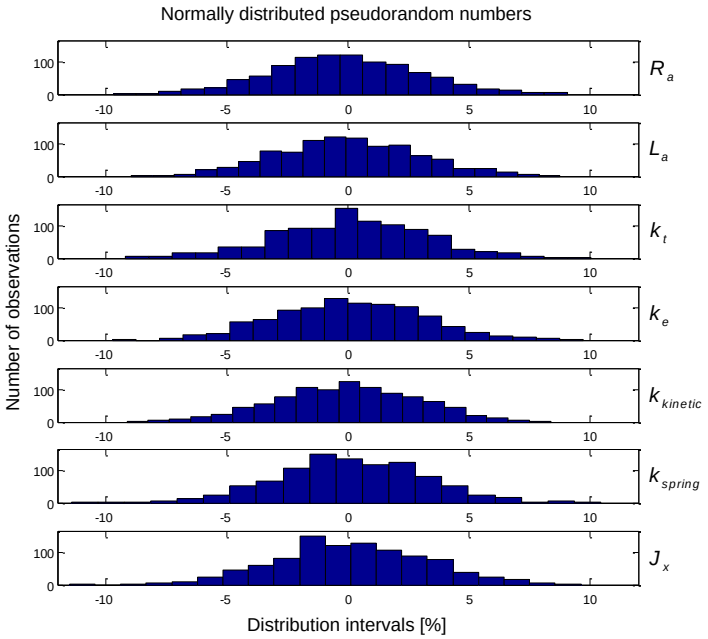

Figure 4.12: Frequency distributions of parameters used for the Monte Carlo analysis (Standard deviation = 3 %, Mean value = 0)

All the random number data used for the parameter variation tests was generated in the early state of the research. The same random number sets have been used for each simulation investigation of robustness to insure that fare comparisons are made. Figure 4.13 shows the number of samples for each variation interval as a function of the standard deviation in percent, in this case for R_a. The standard deviation range generated is from 1% to 30% in steps of 1%.

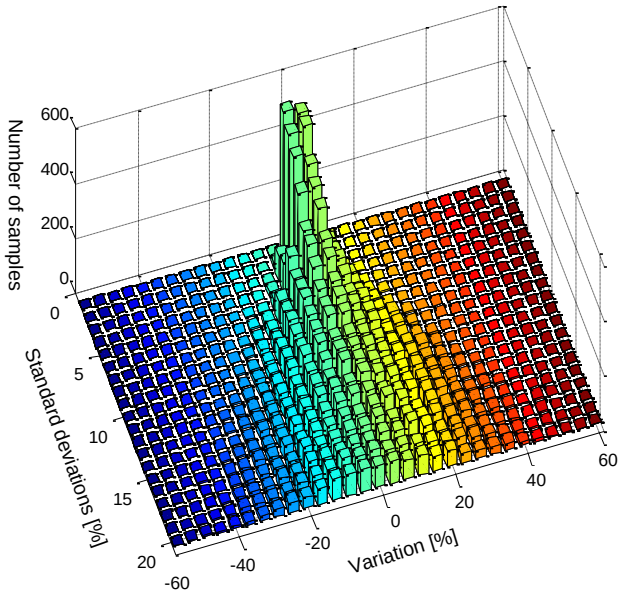

Figure 4.13: Parameter distribution used for the Monte Carlo (R_a for $\sigma[0.01:0.2]$)

The parameter variation validation is done by repeating the simulated closed loop response of a control system, changing the simulated plant parameters from one run to the next while keeping the model parameters fixed at the nominal values, i.e., the controller gains/parameters are fixed. The output responses are assessed against predefined boundaries in Figure 4.14, which cannot be exceeded.

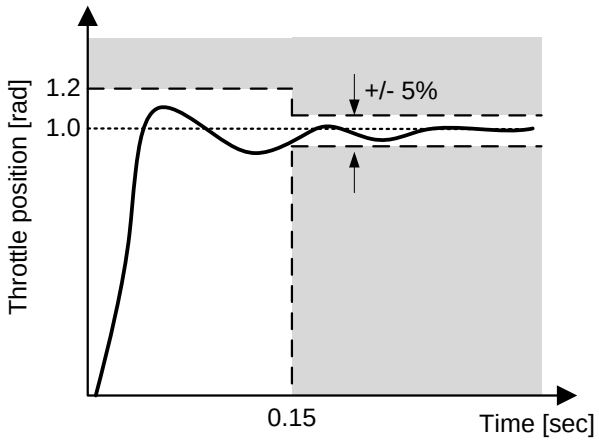

Figure 4.14: Throttle position operation envelope

If a simulation is about to penetrate a boundary it is stopped and the level of the parameter change is logged. The boundaries in Figure 4.14 are designed with room for a controller overshoot of 20% and a steady state error of maximum +/- 5%.

The assessment procedure, common for each controller, is as follows. Each controller is designed using the nominal linear plant model parameters and a specified settling time of 0.1 [sec]. An initial closed loop simulation is carried out with a step reference position applied at $t = 0$ [sec]. The plant model used is the nonlinear model, from subsection 2.5, with nominal parameters. The closed loop output response, $y(t)$, is tested against the defined boundaries of Figure 4.14.If the output response crosses a boundary at this stage the simulation is stopped and the controller is deemed unsuitable as it would be unable to cope with the nonlinear friction effects even with the simulated linear plant parameters equal to the nominal values. Having passed this initial test, a set of 1000 normally distributed values is loaded for each of the seven plant parameters referred to in Figure 4.12 and prepared for the Monte-Carlo analysis simulations, commencing with 1% standard deviation. Then 1000 simulations are run, the seven plant parameters being loaded in sequence from the established set at the beginning of each run. Then the whole set of simulations is repeated for standard deviation increases by 1% until a boundary of Figure 4.14 is crossed, whereupon the simulation sequence for the controller concerned is terminated and the standard deviation noted as a performance measure, the higher the better.

4.3.4.3 Failure Analysis

As described in subsection 1.2.2, in a typical DPF regeneration drive cycle the throttle position could be 95-97% fully closed as shown in Figure 1.5. This will make the engine system very sensitive to a sudden change in the throttle valve

position. In the worst case, the engine could stall due to air starvation. This sudden change in position could be caused by breakage of the pre-loading spring with the consequent step change in the load torque to zero. In this research, the control strategies are tested for the impact of such a spring failure. This is only simulated due to the difficulty of implementing a spring collapse on the real throttle valve system. In the simulation the desired throttle position is set to 1.47 [rad] (~94% maximum) and at $t = 1$ [sec] the spring torque is removed.

4.4 Common Features

4.4.1 Introduction

The purpose of this subsection is to present the common design features that the different controllers under investigation share, to minimise repetition in the subsections dealing with the specific controllers.

4.4.2 Pole Placement Design using the Settling Time Formula

4.4.2.1 Multiple Pole Placement

The settling time T_s, Figure 4.15, is defined as the time it takes from applying an ideal instantaneous step input to the time at which the systems output has entered and remained within a specified range, in this case it is chosen to +/- 5%.

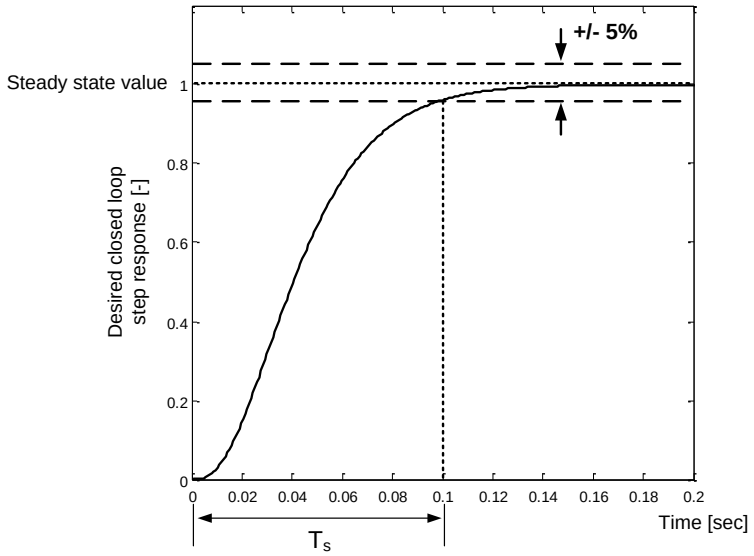

Figure 4.15: Settling time definition

The Dodds 5% settling time formula (Dodds, 2008),

$$T_s = 1.5(1+n)T_c\,, \tag{4.10}$$

will be used throughout to design each controller to meet a settling time specification with zero overshoot. The coincident closed loop pole location is then

$$s_{1,2,\ldots,n} = -\frac{1}{T_c} = -\frac{1.5(1+n)}{T_s} \tag{4.11}$$

$$\frac{Y(s)}{Y_r(s)} = \left[\frac{\frac{1}{T_C}}{s+\frac{1}{T_C}}\right]^n = \left[\frac{\frac{1.5(1+n)}{T_S}}{s+\frac{1.5(1+n)}{T_S}}\right]^n \tag{4.12}$$

where $Y_r(s)$ is the reference input, T_c is the closed-loop time constant and n is order of the control system.

4.4.2.2 Robust Pole Placement

An example of a linear high gain robust control system is used to introduce the *robust pole placement* method (Dodds, 2013). The plant is second order, as shown in Figure 4.16, with a gain of c and two poles at $s_{1,2} = \{0, -a\}$. The two control gains, K and T_c, are calculated to yield the desired closed loop response. The input $D(s)$ is an arbitrary external disturbance signal.

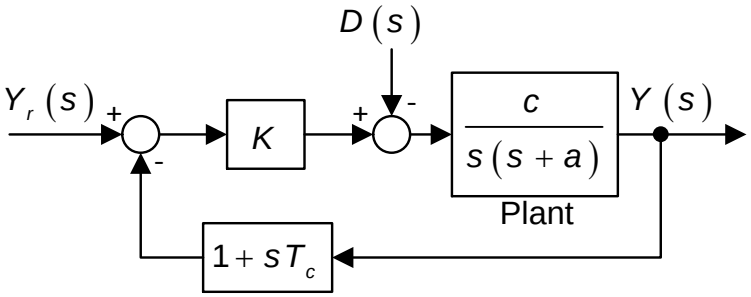

Figure 4.16: Linear high gain robust control system

The closed loop transfer function relationship of Figure 4.16 is

$$Y(s) = \frac{\frac{K \cdot c}{s(s+a)} Y_r(s) - \frac{c}{s(s+a)} D(s)}{1 + \frac{K \cdot c}{s(s+a)}(1 + sT_c)} = \frac{Y_r(s) - \frac{1}{K} D(s)}{\frac{s(s+a)}{K \cdot c} + 1 + sT_c} \tag{4.13}$$

Then

$$\lim_{K \to \infty} Y(s) = \frac{1}{1 + sT_c} Y_r(s) \tag{4.14}$$

This indicates ideal robustness as $Y(s)$ is completely independent of the plant parameters and the external disturbance but in practice, K cannot be infinite but can be made sufficiently large for the closed loop dynamics to be made nearly independent of the plant parameters and the disturbance input. In the

ideal case, the desired closed loop response is dictated by one closed loop pole at $s = -1/T_c$. To analyse the system with finite K, a Root locus plot is shown in Figure 4.17 where the open loop transfer function is $\frac{K \cdot c \cdot (1+sT_c)}{s(s+a)}$ and the close loop poles are at $-1/T_c'$ and $-1/T_f$, and as $K \to \infty$, $T_c' \to T_c$ and $T_f \to 0$.

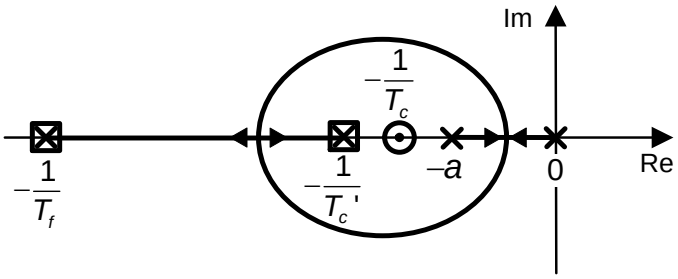

Figure 4.17: Root locus with respect to K

This means that as K is increased, the 'fast' closed loop pole at $-1/T_f$ becomes very large and the closed loop pole approaching $-1/T_c'$ becomes dominant. A more detailed examination of high gain control can be found in the sliding mode control of subsection 4.9.

The magnitude of the fast pole at $s = -1/T_f$ will, in practice, be limited by the sampling period h of the system. The only rigorous way of determining the lower limit of T_f below which instability occurs would be to determine the roots of the characteristic polynomial in the z-plane and ensuring they lie within the unit circle but a guideline that is fairly reliable is $T_f > 2h$. It is possible that some systems would remain stable for $T_f < 2h$ but it must be realised that as T_f is reduced there will always be a threshold, dependent upon the particular system, below which instability will occur. Here, the system will be designed so that

$$2h < T_f \quad T_c \tag{4.15}$$

to be reasonably sure of avoiding instability due to the sampling process and give the system adequate robustness against parameter changes and

disturbances. In any case, confirmation of the correct behaviour by simulation is advised.

Intuitively, the robustness can be thought of as being produced by a high value of the gain, K, that gives the control loop a high degree of stiffness. The question then arises of how the maximum value of K can be calculated for (4.15) to be satisfied. While this is relatively straightforward for the second order example above, it is less so for higher order examples. This problem, however, can be overcome by the method of robust pole placement. In the second order example, this consists of first choosing the closed loop pole positions, one *precisely* at $-1/T_c$ and the other to satisfy (4.15). So this has the advantage over the 'high gain' approach of ensuring a specified closed loop dynamics, while previously this was determined by $T_c' \cong T_c$. Then the controller must have at least two adjustable parameters that can be calculated to yield these closed loop pole locations. A similar approach can be used to design any linear control system of order, n, using n adjustable controller parameters. If a non-overshooting step response is required, then $n-1$ of the closed loop poles can be placed at $-1/T_c$ to yield a specified settling time of T_s (5% criterion) using the settling time formula (4.10) with n replaced by $n-1$. Thus

$$T_c = \frac{T_s}{1.5 \cdot n} \tag{4.16}$$

If the fast pole T_f, however, is not located far enough away from the dominant pole(s) the closed loop response may depart significantly from the ideal response. Hence a minimum pole-to-pole domination ratio $r_{pp\min}$ (Dodds, 2013) is used to insure a minimum distance between the fast pole, T_f, and the dominant pole(s) at $s = -1/T_c$. Inserting the minimum pole-to-pole dominance ratio into inequality (4.15). Thus

$$2h < T_f < \left(T_c / r_{pp\min}\right) \tag{4.17}$$

Figure 4.18 shows an example of the desired pole locations for a controller design using robust pole placement.

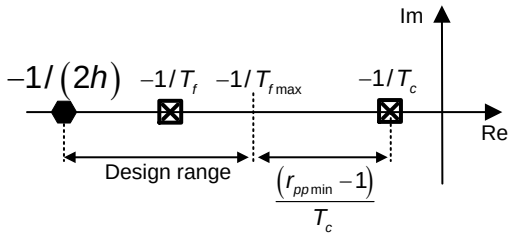

Figure 4.18: Root locus of closed loop system using robust pole placement

Note that $r_{pp\min} = \dfrac{\text{minimum fast pole magnitude}}{\text{dominant pole magnitude}} = \dfrac{1/T_{f\max}}{1/T_c} \Rightarrow \dfrac{1}{T_{f\max}} = r_{pp\min} \cdot \dfrac{1}{T_c}$.

Hence the displacement along the real axis of the *s*-plane between the dominant pole position and the closest position that the fast pole can occupy is $\dfrac{1}{T_{f\max}} - \dfrac{1}{T_c} = (r_{pp\min} - 1)\dfrac{1}{T_c}$ as shown in Figure 4.18.

Although, in theory, the notion of closed loop poles ceases to exist upon loop closure around a *nonlinear* plant, robust pole placement is known to be successful with plants containing continuous nonlinearities. A rudimentary explanation is that the real implementation works in the time domain and the robustness is attained via relatively high gains. It will be seen, for example, in section 4.9 that sliding mode control with a boundary layer forces the state trajectory to reside in a close neighbourhood of a fixed boundary in the state space that realises a prescribed transient response of the closed loop system. This boundary separates the state space into two regions, one for control saturation at the positive limit and the other for control saturation at the negative limit. Plant nonlinearities affect the form of the trajectories approaching the fixed boundary but do not affect the state trajectories within the boundary layer that straddles the fixed boundary. The trajectories are trapped within the boundary layer by the high gains.

4.4.2.3 Partial Pole Placement

If the number, n', of independently adjustable gains of a linear control system is less than its order, n, then complete pole placement as described in subsection 4.4.2.1 cannot be carried out. It is possible, however, to place n' of the closed loop poles and calculate the resulting locations of the remaining $n-n'$ poles. If the n' closed loop poles are placed using the settling time formula to yield a specified settling time of T_s, then this will be achieved in reality if the $n-n'$ poles have considerably larger negative real parts than $-1.5(1+n')/T_s$, since the desired poles will be dominant.

The advantage of pole placement is the use of a simpler controller to achieve the same specified performance to that achievable by a more sophisticated controller that can be designed by complete pole placement. This may, however, not be possible, the real settling time being greater than T_s and the step response possibly containing undesirable oscillatory modes if $n-n'>2$. In this case, it would be possible to find a lower value of T_s that would be realised. If this is too long, then another control technique permitting complete pole placement would be needed.

4.4.2.4 Model for Performance Assessment

In order to assess the simulated and experimental step responses, these are compared with the responses of ideal models implemented in ®Simulink based on the 5% settling time formula. In view of equation (4.12), these can take the form of a chain of identical first order subsystems, as shown in Figure 4.19.

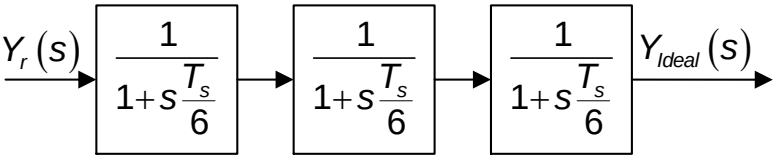

a) n=3

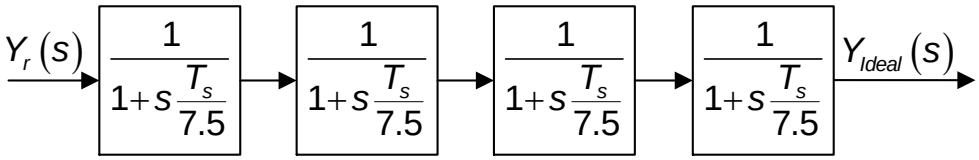

b) n=4

Figure 4.19: Block diagrams for ideal step response generation, a) third order, b) fourth order

4.4.3 Nonlinear Friction and Control Dither

In motion control, static friction can cause the controller to limit cycle due to the nonlinear speed-torque profile (Armstrong-Helouvry and Amin, 1994) (Leonard and Krishnaprasad, 1992). The limit cycle can be minimised by injecting an alternating signal, known as *dither*, into the control input causing an alternating torque or force from the actuator intended to operate the system beyond the peak static friction torque (Figure 2.18). This entails mechanical movement that has to be maintained by a sufficiently high dither signal amplitude. The mechanical movement is kept within acceptable limits by setting the dither frequency to a sufficiently high value, which makes use of the inertia in the mechanism. Dither modifies the nonlinear velocity-torque characteristic by effectively eliminating the static friction (Zames and Shneydor, 1976) (Iannellia et al., 2005) (Zames and Shneydor, 1977). In most cases the frequency of the dither signal is above the cut-off frequency of the closed loop system in which the signal is injected. In this case the dither signal will not have a significant effect on the controlled output due to the filtering properties of the plant.

A variety of different dither signals can be found throughout the industry including random, sinusoidal and pulsed waveforms. A pulse train of constant frequency is used for this research but the amplitude is switched between two levels dependent on the control error magnitude, $|y_r - y|$, as shown in Figure 4.20. When the absolute position difference is smaller than 1% of the maximum angular excursion of $\pi/2$ radians, the dither signal is turned off to insure that it does not unnecessarily move the controlled output away from the setpoint once it is close to it.

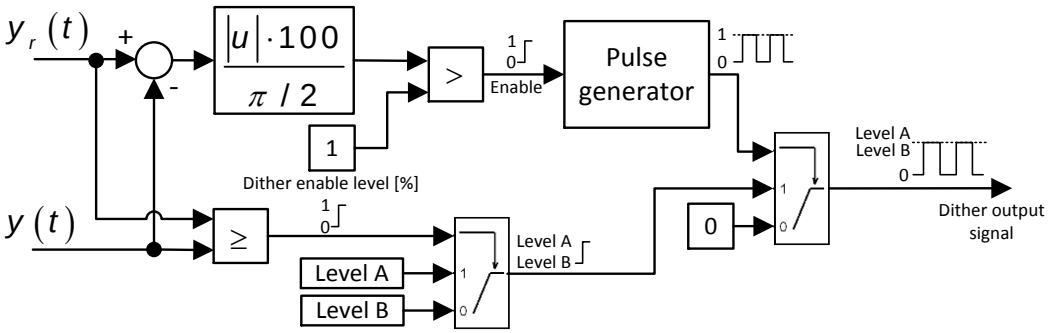

Figure 4.20: Dither signal generator

As shown in Figure 4.21 (and Figure 4.20) the dither signal switches between zero and a positive level, A or a negative level, B that opposes the sign of the error, $y - y_r$. This automatically helps the controller to achieve a small steady state error within the $\pm 1\%$ full scale band.

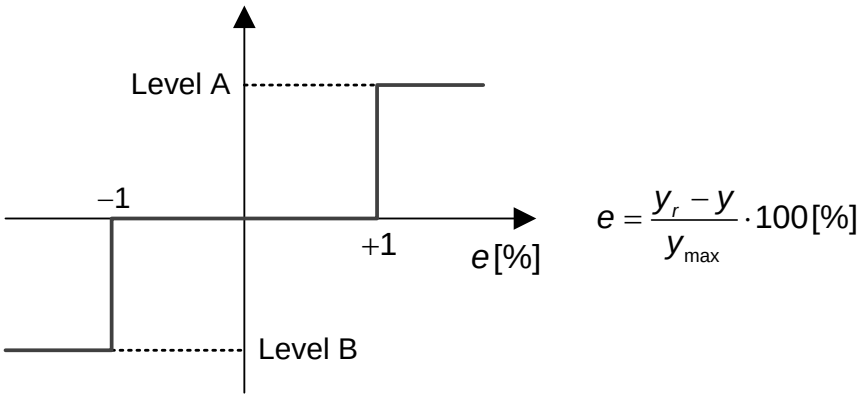

Figure 4.21: Dither signal level

Figure 4.22 shows experimental data in which a proportional controller (Figure 4.1) is applied to the throttle valve, with and without added dither. The gain of the proportional controller is set to $k_p = 7$ and a slow ramp reference input (desired throttle position) is applied. The experimental response without dither shows a staircase type of response which is the effect of the nonlinear static (stick-slip) friction. The response with dither is improved with a much smaller steady state error and smaller short-term variations (deviations from a mean ramp function).

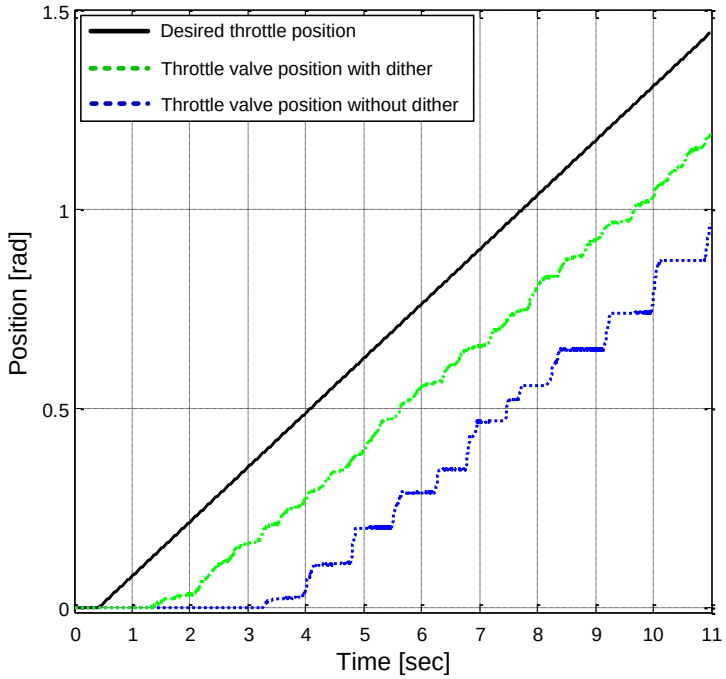

Figure 4.22: Experimental result of a P-controller with and without dither

It should be noted that even with only linear kinetic friction, a proportional controller, in theory, yields a steady state error proportional to the slope of the reference input ramp, so the residual steady state error visible with the dither in Figure 4.22 is not due to the dither not operating correctly.

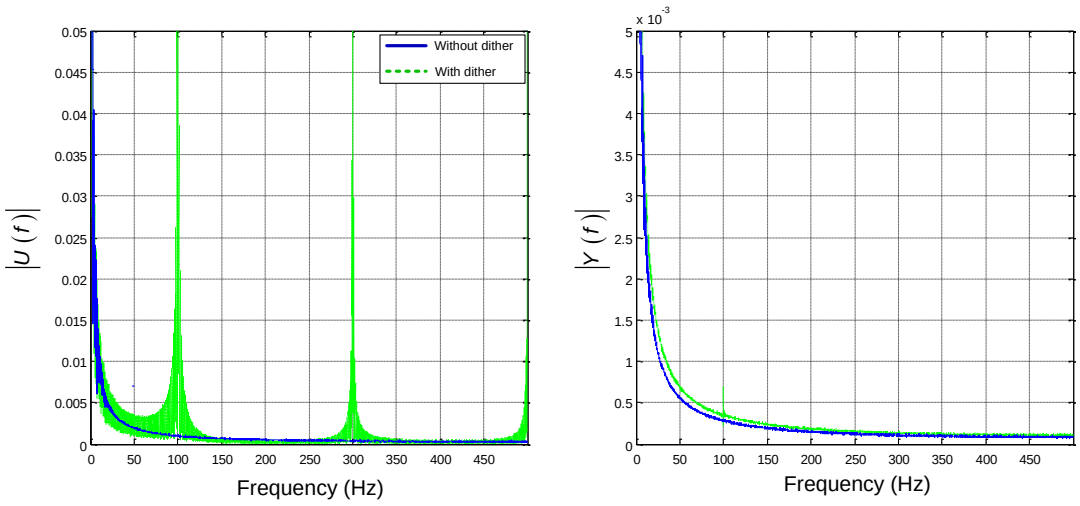

a) Plant input **b) Plant output**

Figure 4.23: Amplitude spectra

As mentioned before, the dither signal frequency should be higher than the plant bandwidth. Figure 4.23 demonstrates this by showing the amplitude spectra of the plant input and output signals. The input and output amplitude spectra without the dither are inserted as references. Figure 4.23 a) shows a high amplitude with the dither at the fundamental frequency of 100 Hz and the odd harmonic frequencies of 300 and 500 Hz which are related to the dither signal square waveform. Most of the dither is filtered out by the throttle valve as shown in Figure 4.23 b).

4.4.4 Integrator Anti Windup

As investigated in subsection 1.2.2, a short settling time, less than 0.1 [sec], will make the output from the controller saturate if a step reference input of substantial amplitude is applied, or if, as occurs in normal operation on a vehicle, very rapid changes of the reference input occur. The saturation is caused by the limitations of the throttle system hardware. The saturation may make the integrator of the controller ramp up indefinitely, referred to as integrator windup, if the position reference input is above a critical value beyond

which the system remains in saturation and is unable to drive the steady state error to zero (Franklin et al., 2002). With smaller reference position inputs, the system is able to come out of saturation and drive the steady state error to zero but the saturation can cause an undesirable overshooting and undershooting that would not occur with linear operation under the same controller gain settings. To circumvent these problems, a strategy for integrator anti-windup can be applied, which will stop the integral action during the saturation. There are multiple ways of implementing an integrator anti-windup strategy (Astrom and Rundqwist, 1989, Franklin et al., 2002). The anti-windup strategy needs to keep the output of the controller within, or close to, the operational limits of the actuator. The strategy used for this research is shown in Figure 4.24.

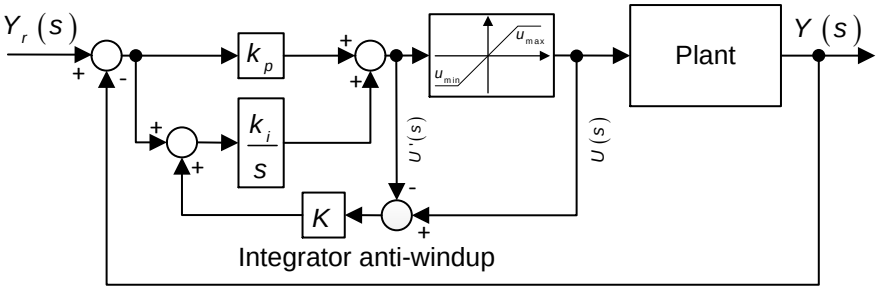

Figure 4.24: PI controller with integrator anti-windup

The essential element is the saturating element with unity gain. During normal operation (unsaturated)

$$u_{\min} < u'(t) < u_{\max} \Rightarrow u(t) = u'(t)$$

and therefore the actuation error, $u(t) - u'(t)$, of the anti-windup loop is zero, rendering this loop inactive. If the system attempts to saturate,

$$u'(t) > u_{\max} \text{ or } u'(t) < u_{\min}$$

and therefore the actuation error is $u(t) - u'(t) \neq 0$. For a sufficiently high value of the gain, K, this error is kept to very small proportions by the anti-windup loop, so $u'(t) \cong u(t) = \pm u_{\max}$. This inhibits the integral action and limits the

demanded controller output to a value exceeding the saturation limit by a negligible amount.

As an example, Figure 4.25 shows the performance of a PI controller applied to a plant with transfer function

$$\frac{Y(s)}{U(s)} = \frac{1}{s} \tag{4.18}$$

with and without the integrator anti-windup.

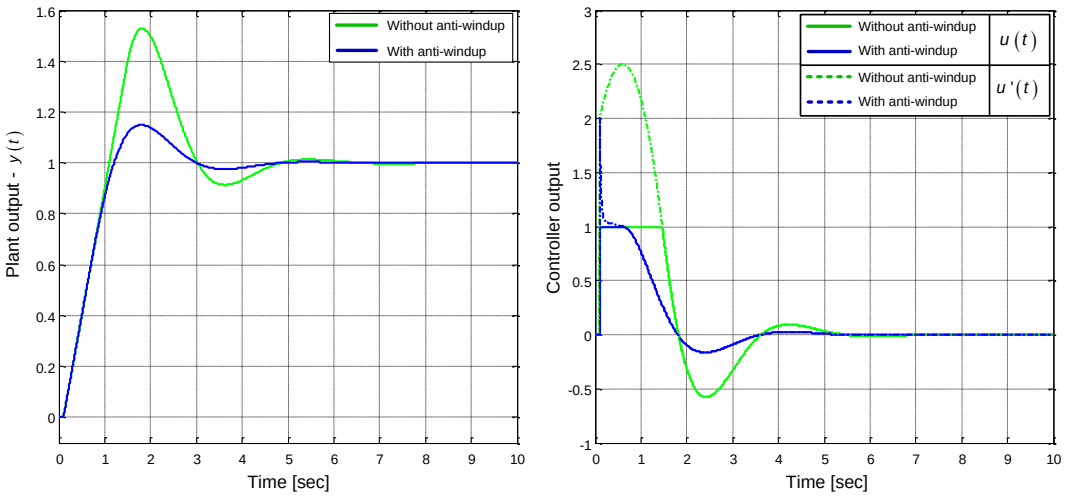

a) Plant output $y(t)$ b) Controller output $u(t)$

Figure 4.25: Integrator anti-windup performance

4.5 Traditional Controllers

4.5.1 Introduction

The well-known workhorse of industrial control systems is the proportional integral derivative (PID) controller shown in the general control loop of Figure 4.26.

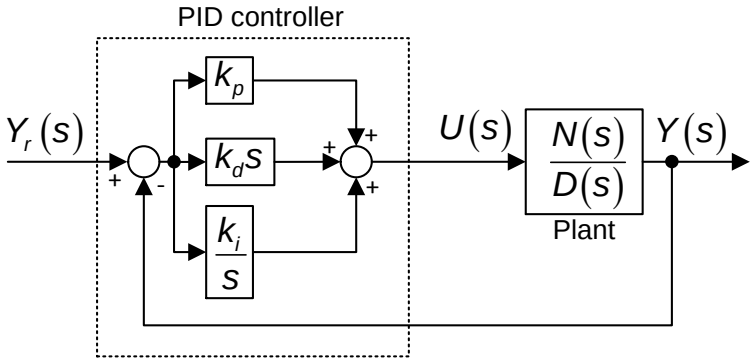

Figure 4.26: The PID controller

Using Mason's rule on Figure 4.26, the closed loop transfer function is

$$\frac{Y(s)}{Y_r(s)} = \frac{\left(k_p + \frac{k_i}{s} + k_d s\right)\frac{N(s)}{D(s)}}{1 - \left[-\left(k_p + \frac{k_i}{s} + k_d s\right)\frac{N(s)}{D(s)}\right]} = \frac{\left(k_d s^2 + k_p s + k_i\right)N(s)}{sD(s) + \left(k_d s^2 + k_p s + k_i\right)N(s)} \quad (4.19)$$

It is immediately evident, however, that this controller introduces two zeros into the closed loop transfer function that are the roots of $k_d s^2 + k_p s + k_i = 0$. Even if the gains, k_p, k_i and k_d, are set to yield real negative closed loop poles, these zeros can cause a single overshoot in the step response and possibly an undershoot too. This will be explained shortly.

One variant of the PID controller, that is available in some industrial controllers, is to change the derivative term to act only on the controlled output, $Y(s)$,

rather than the error, $Y_r(s) - Y(s)$. This yields the DPI controller shown in Figure 4.27.

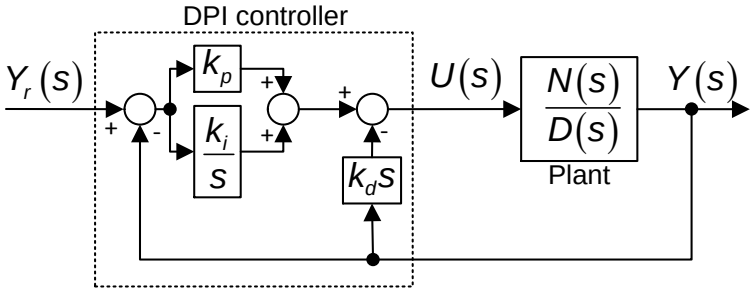

Figure 4.27: The DPI controller with the throttle valve plant

In this case the closed loop transfer function is

$$\frac{Y(s)}{Y_r(s)} = \frac{\left(k_p + \frac{k_i}{s}\right)\frac{N(s)}{D(s)}}{1 - \left[-\left(k_p + \frac{k_i}{s} + k_d s\right)\frac{N(s)}{D(s)}\right]} = \frac{\left(k_p s + k_i\right)N(s)}{sD(s) + \left(k_d s^2 + k_p s + k_i\right)N(s)} \quad (4.20)$$

Thus only one zero is introduced at $-k_i/k_p$ by the controller but this can still cause a single overshoot in the step response, even if all the closed loop poles are real and negative, as will be seen shortly.

The idea leading from the PID to the IPD controller can be extended further by changing the proportional term to be fed only by the controlled output, $Y(s)$, leaving only the integral term to act on the error, $Y_r(s) - Y(s)$, resulting in the IPD controller shown in Figure 4.28.

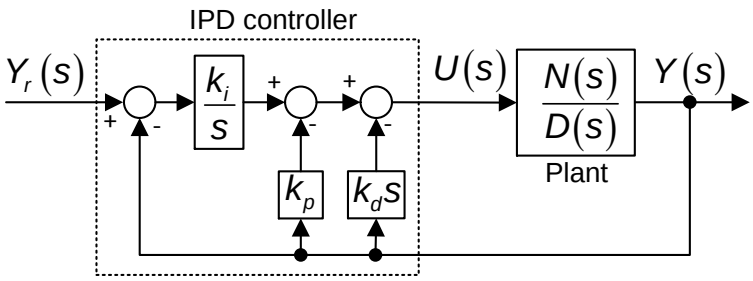

Figure 4.28: The IPD controller

The closed loop transfer function is then

$$\frac{Y(s)}{Y_r(s)} = \frac{\frac{k_i}{s}\frac{N(s)}{D(s)}}{1-\left(-\left(\frac{k_i}{s}+k_p+k_d s\right)\frac{N(s)}{D(s)}\right)} = \frac{k_i N(s)}{sD(s)+\left(k_d s^2+k_p s+k_i\right)N(s)} \quad (4.21)$$

In this case the controller introduces no finite zeros and if all the closed loop poles are negative and real, the step response cannot contain overshoots.

The following subsection explains how finite zeros can cause overshoots and undershoots.

4.5.2 Potential Effects of Zeros

If the plant has no finite zeros and the gains of the IPD controller of subsection 4.5.1 are set to yield real negative closed loop poles, then the step response will be a monotonically increasing function reaching a constant steady state value equal to the reference input step value. Let this step response be $y_{IPD}(t)$. Now let the corresponding step responses from the DPI and PID control loops, with the same reference input, be denoted, $y_{DPI}(t)$ and $y_{PID}(t)$. Next, by inspection of (4.21),

$$Y_{IPD}(s) = \frac{K_i N(s)}{Q(s)} Y_r(s) \tag{4.22}$$

where

$$Q(s) = sD(s) + \left(k_d s^2 + k_p s + k_i\right) N(s). \tag{4.23}$$

Then by inspection of (4.19) and (4.20), with a common $Y_r(s)$,

$$Y_{DPI}(s) = \left(k_p s + k_i\right) \frac{N(s)}{Q(s)} Y_r(s) = \left(\frac{k_p}{k_i} s + 1\right) \frac{k_i N(s)}{Q(s)} Y_r(s) = \left(\frac{k_p}{k_i} s + 1\right) Y_{IPD}(s) \tag{4.24}$$

and

$$Y_{PID}(s) = \left(k_d s^2 + k_p s + k_i\right) \frac{N(s)}{Q(s)} Y_r(s) = \left(\frac{k_d}{k_i} s^2 + \frac{k_p}{k_i} s + 1\right) Y_{IPD}(s) \tag{4.25}$$

Using equation (4.24) and (4.25) the corresponding functions in time are

$$y_{dpi}(t) = y_{ipd}(t) + \frac{k_p}{k_i} \frac{d}{dt}\left(y_{ipd}(t)\right) \tag{4.26}$$

$$y_{pid}(t) = y_{ipd}(t) + \frac{k_p}{k_i} \frac{d}{dt}\left(y_{ipd}(t)\right) + \frac{k_d}{k_i} \frac{d^2}{dt^2}\left(y_{ipd}(t)\right) \tag{4.27}$$

Figure 4.29 shows the simulated step responses of $y_{dpi}(t)$, $y_{pid}(t)$ and $y_{ipd}(t)$. In this case the plant, $N(s)/D(s)$, is the linear throttle valve model and the settling time used to design the controller gains are 0.1 [sec]. The IPD controller achieves the desired non-overshooting step response with the right settling time. However, both the DPI and PID controllers produce an overshoot.

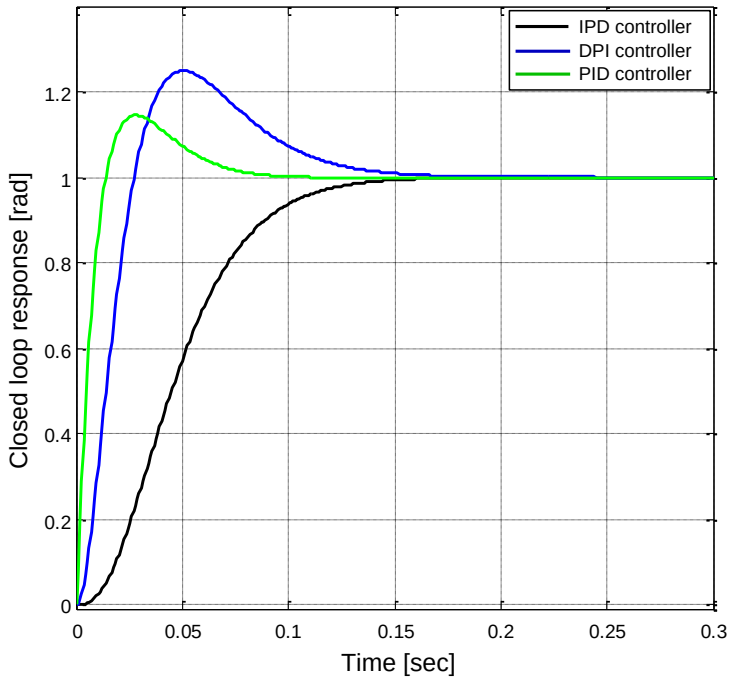

Figure 4.29: The zeros effect on the closed loop step response

In fact, the PID controller has the potential of producing an undershoot as well, due to the second derivative term in (4.27). In this case, it actually reduces the overshoot relative to that of the DPI controller but is insufficient to produce an undershoot. It would therefore appear that the IPD controller would be the best choice. On the other hand, an external pre-compensator is introduced in sections 4.5.3.1 and 4.5.3.4 to cancel the zeros. This gives precisely the same performance and resulting sensitivities, which will be the same in all three cases.

4.5.3 Controller Design

4.5.3.1 IPD Controller

The design of the IPD controller gains are based on the knowledge of the linear throttle valve model, which in this work is referred as *model based control*. The characteristic equation for the IPD closed loop system is then given by equation (4.23) with $N(s) = b_0$ and $D(s) = s^3 + a_2 s^2 + a_1 s + a_0$ from equation (2.41). Thus

$$s^4 + a_2 s^3 + (b_0 k_d + a_1) s^2 + (b_o k_p + a_0) s + b_0 k_i \tag{4.28}$$

This is of the fourth order but has only three design parameters (k_p, k_i, k_d) which makes it impossible to do a full pole assignment. This can be circumvented by doing partial pole assignment as described in section 4.4.2.3.

The IPD loop can be designed by placement of the three poles p_1, p_2 and p_3, to achieve the desired step response. These poles can be chosen freely. Thus

$$s^3 + d_2 s^2 + d_1 s + d_0 = (s + p_1)(s + p_2)(s + p_3) \tag{4.29}$$

Comparing the characteristic polynomial (4.28) with that of (4.29) shows there is has to be one dependent closed loop pole at $s = -q_0$, which requires

$$\begin{aligned} &(s^3 + d_2 s^2 + d_1 s + d_0)(s + q_0) = \\ &\quad s^4 + (d_2 + q_0) s^3 + (d_2 q_0 + d_1) s^2 + (d_1 q_0 + d_0) s + d_0 q_0 \end{aligned} \tag{4.30}$$

Equating the characteristic polynomials of (4.30) and (4.28), and making the controller gains and q_0 the subjects of the resulting equations yields

$$q_0 = a_2 - d_2 \tag{4.31}$$

$$k_d = \frac{d_2 q_0 + d_1 - a_1}{b_0} \tag{4.32}$$

$$k_p = \frac{d_1 q_0 + d_0 - a_0}{b_0} \tag{4.33}$$

$$k_i = \frac{d_0 q_0}{b_0} \tag{4.34}$$

The settling time formula from subsection 4.4.2 will now be used, assuming a third order closed loop response on the assumption that the three coincident closed loop poles at $p_{1,2,3} = -p_c$ are dominant with respect to the pole at $-q_0$. Using the settling time formula, equation (4.11), for the desired close loop settling time, T_s, with $n = 3$ yields $p_c = 6/T_s$. Then

$$\left(s^3 + d_2 s^2 + d_1 s + d_0\right) = \left(s + p_c\right)^3 = \left(s + \frac{6}{T_s}\right)^3 = s^3 + \frac{18}{T_s} s^2 + \frac{108}{T_s^{\,2}} s + \frac{216}{T_s^{\,3}} \tag{4.35}$$

Hence

$$d_2 = 18/T_s,\ d_1 = 108/T_s^{\,2} \text{ and } d_0 = 216/T_s^{\,3} \tag{4.36}$$

Since the dependent pole is located at $s_d = -q_0 = d_2 - a_2 = 18/T_s - a_2$, and

$$s_{1,2,3} = s_c = \frac{6}{T_s} \tag{4.37}$$

then

$$s_d = 3s_c - a_2 \tag{4.38}$$

According to (Dodds, 2013),

$$\left|\mathrm{Re}\left(s_d\right)\right| \geq r_{pp\min} \left|\mathrm{Re}\left(s_c\right)\right| \Rightarrow \left|s_d\right| \geq r_{pp\min} \left|s_c\right| \tag{4.39}$$

where $r_{pp\min}$ is the minimum pole-to-pole dominance ratio for which the effect of the pole at $-s_d$ can be regarded as negligible. This is based on the well-known fact that the larger the real part of a pole in the left half of the *s*-plane, the faster the impulse response of the mode with which the pole is associated will decay. In the case under study, the number of dominant poles is 3 and the number of dominated poles is 1, and the table given in (Dodds, 2013) gives

$$r_{pp\min} = 5.4 \tag{4.40}$$

It is evident from equation (4.38) that equation (4.40) can only be satisfied if

$$3s_c - a_2 \geq 5.4 s_c \Rightarrow -a_2 \geq 2.4 s_c \Rightarrow s_c \leq -a_2/2.4 \tag{4.41}$$

There is therefore an upper limit of $|s_c|$ determined by the plant parameter, a_2, beyond which the desired performance cannot be attained. In view of equation (4.37) and equation (4.41), there is a lower limit on the desired settling time of

$$\left|\frac{6}{T_{s\min}}\right| = |a_2/2.4| \Rightarrow T_{s\min} = \frac{14.4}{a_2} \tag{4.42}$$

The value obtained for a_2 from the experimental tests of Chapter 2 is 3338, giving $T_{s\min} = 0.0043$ [sec]. Since this is far smaller than possible in the throttle valve application, due to control saturation with any significant change in the reference position input and this actually has a lower limit in the region of 0.05 [sec], the partial pole placement is not restrictive. Figure 4.30 shows the relative positions of the dominant and dependent closed loop poles for $T_s = 0.1$ [sec].

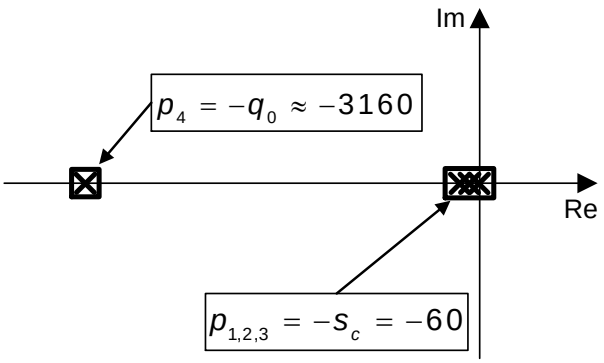

Figure 4.30: Closed loop pole locations for $T_s = 0.1$ [sec]

Figure 4.31 shows the simulated step response using the IPD controller with the linear throttle valve model from Chapter 2.4.2. It is evident that the dependent pole increases the settling time by a negligible amount beyond the nominal value.

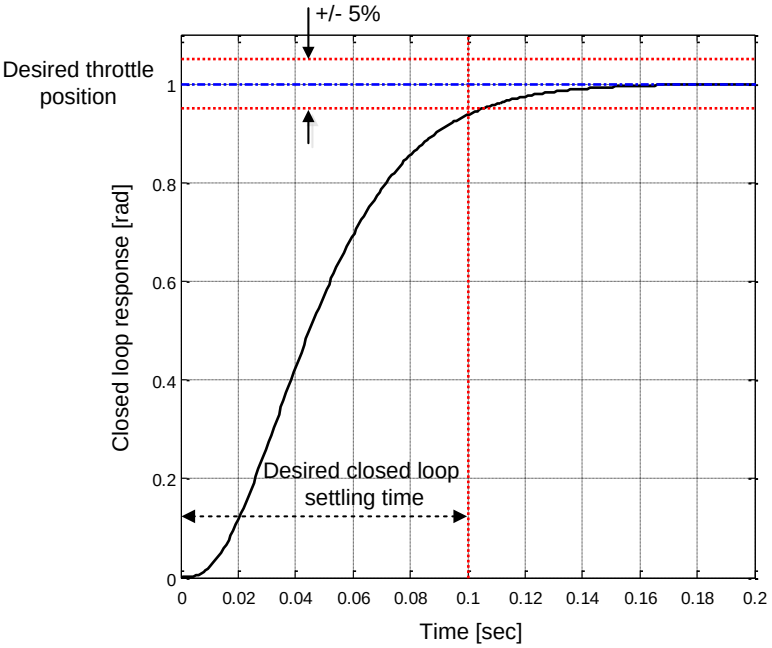

Figure 4.31: Closed loop response of a IPD controller with partial pole placement

It is known from the literature (Aström and Hägglund, 1995) that measurement noise will be amplified by the differentiator in the feedback path of the controller (Figure 4.28). To avoid the amplification of high frequency components of measurement noise by the differentiator that would be applied to the plant control input, a first order low-pass filter (noise filter) can be added in conjunction with the differentiator as shown in Figure 4.32. This low-pass filter has a flat frequency response in the pass-band.

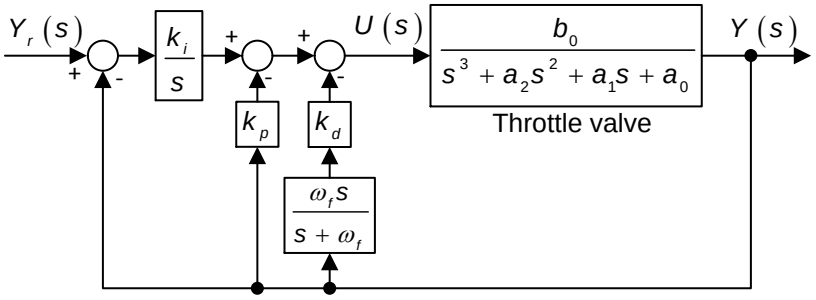

Figure 4.32: Throttle valve and IPD controller with differentiation filter

By using Mason's rule on Figure 4.32, the closed loop transfer function is

$$\frac{Y(s)}{Y_r(s)} = \frac{k_i b_0 s + \omega_f k_i b_0}{s^5 + (\omega_f + a_2)s^4 + (a_2\omega_f + a_1)s^3 + (a_1\omega_f + a_0 + b_0 k_d \omega_f + k_p b_0)s^2 + (a_0\omega_f + k_i b_0 + k_p b_0 \omega_f)s + \omega_f k_i b_0} \quad (4.43)$$

The order increases by one, compared to transfer function (4.21), due to the first order filter used for the differentiator. If the filter cut-off frequency, ω_f, is not included as an adjustable parameter in the pole placement procedure, then partial pole placement of three closed loop poles using the three controller gains leaves two dependent closed loop poles requiring a factor $(s^2 + q_1 s + q_0)$, of the closed loop characteristic polynomial. Then the polynomial (4.30) is replaced by

$$\begin{gathered}(s^3 + d_2 s^2 + d_1 s + d_0)(s^2 + q_1 s + q_0) = 0 \quad \Rightarrow \\ s^5 + (d_2 + q_1)s^4 + (d_2 q_1 + d_1 + q_0)s^3 + (d_1 q_1 + d_0 + d_2 q_0)s^2 \\ + (d_0 q_1 + d_1 q_0)s + d_0 q_0 = 0\end{gathered} \quad (4.44)$$

Equating the denominator of transfer function (4.43) to polynomial (4.44), and solving the resulting equations for the three controller gains and the coefficients, q_0 and q_1, yields

$$q_1 = \omega_f + a_2 - d_2 \quad (4.45)$$

$$q_0 = a_2\omega_f + a_1 - d_1 - d_2 q_1 \quad (4.46)$$

$$k_i = (d_0 q_0)/(\omega_f b_0) \quad (4.47)$$

$$k_p = (d_0 q_1 + d_1 q_0 - a_0\omega_f - k_i b_0)/(\omega_f b_0) \quad (4.48)$$

$$k_d = (d_0 + d_1 q_1 + d_2 q_0 - a_1\omega_f - a_0 - k_p b_0)/(\omega_f b_0) \quad (4.49)$$

Without the noise filter, and assuming no plant modelling errors, the three dominant closed loop poles lie precisely at $s_{1,2,3} = -6/T_s = -60$ for $T_s = 0.1$. The introduction of the filter, however, will cause these poles to shift from this location, but not significantly if

$$\omega_f \geq 6/T_s = 60. \tag{4.50}$$

Otherwise the closed loop poles will be forced to move significantly from the desired location and consequently impair the performance of the control system. ω_f is set to 500 [rad/sec] (~80 [Hz]) to satisfy inequality (4.50) and lower than the free pole at ~3160 [rad/sec], shown in Figure 4.30.

A plot of the closed loop poles and zero locations for the IPD controller with a first order filter and the linear throttle valve plant model is shown in Figure 4.33. The filter introduces a closed loop zero and pole between the dominant pole group and the dependent pole.

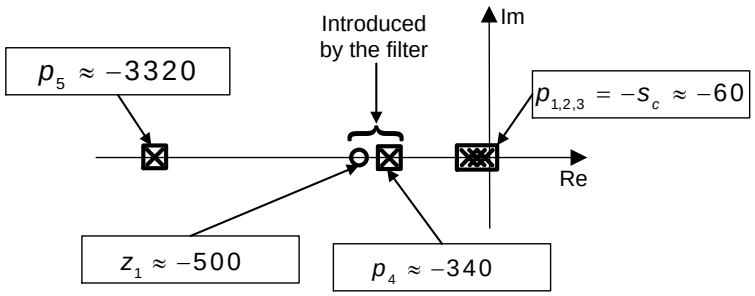

Figure 4.33: The closed loop poles and zero locations for the IPD controller with a differentiating filter

Figure 4.34 shows the impact of the filter on the simulated closed loop step response and the error between the desired and the actual step response. The dashed blue line indicates a precise response when the filters coefficient ω_f is included in the calculations of the gains for the IPD controller, equation (4.45) to (4.49). The dashed red line shows a 4 times higher difference between the desired and the actual step response, when the filter coefficient ω_f is not included in the calculations, equation (4.31) to (4.34).

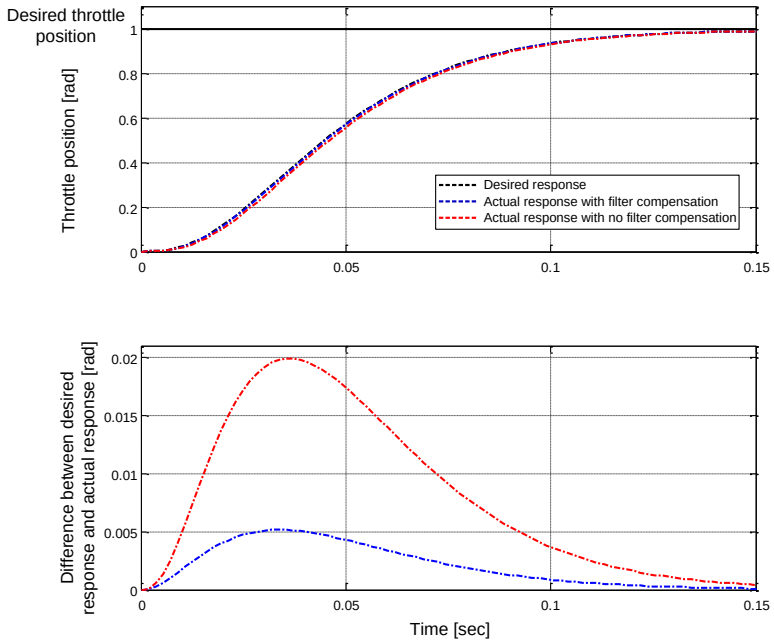

Figure 4.34: Simulated step response with/without noise filter compensation

Although taking the filter into account in the partial pole placement reduces the error by a factor of four, it is not really needed in this case, as from a practical viewpoint, both of the step responses of Figure 4.34 are sufficiently close to the ideal one to be acceptable.

4.5.3.2 DPI Controller

A DPI controller, first introduced in 4.5.1, is shown in Figure 4.35 with a noise filter for the differentiator,

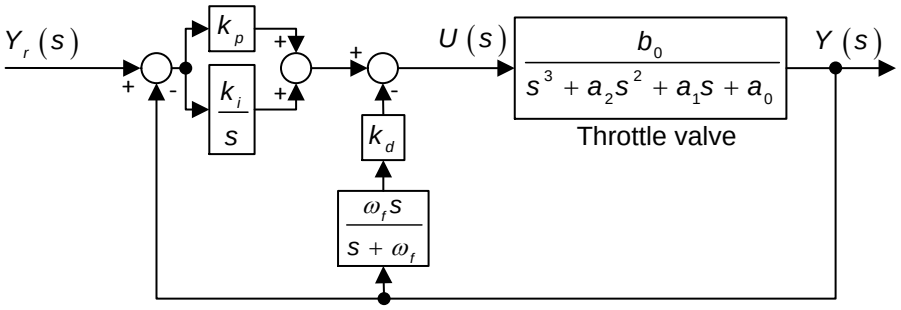

Figure 4.35: DPI controller with differentiation filter

The transfer function in this case is

$$\frac{Y(s)}{Y_r(s)} = \frac{\left(k_p + \frac{ki}{s}\right)\left(\frac{b_0}{s^3+a_2s^2+a_1s+a_0}\right)}{1-\left[-\frac{b_0}{s^3+a_2s^2+a_1s+a_0}\left(k_p + \frac{ki}{s} + \frac{k_d\omega_f s}{s+\omega_f}\right)\right]} \tag{4.51}$$

$$\frac{Y(s)}{Y_r(s)} = \frac{(b_0k_p)s^2 + (k_ib_0 + \omega_f k_p b_0)s + \omega_f k_i b_0}{s^5 + (\omega_f + a_2)s^4 + (a_1 + \omega_f \cdot a_2)s^3 + (a_0 + k_p b_0 + \omega_f a_1 + k_d\omega_f b_0)s^2 + (k_i b_0 + \omega_f a_0 + \omega_f k_p b_0)s + k_i b_0\omega_f} \tag{4.52}$$

The partial pole placement design equations for this DPI controller are identical to those for the IPD controller with the noise filter derived in subsection 4.5.3.1, because the denominator of transfer function (4.52) is identical to the closed loop transfer function (4.43). Hence equations (4.45) to (4.49), inclusive yield the required controller gains, k_d, k_p and k_i together with the dependent pole polynomial coefficients, q_0 and q_1.

The degree of the numerator polynomial of transfer function (4.52), however, has increased by one relative to transfer function (4.43) for the IPD controller, equation (4.43). This introduces a closed loop zero. As described in subsection 4.5.2, and the in literature (Franklin et al., 2002), this zero can cause the step response to overshoot. Figure 4.36 shows the simulated closed loop response

of the DPI and IPD controllers applied to the linear throttle valve model with a settling time of $T_s = 0.1$ [sec]. In this case there is no actuator saturation limits applied in the simulation model.

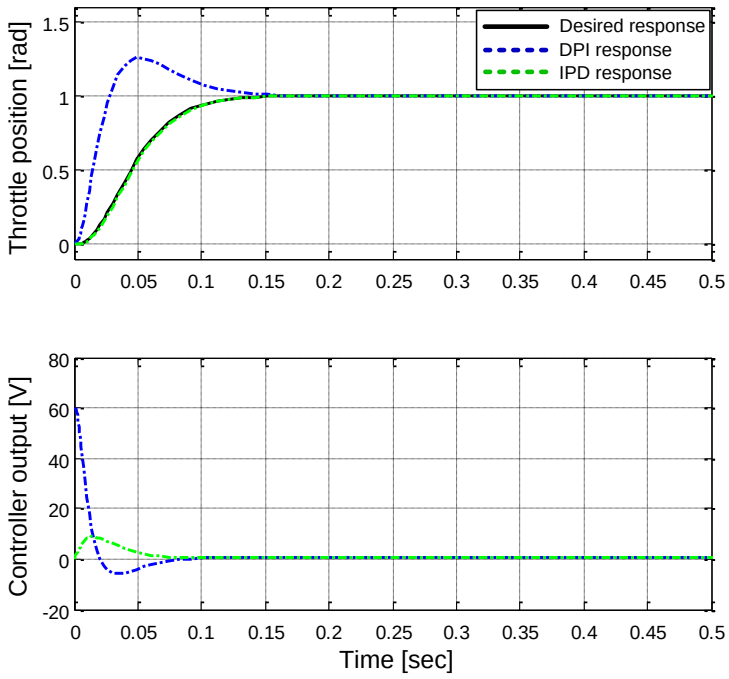

Figure 4.36: The impact of the zero on the closed loop systems response

As well as the overshoot being larger than acceptable, it introduces the further unwanted side effect of excessive initial levels of the control, $u(t)$, as shown in Figure 4.36 during the initial phase $t < 0.015$ [sec]. This can cause a problem on a real system due to the control saturation limits, as investigated in subsection 4.4.4. A simulation of the DPI control system with saturation, at +/-12 Volt, is shown in Figure 4.37. The controller output is saturated at 12 Volt from t =0 to 0.05 [sec], which causes integrator windup and the step response overshoot to increase from about 1.25 to 1.5 [rad], as evident by comparing Figure 4.36 with Figure 4.37.

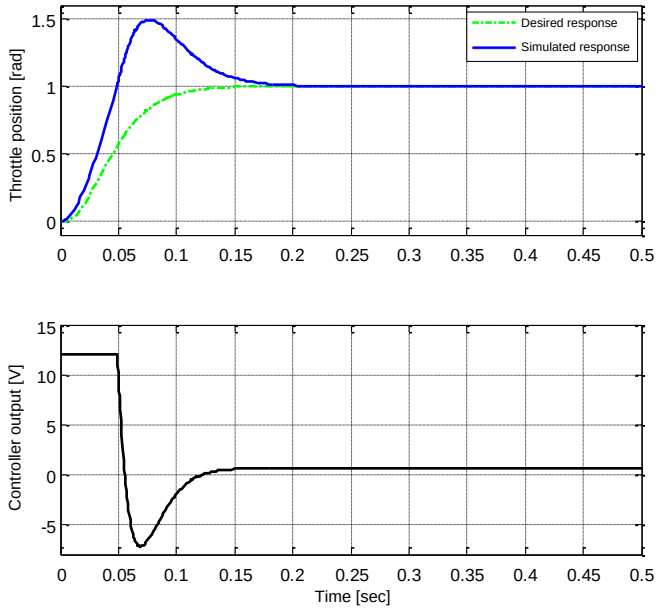

Figure 4.37: Closed loop simulation of the DPI controller with a linear throttle valve plant model and limits on the controller output

To circumvent the overshoot problem, two different strategies have been applied and simulated:

1) A precompensator is used to cancel the closed loop zeros, and

2) An anti-integrator windup strategy is applied.

1) Figure 4.38 shows the DPI controller based system with the precompensator attached. The transfer function, $R(s)/Z(s)$, can be designed to remove the effect of the closed loop zeros and poles by pole-zero cancellation. This is done without changing the characteristic dynamics of the closed loop system.

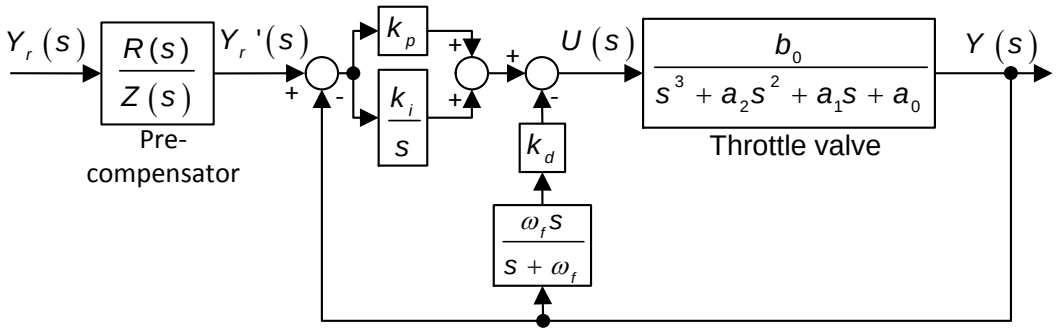

Figure 4.38: DPI controller with precompensator

The precompensator will in this case be used to cancel both of the zeros. This is achieved by making the denominator of the precompensator cancel the numerator, $b_0 k_p s^2 + \left(k_i b_0 + \omega_f k_p b_0\right)s + \omega_f k_i b_0$, of the closed loop transfer function (4.52), but first this may be simplified by normalisation with respect to the constant coefficient to yield

$$\frac{b_0 k_p s^2 + \left(k_i b_0 + \omega_f k_p b_0\right)s + \omega_f k_i b_0}{\omega_f k_i b_0} = \frac{k_p}{\omega_f k_i} s^2 + \left(\frac{1}{\omega_f} + 1\right)s + 1 \tag{4.53}$$

Since the control loop already has a unity DC gain due to the integral term, then the pre-compensator must also have a unity DC gain. Hence the pre-compensator transfer function is simply the reciprocal of polynomial (4.53). Thus

$$\frac{R(s)}{Z(s)} = \frac{1}{\frac{k_p}{\omega_f k_i} s^2 + \left(\frac{1}{\omega_f} + 1\right)s + 1} \tag{4.54}$$

A simulation of a closed loop step response where both zeros are cancelled in this way is shown in Figure 4.39. An important observation is that the controller output does not reach the saturation limit due to the slower reference input, $y_r'(t)$ produced by the precompensator. In this case the precompensator makes the need for an integrator anti windup strategy unnecessary.

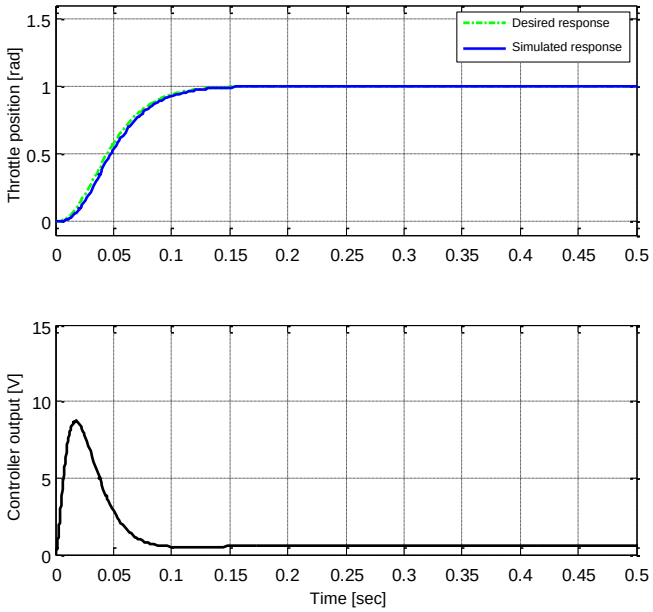

Figure 4.39: Closed loop simulation of the DPI controller with precompensator cancelling both zeros

2) Minimising the overshoot caused by the controller output saturation can be achieved by the integrator anti-windup strategy introduced in subsection 4.4.4. This will limit the saturation by manipulating the integrator input to hold the primary plant control input, u', within limits approximately equal to u_{max} and u_{min} as shown in Figure 4.40, by setting the gain, K, to a sufficiently large value.

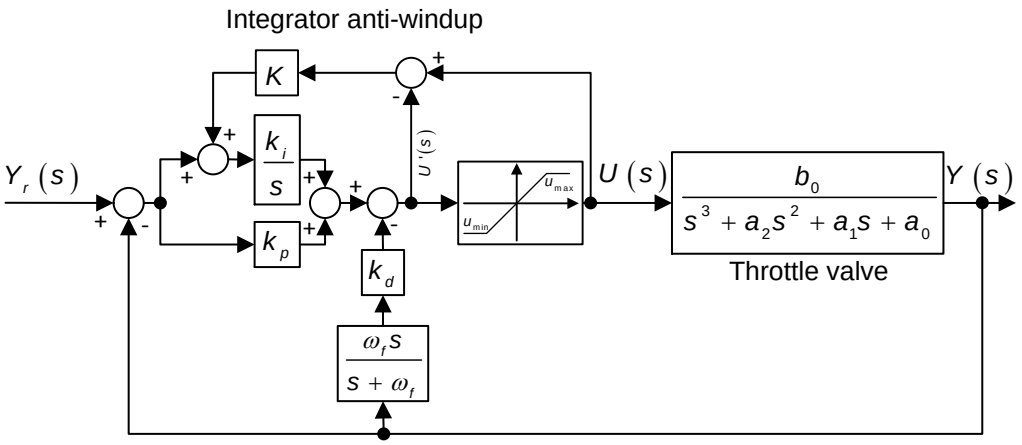

Figure 4.40: DPI controller with integrator anti-windup

Figure 4.41 shows the simulated closed loop step response of the implemented strategy, shown in Figure 4.40, with the integrator anti-windup gain set to $K = 1$.

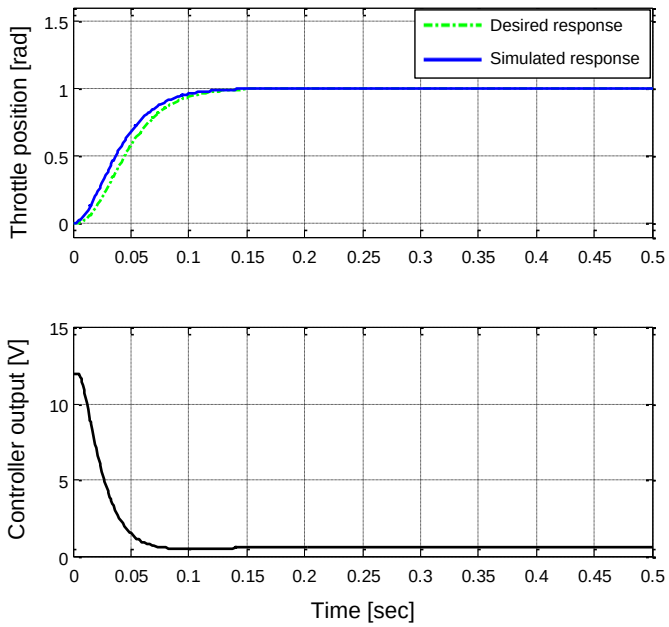

Figure 4.41: Closed loop step response of the DPI controller with integrator anti-windup (Large step)

In this case, the overshoot of the step response has been eliminated due to the action of the anti-windup loop but it is important to note that it cannot be eliminated by this means for reference input steps that are not large enough to cause control saturation, as shown in Figure 4.42.

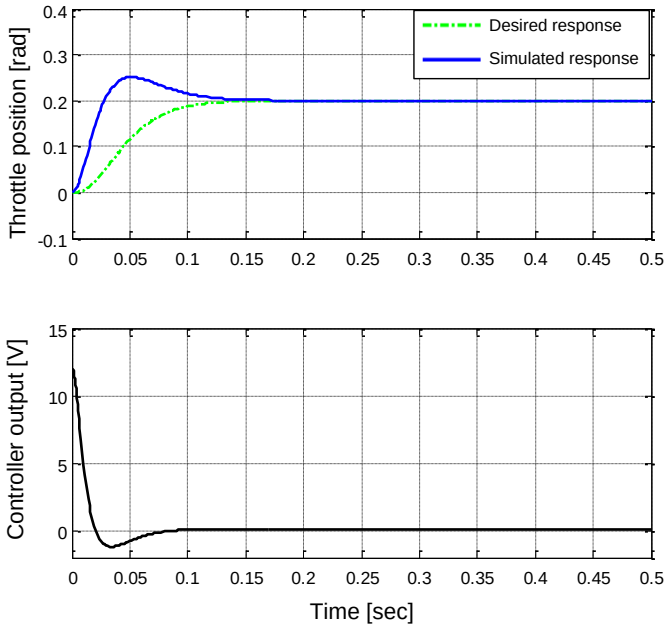

Figure 4.42: Closed loop step response of the DPI controller with integrator anti-windup (Small step)

4.5.3.3 DPI Controller with Feed Forward and Manual Tuning

Throughout industry it is common for suitable controller gains to be found manually by trial-and-error and sometimes by special systematic procedures dependent upon the application. This approach is therefore included in this work to benchmark the other control strategies against, not regarding performance, which would not be expected to be optimal in any sense, but regarding comparisons of the personnel effort needed.

For the tuning of controllers a number of different tools and processes are available such as the Ziegler-Nichols tuning rules (Shahrokhi and Zomorrodi, 2003) (Aström and Hägglund, 1995). For this work the majority of the controller tuning is undertaken with the aid of a toolbox from Mathworks® called *Design Optimisation*.

The controller selected for the manual tuning is one typical for throttle valve position control in the automotive industry. This is the DPI controller with a feed forward loop to compensate for the pre-stressed coil spring torque. The original DPI controller employed was designed in the discrete time domain (z-domain) with discontinuous functions. The discontinuous functions are used for improving the control performance e.g. applying different gains. A simplified model, used for this work, without the discontinuous functions is shown in Figure 4.43.

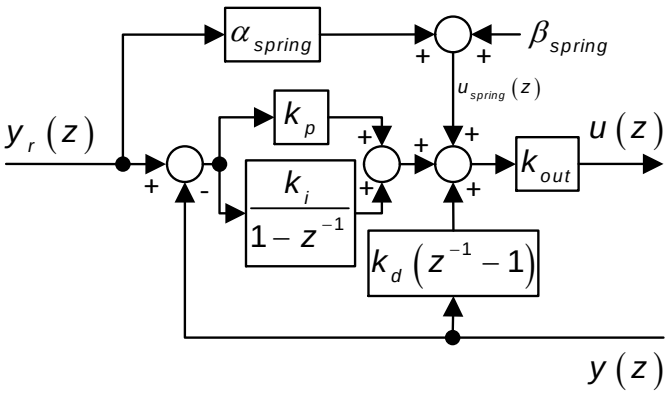

Figure 4.43: Simplified discrete time DPI controller with feed forward

Here, the feed forward signal, $u_{spring}(z) = y_r(z) \cdot \alpha_{spring} + \beta_{spring}$, is used to counteract the torque from the coiled spring and k_{out} is a percent to duty cycle conversion factor, since the coil drive is implemented using pulse width modulated switched power electronics. By using the feed forward compensation, the feedback part of the controller is only required to move the

throttle valve from one position to another with the required closed loop dynamics. The feed forward compensation is useful especially if the coiled spring characteristic is nonlinear, in which case the linear compensation has to be replaced by a nonlinear mapping function.

The discrete time model, Figure 4.43, is converted into a continuous time model used for investigation of sensitivity later on, shown in Figure 4.44,

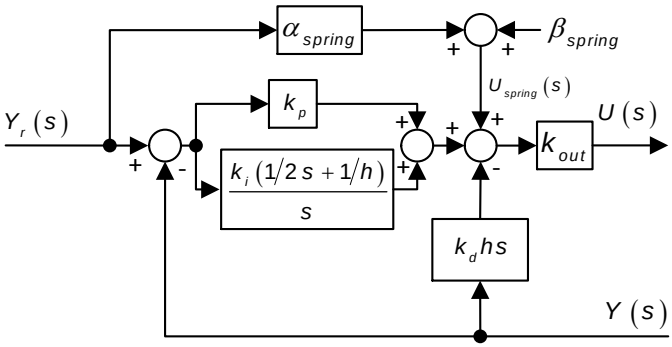

Figure 4.44: Simplified continuous time DPI controller

where h is the sampling time interval.

A Simulink® model of the discrete time IPD controller with the feed forward and the nonlinear throttle model of section 2.5 with sample and hold units at the input and output is used for the Mathworks toolbox tuning. The nonlinear throttle model is used because it includes the pre-stressed coil spring model. The controller reference input $y_r(t)$ is a predefined signal, in this case the staircase shaped waveform of Figure 4.45, shown in green. The *Design Optimisation* toolbox tunes the controller by adjusting the controllers gains until $y(t)$ tracks the desired closed loop response (Figure 4.45, shown in red), while running the Simulink® model. The desired closed loop response is obtained as the output of a chain of four identical first order blocks with time constants set according to the 5% settling time formula with $T_s = 0.1$ [sec].

Other signals were used for the tuning such as ramps and sinusoidal waveforms. The *Design Optimisation* toolbox works in a similar manner to the *Design Optimization* toolbox used in chapter 3.2.

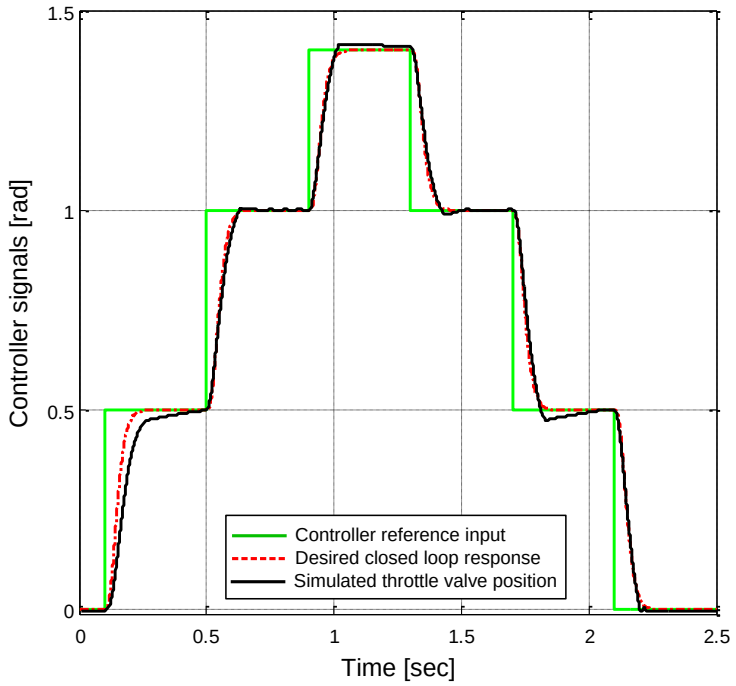

Figure 4.45: Example of a waveform used for the tuning of the DPI

The black waveform in Figure 4.45 is the simulated throttle valve position, $y(t)$, using the final tuned gains, found by the toolbox and manual tuning.

4.5.3.4 PID Controller

A PID controller, first introduced in 4.5.1, with a noise filter for the differentiator is included as it is still arguably the most commonly used controller in industry. This is shown in Figure 4.46 applied to the throttle valve.

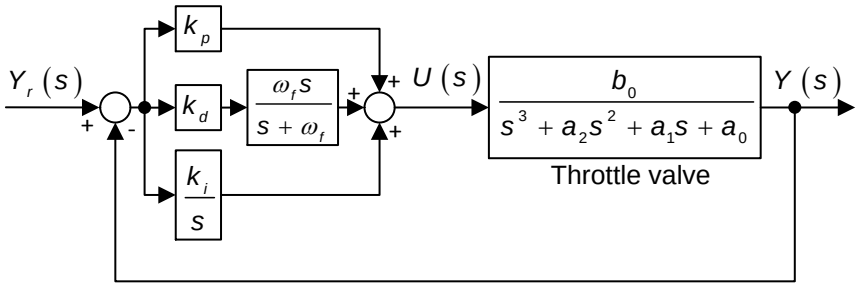

Figure 4.46: PID controller with differentiation noise filter

The closed loop transfer function in this case is

$$\frac{Y(s)}{Y_r(s)} = \frac{\left(k_p + \frac{ki}{s} + \frac{k_d\omega_f s}{s+\omega_f}\right)\left(\frac{b_0}{s^3+a_2s^2+a_1s+a_0}\right)}{1-\left[-\frac{b_0}{s^3+a_2s^2+a_1s+a_0}\left(k_p + \frac{ki}{s} + \frac{k_d\omega_f s}{s+\omega_f}\right)\right]}$$

$$= \frac{\left(b_0k_p + \omega_f k_d b_0\right)s^2 + \left(k_i b_0 + \omega_f k_p b_0\right)s + \omega_f k_i b_0}{s^5 + \left(\omega_f + a_2\right)s^4 + \left(a_1 + \omega_f \cdot a_2\right)s^3 + \left(a_0 + k_p b_0 + \omega_f a_1 + k_d\omega_f b_0\right)s^2} \qquad (4.55)$$
$$+\left(k_i b_0 + \omega_f a_0 + \omega_f k_p b_0\right)s + k_i b_0\omega_f$$

As for the DPI controller, the denominator of the transfer function, which is the closed loop characteristic polynomial, is identical to that of the IPD controller with the measurement noise filtering, given by transfer function (4.43). In this case, the design equations for the controller gains, k_p, k_i and k_d together with the coefficients, q_0 and q_1, of the dependent pole polynomial factor in the partial pole assignment are given by equations (4.45) to (4.49) inclusive. The numerator polynomial of the closed loop transfer function (4.55), is of second degree, indicating the presence of closed loop zeros with a potential overshooting problem. To remove the effect of the zeros both the techniques (1) and (2) investigated in subsection 4.5.3.1 are applied together, i.e., a precompensator to cancel both of the zeros and an integrator anti windup loop. The complete control system is shown in Figure 4.47.

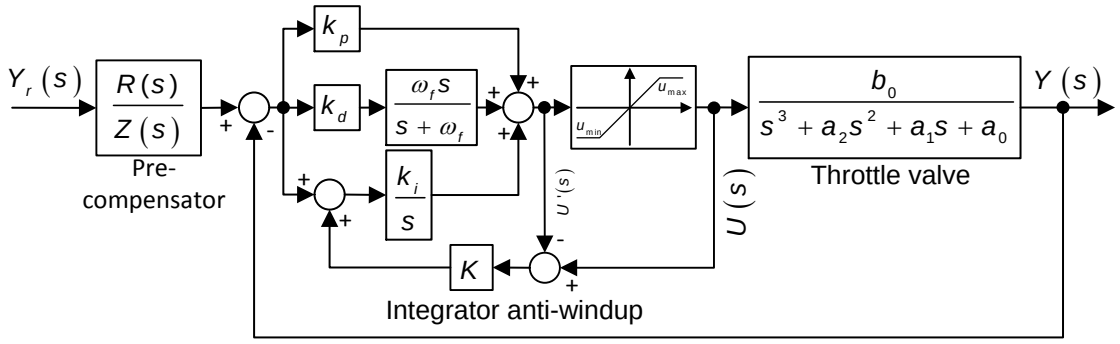

Figure 4.47: PID controller with differentiation filter, precompensator and integrator anti windup

With reference to the numerator of the closed loop transfer function (4.55), the precompensator transfer function $R(s)/Z(s)$ used to cancel the two closed loop zeros is given by

$$\frac{R(s)}{Z(s)} = \frac{\omega_f k_i b_0}{\left(b_0 k_p + \omega_f k_d b_0\right)s^2 + \left(k_i b_0 + \omega_f k_p b_0\right)s + \omega_f k_i b_0} \tag{4.56}$$

A simulation of a closed loop step response where both zeros are cancelled in this way is shown in Figure 4.48. As the DPI controller in subsection 4.5.3.2, the PID controller output does not reach the saturation limit due to the slower reference input, $y_r'(t)$ produced by the precompensator.

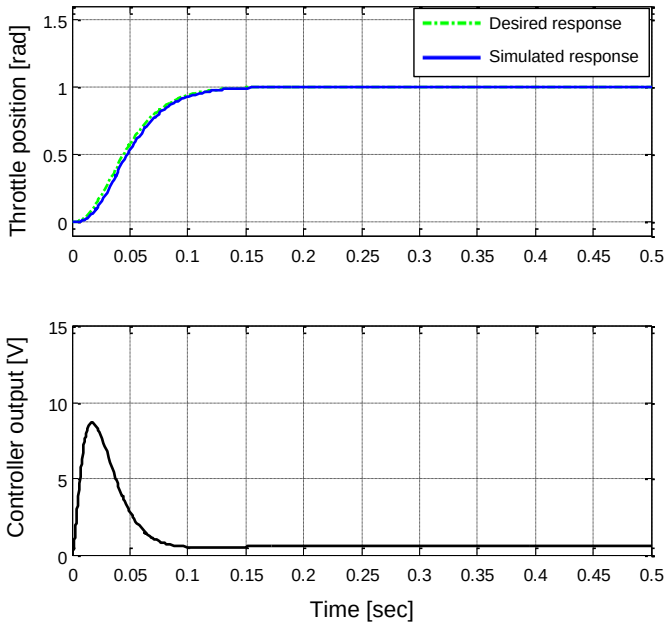

Figure 4.48: Closed loop simulation of the PID controller with precompensator cancelling both zeros

The result of an experimental based comparison of the PID controller with and without a precompensator and integrator anti-windup can be seen in subsection 4.5.4.4 (Figure 4.70).

4.5.4 Simulation and Experimental results

4.5.4.1 IPD Controller

The IPD controller gains are determined as described in subsection 4.5.3.1, equations (4.47) to (4.49) with $T_s = 0.1$ [sec] and $\omega_f = 500$ [rad/sec]. A dither signal is added to the control signal to reduce the effects of the static friction as described in subsection 4.4.3. The integrator anti-windup strategy is enabled to minimise the duration of the control saturation following the application of a step reference input. The IPD controller is tested experimentally with three different

reference input functions as described in subsection 4.3.3. The dSPACE system is used for the experiments as explained in subsection 4.3.2.

The simulation results presented in this subsection are obtained with the full nonlinear plant model presented in section 2.5.

First, simulated and experimental responses to a step reference position change within the throttle valve stop limits are presented in Figure 4.49.

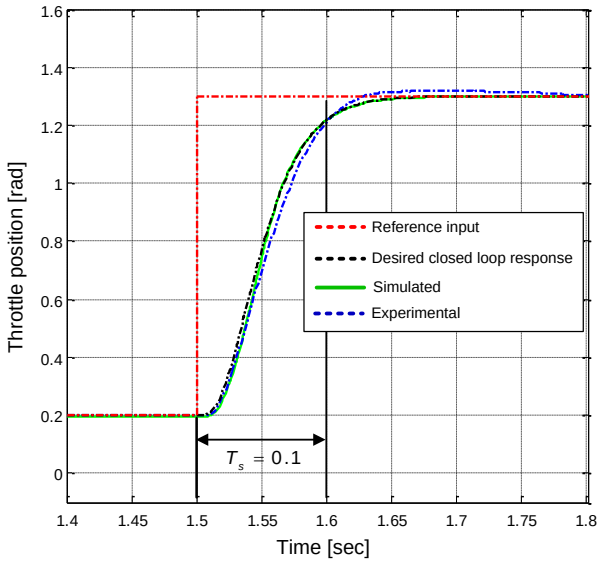

Figure 4.49: Closed loop step response, from 0.2 to 1.3 [rad]

The vertical black lines mark the nominal settling time of $T_s = 0.1$ [sec]. It is evident that both the experimental and simulated responses come close to this at ≈ 1.24 [rad].

Figure 4.50 shows superimposed simulated and experimental closed loop responses using the IPD controller with three different reference input functions, the reasons for which are stated in subsection 4.3.3. In all cases, the simulated and experimental responses are remarkably close.

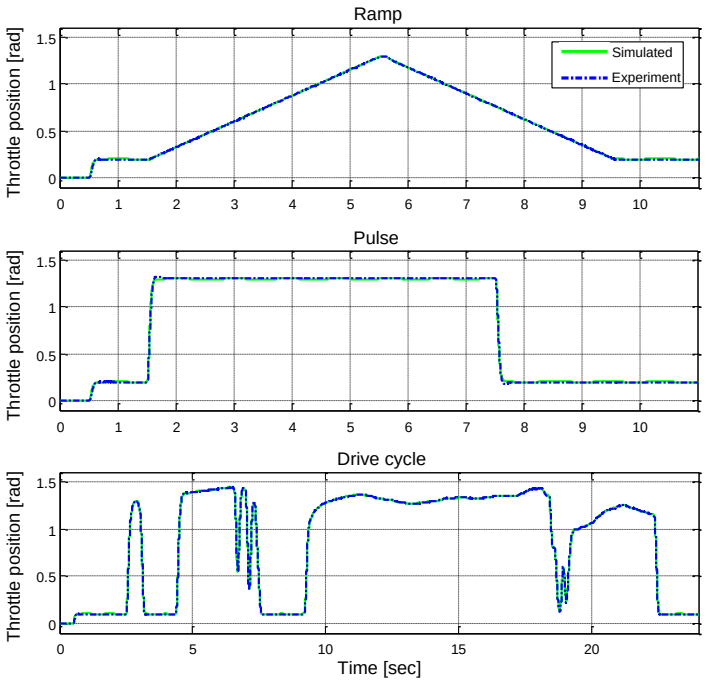

Figure 4.50: Experimental and simulated response of the IPD controller

Figure 4.51 shows the differences between the desired and the experimental closed loop responses corresponding to Figure 4.50. The relatively small differences could be attributed to the accuracy of the plant model but they could also be due to the robustness of the control loop, which would give nearly the same responses despite mismatching between the plant and its model.

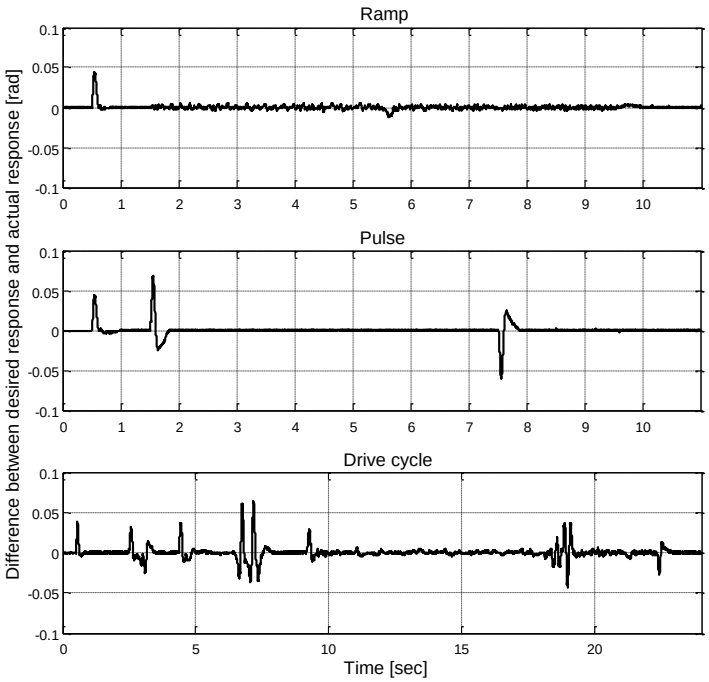

Figure 4.51: The difference between the desired and the experimental closed loop responses

As explained in subsection 4.3.4.3 a spring failure can cause the engine to stall due to air starvation. The behaviour of the IPD controller during a spring break, at $t = 1$ [sec], is simulated using the nonlinear throttle valve model, and the result is shown in Figure 4.52. It shows a good robustness against the disturbance, with an acceptable deviation from the throttle position demand. The oscillations on the control signal at $t = 1.02$ [sec] are the added dither signal that increases in amplitude when the control error, $y_r - y$, exceeds a preset threshold of 1% of the full scale movement range as described in subsection 4.4.3.

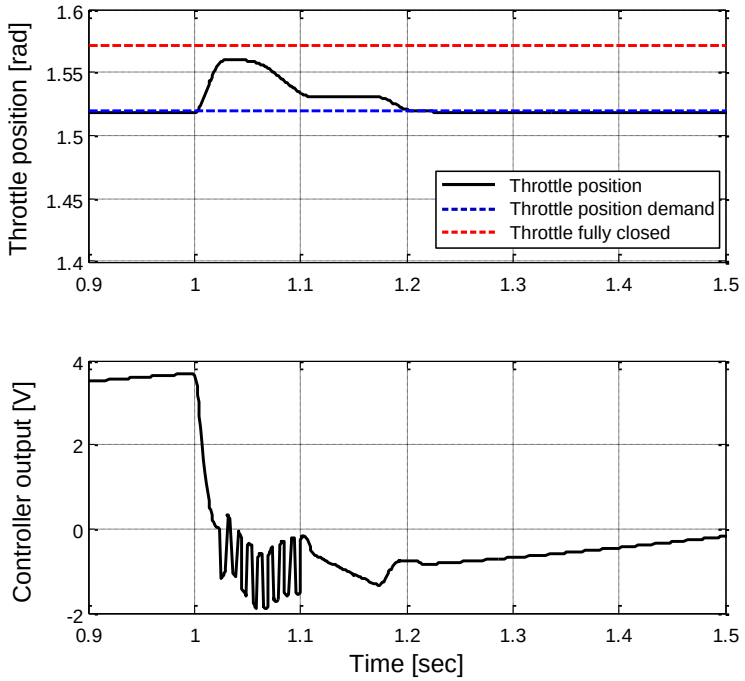

Figure 4.52: IPD controller during a spring failure

The robustness against plant parameter deviations away from the nominal values is tested using the Monte Carlo method described in subsection 4.3.4.2. The result of the parameter variation simulation is shown in Figure 4.53 for the maximum possible standard deviation of $\sigma = 15\%$. The figure shows the operational envelope for 1000 simulation runs, where the blue and red lines are the minimum and maximum values. The nominal parameter closed loop controller response and controller output are shown in black.

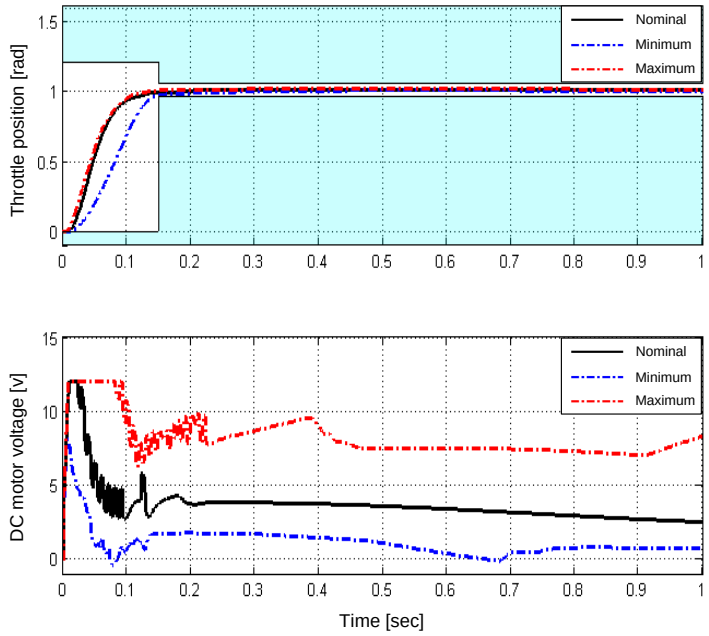

Figure 4.53: Maximum / minimum throttle position and DC motor voltage envelope (Standard deviation: $\sigma = 15\%$)

This indicates that the plant parameters can deviate significantly from the nominal values before having an adverse impact on the performance of the controller.

The sensitivity for the IPD controller is analysed in the frequency domain by using the relationship of equation (4.3) in subsection 4.3.4.1. This is done with the aid of the Matlab Control System Analysis Toolbox and the block diagram of Figure 4.54 implemented in Simulink with $D(s)$ as the input and $V(s)$ as the output to obtain $S_p^C dB(\omega)$.

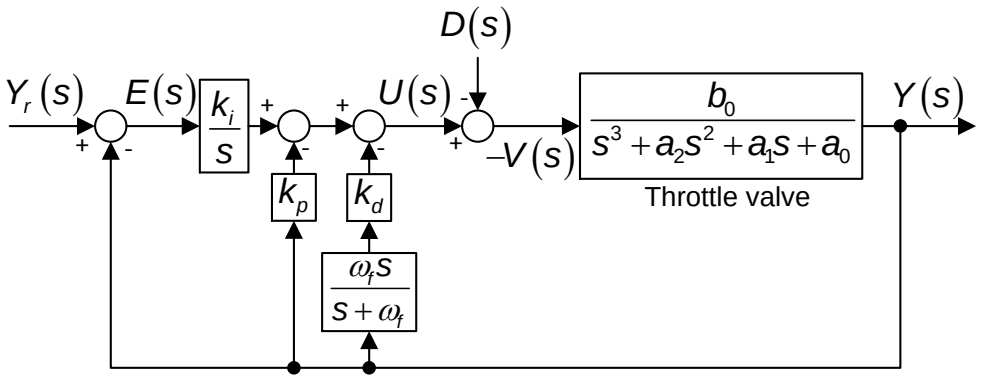

Figure 4.54: Control structure used to analyse the sensitivity

Ignoring the differential filtering term, as ω_f is well outside the control loop bandwidth, the sensitivity transfer function is

$$\frac{V(s)}{D(s)} = S_p^C(s) = \frac{1}{1-\left[-\frac{b_0}{s^3+a_2s^2+a_1s+a_0}.\left(k_d s + k_p + \frac{k_i}{s}\right)\right]}$$

$$= \frac{s^4+a_2s^3+a_1s^2+a_0s}{s^4+a_2s^3+(a_1+b_0k_d)s^2+(a_0+b_0k_p)s+b_0k_i} \qquad (4.57)$$

The sensitivity result is shown in Figure 4.55.

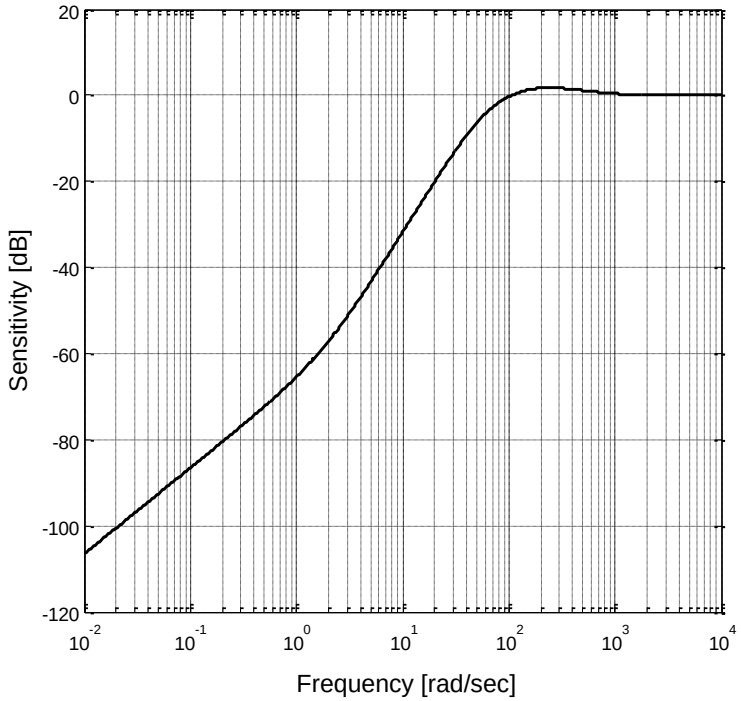

Figure 4.55: IPD sensitivity

This indicates a relatively low sensitivity, equivalent to high robustness. This corresponds well with the time domain result found by the above spring failure analysis and the Monte Carlo parameter variation simulation.

4.5.4.2 DPI Controller

The closed loop characteristic polynomial for the DPI controller is the same as that for the IPD controller and therefore the gains are calculated as described in subsection 4.5.3.1, equations (4.47) to (4.49) with $T_s = 0.1$ [sec] and $\omega_f = 500$ [rad/sec]. The precompensator is designed to cancel both zeros, as described in subsection 4.5.3.2. A dither signal is added to the control signal to reduce the effects of the static friction as described in subsection 4.4.3. The integrator anti-windup strategy is enabled to minimise the duration of any control saturation occurring following application of a step reference input. The DPI controller is tested experimentally with three different reference input functions, the

description and purpose of which are given in subsection 4.3.3. The dSPACE system is used for the experiments as explained in subsection 4.3.2.

The simulation results presented in this subsection are obtained with the full nonlinear plant model presented in section 2.5.

First, simulated and experimental responses to a step reference position change within the throttle valve stop limits are presented in Figure 4.56.

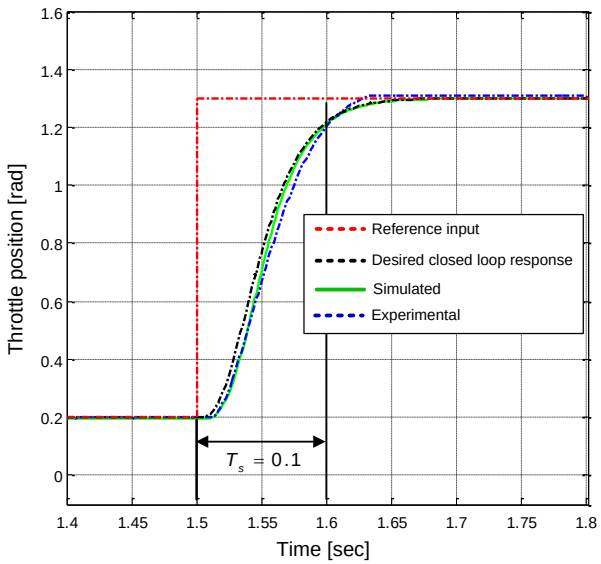

Figure 4.56: Closed loop step response, from 0.2 to 1.3 [rad]

The vertical black lines mark the nominal settling time of $T_s = 0.1$ [sec]. It is evident that both the experimental and simulated responses come close to this at ≈ 1.24 [rad].

Figure 4.55 shows the simulated and experimental closed loop responses of the DPI controller.

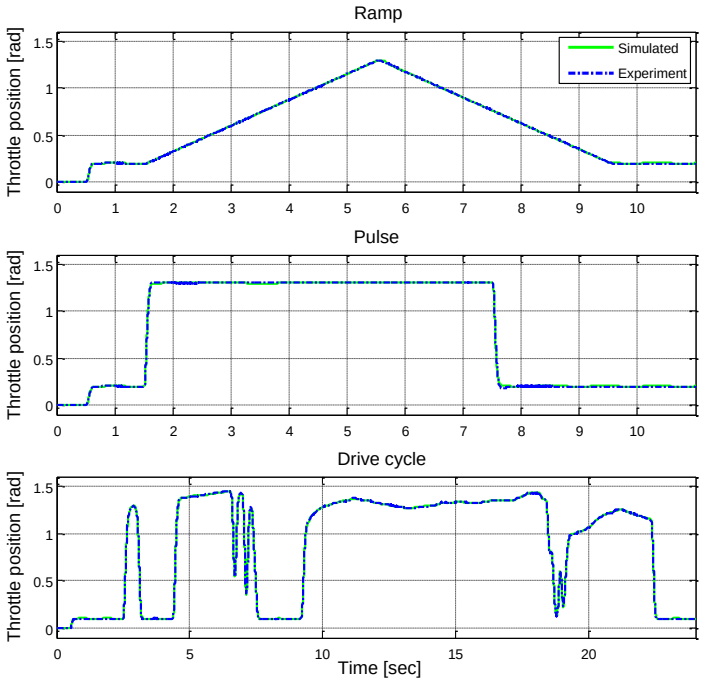

Figure 4.57: Experimental and simulated response of the DPI controller

The relatively small differences could be attributed to the accuracy of the plant model but they could also be due to the robustness of the control loop, which would give nearly the same responses despite mismatching between the plant and its model.

Figure 4.58 shows the difference between the desired and the experimental closed loop responses, indicating good tracking and negligible steady state error.

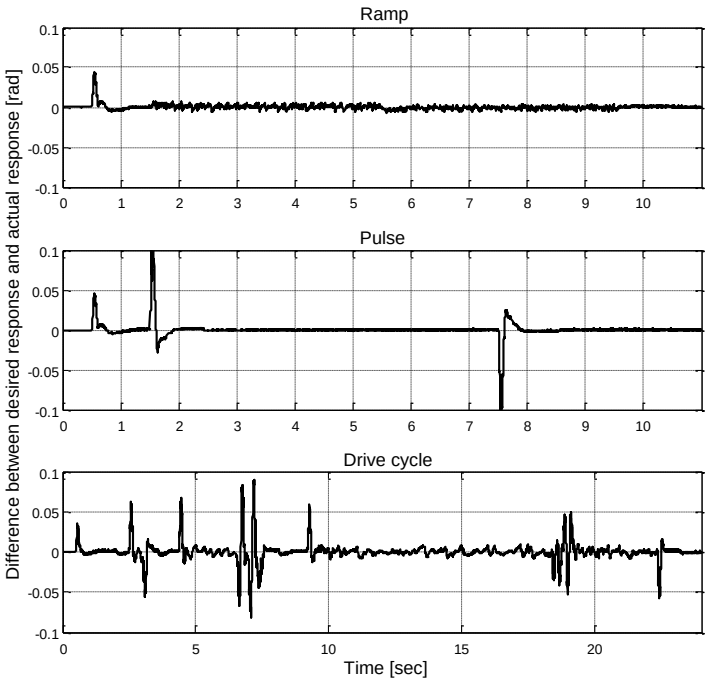

Figure 4.58: The difference between the desired and the experimental closed loop responses

As described in subsection 4.3.4.3 a spring failure can cause the engine to stall due to air starvation. The behaviour of the DPI controller during a spring break, at $t = 1$ [sec], is simulated using the nonlinear throttle valve model, and the result is shown in Figure 4.59. It shows a good robustness against the disturbance, with little deviation from the throttle position demand. The oscillations on the control signal at $t = 1.02$ [sec] are the added dither signal that increases in amplitude when the control error, $y_r - y$, exceeds a preset threshold of 1% of the full scale movement range as described in subsection 4.4.3.

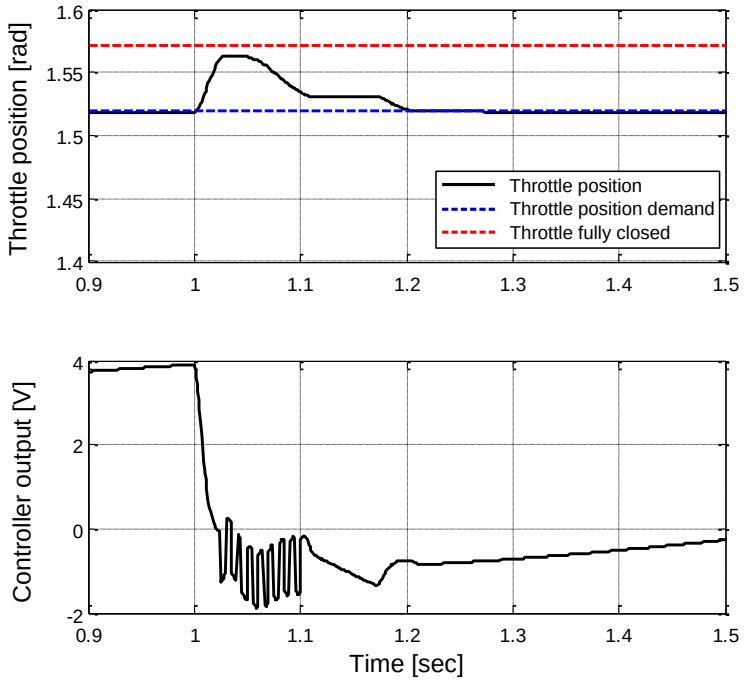

Figure 4.59: DPI controller during a spring failure

The robustness against plant parameter deviations away from the nominal values is tested using the Monte Carlo method described in subsection 4.3.4.2. The parameter variation simulation uses the nonlinear throttle valve model with the controller output saturation, integrator anti-windup, dither and the precompensator. The result of the parameter variation simulation is shown in Figure 4.60 for the maximum possible standard deviation of $\sigma = 14\%$. The figure shows the operational envelope for 1000 simulation runs, where the blue and red lines are the minimum and maximum values. The nominal parameter closed loop controller response and controller output are shown in black.

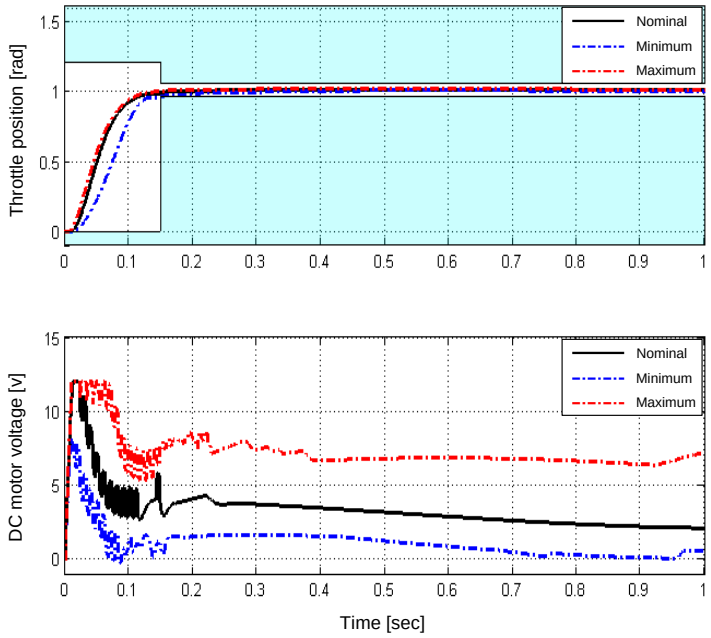

Figure 4.60: Maximum / minimum throttle position and DC motor voltage envelope (Standard deviation: $\sigma = 14\%$)

This indicates that the plant parameters can deviate significantly from the nominal values before having an adverse impact on the performance of the controller.

The sensitivity for the DPI controller is analysed in the frequency domain by using the relationship of equation (4.3) in subsection 4.3.4.1. This is done with the aid of the Matlab Control System Analysis Toolbox and the block diagram of Figure 4.61 implemented in Simulink with $D(s)$ as the input and $V(s)$ as the output to obtain $S_p^C dB(\omega)$.

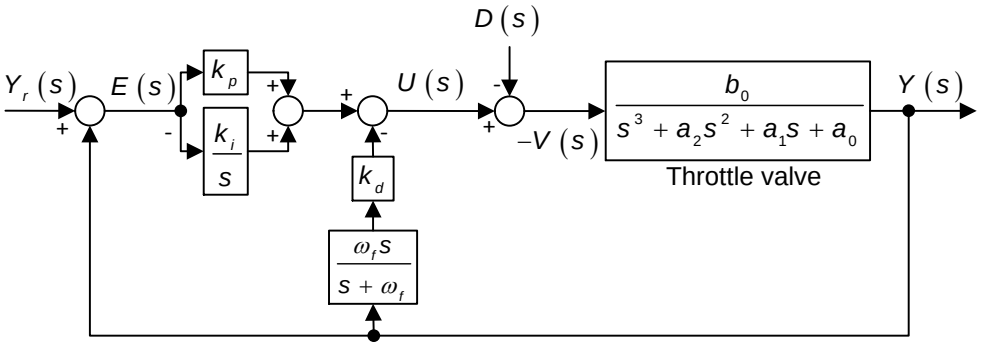

Figure 4.61: Control structure used to analyse the sensitivity

Ignoring the differential filtering term, as ω_f is well outside the control loop bandwidth, the sensitivity transfer function is

$$\frac{V(s)}{D(s)} = S_p^C(s) = \frac{1}{1-\left[-\frac{b_0}{s^3+a_2s^2+a_1s+a_0}.\left(k_ds+k_p+\frac{k_i}{s}\right)\right]}$$

$$= \frac{s^4+a_2s^3+a_1s^2+a_0s}{s^4+a_2s^3+(a_1+b_0k_d)s^2+(a_0+b_0k_p)s+b_0k_i} \qquad (4.58)$$

The sensitivity result is shown in Figure 4.62.

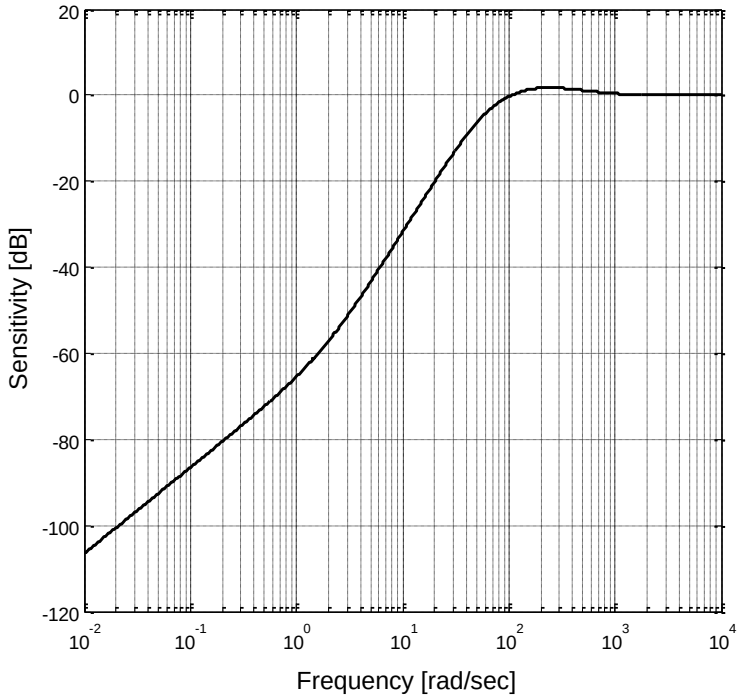

Figure 4.62: DPI sensitivity

This indicates a relatively low sensitivity, equivalent to high robustness. This corresponds well with the time domain result found by the above spring failure analysis and the Monte Carlo parameter variation simulation.

4.5.4.3 DPI Controller with Feed Forward and Manual Tuning

The gains used for the simulations and experiments were found as described in subsection 4.5.3.3, where:

$\alpha_{spring} = 5$

$\beta_{spring} = 15$

$k_p = 52$

$k_i = 0.24$

$k_d = 95$

$k_{out} = 12/100$

A dither signal is added to the control signal to reduce the effects of the static friction as described in subsection 4.4.3. The integrator anti-windup strategy is enabled to minimise the saturation during the step reference input. The DPI controller with feed forward is tested experimentally with three different reference input functions as described in subsection 4.3.3. The dSPACE system is used for the experiments as explained in subsection 4.3.2.

The simulation results presented in this subsection are obtained with the full nonlinear plant model presented in section 2.5.

First, simulated and experimental responses to a step reference position change within the throttle valve stop limits are presented in Figure 4.63.

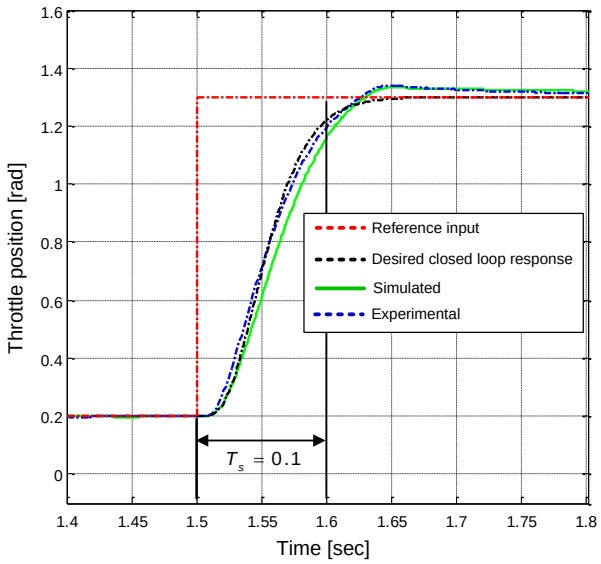

Figure 4.63: Closed loop step response, from 0.2 to 1.3 [rad]

The vertical black lines mark the nominal settling time of $T_s = 0.1$ [sec]. It is evident that both the experimental and simulated responses come close to this at ≈ 1.24 [rad].

Figure 4.64 shows the simulated and experimental closed loop response of the DPI controller with three different reference input functions which indicates a good correlation between the two.

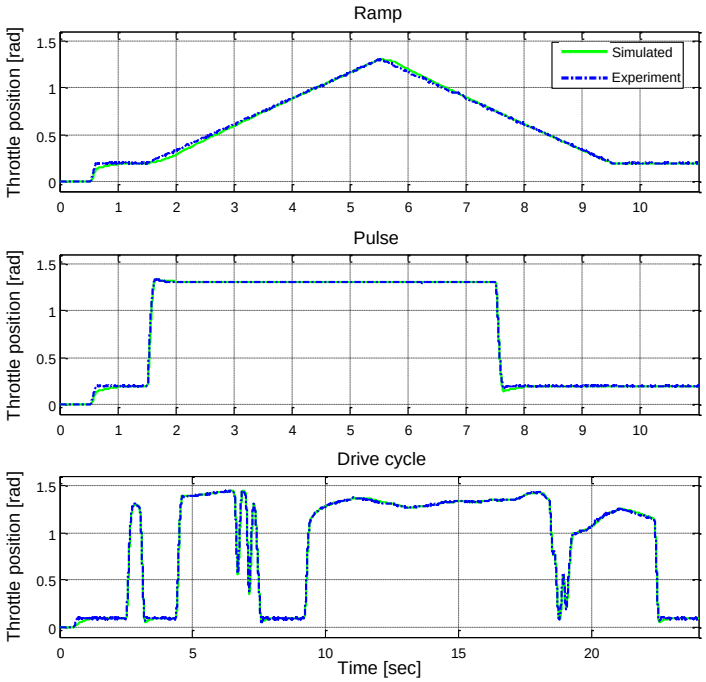

Figure 4.64: Experimental and simulated response of the DPI controller

The relatively small differences could be attributed to the accuracy of the plant model but they could also be due to the robustness of the control loop, which would give nearly the same responses despite mismatching between the plant and its model.

Figure 4.65 shows the difference between the desired and the experimental closed loop response, indicating good tracking and a small steady state error.

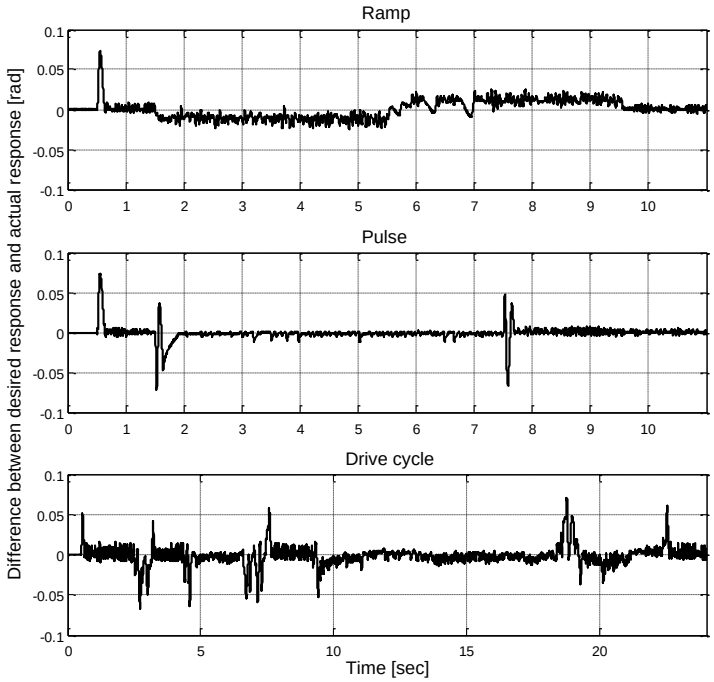

Figure 4.65: The difference between the desired and the experimental closed loop responses

As described in subsection 4.3.4.3 a spring failure can cause the engine to stall due to air starvation. The behaviour of the DPI controller with feed forward during a spring break, at $t = 1$ [sec], is simulated using the nonlinear throttle valve model, and the result is shown in Figure 4.66. The slow throttle position response would cause the throttle valve to remain closed for seconds, which would result in an engine stall. The oscillations on the control signal at $t \approx 1$ [sec] are the added dither signal that increases in amplitude when the control error, $y_r - y$, exceeds a preset threshold of 1% of the full scale movement range as described in subsection 4.4.3.

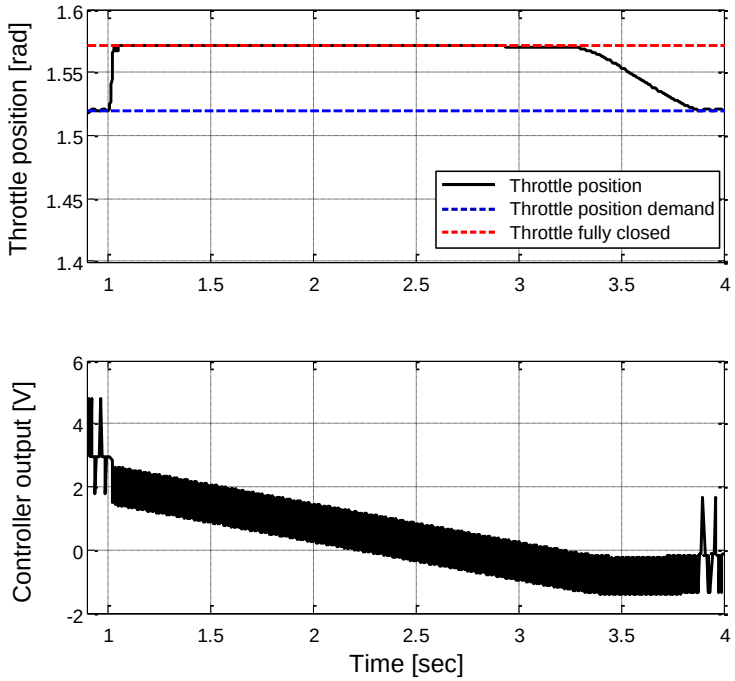

Figure 4.66: DPI controller with feed forward during a spring failure

The slow recovery is due to the tuning giving the integral gain a low value of, $k_i = 0.24$. During the tuning the feed forward spring compensation was active and therefore there was no need for a fast integration action.

The robustness against plant parameter deviations away from the nominal values is tested using the Monte Carlo method described in subsection 4.3.4.2. The parameter variation simulation uses the nonlinear throttle valve model with the controller output saturation, integrator anti-windup, dither and the precompensator. The result of the parameter variation simulation is shown in Figure 4.67 for the maximum possible standard deviation of $\sigma = 2\%$. The figure shows the operational envelope for 1000 simulation runs, where the blue and red lines are the minimum and maximum values. The nominal parameter closed loop controller response and controller output are shown in black.

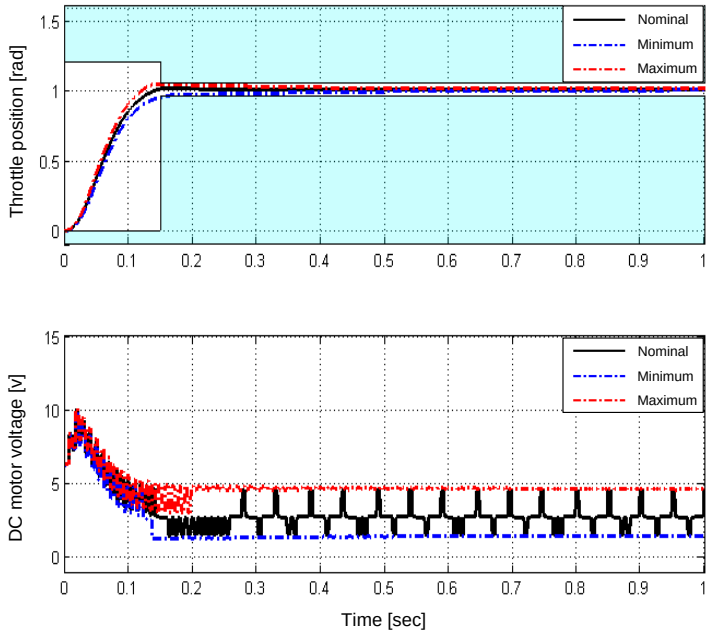

Figure 4.67: Maximum / minimum throttle position and DC motor voltage envelope (Standard deviation: $\sigma = 2\%$)

The result shows that the system is very sensitive to parameter variations. This result is difficult to compare directly with the model based control designs in this work due to the way the Monte Carlo test is performed.

The sensitivity for the DPI controller is analysed in the frequency domain by using the relationship of equation (4.3) in subsection 4.3.4.1. This is done with the aid of the Matlab Control System Analysis Toolbox and the block diagram of Figure 4.68 implemented in Simulink with $D(s)$ as the input and $V(s)$ as the output to obtain $S_p^C dB(\omega)$.

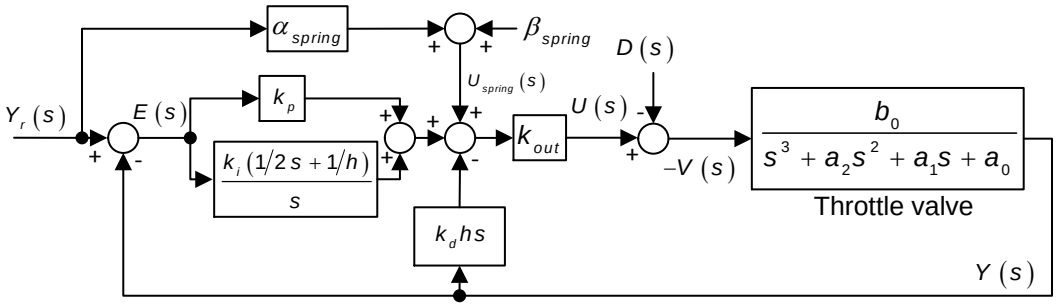

Figure 4.68: Control structure used to analyse the sensitivity

The transfer function is

$$\frac{V(s)}{D(s)} = S_p^C(s) = \frac{1}{1 - \left[-\frac{b_0 k_{out}}{s^3 + a_2 s^2 + a_1 s + a_0} \cdot \left(k_d h s + k_p + \alpha_{spring} + \frac{k_i(1/2\,s + 1/h)}{s} \right) \right]}$$

$$= \frac{s^4 + a_2 s^3 + a_1 s^2 + a_0 s}{s^4 + a_2 s^3 + (a_1 + b_0 k_{out} k_d h) s^2 + \left[a_0 + b_0 k_{out} (k_p + \alpha_{spring} + k_i/2) \right] s + b_0 k_{out} k_i / h} \tag{4.59}$$

The sensitivity result is shown in Figure 4.69.

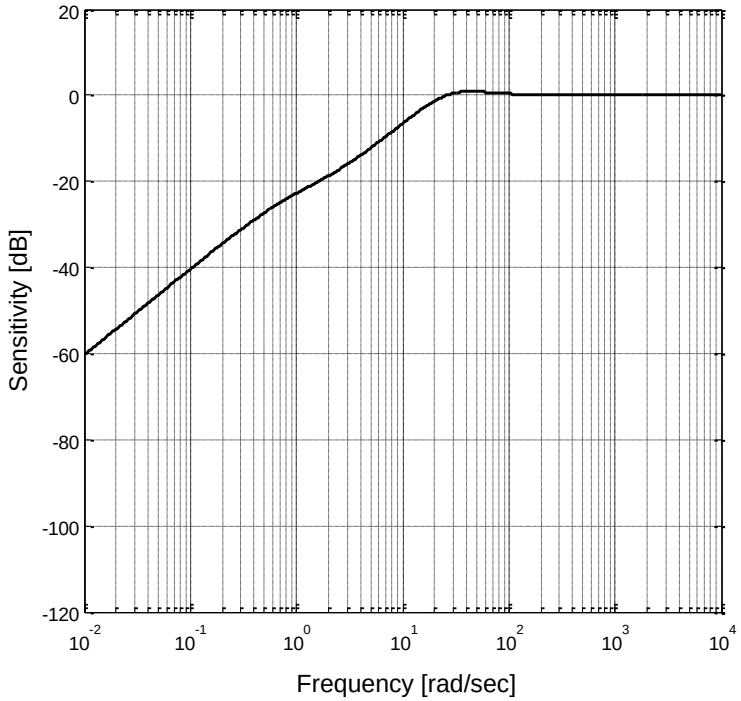

Figure 4.69: Manually tuned DPI sensitivity

This indicates a relatively high sensitivity, equivalent to low robustness. This corresponds well with the time domain result found by the above spring failure analysis and the Monte Carlo parameter variation simulation.

4.5.4.4 PID Controller

The closed loop characteristic polynomial for the PID controller is the same as that for the IPD controller and therefore the gains are determined as in subsection 4.5.3.1, equation (4.47) to (4.49) with $T_s = 0.1$ [sec] and $\omega_f = 500$ [rad/sec]. The precompensator is designed to cancel both zeros, as described in subsection 4.5.3.4. A dither signal is added to the control signal to reduce the effects of the static friction as described in subsection 4.4.3.

The simulation results presented in this subsection are obtained with the full nonlinear plant model presented in section 2.5.

Figure 4.70 shows three experimental step responses with 1) the basic PID controller (black line), 2) as (1) with integrator anti-windup introduced (green line) and 3) as (2) with a precompensator introduced (blue line). The PID controller without integrator anti-windup and precompensator has an overshoot as expected, which correlate well with the simulations in subsection 4.5.3.2 and 4.5.3.4.

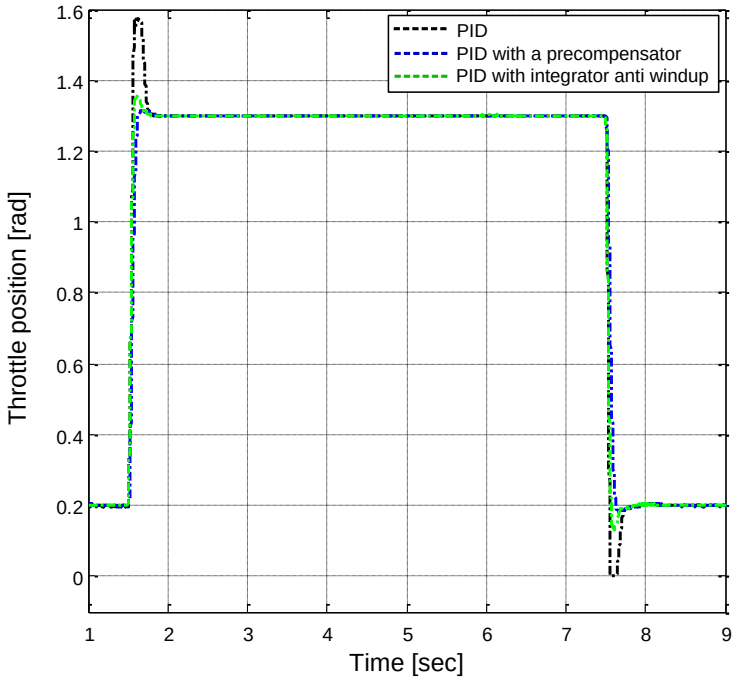

Figure 4.70: PID closed loop step response

First, simulated and experimental responses to a step reference position change within the throttle valve stop limits are presented in Figure 4.71.

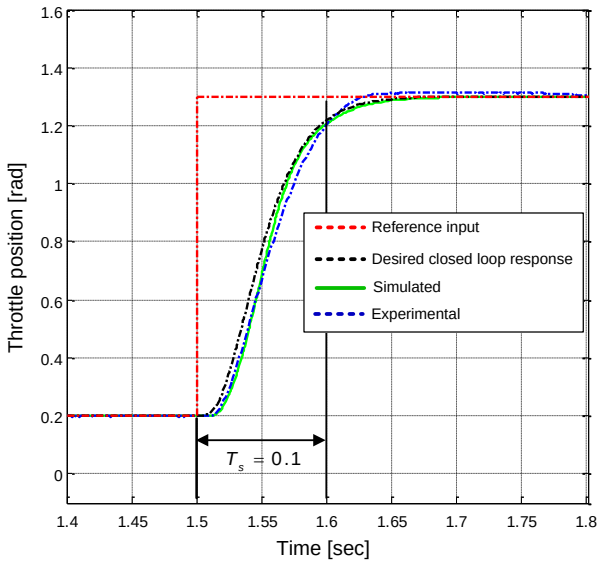

Figure 4.71: Closed loop step response, from 0.2 to 1.3 [rad], using a precompensator

The vertical black lines mark the nominal settling time of $T_s = 0.1\,[\text{sec}]$. It is evident that both the experimental and simulated responses come close to this at ≈ 1.24 [rad].

The PID controller is tested experimentally with three different reference input functions as described in subsection 4.3.3. Figure 4.72 shows the simulated and experimental closed loop responses which indicates a good correlation between the two. The integrator anti-windup strategy is enabled to minimise the duration of any saturation following a step reference input.

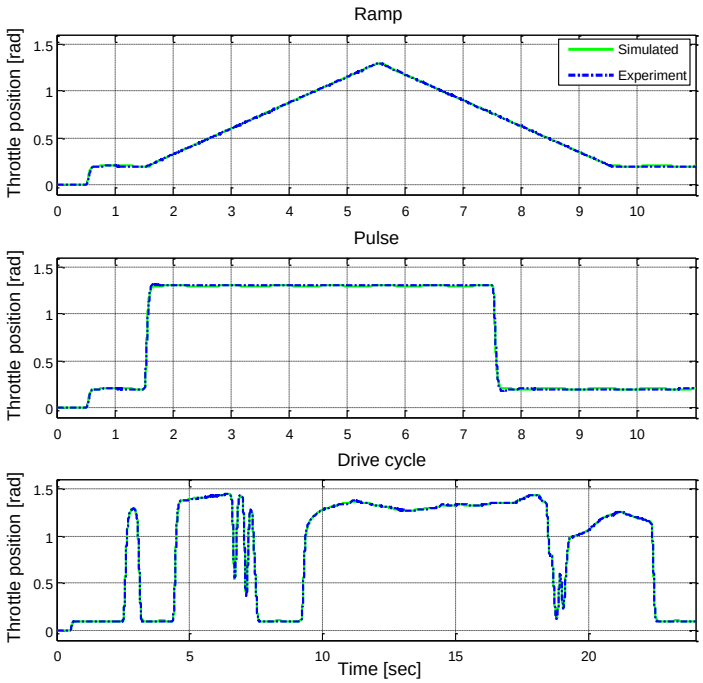

Figure 4.72: Experimental and simulated response of the PID controller

The relatively small differences could be attributed to the accuracy of the plant model but they could also be due to the robustness of the control loop, which would give nearly the same responses despite mismatching between the plant and its model.

Figure 4.73 shows the difference between the desired and the experimental closed loop responses, indicating good tracking and negligible steady state error.

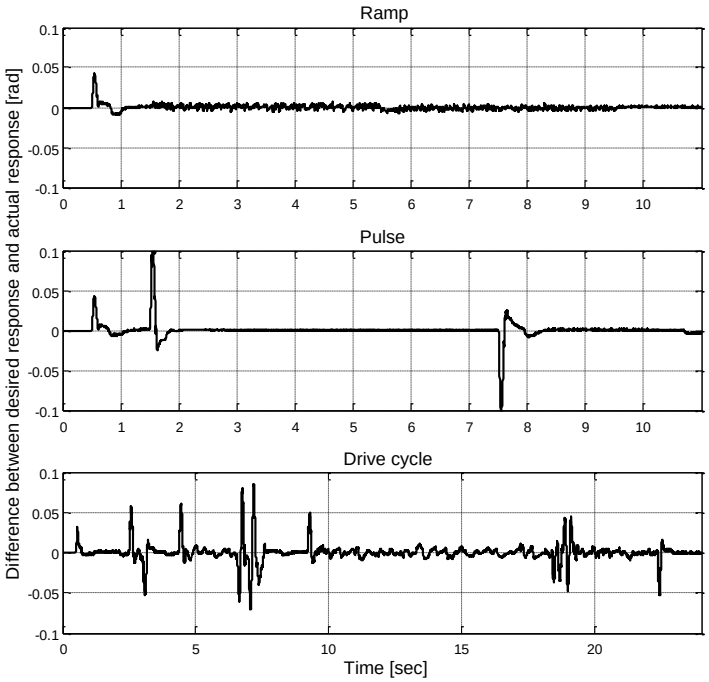

Figure 4.73: The difference between the desired and the experimental closed loop responses

As described in subsection 4.3.4.3 a spring failure can cause the engine to stall due to air starvation. The behaviour of the DPI controller during a spring break, at $t = 1$ [sec], is simulated using the nonlinear throttle valve model, and the result is shown in Figure 4.74. It shows a good robustness against the disturbance, with little deviation from the throttle position demand. The oscillations on the control signal at $t = 1.02$ [sec] are the added dither signal that increases in amplitude when the control error, $y_r - y$, exceeds a preset threshold of 1% of the full scale movement range as described in subsection 4.4.3.

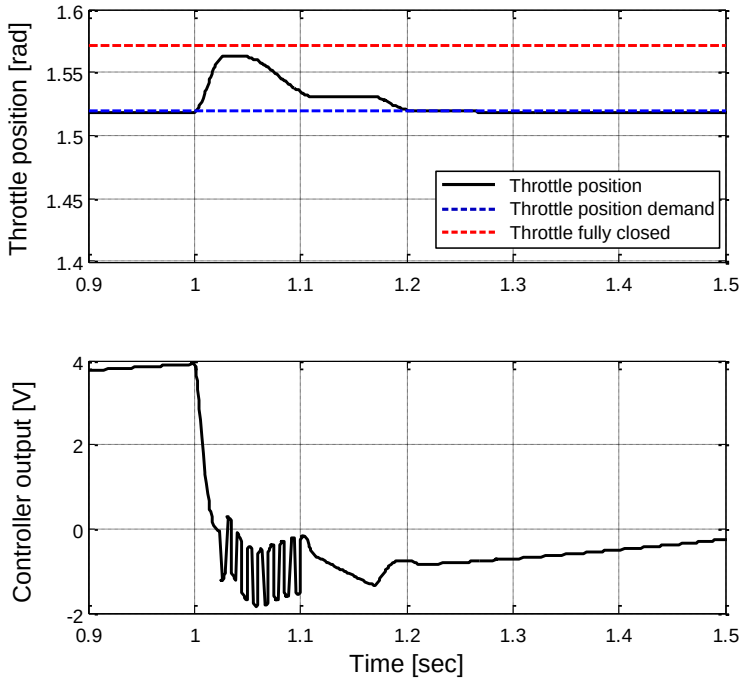

Figure 4.74: PID controller during a spring failure

The robustness against plant parameter deviations away from the nominal values is tested using the Monte Carlo method described in subsection 4.3.4.2. The parameter variation simulation uses the nonlinear throttle valve model with the controller output saturation, integrator anti-windup, dither and the precompensator. The result is shown in Figure 4.75 for the maximum possible standard deviation of $\sigma = 14\%$. The figure shows the operational envelope for 1000 simulation runs, where the blue and red lines are the minimum and maximum values. The nominal parameter closed loop controller response and controller output are shown in black.

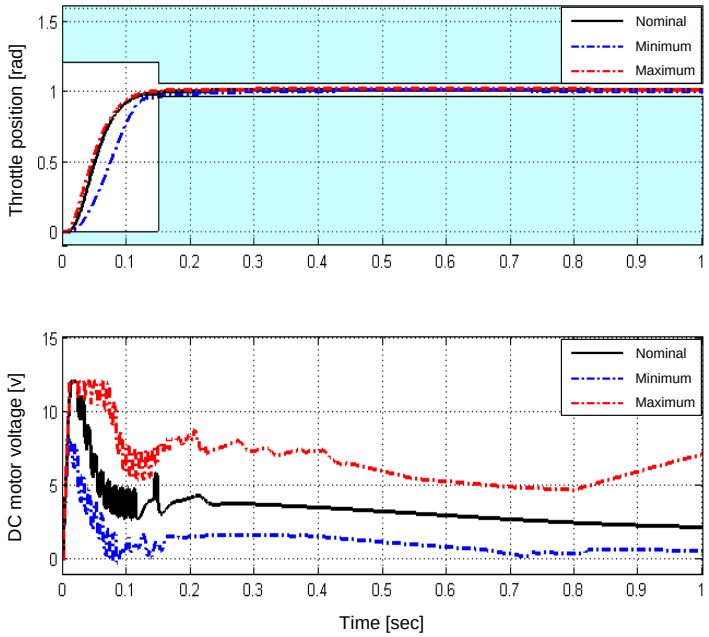

Figure 4.75: Maximum / minimum throttle position and DC motor voltage envelope (Standard deviation: $\sigma = 14\%$)

This indicates that the plant parameters can deviate significantly from the nominal values before having an adverse impact on the performance of the controller.

The sensitivity for the PID controller is analysed in the frequency domain by using the relationship of equation (4.3) in subsection 4.3.4.1. This is done with the aid of the Matlab Control System Analysis Toolbox and the block diagram of Figure 4.76 implemented in Simulink with $D(s)$ as the input and $V(s)$ as the output to obtain $S_p^C dB(\omega)$.

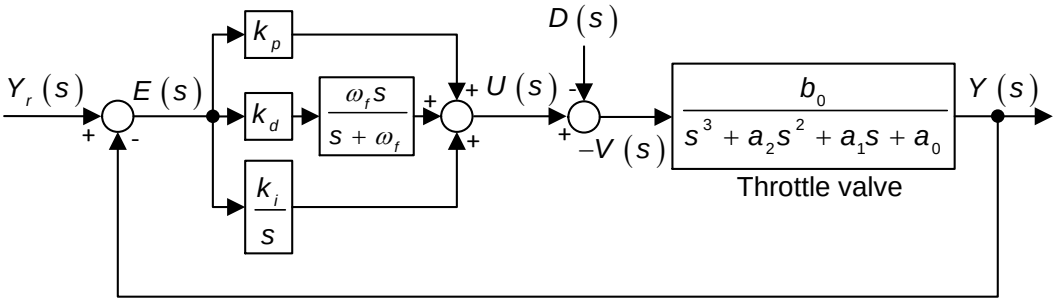

Figure 4.76: Control structure used to analyse the sensitivity

Ignoring the differential filtering term, as ω_f is well outside the control loop bandwidth, the sensitivity transfer function is

$$\frac{V(s)}{D(s)} = \frac{1}{1-\left[-\frac{b_0}{s^3+a_2s^2+a_1s+a_0}.\left(k_d s+k_p+\frac{k_i}{s}\right)\right]}$$

$$= \frac{s^4+a_2s^3+a_1s^2+a_0s}{s^4+a_2s^3+\left(a_1+b_0k_d\right)s^2+\left(a_0+b_0k_p\right)s+b_0k_i} \qquad (4.60)$$

The sensitivity result is shown in Figure 4.77.

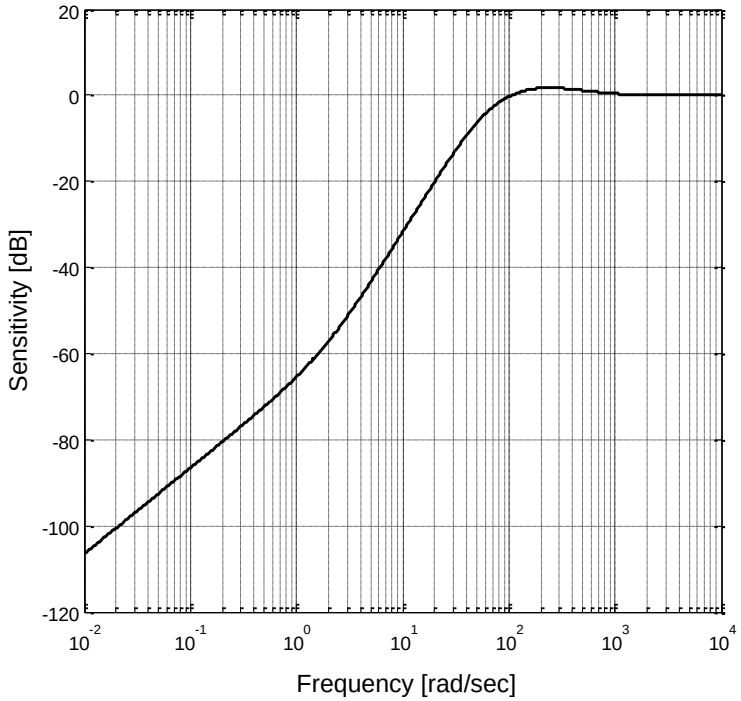

Figure 4.77: PID sensitivity

This indicates a relatively low sensitivity, equivalent to high robustness. This corresponds well with the time domain result found by the above spring failure analysis and the Monte Carlo parameter variation simulation.

4.6 Linear State Feedback Control

4.6.1 Basic Linear State Feedback Control

Let the general linear, SISO, time invariant (LTI) plant be represented by the state space equations,

$$\dot{\mathbf{x}} = \mathbf{A}\mathbf{x} + \mathbf{b}u,\ y = \mathbf{c}^{\mathrm{T}}\mathbf{x} \tag{4.61}$$

where $\mathbf{x} \in \Re^n$ is the state vector, u is the scalar control input, y is the scalar measured output and y_r is the corresponding reference input. Here, $\mathbf{A}$ is the plant matrix, $\mathbf{b}$ is the input matrix, and $\mathbf{c}^{\mathrm{T}}$ is the output matrix, linear state feedback (LSF) control is a feedback control technique in which the state vector, $\mathbf{x}$, is fed back to the control input according to the control law,

$$u = y_r r - \mathbf{g}^{\mathrm{T}}\mathbf{x} \tag{4.62}$$

Since the components of the gain vector, $\mathbf{g}$, are independently adjustable, it is possible, in theory, to place the full set of closed loop poles at predetermined locations in the s-plane (Franklin et al., 2002). The plant must be controllable in order to implement this method, or any other control system that can be designed by pole placement. Provided there is full access to all the states in the real plant, as shown in Figure 4.78, the control engineer is free to design the system to achieve a desired closed loop transient response.

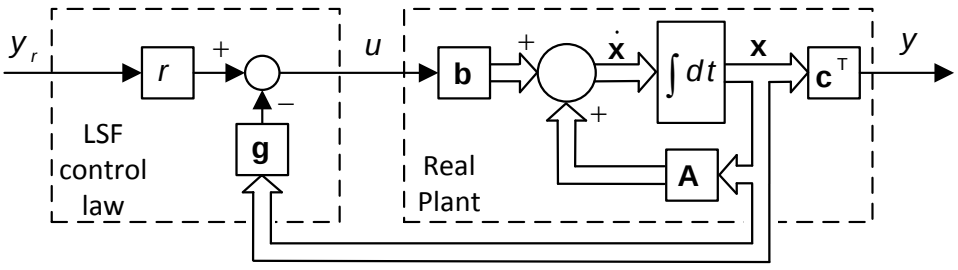

Figure 4.78: LSF control system

This can be done by determining the characteristic polynomial of the closed loop system using Figure 4.78 and equating this with the polynomial of the same order

found by using the settling time formula as in subsection 4.4.2. The gain r is adjusted usually to yield zero steady state error of the step response, but the accuracy of this depends upon the accuracy of the assumed plant state space equations.

4.6.2 State Observer

The LSF of subsection 4.6.1 requires that all the state variables are available from the plant. In some cases it is difficult to gain access to some states due to the cost of the required instrumentation or the fact that it might not be physically possible to measure all of them, as in some chemical processes. However, methods to reconstruct the missing states or all the state variables have been developed during the last 50 years. The first paper to investigate the general observer theory is in the paper 'On the General Theory of Control Systems' by R.E. Kalman (Kalman, 1960), but this had an accent on the stochastic aspect, i.e., minimising the random errors in the state estimate due to plant noise and measurement noise. A complete theory for the non–statistical state estimation problem was developed by David Luenberger (Luenberger, 1964) and followed by a more general paper (Luenberger, 1971).

Figure 4.79 shows the block diagram of the generic SISO linear state feedback control system employing a state observer producing the state estimate, $\hat{\mathbf{x}}$, needed for the control.

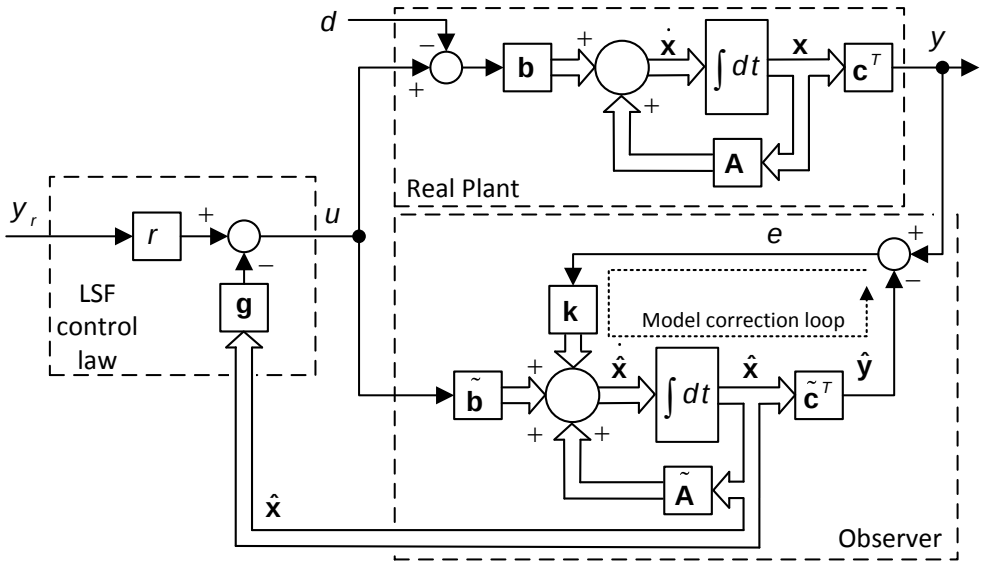

Figure 4.79: LSF control system with a state observer

In the notation of this subsection, the estimate of a constant parameter, P, is denoted by $\tilde{P}$. The state observer is based on a model of the 'real plant' driven by the same control input as applied to the real plant, whose state is controlled to follow that of the real plant by means of a correction loop actuated by the error, $e = y - \hat{y}$, and applied to the integrator inputs of the plant model via a gain vector, $\mathbf{k}$. By choosing a suitable set of correction loop gains, the error, $e(t)$, is made to converge towards zero such that $\hat{\mathbf{x}} \to \mathbf{x}$, once the correction loop has settled, as required.

The complete set of equations obeyed by the system in Figure 4.79 is as follows.

$$\dot{\mathbf{x}} = \mathbf{A}\mathbf{x} + \mathbf{b}u, \; y = \mathbf{c}^{\mathrm{T}}\mathbf{x} \tag{4.63}$$

$$\dot{\hat{\mathbf{x}}} = \tilde{\mathbf{A}}\hat{\mathbf{x}} + \tilde{\mathbf{b}}u + \mathbf{k}\left(y - \hat{y}\right), \; \hat{y} = \tilde{\mathbf{c}}^{\mathrm{T}}\hat{\mathbf{x}} \tag{4.64}$$

$$u = y_r r - \mathbf{g}\hat{\mathbf{x}} \tag{4.65}$$

where $\mathbf{k}$ is the observer correction loop gain vector and $\tilde{\mathbf{A}},\tilde{\mathbf{b}},\tilde{\mathbf{c}}^{\mathrm{T}}$ are the matrices of the plant model parameters corresponding to $\mathbf{A},\mathbf{b},\mathbf{c}^{\mathrm{T}}$ assumed for the real plant.

The need for the correction loop indicated in Figure 4.79 is best understood by considering the situation that would occur without it. Suppose that the model correction loop is opened by setting $\mathbf{k}=\left[k_1 k_2 \ldots k_n\right]=0$. Then an error, $e=y-\hat{y}$, will occur if

1) the model parameters are mismatched, i.e., $\left\{\tilde{\mathbf{A}},\tilde{\mathbf{b}},\tilde{\mathbf{c}}\right\}\neq\left\{\mathbf{A},\mathbf{b},\mathbf{c}\right\}$
2) the initial model and plant states are different, i.e., $\mathbf{x}(0)\neq\hat{\mathbf{x}}(0)$
3) a disturbance signal is present, i.e., $d\neq 0$.

Without the correction loop, this error may grow, but closure of the correction loop will drive the error to negligible proportions, in the presence of conditions (1), (2) and (3), ensuring $\hat{\mathbf{x}}\cong\mathbf{x}$ if the observer is designed correctly. This can be achieved by determining the correction loop gain vector, $\mathbf{k}$, using pole placement but only if the plant is observable (Dodds, 2013).

It is straightforward to show that the state estimation error, $\boldsymbol{\varepsilon}=\hat{\mathbf{x}}-\mathbf{x}$, may be made to converge towards zero from an arbitrary initial conditions on the assumption that $\tilde{\mathbf{A}}=\mathbf{A}$ and $\tilde{\mathbf{b}}=\mathbf{b}$. Then subtracting equation (4.63) from equation (4.64) yields

$\dot{\hat{\mathbf{x}}}-\dot{\mathbf{x}}=\mathbf{A}\left(\hat{\mathbf{x}}-\mathbf{x}\right)+\mathbf{k}\left(y-\hat{y}\right)=\mathbf{A}\left(\hat{\mathbf{x}}-\mathbf{x}\right)+\mathbf{k}\mathbf{c}^{\mathrm{T}}\left(\mathbf{x}-\hat{\mathbf{x}}\right)=\mathbf{A}\left(\hat{\mathbf{x}}-\mathbf{x}\right)-\mathbf{k}\mathbf{c}^{\mathrm{T}}\left(\hat{\mathbf{x}}-\mathbf{x}\right)$, i.e,

$$\dot{\boldsymbol{\varepsilon}}=\left[\mathbf{A}-\mathbf{k}\mathbf{c}^{\mathrm{T}}\right]\boldsymbol{\varepsilon} \tag{4.66}$$

If the gain matrix, $\mathbf{k}$, is chosen so that the eigenvalues of the matrix, $\mathbf{A}-\mathbf{k}\mathbf{c}^{\mathrm{T}}$, have negative real parts, then $\boldsymbol{\varepsilon}\to 0$ as $t\to\infty$.

The gain vector, $\mathbf{k}$, can be chosen independently from the control law gain vector, $\mathbf{g}^T$, as the separation principle applies (Franklin et al., 2002) if $\{\mathbf{A},\mathbf{b},\mathbf{c}\} = \{\tilde{\mathbf{A}},\tilde{\mathbf{b}},\tilde{\mathbf{c}}\}$ and in practice this may be assumed.

The dynamic behaviour of the correction loop depends on its characteristic equation, which can be found using Mason's formula on Figure 4.79 to obtain

$$\det\left(s\mathbf{I} - \left[\tilde{\mathbf{A}} - \tilde{\mathbf{C}}\mathbf{k}\right]\right) = 0 \tag{4.67}$$

The pole placement can then be carried out using the settling time formula as follows

$$\det\left(s\mathbf{I} - \left[\tilde{\mathbf{A}} - \tilde{\mathbf{C}}\mathbf{k}\right]\right) = \left[s + 1.5(1+n)/T_{so}\right]^n \tag{4.68}$$

where T_{so} is the observer settling time and n is system order. To achieve the desired closed loop step response with an arbitrary initial state estimation error, the settling time for the observer, T_{so}, has to be chosen considerably shorter than the settling time, T_s, for the control law. It is usual to choose T_{so}, to satisfy $T_{so} < T_s/5$. In (Franklin et al., 2002), this condition is stated in terms of the observer correction loop poles and the main control loop poles. In some cases the ratio, T_s/T_{so}, is increased considerably, beyond the minimum value of 5, such as $T_s/T_{so} > 500$ to obtain a satisfactory closed loop system response in the presence of significant plant modelling errors. Reducing T_{so}, however, increases the noise content of the state estimate due to measurement noise, i.e., noise that originates in the measurement instrumentation, through an associated general increase in the elements of $\mathbf{k}$.

An example of a third order observer structure for a plant without finite zeros is shown in Figure 4.80, the structure of the plant model is the same as that of the assumed plant.

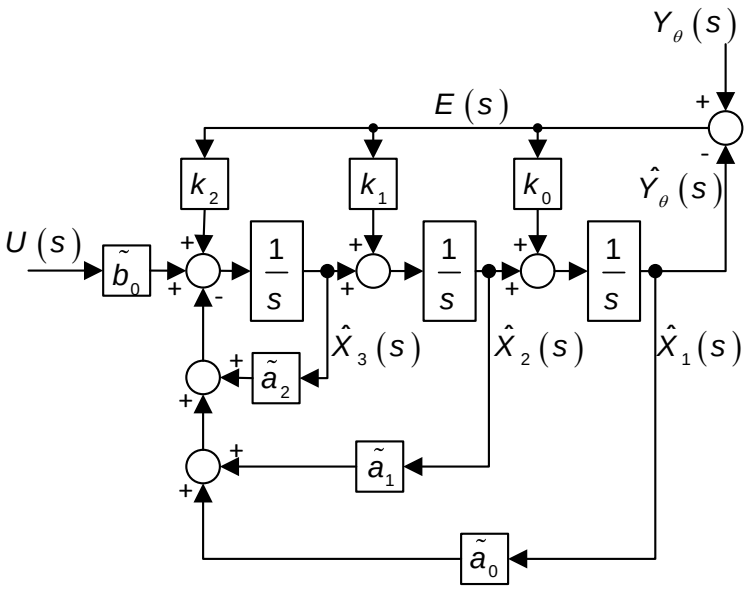

Figure 4.80: A basic third order observer structure

The characteristic equation of the observer is

$$1+\left(\tilde{a}_2\frac{1}{s}+\tilde{a}_1\frac{1}{s^2}+\tilde{a}_0\frac{1}{s^3}+k_0\frac{1}{s}+k_1\frac{1}{s^2}+k_2\frac{1}{s^3}\right)+$$
$$\left(k_0\frac{1}{s}\cdot\tilde{a}_2\frac{1}{s}\right)+\left(k_0\frac{1}{s}\cdot\tilde{a}_1\frac{1}{s^2}\right)+\left(k_1\frac{1}{s^2}\cdot\tilde{a}_2\frac{1}{s}\right)=0 \quad \Rightarrow \quad (4.69)$$
$$s^3+s^2\left(\tilde{a}_2+k_0\right)+s\left(\tilde{a}_1+k_1+k_0\right)+\tilde{a}_0+\tilde{a}_1k_0+\tilde{a}_2k_1+k_2=0$$

Using the Dodds settling time formula to obtain a non-overshooting closed loop response for a third order system, $n=3$, with the observer settling time T_{so} yields the desired closed loop characteristic polynomial,

$$\left(s+\frac{6}{T_{so}}\right)^3=s^3+\frac{18}{T_{so}}s^2+\frac{108}{T_{so}{}^2}s+\frac{216}{T_{so}{}^3} \quad (4.70)$$

Equating the characteristic polynomials (4.69) and (4.70), and isolating the three control parameters yields,

k_0:

$$\tilde{a}_2+k_0=\frac{18}{T_{so}}\Rightarrow k_0=\frac{18}{T_{so}}-\tilde{a}_2 \quad (4.71)$$

k_1:

$$\tilde{a}_1 + k_1 + k_0 = \frac{108}{T_{so}^{\ 2}} \Rightarrow k_1 = \frac{108}{T_{so}^{\ 2}} - \tilde{a}_1 - k_0 \tag{4.72}$$

k_2:

$$\tilde{a}_0 + \tilde{a}_1 k_0 + \tilde{a}_2 k_1 + k_2 = \frac{216}{T_{so}^{\ 3}} \Rightarrow k_2 = \frac{216}{T_{so}^{\ 3}} - \tilde{a}_0 - \tilde{a}_1 k_0 - \tilde{a}_2 k_1 \tag{4.73}$$

4.6.3 Controller Design

4.6.3.1 Linear State Feedback with Integrator for Steady State Error Elimination

The LSF controller shown in Figure 4.78 will have a steady state error for a constant reference input if there is 1) a parameter difference between the plant model and the plant or 2) an external disturbance. This can be circumvented by adding an integrator in the forward path, shown in the general SISO control system of Figure 4.81. Also the adjustable gain, k_i, permits design by pole assignment.

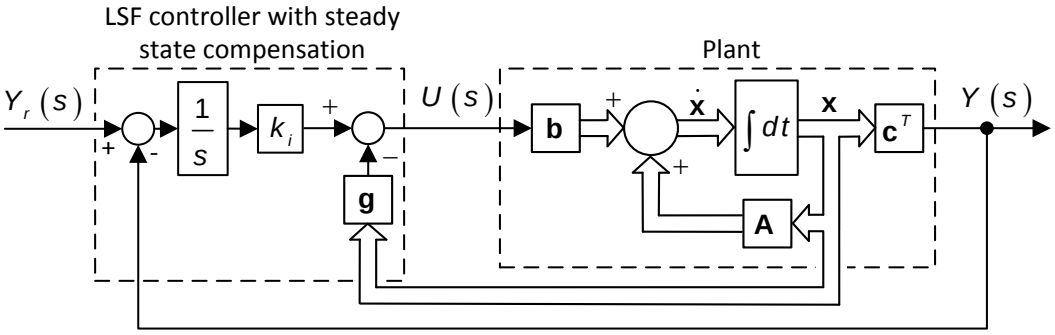

Figure 4.81: LSF plus integral control

Figure 4.82 shows an LSF control system with a linear model of the throttle valve, for the determination of the controller gains.

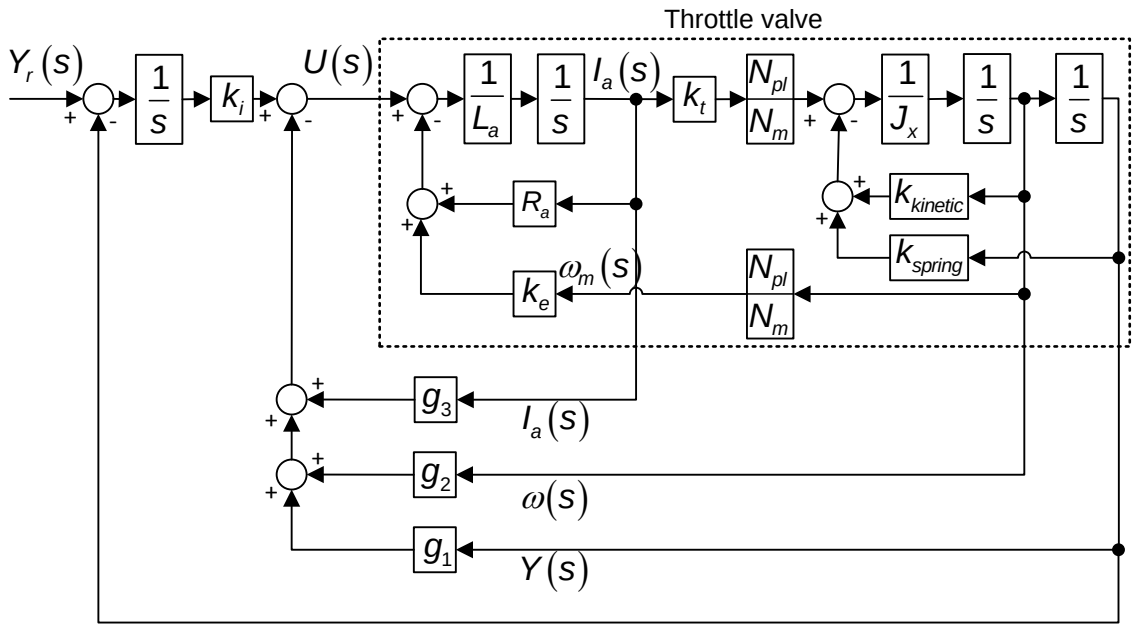

Figure 4.82: LSF control of the throttle valve with steady state compensation

Using Mason's rule on Figure 4.82 to get the closed loop transfer function (detailed calculation in Appendix A.3)

$$\frac{Y(s)}{Y_r(s)} = \frac{b_0}{s^4 + a_3 s^3 + a_2 s^2 + a_1 s + a_0} \tag{4.74}$$

where:

$$b_0 = \frac{k_t}{L_a}\frac{N_{pl}}{N_m}\frac{k_i}{J_x}$$

$$a_0 = \frac{k_t}{L_a}\frac{N_{pl}}{N_m}\frac{k_i}{J_x}$$

$$a_1 = \frac{R_a}{L_a}\frac{k_{spring}}{J_x} + \frac{k_t}{L_a}\frac{N_{pl}}{N_m}\frac{g_1}{J_x} + \frac{g_3}{L_a}\frac{k_{spring}}{J_x}$$

$$a_2 = \frac{k_{spring}}{J_x} + \frac{k_t}{L_a}\frac{k_e}{J_x}\left(\frac{N_{pl}}{N_m}\right)^2 + \frac{R_a}{L_a}\frac{k_{kinetic}}{J_x} + \frac{k_t}{L_a}\frac{N_{pl}}{N_m}\frac{g_2}{J_x} + \frac{g_3}{L_a}\frac{k_{kinetic}}{J_x}$$

$$a_3 = \frac{R_a}{L_a} + \frac{k_{kinetic}}{J_x} + \frac{g_3}{L_a}$$

Using the desired transfer function (4.12) based on the settling time formula to obtain a non-overshooting closed loop step response for a fourth order system, $n = 4$, the characteristic polynomial is

$$\left(s + \frac{15}{2T_s}\right)^4 = s^4 + \frac{30}{T_s}s^3 + \frac{1350}{4T_s^{\,2}}s^2 + \frac{13500}{8T_s^3}s + \frac{50625}{16T_s^4} \tag{4.75}$$

Equating the characteristic polynomial (4.75) and the denominator from equation (4.74) gives

g_3:

$$\frac{30}{T_s} = \frac{R_a}{L_a} + \frac{k_{kinetic}}{J_x} + \frac{g_3}{L_a} \Rightarrow g_3 = \left(\frac{30}{T_s} - \frac{R_a}{L_a} - \frac{k_{kinetic}}{J_x}\right)L_a \tag{4.76}$$

g_2:

$$\begin{aligned} &\frac{1350}{4T_s^{\,2}} = \frac{k_{spring}}{J_x} + \frac{k_t}{L_a}\frac{k_e}{J_x}\left(\frac{N_{pl}}{N_m}\right)^2 + \frac{R_a}{L_a}\frac{k_{kinetic}}{J_x} + \frac{k_t}{L_a}\frac{N_{pl}}{N_m}\frac{g_2}{J_x} + \frac{g_3}{L_a}\frac{k_{kinetic}}{J_x} \Rightarrow \\ &g_2 = \left(\frac{1350}{4T_s^{\,2}} - \frac{k_{spring}}{J_x} - \frac{k_t}{L_a}\frac{k_e}{J_x}\left(\frac{N_{pl}}{N_m}\right)^2 - \frac{R_a}{L_a}\frac{k_{kinetic}}{J_x} - g_3\frac{1}{L_a}\frac{k_{kinetic}}{J_x}\right)\frac{L_a}{k_t}\frac{N_m}{N_{pl}}J_x \end{aligned} \tag{4.77}$$

g_1:

$$\begin{aligned} &\frac{13500}{8T_s^3} = \frac{R_a}{L_a}\frac{k_{spring}}{J_x} + \frac{k_t}{L_a}\frac{N_{pl}}{N_m}\frac{g_1}{J_x} + \frac{g_3}{L_a}\frac{k_{spring}}{J_x} \Rightarrow \\ &g_1 = \left(\frac{13500}{8T_s^3} - \frac{R_a}{L_a}\frac{k_{spring}}{J_x} - \frac{g_3}{L_a}\frac{k_{spring}}{J_x}\right)\frac{L_a}{k_t}\frac{N_m}{N_{pl}}J_x \end{aligned} \tag{4.78}$$

k_i:

$$\frac{50625}{16T_s^4} = \frac{k_t}{L_a}\frac{N_{pl}}{N_m}\frac{k_i}{J_x} \Rightarrow k_i = \frac{50625}{16T_s^4}\frac{J_x}{k_t}\frac{N_m}{N_{pl}}L_a \tag{4.79}$$

Figure 4.83 shows the closed loop poles location for the LSF controller and linear throttle valve with a settling time of $T_s = 0.1$ [sec].

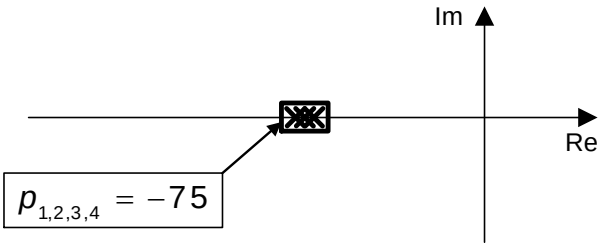

Figure 4.83: The closed loop pole location of the LSF control loop

4.6.3.2 LSF Controller with Integrator for Steady State Error Elimination and Robust Pole Placement

To design a robust set of closed loop poles, one pole can be placed at a location away from the dominant pole group, investigated in subsection 4.4.2.2. The minimum pole-to-pole dominance ratio, $r_{pp\min}$, is used to insure that the single fast pole is located a minimum distance away from the dominant poles. This is also needed to obtain the robustness. For a fourth order system, $n = 4$, with three dominant poles, $s_{1,2,3}$, all at the same location, and one fast pole q, the desired characteristic polynomial is

$$(s+p)^3 (s+q) \tag{4.80}$$

$$\begin{gathered}(s^3 + 3ps^2 + 3p^2 s + p^3)(s+q) = \\ s^4 + s^3(3p+q) + s^2(3p^2 + 3pq) + s(p^3 + 3p^2 q) + p^3 q\end{gathered} \tag{4.81}$$

Using the multiple pole location, $p = -s_{1,2,3}$ given by equation (4.11) based on the settling time formula (4.10), for $n = 3$, equation (4.81) becomes

$$s^4 + s^3\left(\frac{18}{T_s} + q\right) + s^2\left(\frac{18}{T_s}q + \frac{108}{T_s{}^2}\right) + s\left(\frac{108}{T_s{}^2}q + \frac{216}{T_s{}^3}\right) + \frac{216}{T_s{}^3}q \tag{4.82}$$

where $q = (6/T_s)\cdot r_{pp}$.

Equating the denominator from equation (4.74) and the characteristic polynomial (4.82), and solving the resulting equations for the four control parameters yields,

g_3:

$$\frac{18}{T_s}+q=\frac{R_a}{L_a}+\frac{k_{kinetic}}{J_x}+\frac{g_3}{L_a}\Rightarrow g_3=\left(\frac{18}{T_s}+q-\frac{R_a}{L_a}-\frac{k_{kinetic}}{J_x}\right)L_a \tag{4.83}$$

g_2:

$$\begin{aligned}&\frac{18}{T_s}q+\frac{108}{T_s^{\,2}}=\frac{k_{spring}}{J_x}+\frac{k_t}{L_a}\frac{k_e}{J_x}\left(\frac{N_{pl}}{N_m}\right)^2+\frac{R_a}{L_a}\frac{k_{kinetic}}{J_x}+\frac{k_t}{L_a}\frac{N_{pl}}{N_m}\frac{g_2}{J_x}+\frac{g_3}{L_a}\frac{k_{kinetic}}{J_x}\Rightarrow\\&g_2=\left(\frac{18}{T_s}q+\frac{108}{T_s^{\,2}}-\frac{k_{spring}}{J_x}-\frac{k_t}{L_a}\frac{k_e}{J_x}\left(\frac{N_{pl}}{N_m}\right)^2-\frac{R_a}{L_a}\frac{k_{kinetic}}{J_x}-g_3\frac{1}{L_a}\frac{k_{kinetic}}{J_x}\right)\frac{L_a}{k_t}\frac{N_m}{N_{pl}}J_x\end{aligned} \tag{4.84}$$

g_1:

$$\begin{aligned}&\frac{108}{T_s^{\,2}}q+\frac{216}{T_s^{\,3}}=\frac{R_a}{L_a}\frac{k_{spring}}{J_x}+\frac{k_t}{L_a}\frac{N_{pl}}{N_m}\frac{g_1}{J_x}+\frac{g_3}{L_a}\frac{k_{spring}}{J_x}\Rightarrow\\&g_1=\left(\frac{108}{T_s^{\,2}}q+\frac{216}{T_s^{\,3}}-\frac{R_a}{L_a}\frac{k_{spring}}{J_x}-\frac{g_3}{L_a}\frac{k_{spring}}{J_x}\right)\frac{L_a}{k_t}\frac{N_m}{N_{pl}}J_x\end{aligned} \tag{4.85}$$

k_i:

$$\frac{216}{T_s^{\,3}}q=\frac{k_t}{L_a}\frac{N_{pl}}{N_m}\frac{k_i}{J_x}\Rightarrow k_i=\frac{216}{T_s^{\,3}}q\frac{J_x}{k_t}\frac{N_m}{N_{pl}}L_a \tag{4.86}$$

Using equation (4.16) and inequality (4.17)

$$T_f<\frac{T_s}{(1.5\cdot n)r_{pp\min}} \tag{4.87}$$

For a system of $n=3$ and with 3 dominant poles $r_{pp\min}=5.4$ (Dodds, 2013). Using this for $T_s=0.1$ [sec]

$$T_f<\frac{T_s}{(1.5\cdot n)r_{pp\min}}\Rightarrow T_f<0.0041 \tag{4.88}$$

Figure 4.84 shows the closed loop pole locations for the LSF controller with a robust pole-to-pole ratio of 20 and a settling time of $T_s=0.1$ [sec].

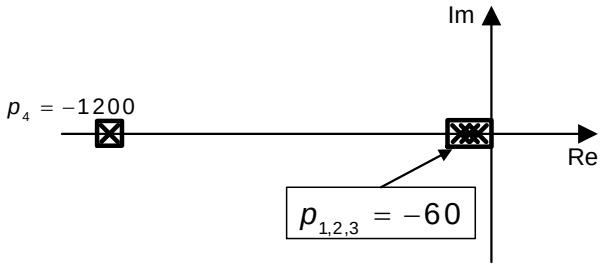

Figure 4.84: Pole locations of an LSF plus integral control loop with a robust pole-to-pole ratio of 20

There are three poles located at $s_{1,2,3} = -60$ and the fast one at $s_f = -1200$, indicating that the fast pole is further away than the recommended threshold of $s_f = -1/(2h) = -500$, according to inequality (4.17). Despite this, as will be seen in subsection 4.6.4.2, the system performs correctly. This emphasises the fact that inequality (4.17) is not a rigorous stability criterion but just a general guideline.

4.6.3.3 Observer Aided LSF Control with Integrator for Steady State Error Elimination and Robust Pole Placement

As Figure 4.81 shows, the LSF controller needs to have access to all the plant states. In the case of the throttle valve, the throttle position and DC motor current can be measured, and the velocity can be calculated by differentiating the throttle position. However if the DC motor current measurement could be eliminated from the control strategy it could save on the cost of the electronic controller unit (ECU), in which the control strategies are implemented.

Figure 4.85 shows the LSF controller from subsection 4.6.3.1 combined with the observer of Figure 4.80.

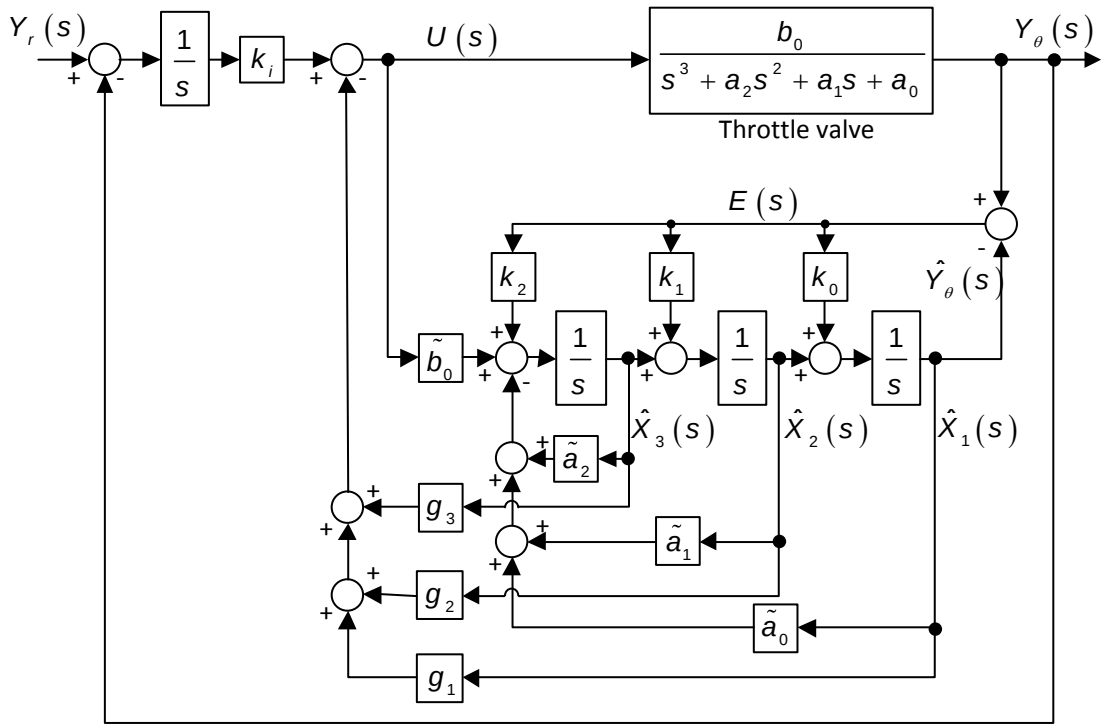

Figure 4.85: Observer aided LSF control with integrator for steady state error elimination

The real plant position output, $Y_\theta(s)$, is used directly for the integral outer loop. The other option, however, is to use the estimated position, $\hat{Y}_\theta(s)$, from the observer for this loop. This would reduce the impact of measurement noise but there could be a difference between the two transient responses. Simulations and experiments using both signals have been done, however, without finding a notable difference in the results. This is due to a) the noise from the throttle measurement potentiometer being relatively small and b) the initial observer and plant states being well matched.

The design of the LSF plus integral controller and the observer are carried out separately, assuming that the separation principle applies (Franklin et al., 2002). Figure 4.86 shows the LSF plus integral controller, used for the determination of the LSF gains.

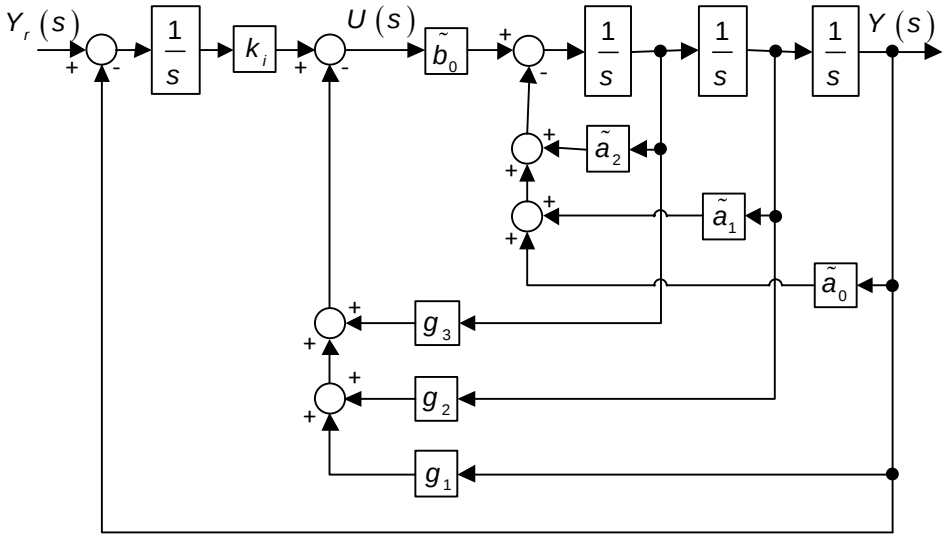

Figure 4.86: Simplified control system block diagram for design of the LSF controller

Here

$$\tilde{a}_0 = \tilde{R}_a \tilde{k}_{spring} / \left(\tilde{L}_a \tilde{J}_x \right)$$

$$\tilde{a}_1 = \tilde{k}_{spring} / \tilde{J}_x + \tilde{k}_e \tilde{k}_t / \left(\tilde{L}_a \tilde{J}_x \right) \left(\tilde{N}_{pl} / \tilde{N}_m \right)^2 + \tilde{R}_a \tilde{k}_{kinetic} / \left(\tilde{L}_a \tilde{J}_x \right)$$

$$\tilde{a}_2 = \tilde{R}_a / \tilde{L}_a + \tilde{k}_{kinetic} \tilde{J}_x$$

$$\tilde{b}_0 = \tilde{k}_t \tilde{N}_{pl} / \left(\tilde{L}_a \tilde{N}_m \tilde{J}_x \right)$$

Using Mason's rule to get the closed loop transfer function of Figure 4.86 yields

$$\frac{Y(s)}{Y_r(s)} = \frac{k_i \tilde{b}_0}{s^4 + \left(\tilde{a}_2 + \tilde{b}_0 g_3 \right) s^3 + \left(\tilde{a}_1 + \tilde{b}_0 g_2 \right) s^2 + \left(\tilde{a}_0 + \tilde{b}_0 g_1 \right) s + k_i \tilde{b}_0} \tag{4.89}$$

A set of robust closed loop poles will be determined as in subsection 4.6.3.2 by using the settling time formula for the dominant poles. Equating the characteristic polynomial (4.82) and the denominator from equation (4.89), and solving the resulting equations for the four control parameters yields,

g_3:

$$\frac{18}{T_s} + q = \tilde{a}_2 + \tilde{b}_0 g_3 \Rightarrow g_3 = \left(\frac{18}{T_s} + q - \tilde{a}_2 \right) / \tilde{b}_0 \tag{4.90}$$

g_2:

$$\frac{18}{T_s} q + \frac{108}{T_s^2} = \tilde{a}_1 + \tilde{b}_0 g_2 \Rightarrow g_2 = \left(\frac{18}{T_s} q + \frac{108}{T_s^2} - \tilde{a}_1 \right) / \tilde{b}_0 \tag{4.91}$$

g_1:

$$\frac{108}{T_s^2} q + \frac{216}{T_s^3} = \tilde{a}_0 + \tilde{b}_0 g_1 \Rightarrow g_1 = \left(\frac{108}{T_s^2} q + \frac{216}{T_s^3} - \tilde{a}_0 \right) / \tilde{b}_0 \tag{4.92}$$

k_i:

$$\frac{216}{T_s^3} q = k_i \tilde{b}_0 \Rightarrow k_i = \left(\frac{216}{T_s^3} q \right) / \tilde{b}_0 \tag{4.93}$$

where $q = (6 / T_s) \cdot r_{pp}$. The minimum ratio for r_{pp} is the same as for the controller designed in subsection 4.6.3.1.

The observer gains are determined by using the settling time formula as in subsection 4.6.2 and the working is repeated here for convenience (Figure 4.87).

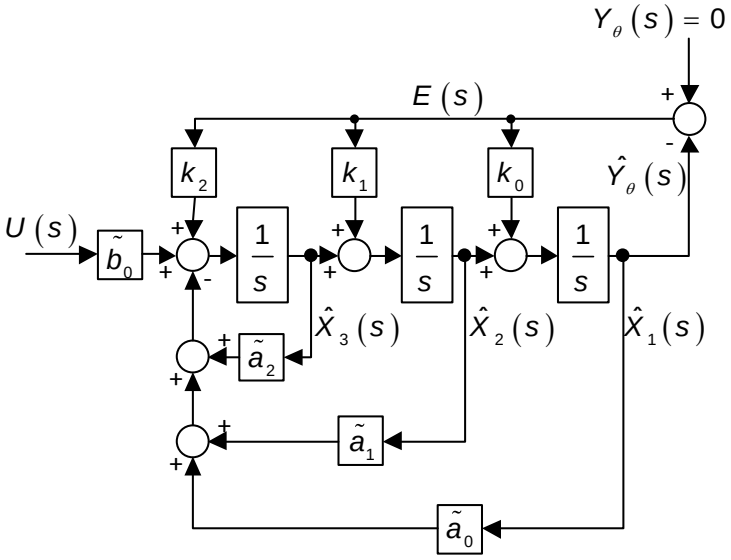

Figure 4.87: Third order observer structure

The observer characteristic equation (4.69) is

$$s^3 + s^2\left(\tilde{a}_2 + k_0\right) + s\left(\tilde{a}_1 + k_1 + k_0\right) + \tilde{a}_0 + \tilde{a}_1 k_0 + \tilde{a}_2 k_1 + k_2 = 0 \tag{4.94}$$

Using the Dodds settling time formula to obtain a non-overshooting closed loop response for a third order system, $n = 3$, with the observer settling time T_{so} yields the desired closed loop characteristic polynomial,

$$\left(s + \frac{6}{T_{so}}\right)^3 = s^3 + \frac{18}{T_{so}} s^2 + \frac{108}{T_{so}^{\ 2}} s + \frac{216}{T_{so}^{\ 3}} \tag{4.95}$$

Equating the characteristic polynomials (4.94) and (4.95), and solving the resulting three equations for the observer gains yields,

k_0:

$$\tilde{a}_2 + k_0 = \frac{18}{T_{so}} \Rightarrow k_0 = \frac{18}{T_{so}} - \tilde{a}_2 \tag{4.96}$$

k_1:

$$\tilde{a}_1 + k_1 + k_0 = \frac{108}{T_{so}^{\ 2}} \Rightarrow k_1 = \frac{108}{T_{so}^{\ 2}} - \tilde{a}_1 - k_0 \tag{4.97}$$

k_2:

$$\tilde{a}_0 + \tilde{a}_1 k_0 + \tilde{a}_2 k_1 + k_2 = \frac{216}{T_{so}^{\ 3}} \Rightarrow k_2 = \frac{216}{T_{so}^{\ 3}} - \tilde{a}_0 - \tilde{a}_1 k_0 - \tilde{a}_2 k_1 \tag{4.98}$$

The observer settling time, T_{so}, is chosen 20 times faster than the settling time, T_s, which is used for the design of the controller gains.

Integrator anti-windup

If the controller settling time, T_s, is chosen much lower than 0.1 [sec] the control output will saturate for a significant period of time following a large step reference input change, causing the controller to overshoot, due to the integrator wind-up. To circumvent this problem the integrator anti-windup strategy from subsection 4.4.4 is added. The final block diagram is shown in Figure 4.88.

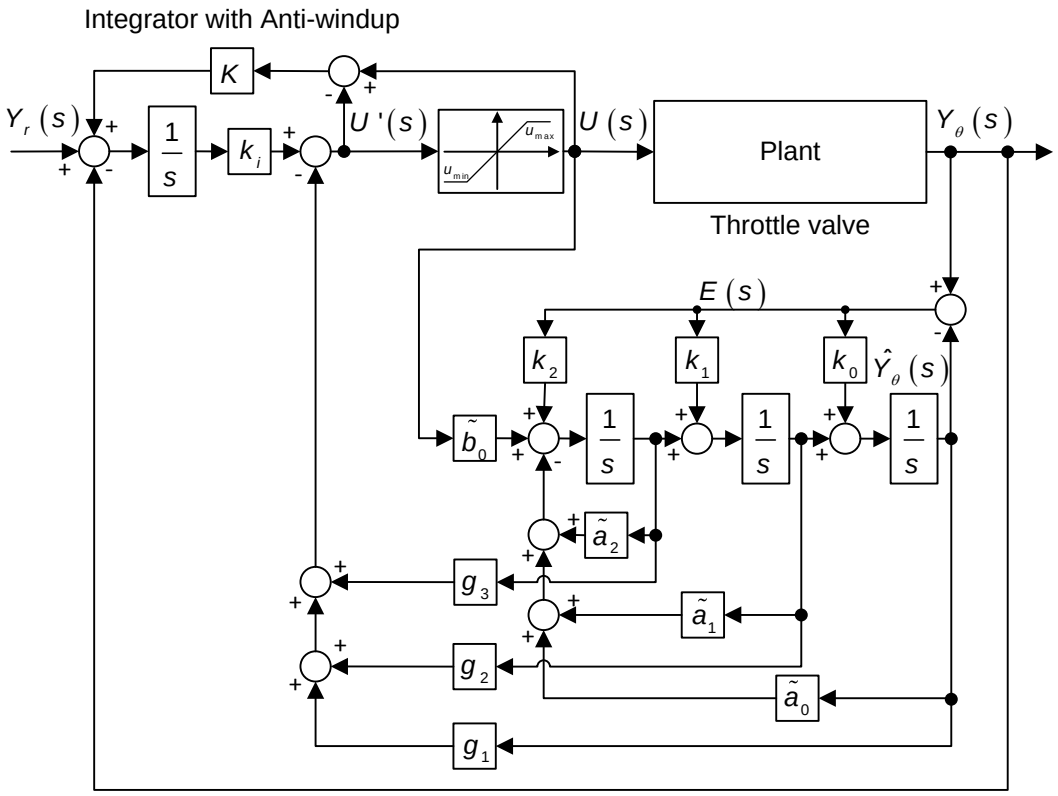

Figure 4.88: Observer aided LSF with integrator anti-windup used for the experiments and simulations

A suitable value of $K = 0.012$ was first found by repeatedly simulating the closed loop system step response with reducing settling times and afterwards validating the results experimentally. Figure 4.89 shows the results. The overshoot is reduced by 14% with $K = 0.012$, but can be reduces further by increasing the value of K.

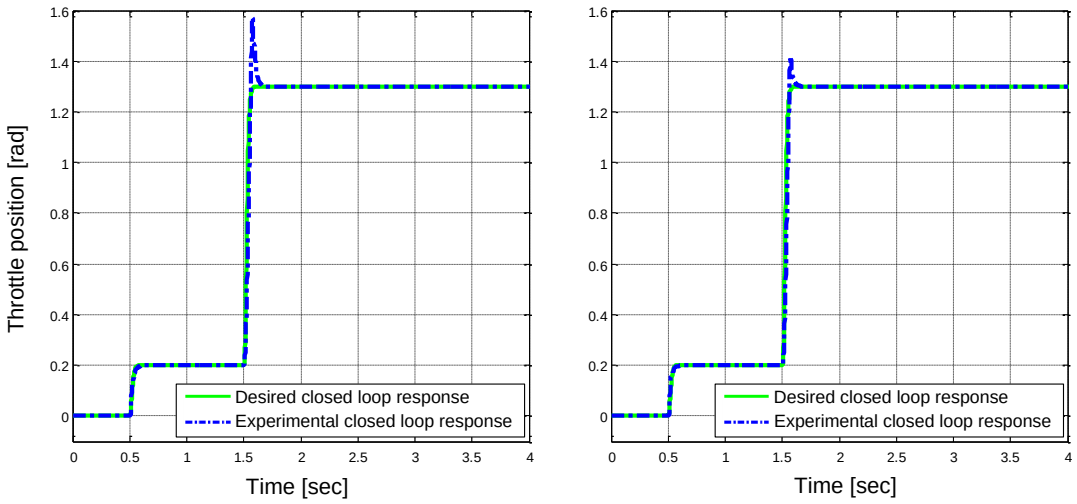

a) Without integrator anti-windup b) With integrator anti-windup

Figure 4.89: Throttle valve step response with/without integrator anti-windup (K=0.012)

4.6.3.4 Restructured Observer Aided LSF Control with Integrator for Steady State Error Elimination and Robust Pole Placement

The idea of restructuring the observer originates from the *observer based robust control* (OBRC) structure investigated in section 4.7. This new structure is investigated in view of the particular way the OBRC works but is included here to find out if it enhances the performance of a control system employing conventional linear state feedback control.

Figure 4.90 a) shows a conventional observer structure for a triple integrator plant with an input gain, $\tilde{b}_m$, and the correction loop implemented in three parts with the error applied to each integrator input via a separately adjustable gain, as in subsection 4.6.2. The three correction loop parts, however, can be combined into one thereby forming a single loop structure as shown in Figure 4.90 (b).

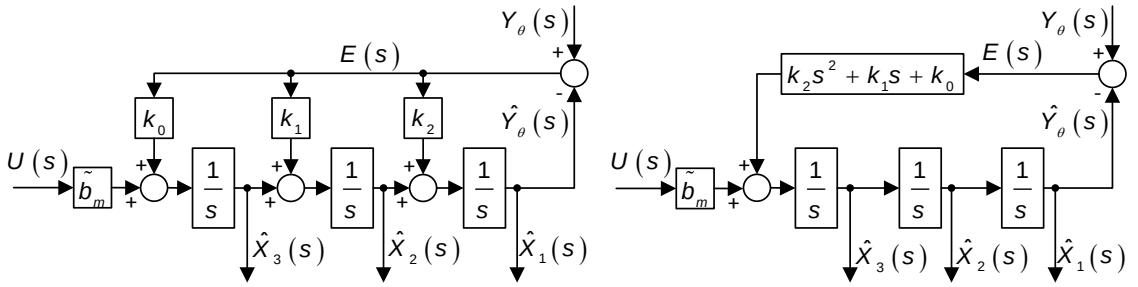

a) Basic observer b) Restructured observer

Figure 4.90: Restructure a basic observer to a single correction loop

As they stand, the two observers are mathematically equivalent, and in the OBRC application, the output of the block with transfer function, $k_2s^2 + k_1s + k_0$, is used. In practice the differentiators in this block will amplify any measurement noise from $Y_\theta(s)$ with accentuation of high frequency components. This problem can be circumvented by adding a low pass noise filter to the correction loop (Dodds, 2013). Figure 4.91 shows an observer having the single loop correction with the added third order noise filter, having denominator polynomial coefficients, f_2, f_1 and f_0. Provided the correction loop is stable in that all the *six* poles lie in the left half of the *s*-plane then the error, $e(t)$, will decay towards zero as required. By choosing the filter poles sufficient large, they will have an insignificant impact on the observer's ability to drive the error $e(t)$ to zero, but in the extreme the measurement noise problem will resurface through too high a cut-off frequency. Suitable filter gains (f_2, f_1, f_0) are found as a part of the observer gain design, which is shown later on in this section.

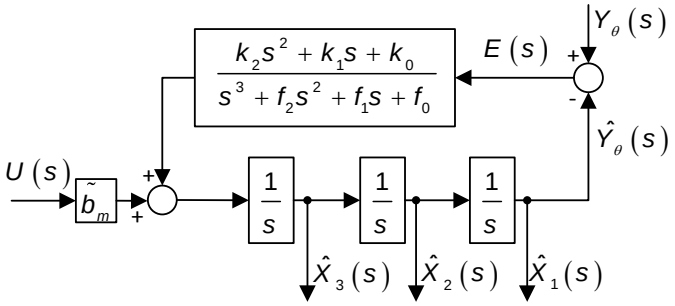

Figure 4.91: Single correction loop observer with noise filter

The restructured observer combined with LSF controller is shown in Figure 4.92 applied to the throttle valve model instead of the triple integrator.

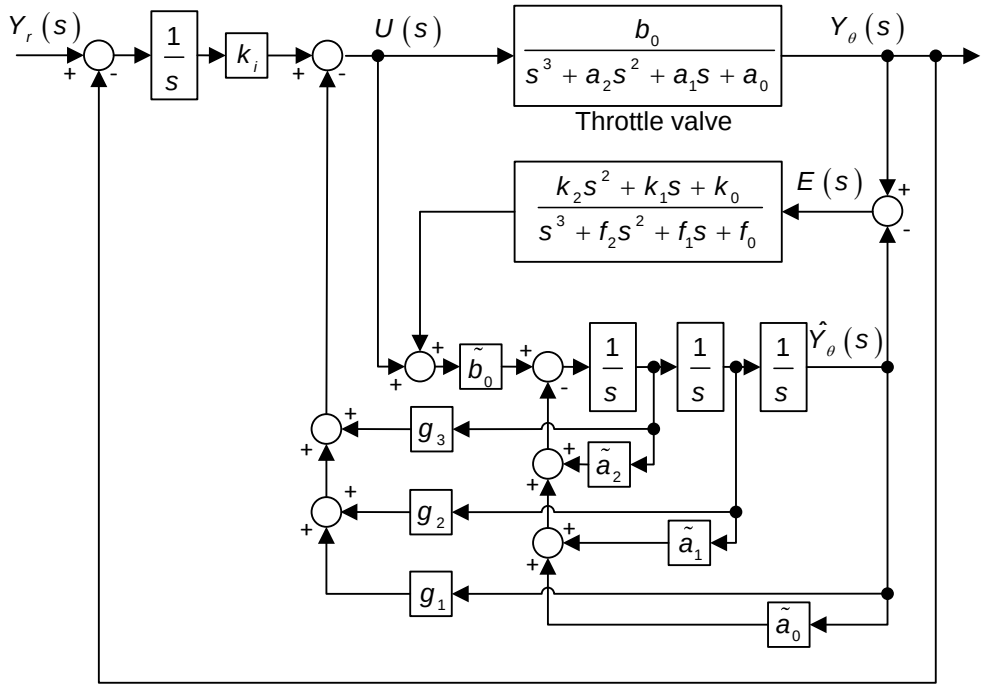

Figure 4.92: Single correction loop observer aided LSF with integrator for steady state compensation

As previously, the LSF controller and observer are designed separately, assuming that the separation principle applies (Franklin et al., 2002). This enables the LSF controller design of subsection 4.6.3.3 to be used. A block diagram of the observer is shown in Figure 4.93.

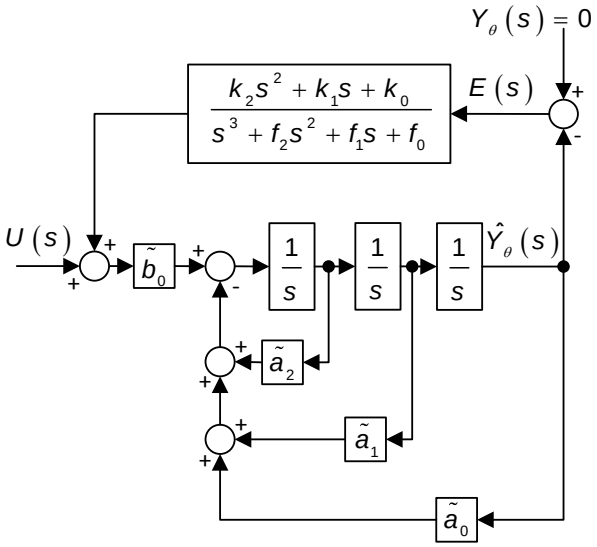

Figure 4.93: Observer with single loop correction controller

It will be ensured that all six of the correction loop poles lie in the left half of the *s*-plane by pole placement using the filter coefficients, f_0, f_1 and f_2, as well as the gains, k_0, k_1 and k_2. This is actually similar to the approach in the polynomial control of section 4.8. The observer characteristic polynomial is given by

$$1+\frac{\tilde{b}_0}{s^3+\tilde{a}_2 s^2+\tilde{a}_1 s+\tilde{a}_0}\cdot\frac{k_2 s^2+k_1 s+k_0}{s^3+f_2 s^2+f_1 s+f_0}=0\Rightarrow$$

$$\begin{aligned}s^6+(f_2+\tilde{a}_2)s^5+(f_1+\tilde{a}_2 f_2+\tilde{a}_1)s^4+(f_0+\tilde{a}_2 f_1+\tilde{a}_1 f_2+\tilde{a}_0)s^3+\\(\tilde{a}_2 f_0+\tilde{a}_1 f_1+\tilde{a}_0 f_2+\tilde{b}_0 k_2)s^2+(\tilde{a}_1 f_0+\tilde{a}_0 f_1+\tilde{b}_0 k_1)s+\tilde{a}_0 f_0+\tilde{b}_0 k_0=0\end{aligned} \quad (4.99)$$

Using the settling time formula to design a non-oscillatory correction loop response for a sixth order system, $n=6$,

$$\left(s+\frac{21}{2T_{so}}\right)^6=s^6+6qs^5+15q^2s^4+20q^3s^3+15q^4s^2+6q^5s+q^6 \quad (4.100)$$

where $q=21/(2\cdot T_{so})$ and T_{so} is the settling time for the combined observer correction loop and the noise filter. It is important to note that with this approach the effective cut-off frequency will be of the same order as the correction loop

bandwidth, which will achieve more effective filtering than by the approach of designing the filter separately with a much higher bandwidth than the correction loop so as to avoid instability. Equating the characteristic polynomials equations (4.99) and (4.100), and solving the resulting six equations for the correction loop gains and filtering coefficients yields

f_2:

$$f_2 + \tilde{a}_2 = 6q \Rightarrow f_2 = 6q - \tilde{a}_2 \tag{4.101}$$

f_1:

$$f_1 + \tilde{a}_2 f_2 + \tilde{a}_1 = 15q^2 \Rightarrow f_1 = 15q^2 - \tilde{a}_2 f_2 - \tilde{a}_1 \tag{4.102}$$

f_0:

$$f_0 + \tilde{a}_2 f_1 + \tilde{a}_1 f_2 + \tilde{a}_0 = 20q^3 \Rightarrow f_0 = 20q^3 - \tilde{a}_2 f_1 - \tilde{a}_1 f_2 - \tilde{a}_0 \tag{4.103}$$

k_2:

$$\tilde{a}_2 f_0 + \tilde{a}_1 f_1 + \tilde{a}_0 f_2 + \tilde{b}_0 k_2 = 15q^4 \Rightarrow k_2 = \left(15q^4 - \tilde{a}_2 f_0 - \tilde{a}_1 f_1 - \tilde{a}_0 f_2\right) / \tilde{b}_0 \tag{4.104}$$

k_1:

$$\tilde{a}_1 f_0 + \tilde{a}_0 f_1 + \tilde{b}_0 k_1 = 6q^5 \Rightarrow k_1 = \left(6q^5 - \tilde{a}_1 f_0 - \tilde{a}_0 f_1\right) / \tilde{b}_0 \tag{4.105}$$

k_0:

$$\tilde{a}_0 f_0 + \tilde{b}_0 k_0 = q^6 \Rightarrow k_0 = \left(q^6 - \tilde{a}_0 f_0\right) / \tilde{b}_0 \tag{4.106}$$

4.6.4 Simulation and Experimental results

4.6.4.1 Linear State Feedback with Integrator for Steady State Error Elimination

The LSF controller gains are designed as described in subsection 4.6.3.1, equations (4.76) to (4.79) with $T_s = 0.1$ [sec]. A dither signal is added to the control signal to reduce the effects of the static friction as described in subsection 4.4.3. The integrator anti-windup strategy is enabled to minimise the duration of the control saturation following the application of a step reference

input. The LSF controller is tested experimentally with three different reference input functions as described in subsection 4.3.3. The dSPACE system is used for the experiments as explained in subsection 4.3.2.

The simulation results presented in this subsection are obtained with the full nonlinear plant model presented in section 2.5.

First, simulated and experimental responses to a step reference position change within the throttle valve stop limits are presented in Figure 4.94.

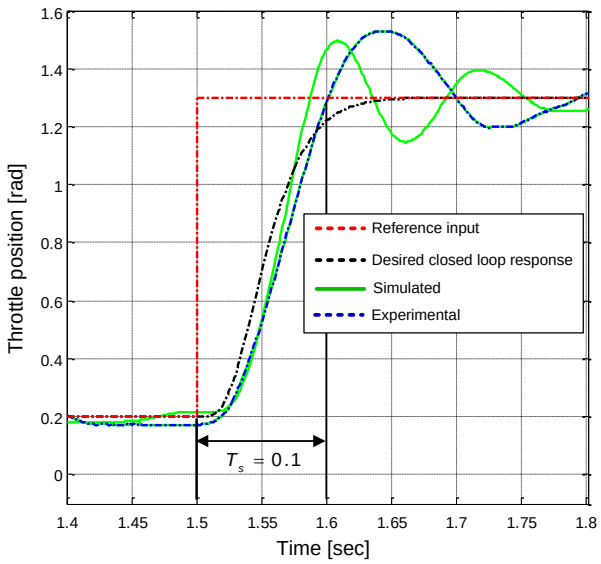

Figure 4.94: Closed loop step response, from 0.2 to 1.3 [rad]

The vertical black lines mark the nominal settling time of $T_s = 0.1\,[\text{sec}]$. It is evident that both the experimental and simulated responses do not match the desired settling time and do not exhibit the intended closed loop dynamics. It should be mentioned that a simulation with the linear plant model and perfectly matched controller yielded the ideal step response. It was observed that control saturation did not occur during these oscillatory responses. This behaviour is therefore attributed to static friction.

Figure 4.95 shows the simulated and experimental closed loop response of the LSF controller with three different reference input functions, as described in subsection 4.3.3, which indicates oscillations in both the experimental and simulated responses, more so in the experimental one.

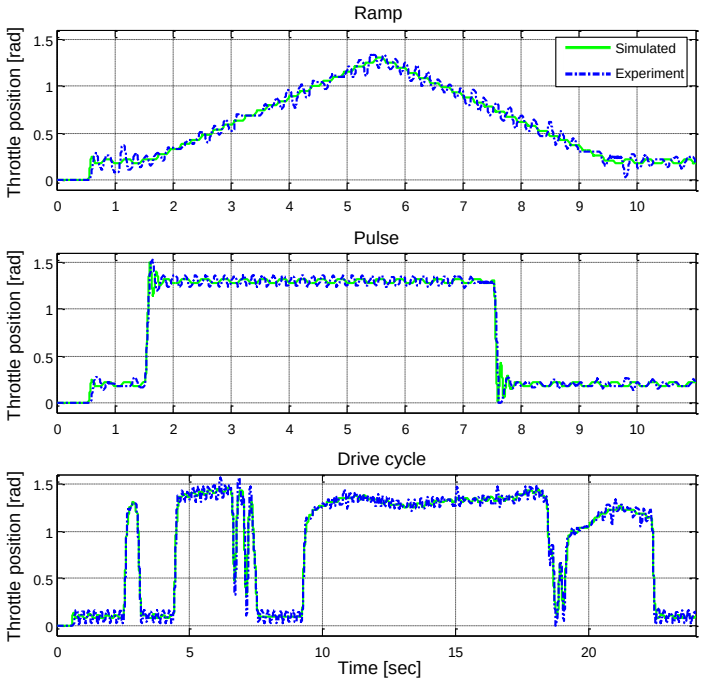

Figure 4.95: Experimental and simulated response of the LSF controller with steady state compensation

Figure 4.96 shows the difference between the experimental and simulated responses. In view of the poor oscillatory experimental performance of this design, it is not taken further.

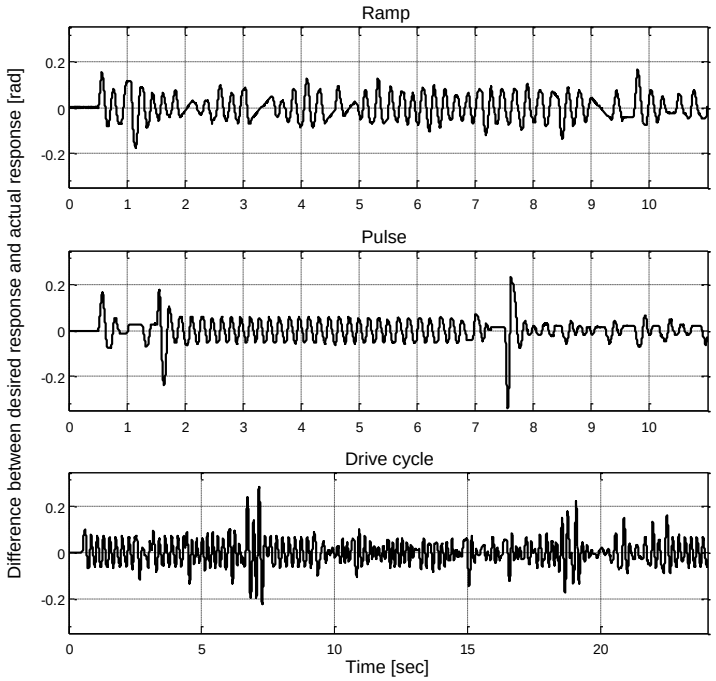

Figure 4.96: The difference between the desired and the experimental closed loop response

Since these differences are considerable, they are attributed to plant modelling errors, particularly in the area of the stick-slip friction, which causes a limit cycle with an integral term included in the controller, and the fact that the LSF controller is not robust with this particular pole placement.

4.6.4.2 LSF Controller with Integrator for Steady State Error Elimination and Robust Pole Placement

The LSF controller gains are determined as described in subsection 4.6.3.2, equation (4.83) to (4.86) with $T_s = 0.1$ [sec] and a robust pole-to-pole ratio of 50. A dither signal is added to the control signal to reduce the effects of the static friction as described in subsection 4.4.3. The integrator anti-windup strategy is enabled to minimise the saturation during the step reference input. The LSF controller is tested experimentally with three different reference input functions

as described in subsection 4.3.3. The dSPACE system is used for the experiments as explained in subsection 4.3.2.

The simulation results presented in this subsection are obtained with the full nonlinear plant model presented in section 2.5.

First, simulated and experimental responses to a step reference position change within the throttle valve stop limits are presented in Figure 4.97.

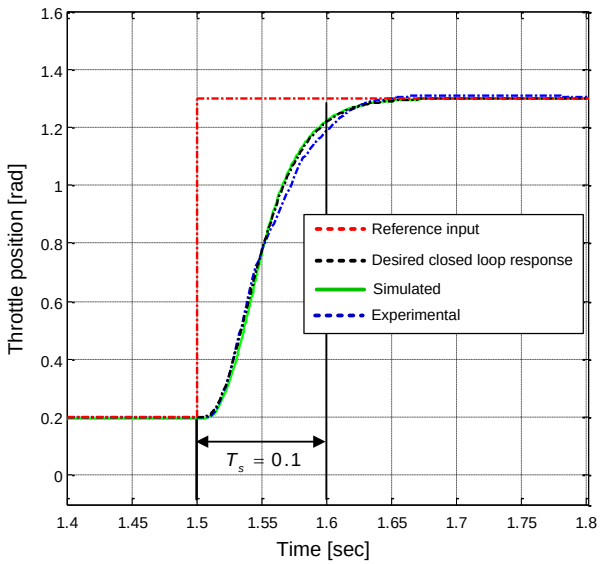

Figure 4.97: Closed loop step response, from 0.2 to 1.3 [rad]

The vertical black lines mark the nominal settling time of $T_s = 0.1$ [sec]. It is evident that both the experimental and simulated responses come close to this at ≈ 1.24 [rad].

Figure 4.98 shows the simulated and experimental closed loop responses.

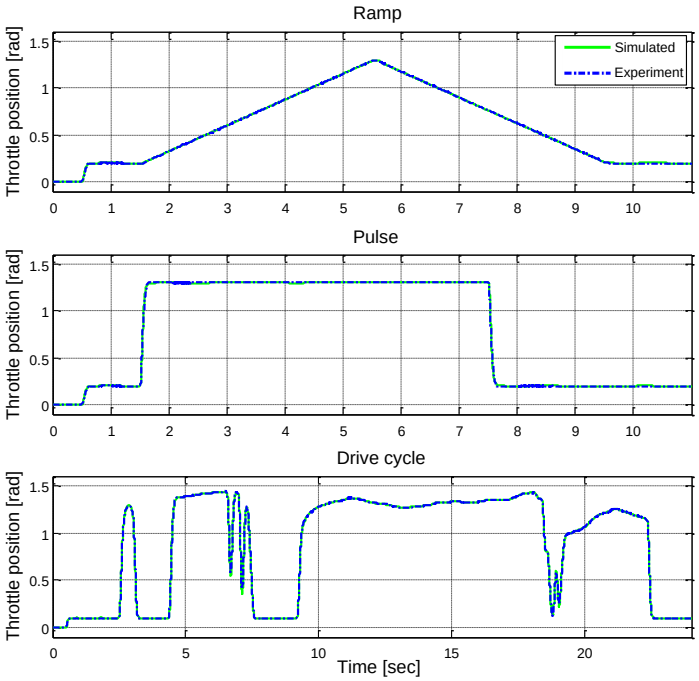

Figure 4.98: Experimental and simulated response of the LSF controller with integrator using robust pole placement

Figure 4.99 shows very small differences between the desired and the experimental closed loop responses (Figure 4.98) Hence the robust pole placement has been very effective.

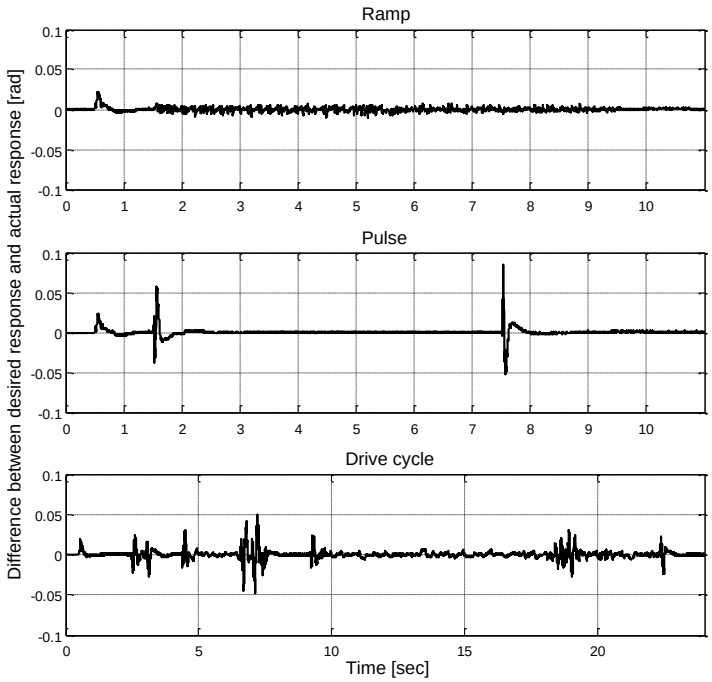

Figure 4.99: The difference between the desired and the experimental closed loop responses

As described in subsection 4.3.4.3 a spring failure can cause the engine to stall due to air starvation. The behaviour of the LSF controller during a spring break, at $t = 1$ [sec], is simulated using the nonlinear throttle valve model, and the result is shown in Figure 4.100. It shows a good robustness against the disturbance, with little deviation from the throttle position demand. The oscillations on the control signal at $t = 1.02$ [sec] are the added dither signal that increases in amplitude when the control error, $y_r - y$, exceeds a preset threshold of 1% of the full scale movement range as described in subsection 4.4.3.

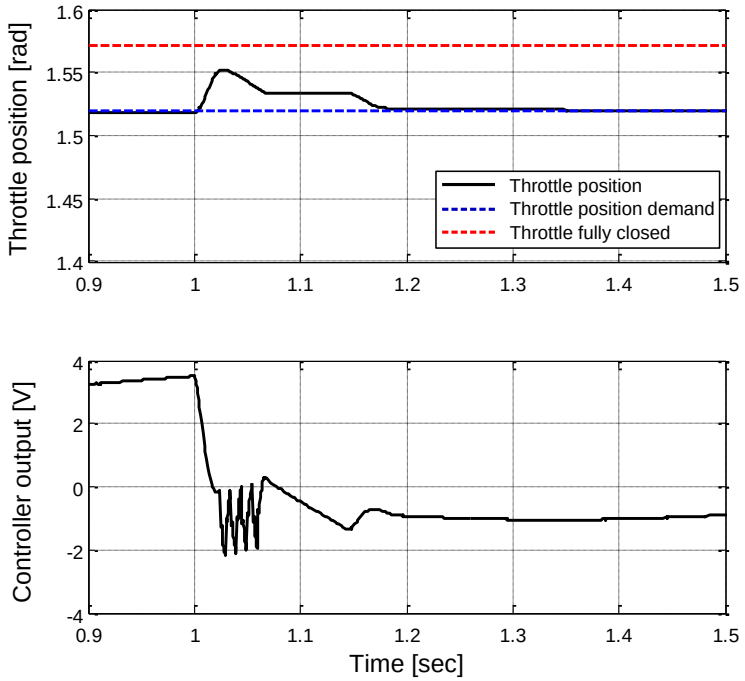

Figure 4.100: LSF with integrator controller during a spring failure

Figure 4.101 shows the difference between the desired (with ideal closed loop transfer function) and simulated closed loop step responses with different pole-to-pole ratios. The nonlinear throttle valve plant model is used for these simulations with a settling time of $T_s = 0.1$ [sec]. The plot shows that the difference is getting smaller when the pole-to-pole ratio rises, indicating a better robustness for $r_{pp} > 5$. For $r_{pp} = 1$, the pole placement is coincident (non-robust) as in subsection 4.6.4.1 and the unacceptable oscillations are again evident.

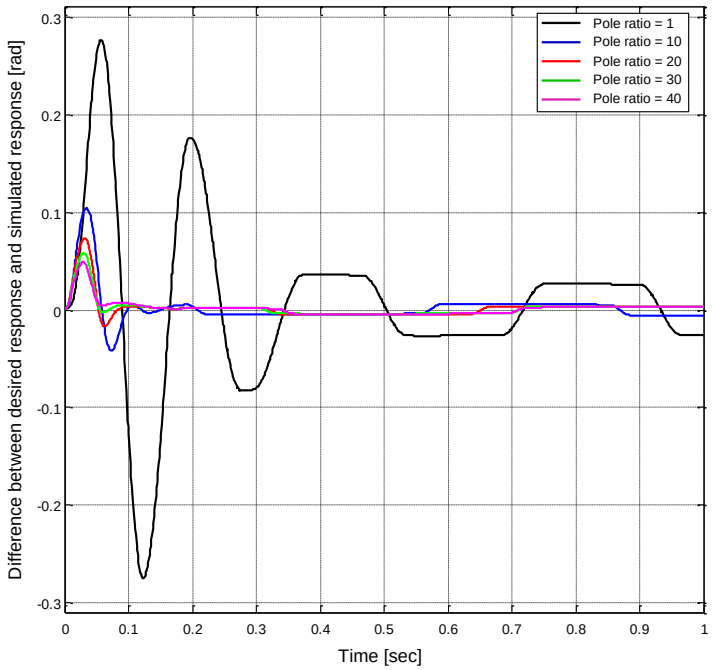

Figure 4.101: Simulated closed loop response difference done for a number of different robust pole placement ratios

The robustness against plant parameter deviations away from the nominal values is tested using the Monte Carlo method described in subsection 4.3.4.2. The parameter variation simulation uses the nonlinear throttle valve model with the controller output saturation, integrator anti-windup and dither. The LSF gains are designed using a robust pole-to-pole ration of 20. The result of the parameter variation simulation is shown in Figure 4.102 for the maximum possible standard deviation of $\sigma = 10\%$. The figure shows the operational envelope for 1000 simulation runs, where the blue and red lines are the minimum and maximum values. The nominal parameter closed loop controller response and controller output are shown in black.

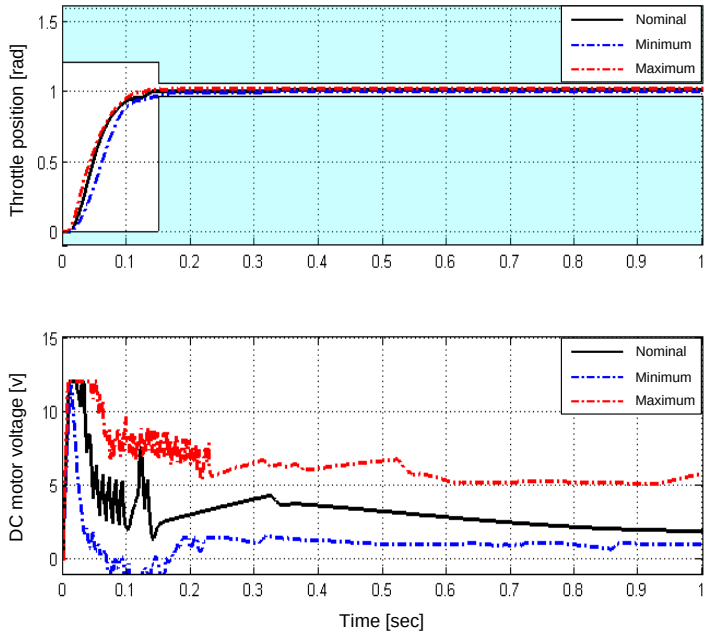

Figure 4.102: Maximum / minimum throttle position and DC motor voltage envelope (Standard deviation: $\sigma = 10\%$)

Further simulations were performed to find the standard deviation for other robust pole-to-pole ratios and the results are shown in Table 4.1.

Table 4.1

Pole ratio	20	30	40	50
σ [%]	10	14	15	16

A standard deviation from 10 to 16%, Table 4.1, indicates that the estimated parameters used for the control gain design can vary significantly before having an impact on the performance of the controller.

The sensitivity for the LSF controller is analysed in the frequency domain by using the relationship of equation (4.3) in subsection 4.3.4.1. This is done with the aid of the Matlab Control System Analysis Toolbox and the block diagram of

Figure 4.103 implemented in Simulink with $D(s)$ as the input and $V(s)$ as the output to obtain $S_p^c dB(\omega)$.

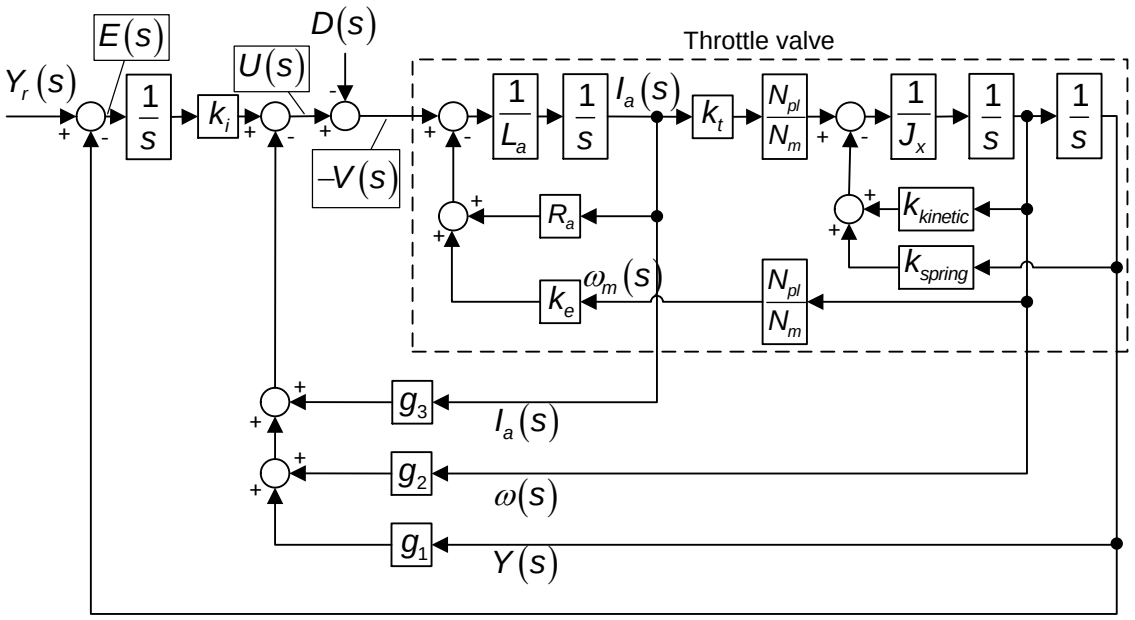

Figure 4.103: Control structure used to analyse the sensitivity

The sensitivity of the LSF controller is shown in Figure 4.104 for a robust pole-to-pole ratio of 20. The figure indicates a relatively low sensitivity, equivalent to high robustness. This corresponds well with the time domain result found by the above spring failure analysis and the Monte Carlo parameter variation simulations, in Table 4.1. Increasing the robust pole-to-pole ratio as per Table 4.1 only enhance the robustness with a small amount.

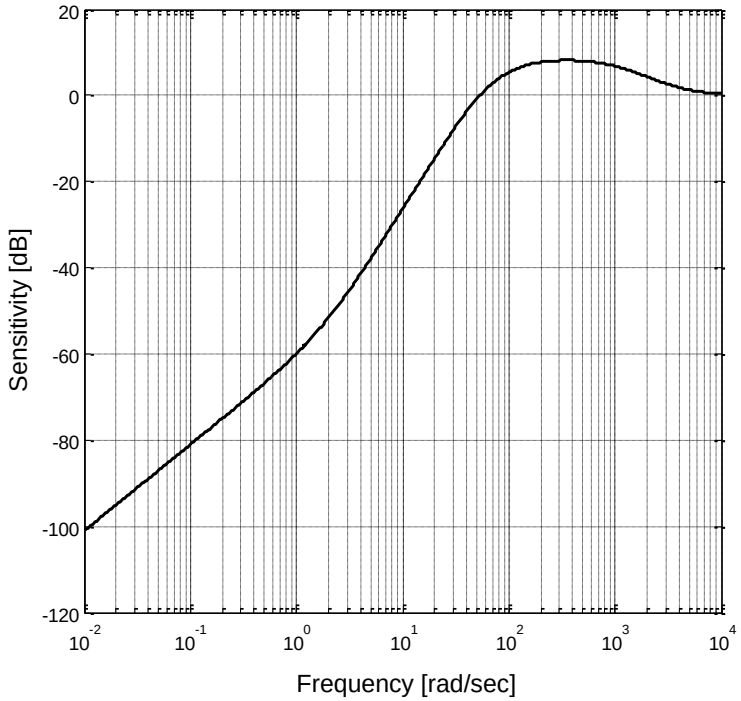

Figure 4.104: LSF with integrator sensitivity

This indicates a relatively low sensitivity, equivalent to high robustness. This corresponds well with the time domain result found by the above spring failure analysis and the Monte Carlo parameter variation simulation.

4.6.4.3 Observer Aided LSF Control with Integrator for Steady State Error Elimination and Robust Pole Placement

The LSF controller gains are determined as described in subsection 4.6.3.3, equation (4.90) to (4.93) with $T_s = 0.1$ [sec] and a robust pole-to-pole ratio of 50. The observer gains are designed using equation (4.96) to (4.98) with $T_{so} = T_s / 20$. A dither signal is added to the control signal to reduce the effects of the static friction as described in subsection 4.4.3. The integrator anti-windup strategy is enabled to minimise the saturation during the step reference input. The observer aided LSF controller is tested experimentally with three different

reference input functions as described in subsection 4.3.3. The dSPACE system is used for the experiments as explained in subsection 4.3.2.

The simulation results presented in this subsection are obtained with the full nonlinear plant model presented in section 2.5.

First, simulated and experimental responses to a step reference position change within the throttle valve stop limits are presented in Figure 4.105.

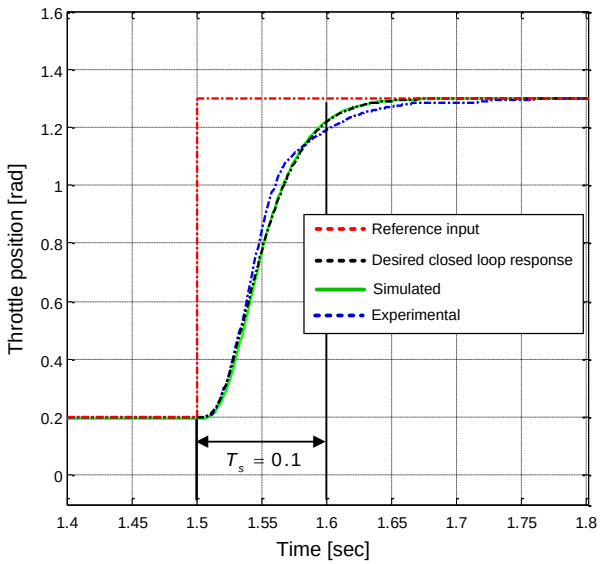

Figure 4.105: Closed loop step response, from 0.2 to 1.3 [rad]

The vertical black lines mark the nominal settling time of $T_s = 0.1$ [sec]. It is evident that both the experimental and simulated responses come close to this at ≈ 1.24 [rad].

Figure 4.106 shows the simulated and experimental closed loop responses.

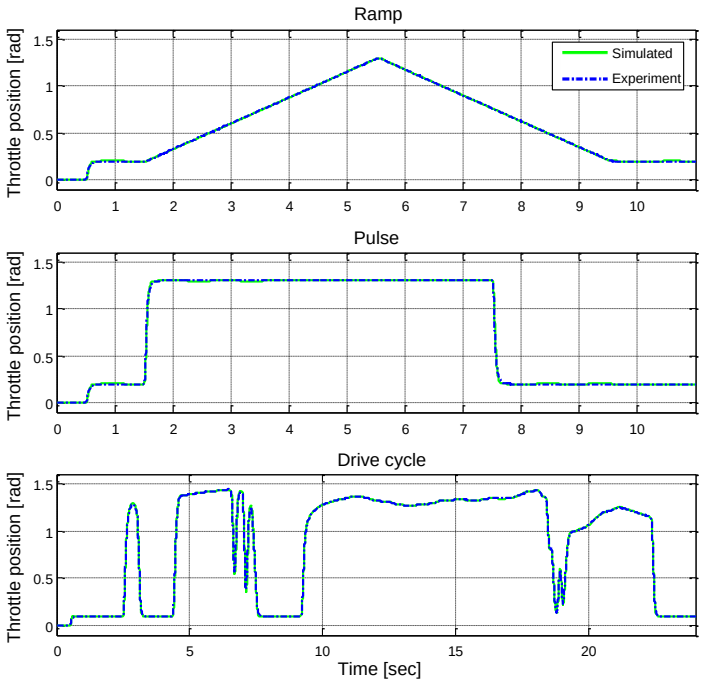

Figure 4.106: Experimental and simulated response of the observer aided LSF controller with integrator using robust pole placement

Figure 4.107 shows very small differences between the desired and the experimental closed loop response (Figure 4.106), again indicating that the robust pole placement has been very effective.

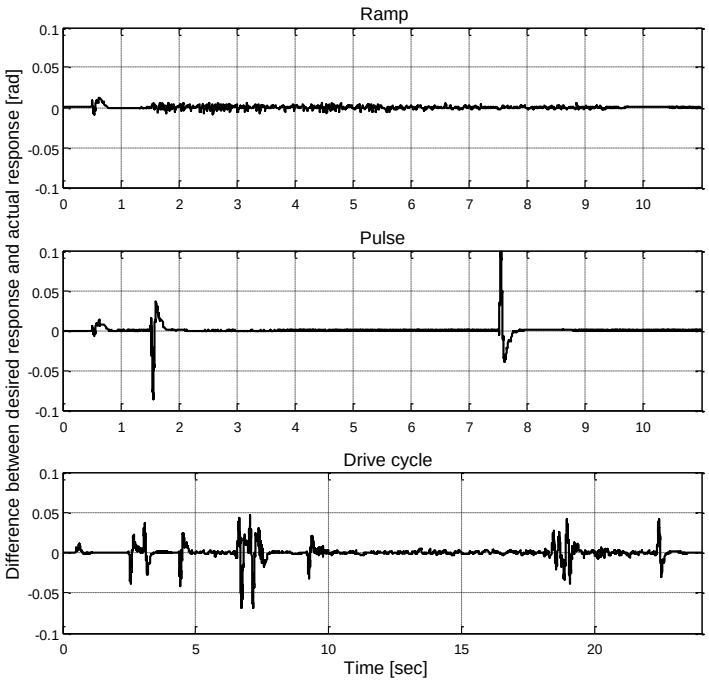

Figure 4.107: The difference between the desired and the experimental closed loop responses

As described in subsection 4.3.4.3 a spring failure can cause the engine to stall due to air starvation. The behaviour of the observer aided LSF controller during a spring break, at $t = 1$ [sec], is simulated using the nonlinear throttle valve model, and the result is shown in Figure 4.108. It shows a good robustness against the disturbance, with little deviation from the throttle position demand. The oscillations on the control signal at $t = 1.02$ [sec] are the added dither signal that increases in amplitude when the control error, $y_r - y$, exceeds a preset threshold of 1% of the full scale movement range as described in subsection 4.4.3.

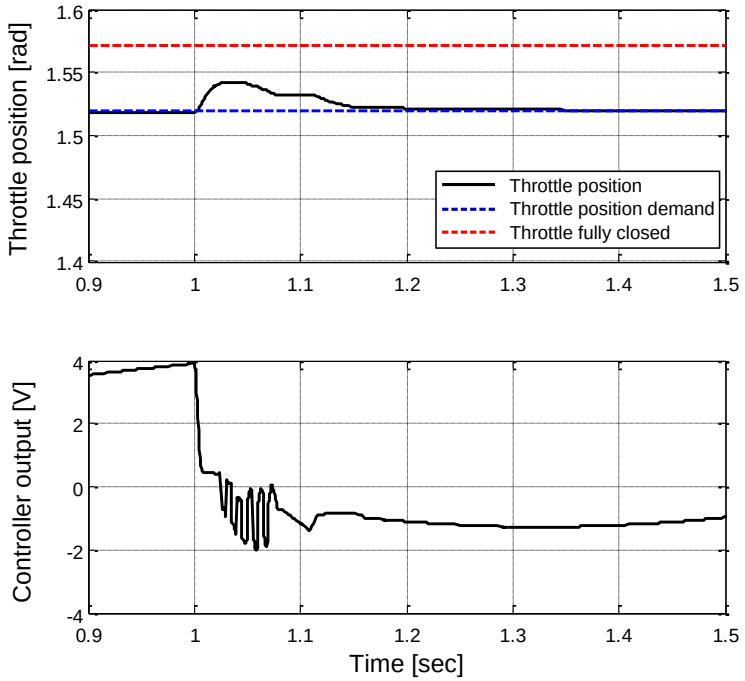

Figure 4.108: Observer aided LSF controller during a spring failure

The robustness against plant parameter variations away from the nominal values is tested using the Monte Carlo method described in subsection 4.3.4.2. The parameter variation simulation uses the nonlinear throttle valve model with the controller output saturation, integrator anti-windup and dither. The LSF controller and the observer gains are designed as described in the start of this subsection. The result of the parameter variation simulation is shown in Figure 4.109 for the maximum possible standard deviation of $\sigma = 15\%$. The figure shows the operational envelope for 1000 simulation runs, where the blue and red lines are the minimum and maximum values. The nominal parameter closed loop controller response and controller output are shown in black.

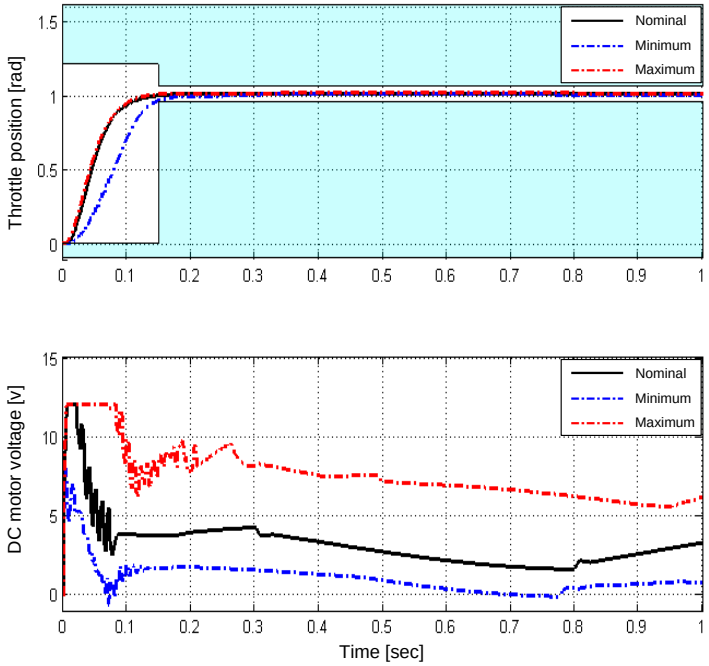

Figure 4.109: Maximum / minimum throttle position and DC motor voltage envelope (Standard deviation: $\sigma = 15\%$)

This indicates that the plant parameters can deviate significantly from the nominal values before having an adverse impact on the performance of the controller.

The sensitivity for the observer aided LSF controller is analysed in the frequency domain by using the relationship of equation (4.3) in subsection 4.3.4.1. This is done with the aid of the Matlab Control System Analysis Toolbox and the block diagram of Figure 4.110 implemented in Simulink with $D(s)$ as the input and $V(s)$ as the output to obtain $S_p^C dB(\omega)$.

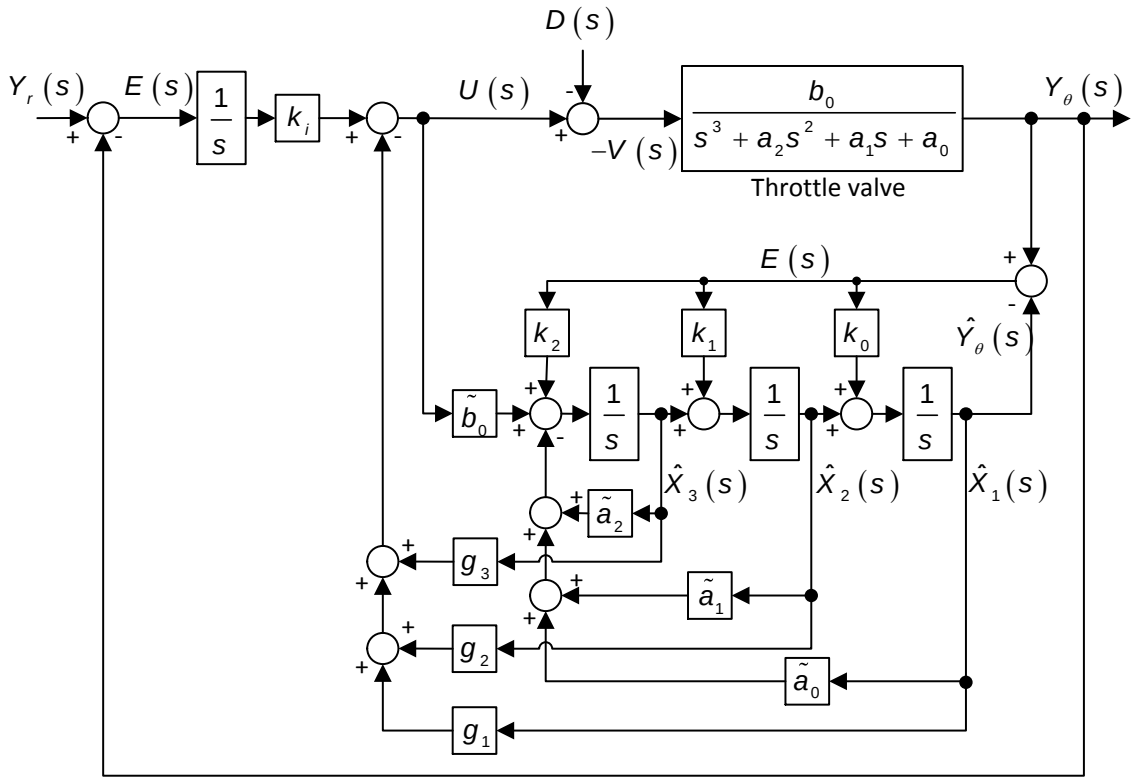

Figure 4.110: Control structure used to analyse the sensitivity

The sensitivity of the observer aided LSF controller is shown in Figure 4.111 for a robust pole-to-pole ratio of 50 and $T_{so} = T_s / 20$. The figure indicates a relatively low sensitivity, equivalent to high robustness. This corresponds well with the time domain result found by the above spring failure analysis and the Monte Carlo parameter variation simulation.

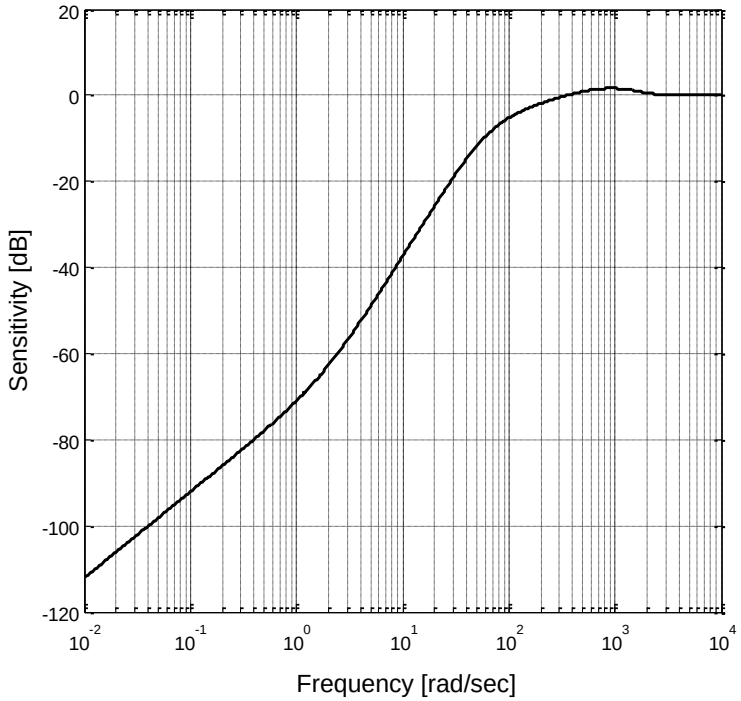

Figure 4.111: Observer aided LSF control with integral term sensitivity

4.6.4.4 Restructured Observer Aided LSF Control with Integrator for Steady State Error Elimination and Robust Pole Placement

The LSF controller gains are determined as described in subsection 4.6.3.3, equation (4.90) to (4.93) with $T_s = 0.1$ [sec] and a robust pole-to-pole ratio of 50. The observer gains are designed using equation (4.101) to (4.106), subsection 4.6.3.4, with $T_{so} = T_s / 10$. A dither signal is added to the control signal to reduce the effects of the static friction as described in subsection 4.4.3. The integrator anti-windup strategy is enabled to minimise the saturation during the step reference input. The observer aided LSF controller is tested experimentally with three different reference input functions as described in subsection 4.3.3. The dSPACE system is used for the experiments as explained in subsection 4.3.2.

The simulation results presented in this subsection are obtained with the full nonlinear plant model presented in section 2.5.

First, simulated and experimental responses to a step reference position change within the throttle valve stop limits are presented in Figure 4.112.

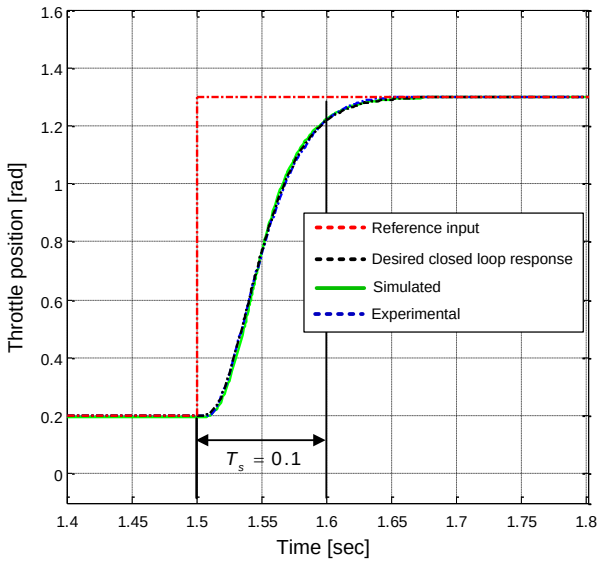

Figure 4.112: Closed loop step response, from 0.2 to 1.3 [rad]

The vertical black lines mark the nominal settling time of $T_s = 0.1\,[\text{sec}]$. It is evident that both the experimental and simulated responses come close to this at ≈ 1.24 [rad].

Figure 4.113 shows the simulated and experimental closed loop responses.

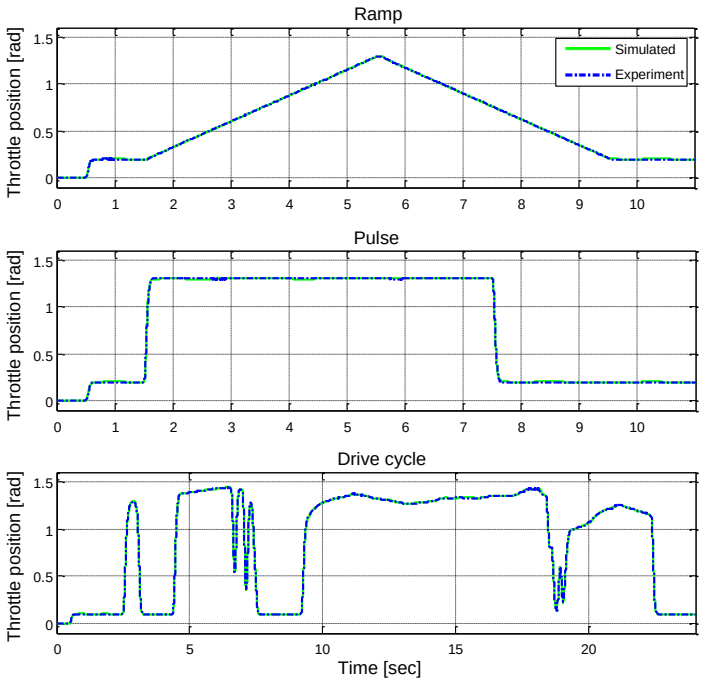

Figure 4.113: Experimental and simulated response of the restructured observer aided LSF controller with integrator using robust pole placement

Figure 4.114 shows very small differences between the desired and the experimental closed loop response (Figure 4.113), indicating yet again that the robust pole placement has been very effective.

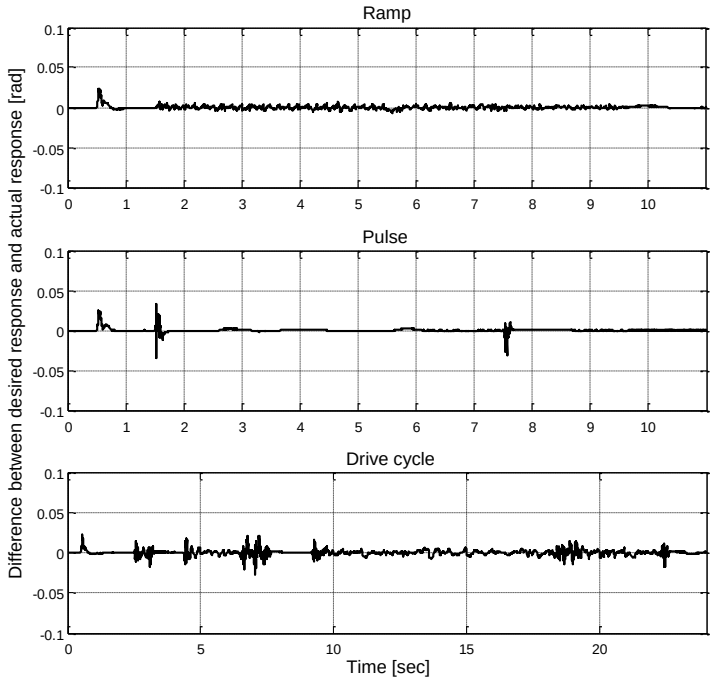

Figure 4.114: The difference between the desired and the experimental closed loop responses

As described in subsection 4.3.4.3 a spring failure can cause the engine to stall due to air starvation. The behaviour of the observer aided LSF controller during a spring break, at $t = 1$ [sec], is simulated using the nonlinear throttle valve model, and the result is shown in Figure 4.115. It shows a good robustness against the disturbance, with little deviation from the throttle position demand. The oscillations on the control signal at $t = 1.02$ [sec] are the added dither signal that increases in amplitude when the control error, $y_r - y$, exceeds a preset threshold of 1% of the full scale movement range as described in subsection 4.4.3.

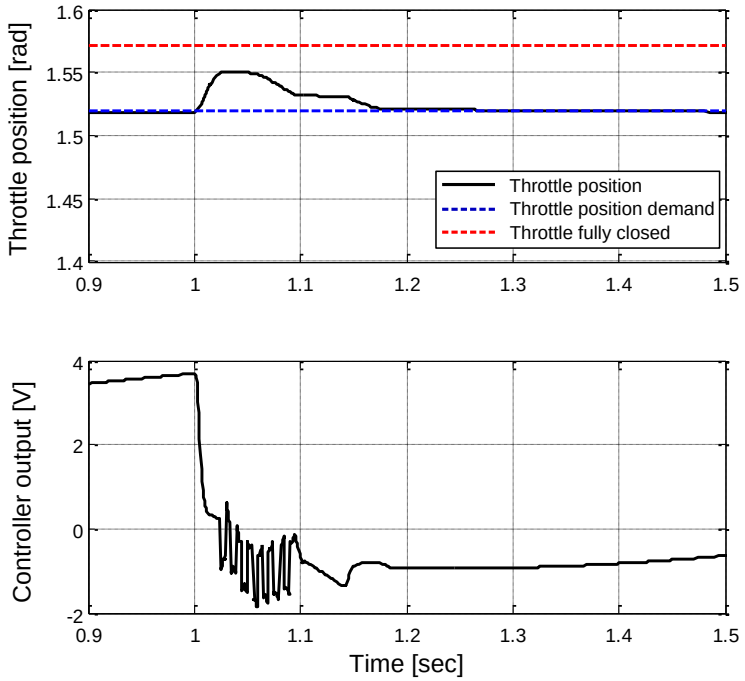

Figure 4.115: Restructured observer aided LSF with integrator during a spring failure

The robustness against plant parameter deviations away from the nominal values is tested using the Monte Carlo method described in subsection 4.3.4.2. The parameter variation simulation uses the nonlinear throttle valve model with the controller output saturation, integrator anti-windup and dither. The LSF controller and the observer gains are designed as described in the start of this subsection. The result of the parameter variation simulation is shown in Figure 4.116 for the maximum possible standard deviation of $\sigma = 15\%$. The figure shows the operational envelope for 1000 simulation runs, where the blue and red lines are the minimum and maximum values. The nominal parameter closed loop controller response and controller output are shown in black.

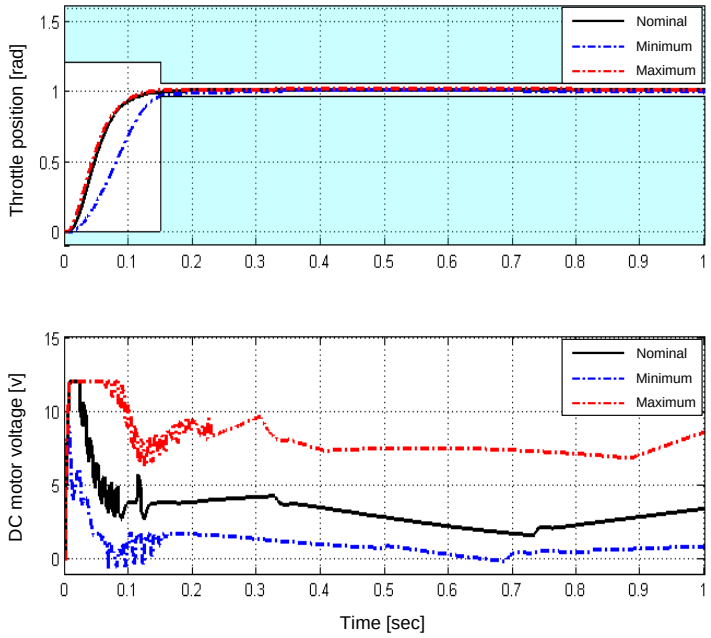

Figure 4.116: Maximum / minimum throttle position and DC motor voltage envelope (Standard deviation: $\sigma = 15\%$)

This indicates that the plant parameters can deviate significantly from the nominal values before having an adverse impact on the performance of the controller.

The sensitivity for the restructured observer aided LSF controller is analysed in the frequency domain by using the relationship of equation (4.3) in subsection 4.3.4.1. This is done with the aid of the Matlab Control System Analysis Toolbox and the block diagram of Figure 4.117 implemented in Simulink with $D(s)$ as the input and $V(s)$ as the output to obtain $S_p^C dB(\omega)$.

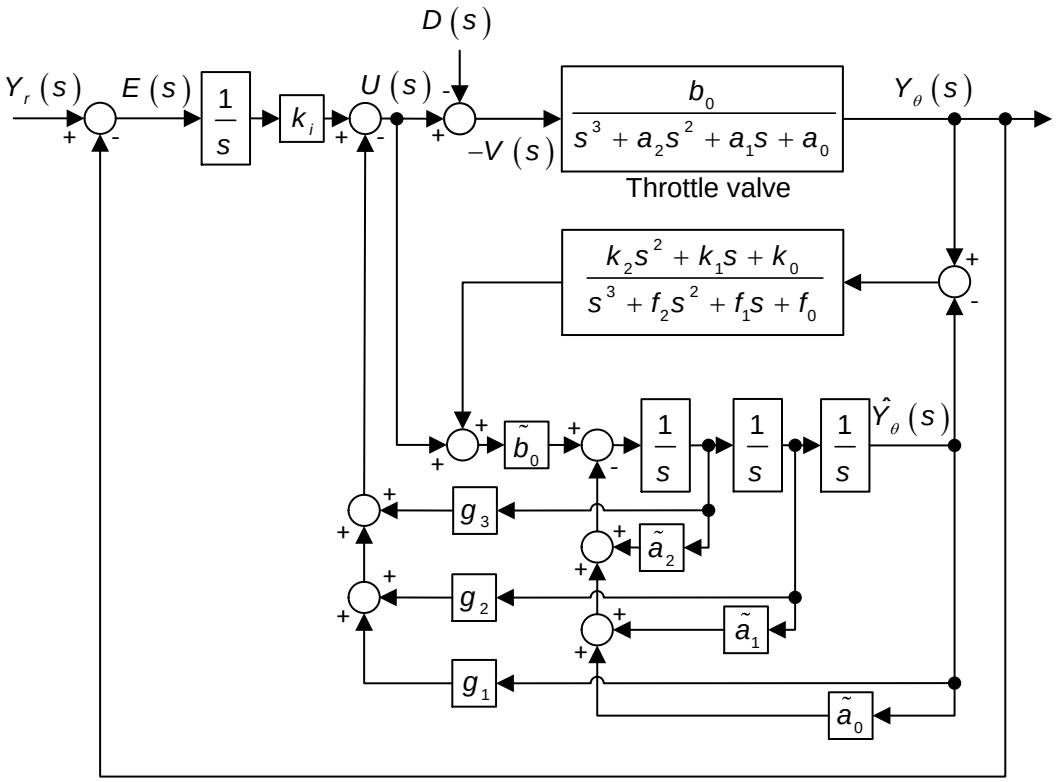

Figure 4.117: Control structure used to analyse the sensitivity

The sensitivity of the restructured observer aided LSF controller is shown in Figure 4.118 for a robust pole-to-pole ratio of 50 and $T_{so} = T_s / 10$. The figure indicates a relatively low sensitivity, equivalent to high robustness. This corresponds well with the time domain result found by the above spring failure analysis and the Monte Carlo parameter variation simulation.

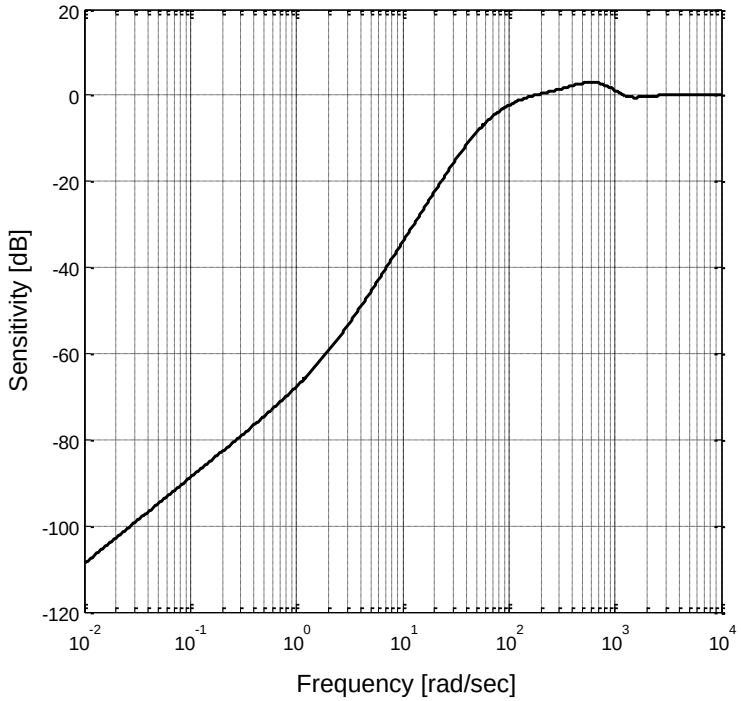

Figure 4.118: Restructured observer aided LSF control with integrator sensitivity

4.7 Observer Based Robust Control

4.7.1 Introduction and Brief History

The *observer based robust control* (OBRC) control technique was instigated in (Dodds, 2007) and further investigated in (Stadler et al., 2007) (Stadler, 2008) (Fallahi, 2013). In OBRC, an observer is used to estimate the external disturbance referred to the control input. Plant parametric uncertainties can be represented by part of such an external disturbance. The estimate from the observer is therefore a combination of plant parametric errors and physical external disturbances, if they exist. This disturbance estimate is added to the control signal with the aim of cancelling both the physical disturbance and the effects of the plant parameter errors.

Let $G_m(s)$ be a model of the plant with transfer function, $G(s)$, where an input, $U_e(s)$, exists so that $Y_m(s) = Y(s)$ as shown in Figure 4.119.

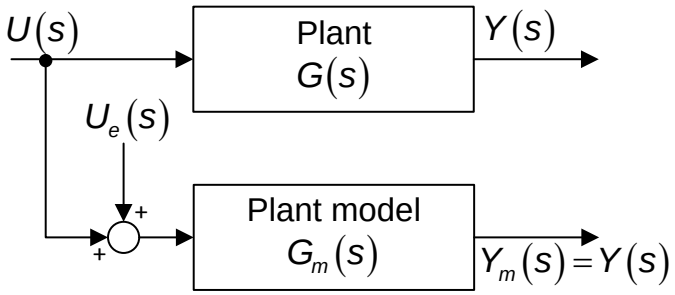

Figure 4.119: Plant and model mismatch

The signal $U_e(s)$ can be estimated by using the restructured observer from subsection 4.6.3.4, called the single correction loop observer. This employs a correction loop controller, $H_o(s)$, as shown in Figure 4.120.

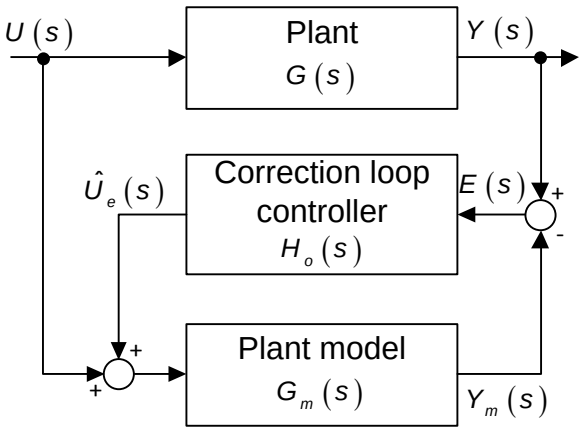

Figure 4.120: Correction loop controller used for estimating the disturbance $U_e(s)$

The closed loop transfer function, $Y_m(s)/U(s)$, depends on $G_m(s)$ and $H_o(s)$ as well as $G(s)$, but if the correction loop controller is designed to achieve $E(s) \cong 0$, then $Y_m(s) \cong Y(s)$ so that $Y_m(s)/U(s) \cong Y(s)/U(s) = G(s)$. This, however, requires $H_o(s)$ to embody relatively large gains.

Figure 4.121 shows Figure 4.120 with the plant represented by its model and the disturbance input as in Figure 4.119.

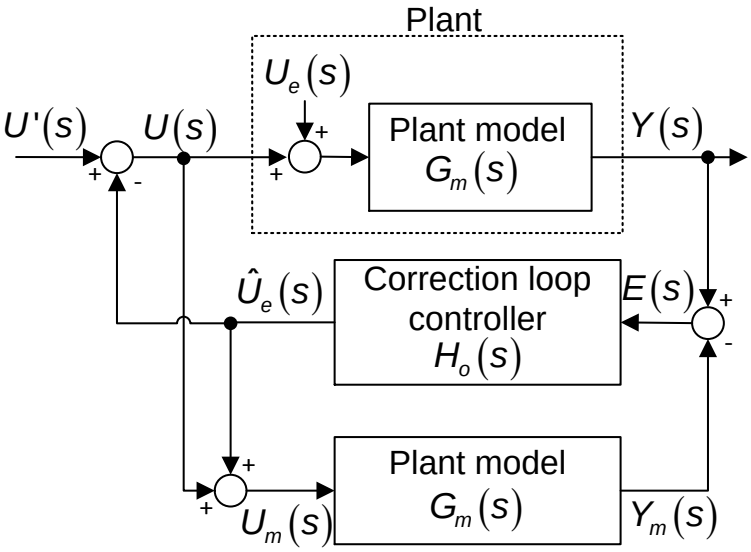

Figure 4.121: Subtraction of $\hat{U}_e(s)$ from control input to compensate $U_e(s)$.

Through the action of the correction loop controller, the error, $E(s)$, is maintained with negligible proportions regardless of $U(s)$. It then becomes apparent that the disturbance estimate, $\hat{U}_e(s)$, may be used to reduce the effect of the actual disturbance, $U_e(s)$, by forming a primary control input, $U'(s)$, applied to both the plant and its model, from which $\hat{U}_e(s)$ is subtracted, as shown. It is evident that in the hypothetical, ideal case of $\hat{U}_e(s) = U_e(s)$, the disturbance cancellation would be complete, giving a perfectly robust system.

Next, it is possible to simplify the connections on the left hand side of the blocks of Figure 4.121, resulting in the block diagram of Figure 4.122, which is functionally identical.

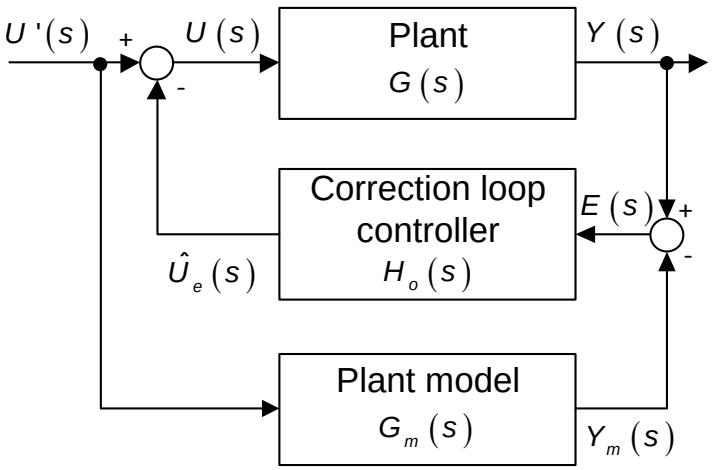

Figure 4.122: Input conversion block diagram

It is now evident that the primary control variable, $U'(s)$, is applied directly to the plant model. Since the state variables of the plant model are available, they can be used to complete a linear state feedback model control loop, as shown in the complete OBRC block diagram of Figure 4.123.

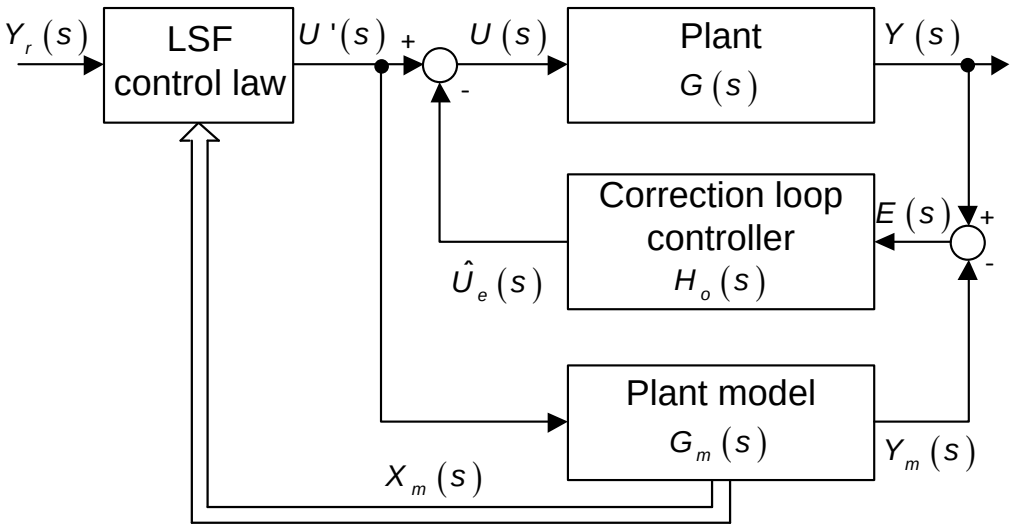

Figure 4.123: Overall OBRC structure for a single input, single output plant

4.7.2 Controller Design

A third order OBRC with a LSF controller is shown in Figure 4.124 applicable to the throttle valve.

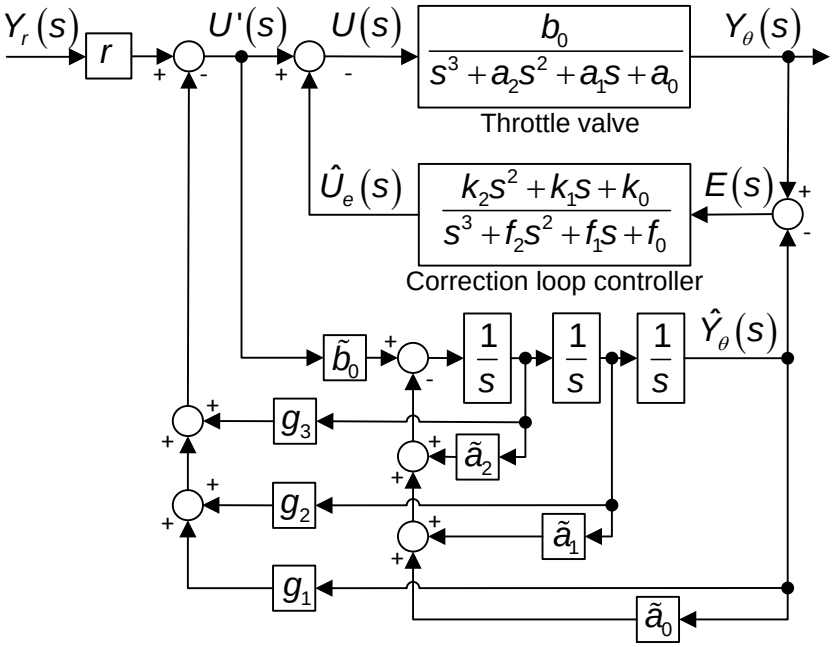

Figure 4.124: OBRC structure with a LSF controller

For standard linear state feedback controllers using observers, the separation principle applies (Dodds, 2013) through the assumption of the plant and its model being identical. In OBRC, this assumption cannot be made but if the correction loop controller is first designed to maintain $E(s) \cong 0$ regardless of the real plant, then the design of the LSF controller can be performed subsequently and separately from the observer as if the separation principle did apply.

In view of the forgoing discussion, the complete closed loop control system dynamics are those of the LSF applied to the plant model. With reference to Figure 4.124, the relevant closed loop transfer function is

$$\frac{\hat{Y}_\theta(s)}{Y_r(s)} = \frac{r \cdot \tilde{b}_0}{s^3 + \left(\tilde{a}_2 + \tilde{b}_0 g_3\right)s^2 + \left(\tilde{a}_1 + \tilde{b}_0 g_2\right)s + \tilde{a}_0 + \tilde{b}_0 g_1}, \qquad (4.107)$$

where r is the reference input scaling coefficient needed for a unity DC gain.

The plant model transfer function coefficients are calculated using the estimates of the physical plant parameters discussed in Chapter 2, as follows.

$$\tilde{a}_0 = \tilde{R}_a \tilde{k}_{spring} / \left(\tilde{L}_a \tilde{J}_x\right)$$

$$\tilde{a}_1 = \tilde{k}_{spring} / \tilde{J}_x + \tilde{k}_e \tilde{k}_t / \left(\tilde{L}_a \tilde{J}_x\right)\left(\tilde{N}_{pl} / \tilde{N}_m\right)^2 + \tilde{R}_a \tilde{k}_{kinetic} / \left(\tilde{L}_a \tilde{J}_x\right)$$

$$\tilde{a}_2 = \tilde{R}_a / \tilde{L}_a + \tilde{k}_{kinetic} \tilde{J}_x$$

$$\tilde{b}_0 = \tilde{k}_t \tilde{N}_{pl} / \left(\tilde{L}_a \tilde{N}_m \tilde{J}_x\right)$$

Designing the control loop by the method of pole assignment using the settling time formula for $n = 3$, the desired characteristic polynomial is

$$\left(s+\frac{6}{T_s}\right)^3 = s^3 + \frac{18}{T_s}s^2 + \frac{108}{T_s^2}s + \frac{216}{T_s^3} \tag{4.108}$$

where T_s is the settling time of the step response (5% criterion). Equating the polynomial (4.108) and the denominator from equation (4.107) yields the following gain formulae.

g_3:

$$\frac{18}{T_s} = \tilde{a}_2 + \tilde{b}_0 g_3 \Rightarrow g_3 = \left(\frac{18}{T_s} - \tilde{a}_2\right) / \tilde{b}_0 \tag{4.109}$$

g_2:

$$\frac{108}{T_s^2} = \tilde{a}_1 + \tilde{b}_0 g_2 \Rightarrow g_2 = \left(\frac{108}{T_s^2} - \tilde{a}_1\right) / \tilde{b}_0 \tag{4.110}$$

g_1:

$$\frac{216}{T_s^3} = \tilde{a}_0 + \tilde{b}_0 g_1 \Rightarrow g_1 = \left(\frac{216}{T_s^3} - \tilde{a}_0\right) / \tilde{b}_0 \tag{4.111}$$

To find the value for r the *final value theorem* is used with a unit-step input ($U(s) = 1/s$),

$$\begin{aligned} &\frac{\hat{Y}(s)}{Y_r(s)} = \lim_{s\to 0} s\left(\frac{\hat{Y}(s)}{Y_r(s)}\right)\frac{1}{s} = 1 \Rightarrow \\ &\lim_{s\to 0}\left[\frac{r\cdot\tilde{b}_0}{s^3 + \left(\tilde{a}_2 + \tilde{b}_0 g_3\right)s^2 + \left(\tilde{a}_1 + \tilde{b}_0 g_2\right)s + \tilde{a}_0 + \tilde{b}_0 g_1}\right] = 1 \Rightarrow \\ &\frac{r\cdot\tilde{b}_0}{\tilde{a}_0 + \tilde{b}_0 g_1} = 1 \Rightarrow r = \frac{\tilde{a}_0}{\tilde{b}_0} + g_1 \end{aligned} \tag{4.112}$$

For the observer, the correction loop controller parameters are found as in subsection 4.6.3.4. The correction loop characteristic polynomial is

$$s^6+\left(f_2+\tilde{a}_2\right)s^5+\left(f_1+\tilde{a}_2f_2+\tilde{a}_1\right)s^4+\left(f_0+\tilde{a}_2f_1+\tilde{a}_1f_2+\tilde{a}_0\right)s^3+\\ \left(\tilde{a}_2f_0+\tilde{a}_1f_1+\tilde{a}_0f_2+\tilde{b}_0k_2\right)s^2+\left(\tilde{a}_1f_0+\tilde{a}_0f_1+\tilde{b}_0k_1\right)s+\tilde{a}_0f_0+\tilde{b}_0k_0 \quad (4.113)$$

An initial simulation was carried out using multiple pole placement for the observer model correction loop and for the linear state feedback control loop, using the settling time formula for each, with various ratios between the two settling times, the observer settling time being shorter in all cases. The simulation results proved satisfactory with a linear plant model but unfortunately instability occurred with the full nonlinear model, this poor result being confirmed experimentally. The problem was attributed to the stick-slip friction. Subsequently the investigation was carried further by considering other pole placement patterns. As the correct operation of the observer model correction loop is critical, different pole placements were considered for this, the linear state feedback poles being left as previously. Satisfactory performance was found for the distributed observer correction loop pole pattern shown in Figure 4.125.

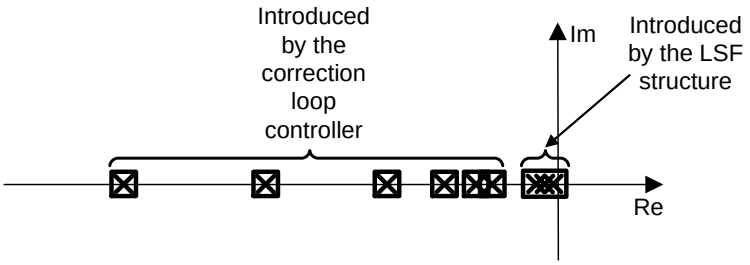

Figure 4.125: Individual pole placement used for OBRC

In an attempt to achieve the desired robustness, the observer correction loop poles were separated from the multiple pole set of the linear state feedback loop whose settling time was T_s, using the pole-to-pole dominance ratios, r_{ppi}, (Dodds, 2013), for the i^{th} correction loop pole, p_i, $i=1,2,\ldots,6$. The reason for this is that the dominated poles (in this case the observer correction loop poles) give the system more robustness through being produced by larger gains that

give the control loop stiffness that would not be obtained without this dominance. Given that no coincident correction loop pole location worked, the only choice was to spread the poles. This was done heuristically but with the constraint that $r_{ppi} > r_{pp\min}$. Referring to Figure 4.125, there are three dominant poles due to the linear state feedback loop and six dominated poles, p_i. Let them be arranged such that $|p_{k-1}| < |p_k|$, $k = 2,3,\ldots,6$. The observer correction loop pole with the most influence is the one with the magnitude, $|p_1|$. Let the dominant (LSF loop) pole location be $|p_d|$. Then according to (Dodds, 2013),

$$\frac{|p_1|}{|p_d|} \geq r_{pp\min} \tag{4.114}$$

where $r_{pp\min} = 5.4$. The LSF loop settling time is given by

$$T_s = \left.\frac{1.5(1+n)}{|p_d|}\right|_{n=3} = \frac{6}{|p_d|} \Rightarrow |p_d| = \frac{6}{T_s} \tag{4.115}$$

Then inequality (4.114) may be rewritten as

$$|p_1| \geq \frac{6 r_{pp\min}}{T_s} \tag{4.116}$$

In this case, $T_s = 0.1$ [sec]. Then $|p_1| \geq 324$.

The observer correction loop poles are chosen via r_{ppi} as

$$\left\{r_{ppi}\right\}_{i=1,2,\ldots,6} = \{5.5, 6, 8.5, 20, 42.5, 57.5\} \tag{4.117}$$

The corresponding pole magnitudes are then chosen as

$$\left\{|p_i|\right\} = \left\{\frac{6 r_{ppi}}{T_s}\right\}_{i=1,2,\ldots,6} = \{330, 360, 510, 1200, 2550, 3450\} \tag{4.118}$$

Using equation (4.117) the desired characteristic polynomial is then,

$$(s+p_1)(s+p_2).....(s+p_6) \tag{4.119}$$

The calculation of the characteristic polynomial is performed by using Matlab® numerically and the result is given in the form,

$$s^6 + d_5 s^5 + d_4 s^4 + d_3 s^3 + d_2 s^2 + d_1 s + d_0 \tag{4.120}$$

where d_n are the calculated coefficients for $n = [0..5]$

Equating the polynomials (4.113) and (4.120) yields

f_2:

$$f_2 + \tilde{a}_2 = d_5 \Rightarrow f_2 = d_5 - \tilde{a}_2 \tag{4.121}$$

f_1:

$$f_1 + \tilde{a}_2 f_2 + \tilde{a}_1 = d_4 \Rightarrow f_1 = d_4 - \tilde{a}_2 f_2 - \tilde{a}_1 \tag{4.122}$$

f_0:

$$f_0 + \tilde{a}_2 f_1 + \tilde{a}_1 f_2 + \tilde{a}_0 = d_3 \Rightarrow f_0 = d_3 - \tilde{a}_2 f_1 - \tilde{a}_1 f_2 - \tilde{a}_0 \tag{4.123}$$

k_2:

$$\tilde{a}_2 f_0 + \tilde{a}_1 f_1 + \tilde{a}_0 f_2 + \tilde{b}_0 k_2 = d_2 \Rightarrow k_2 = \left(d_2 - \tilde{a}_2 f_0 - \tilde{a}_1 f_1 - \tilde{a}_0 f_2\right) / \tilde{b}_0 \tag{4.124}$$

k_1:

$$\tilde{a}_1 f_0 + \tilde{a}_0 f_1 + \tilde{b}_0 k_1 = d_1 \Rightarrow k_1 = \left(d_1 - \tilde{a}_1 f_0 - \tilde{a}_0 f_1\right) / \tilde{b}_0 \tag{4.125}$$

k_0:

$$\tilde{a}_0 f_0 + \tilde{b}_0 k_0 = d_0 \Rightarrow k_0 = \left(d_0 - \tilde{a}_0 f_0\right) / \tilde{b}_0 \tag{4.126}$$

4.7.3 Simulation and Experimental results

The OBRC's gains are determined as described in subsection 4.7.2. The LSF structures gains are found using equation (4.109) to (4.111) with $T_s = 0.1$ [sec] and the OBRCs correction loop gains are found by placing the six poles individually with a robust pole ratio of equation (4.117). A dither signal is added to the control signal to reduce the effects of the static friction as described in subsection 4.4.3. No integrator anti-windup strategy is enabled during the experiments. The OBRC is tested experimentally with three different reference

input functions as described in subsection 4.3.3. The dSPACE system is used for the experiments as explained in subsection 4.3.2.

The simulation results presented in this subsection are obtained with the full nonlinear plant model presented in section 2.5.

First, simulated and experimental responses to a step reference position change within the throttle valve stop limits are presented in Figure 4.126.

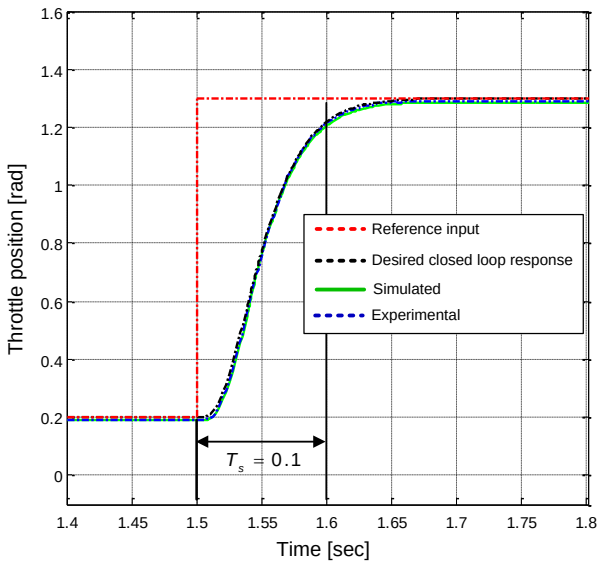

Figure 4.126: Closed loop step response, from 0.2 to 1.3 [rad]

The vertical black lines mark the nominal settling time of $T_s = 0.1$ [sec]. It is evident that both the experimental and simulated responses come close to this at ≈ 1.24 [rad].

Figure 4.127 shows the simulated and experimental closed loop responses.

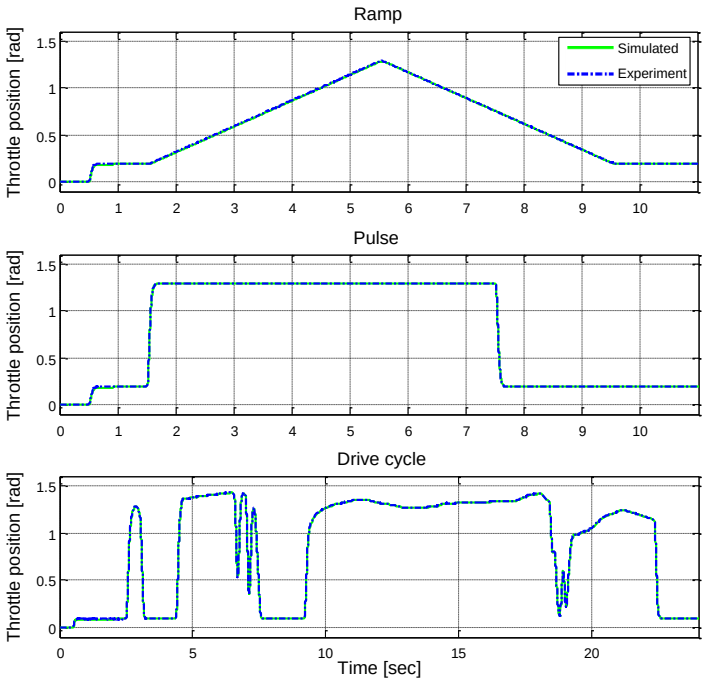

Figure 4.127: Experimental and simulated response of the OBRC

Figure 4.128 shows very small differences between the desired and the experimental closed loop responses (Figure 4.127), resulting from the robustness of this control technique.

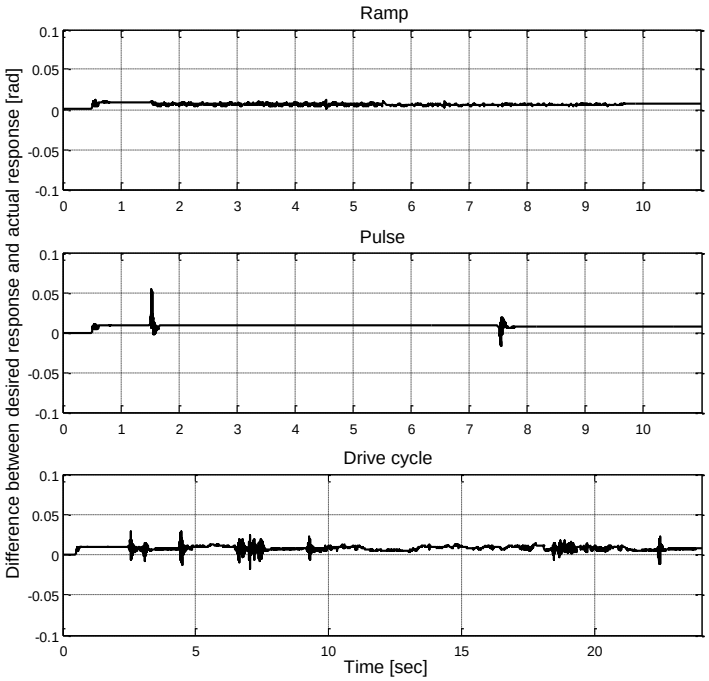

Figure 4.128: The difference between the desired and the experimental closed loop responses

As described in subsection 4.3.4.3 a spring failure can cause the engine to stall due to air starvation. The behaviour of the OBRC during a spring break, at $t = 1$ [sec], is simulated using the nonlinear throttle valve model, and the result is shown in Figure 4.129. It shows a good robustness against the disturbance, with little deviation from the throttle position demand.

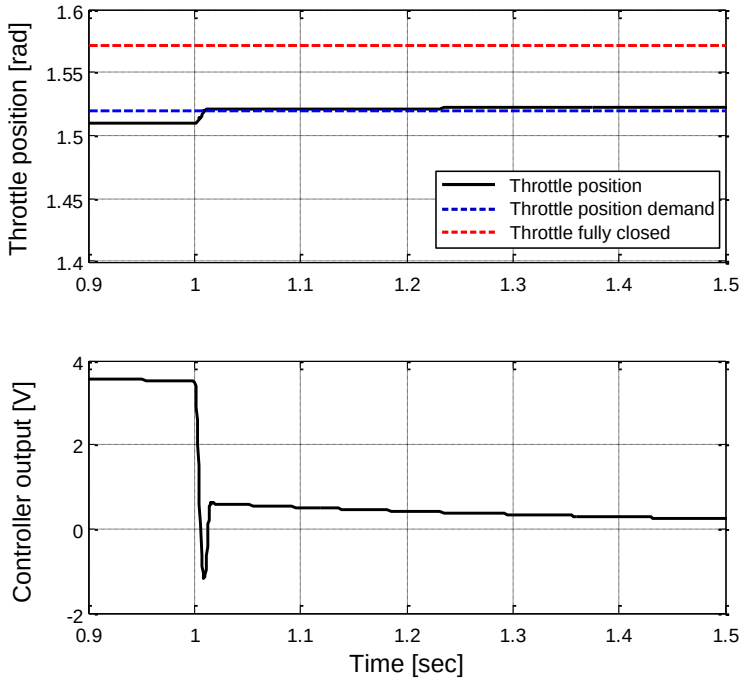

Figure 4.129: OBRC during a spring failure

The robustness against plant parameter variations away from the nominal values is tested using the Monte Carlo method described in subsection 4.3.4.2. The parameter variation simulation uses the nonlinear throttle valve model with the controller output saturation, integrator anti-windup and dither. The result of the parameter variation simulation is shown in Figure 4.130 for the maximum possible standard deviation of $\sigma = 10\%$. The figure shows the operational envelope for 1000 simulation runs, where the blue and red lines are the minimum and maximum values. The nominal parameter closed loop controller response and controller output are shown in black.

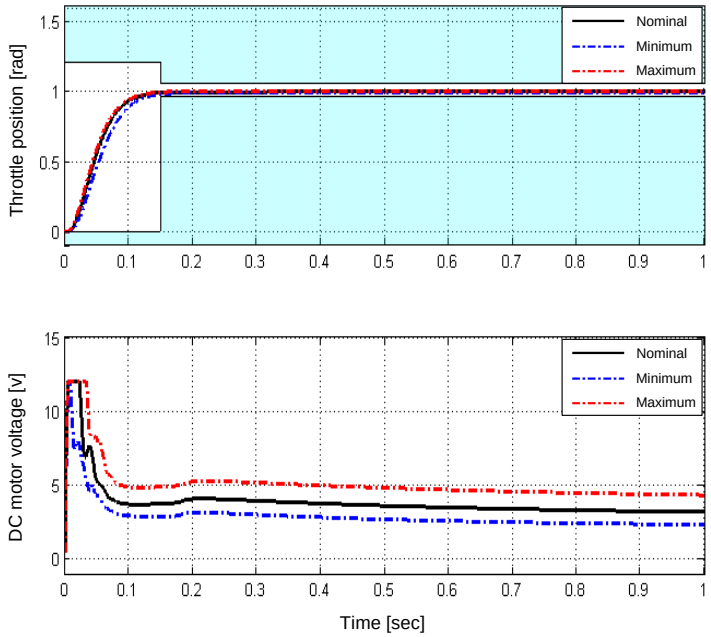

Figure 4.130: Maximum / minimum throttle position and DC motor voltage envelope (Standard deviation: $\sigma = 10\%$)

This indicates that the plant parameters can deviate significantly from the nominal values before having an adverse impact on the performance of the controller.

The sensitivity for the OBRC is analysed in the frequency domain by using the relationship of equation (4.3) in subsection 4.3.4.1. This is done with the aid of the Matlab Control System Analysis Toolbox and the block diagram of Figure 4.131 implemented in Simulink with $D(s)$ as the input and $V(s)$ as the output to obtain $S_p^C dB(\omega)$.

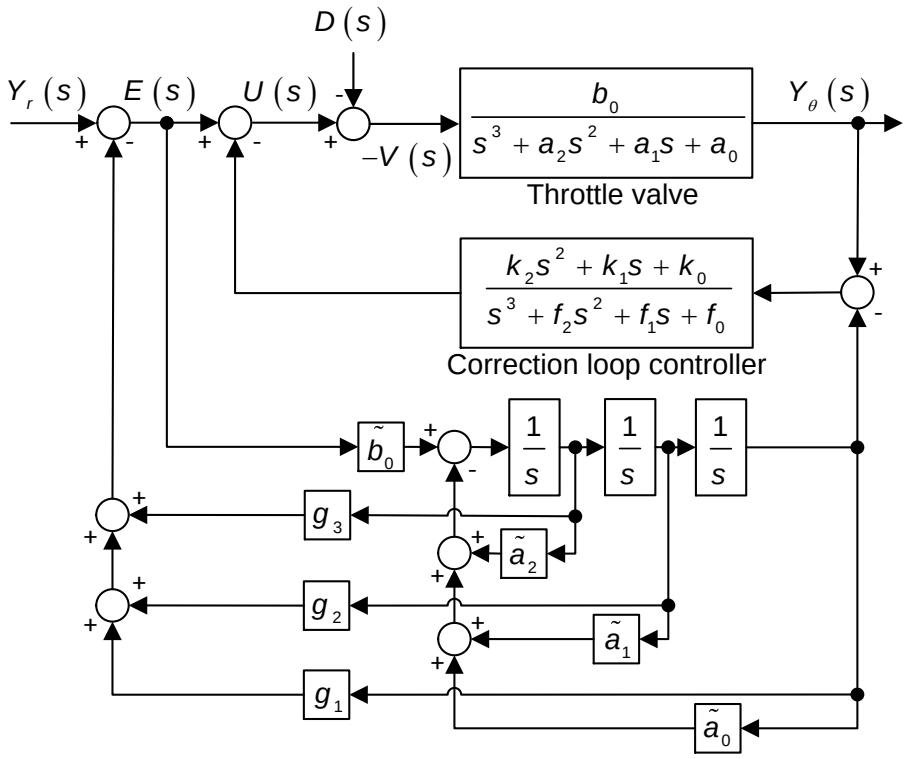

Figure 4.131: Control structure used to analyse the sensitivity

The sensitivity of the OBRC is shown in Figure 4.132. The figure indicates an average sensitivity, equivalent to average robustness. This corresponds well with the time domain result found by the above spring failure analysis and the Monte Carlo parameter variation simulation.

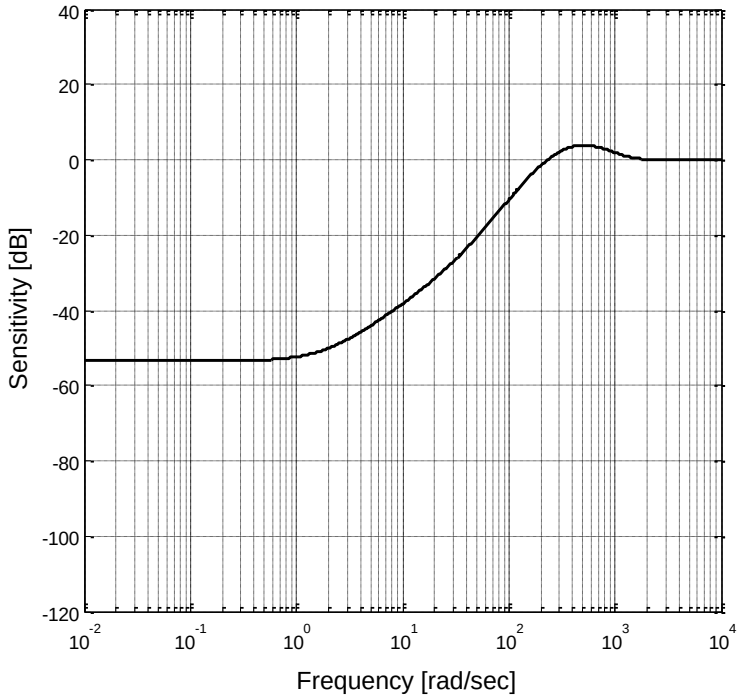

Figure 4.132: OBRC sensitivity

4.8 Polynomial Control

4.8.1 Introduction and Brief History

Any linear controller for SISO plants with two inputs, $Y_r(s)$, $Y(s)$ and one output $U(s)$ can be represented by the general transfer function relationship,

$$U(s) = G_r(s)Y_r(s) - G_y(s)Y(s) \tag{4.127}$$

This is illustrated pictorially in Figure 4.133 for a control system employing a PID controller.

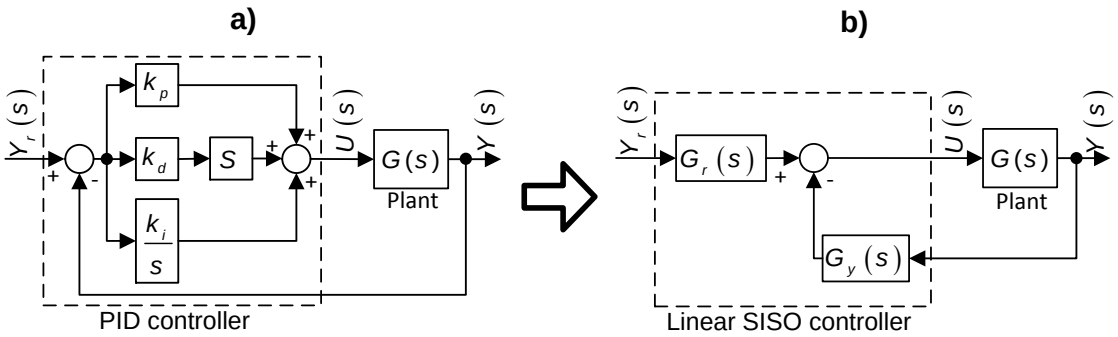

Figure 4.133: a) PID controller converted into the b) basic linear SISO controller form

Using Mason's formula on the PID control structure in Figure 4.133 a) with $G(s)$ removed,

$$U(s) = Y_r(s)\left[\frac{k_d s^2 + k_p s + k_i}{s}\right] - Y(s)\left[\frac{k_d s^2 + k_p s + k_i}{s}\right] \tag{4.128}$$

Comparing equation (4.127) and equation (4.128) then shows that the two transfer functions of the general linear SISO form are identical and given by $G_r(s) = G_y(s) = \left(k_d s^2 + k_p s + k_i\right)/s$.

The polynomial controller has a different structure to the general SISO form of Figure 4.133 but is also general in that it can represent any other linear SISO controller. Its name is due to the polynomials of its transfer functions being

shown explicitly, its design being via the choice of their coefficients. It is particularly interesting since it only requires $Y_r(s)$ and $Y(s)$ as inputs but can be designed by complete pole assignment for any linear plant if an accurate model is available. Before this, the only available linear controller with this capability was the linear state feedback controller supported by an observer that had to be designed separately.

Before proceeding further, it must be stated that the polynomial controller has precisely the same structure as the now well established RST controller, which is a digital controller formulated in the z-domain (Landau and Zito, 2006). The RST controller is already used by the process industry in a wide range of different applications. Figure 4.134 shows the block diagram of a general control system employing this controller.

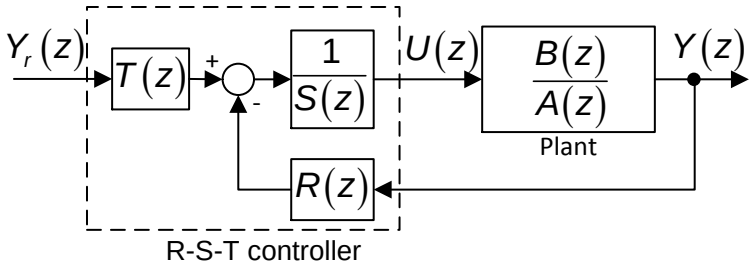

Figure 4.134: Digital R-S-T controller canonical structure

The acronym, RST, just consists of the symbols used for the polynomials of the controller. It is really a *polynomial controller* and this more descriptive title is preferred in this work, particularly as it will be considered in the s-domain.

The purposes of the components of the RST controller are as follows.

$R(z)$: Polynomial of a specific degree whose coefficients can be used for design of the controller by pole assignment.

$S(z)$: A polynomial of a certain minimum order that renders the controller realisable by ensuring that it is a causal system (i.e., its output can be calculated using present and past known values of its inputs, in contrast to future values that are unknown) and whose coefficients can also be used for design of the controller by pole assignment. This also provides a filtering function to alleviate the effects of measurement noise.

$T(z)$: Reference input polynomial that can be used to cancel the closed loop poles for dynamic lag compensation.

The transfer function relationship of the RST controller can be expressed in the form of equation (4.127), but in the z-domain, using Figure 4.134, as follows.

$$U(z) = \frac{R(z)}{S(z)} Y(z) + \frac{T(z)}{S(z)} Y_r(z) \tag{4.129}$$

It is therefore possible to realise a wide range of different controllers within the RST controller. The design procedure for determining the polynomials of the RST controller given by (Landau and Zito, 2006) is different from that developed here, which is a straightforward pole placement procedure based on the settling time formula of Dodds (2013), that applies in the continuous s-domain as well as the discrete z-domain.

4.8.2 Basic Polynomial Controller

The *Polynomial Controller* structure, shown in Figure 4.135, is identical to that of the RST controller but a different notation is used for the controller polynomials to avoid confusion with the RST controller, which is strictly formulated in the discrete time domain.

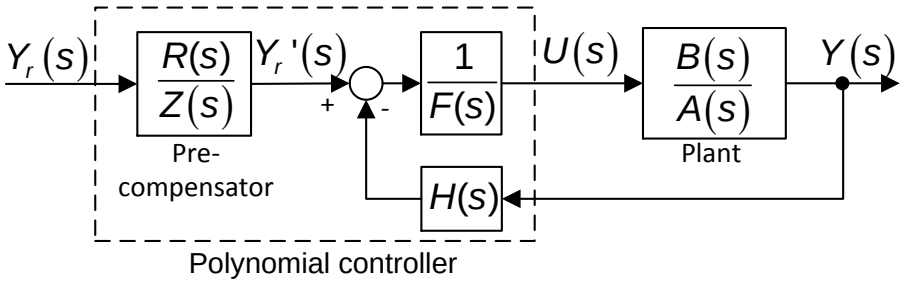

Figure 4.135: The general structure of the Polynomial control system

The polynomial controller is considered in the s-domain henceforth or the z-domain (Dodds, 2013).

The transfer function relationship of this controller is obtained from Figure 4.135 as

$$U(s) = \frac{1}{F(s)}\left[\frac{R(s)}{Z(s)}Y_r(s) - H(s)\cdot Y(s)\right] \tag{4.130}$$

The purposes of the component polynomials are similar to those already stated in subsection 4.8.1 in the z-domain for the RST controller but, in part, have different interpretations in the continuous s-domain and are therefore given again as follows.

$H(s)$: Feedback polynomial with a minimum number of coefficients equal to its degree, n_h, sufficient to enable design of the controller by complete pole placement.

$F(s)$: Filter polynomial with a minimum number of coefficients equal to its degree, n_f, that avoids having to estimate the output derivatives that would otherwise be required to implement $H(s)$, the transfer function, $1/F(s)$ also forming a low pass filter that avoids amplification of high frequency components of measurement noise that would otherwise occur due to the presence of $H(s)$.

$R(s)$: Pre-compensator numerator polynomial for cancellation of the closed loop poles, if needed, to achieve zero dynamic lag between $y_r(t)$ and $y(t)$.

$Z(s)$: Pre-compensator denominator polynomial for cancellation of any closed loop zeros, if necessary, to prevent over/under-shooting of the step response that would otherwise occur, or as part of the process of achieving zero dynamic lag, in conjunction with $R(s)$. In the throttle valve application, errors due to stick-slip friction are reduced by using short settling times, while respecting the stability limits set by the sampling time and any position sensor lag, to 'tighten' the control loop but this can cause too much throttle activity in normal operation. To overcome this problem, the short control loop settling time is maintained while the overall settling time is increased using external pole placement via $Z(s)$.

The pre-compensator polynomials may be written as

$$R(s)=\sum_{i=0}^{n_r} r_i s^i \quad \text{and} \quad Z(s)=\sum_{i=0}^{n_z} z_i s^i \tag{4.131}$$

It should be noted that to independently place all the zeros of the pre-compensator, only n_r of the n_r+1 coefficients of $R(s)$ are needed. Similarly, only n_z of the n_z+1 coefficients of $Z(s)$ are needed to independently place all the poles of the pre-compensator. To fix the DC gain, $Y(0)/Y_r(0)$, of the control system to unity, which is usual, the DC gain, $Y_r'(0)/Y_r(0)$, of the pre-compensator has to be set equal to the reciprocal of the DC gain, $Y(0)/Y_r'(0)$, of the feedback control loop. For this, one more coefficient is needed. This will be done by normalisation with respect to the coefficient of s^{n_z} in $Z(s)$, i.e.,

$$z_0 = 1 \tag{4.132}$$

Then the DC gain of the control system is r_0 .

The closed loop transfer function obtained from Figure 4.135 is

$$\frac{Y(s)}{Y_r(s)} = \frac{R(s)}{Z(s)} \frac{B(s)}{A(s)F(s)+B(s)H(s)} \tag{4.133}$$

The pole placement design of the feedback control loop, however, may be carried out independently from that of the pre-compensator and this uses its characteristic polynomial,

$$A(s)F(s)+B(s)H(s) \tag{4.134}$$

The coefficients of the polynomials,

$$H(s) = \sum_{i=0}^{n_h} h_i s^i \quad \text{and} \quad F(s) = \sum_{i=0}^{n_f} f_i s^i \tag{4.135}$$

As will be seen, $F(s)$ may be normalised with respect to the coefficient of s^{n_f} without preventing the system from being designable by complete pole placement (Dodds, 2013). Thus

$$f_{n_f} = 1 \tag{4.136}$$

are used for the pole placement.

The plant transfer function polynomial coefficients are given by

$$A(s) = \sum_{i=0}^{n_a} a_i s^i \quad \text{and} \quad B(s) = \sum_{i=0}^{n_b} b_i s^i \tag{4.137}$$

where $n_a > n_b$. No loss of generality is suffered by normalisation w.r.t. the coefficient of s^{n_a} . Hence

$$a_{n_a} = 1 \tag{4.138}$$

The order of the feedback control loop is equal to the degree of the characteristic polynomial (4.134), which is

$$N = \max\left\{\deg\left(A(s)F(s)\right), \deg\left(B(s)H(s)\right)\right\} = \max\left\{n_a + n_f, n_b + n_h\right\} \quad (4.139)$$

A system design constraint is that the degree of $H(s)$ is limited so as to avoid any algebraic loops, requiring that the relative degree of the loop transfer function is positive. By inspection of Figure 4.135, the loop transfer function is

$$L(s) = \frac{B(s)}{A(s)} . \frac{H(s)}{F(s)} \quad (4.140)$$

The relative degree is therefore

$$r = \left(n_a + n_f\right) - \left(n_b + n_h\right) \quad (4.141)$$

and since $r > 0$, it follows that

$$\left(n_a + n_f\right) > \left(n_b + n_h\right) \quad (4.142)$$

In view of equation (4.139) and inequality (4.142), the system order has to be

$$N = n_a + n_f \quad (4.143)$$

For complete pole placement to be possible, then the total number of independently adjustable controller parameters has to be equal to N. The only adjustable parameters are the $n_h + 1$ coefficients of $H(s)$ and the n_f coefficients of $F(s)$. Hence

$$n_h + n_f + 1 = N \quad (4.144)$$

In view of (4.143) and (4.144),

$$n_h + n_f + 1 = n_a + n_f \Rightarrow n_h = n_a - 1 \quad (4.145)$$

A final design constraint is that the degree of $F(s)$ needs to be sufficiently high to avoid amplification of the high frequency components of measurement noise due to the differentiating action of $H(s)$. With reference to Figure 4.135, this requires the relative degree of the transfer function, $H(s)/F(s)$, to be non-negative. Thus

$$n_f \geq n_h \quad (4.146)$$

Then from inequality (4.146) and equation (4.145),

$$n_f \geq n_h = n_a - 1 \tag{4.147}$$

Finally, to achieve a unity closed loop DC gain the coefficient r_0 of $R(s)$ can be used. The required value for r_0 can be found by setting $s = 0$ in transfer function (4.133) and then equating this to unity. Thus, recalling $z_0 = 1$ (equation (4.132),

$$K_{DC,CL} = \frac{Y(0)}{Y_r(0)} = \frac{r_0 \cdot b_0}{z_0(a_0 f_0 + b_0 h_0)} = 1 \Rightarrow r_0 = \frac{a_0 f_0 + b_0 h_0}{b_0} \tag{4.148}$$

The details of the pole placement design will be presented in subsection 4.8.4 applied to the throttle linear valve model.

4.8.3 Polynomial Control with Additional Integrator for Zero Steady State Error in the Step Response

The polynomial control in its original form will allow a steady state error to occur in the step response due to the friction of the throttle valve. This problem can be circumvented by adding an extra integrator in the forward path of the control loop, as shown in Figure 4.136.

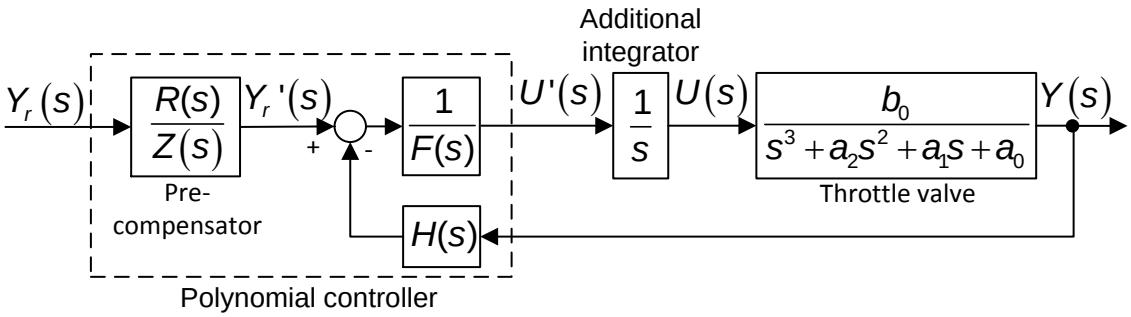

Figure 4.136: Polynomial control of throttle valve with additional integrator

It is evident from this figure that the additional integrator and the throttle valve together can be considered as the plant to control with control input, $U'(s)$, for the purpose of determining the controller polynomials. This will be referred to as

the augmented plant. Then the theory of sub-section 4.8.2 can be applied directly.

The augmented plant order is that for the throttle valve plus that of the the extra integrator, i.e., $N = 3 + 1 = 4$, the augmented plant transfer function being

$$G'(s) = \frac{Y(s)}{U(s)} = \frac{B(s)}{A(s)} = \frac{1}{s}\frac{b_0}{s^3 + a_2' s^2 + a_1' s + a_0'} = \frac{b_0}{s^4 + a_2' s^3 + a_1' s^2 + a_0' s}$$

$$= \frac{b_0}{s^4 + a_3 s^3 + a_2 s^2 + a_1 s + a_0} \tag{4.149}$$

in the standard form, where

$$a_3 = a_2', a_2 = a_1', a_1 = a_0' \text{ and } a_0 = 0 \tag{4.150}$$

4.8.4 Controller Design

4.8.4.1 Polynomial Control with Additional Integrator for Steady State Error Elimination

The design of the control system of Figure 4.136 by pole assignment will now be presented together with the results of a preliminary simulation that necessitated a change to robust pole assignment, which is explained within this subsection.

First, the degrees of the controller polynomials, $F(s)$, $H(s)$ are determined by (4.147). Thus

$$n_h = n_a - 1 = 4 - 1 = 3 \Rightarrow n_f \geq n_a - 1 = 3$$

Hence for the minimum order system, $n_f = 3$. Hence

$$\frac{1}{F(s)} = \frac{1}{s^3 + f_2 s^2 + f_1 s + f_0} \tag{4.151}$$

$$H(s) = h_3 s^3 + h_2 s^2 + h_1 s + h_0 \tag{4.152}$$

Using equation (4.148) to determine r_0 yields

$$r_0 = \left.\frac{a_0 f_0 + b_0 h_0}{b_0}\right|_{a_0=0} = h_0 \tag{4.153}$$

The details of the polynomial controller are shown in Figure 4.137.

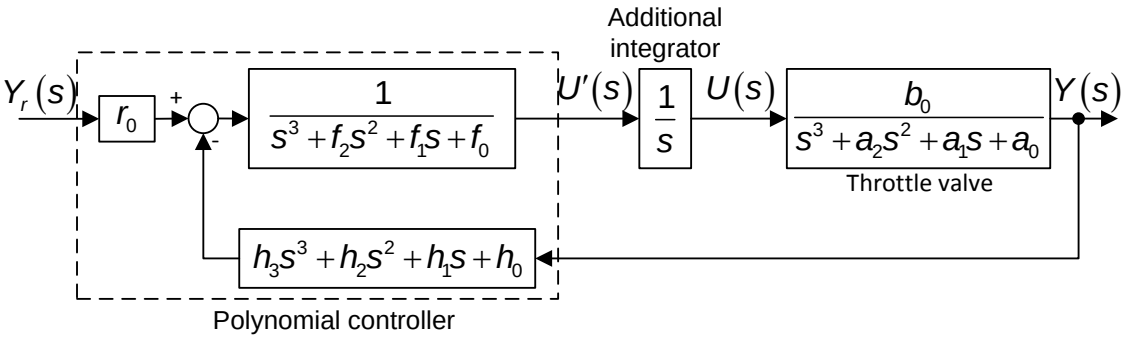

Figure 4.137: Control system of Figure 4.136 showing controller polynomials

Equating the closed loop characteristic polynomial (4.134) to the desired characteristic polynomial, which has to be of the same degree, yields

$$\begin{aligned}
&A(s)F(s) + B(s)H(s) \\
&= \left(s^4 + a_2' s^3 + a_1' s^2 + a_0' s\right)\left(s^3 + f_2 s^2 + f_1 s + f_0\right) + \left(b_0\right)\left(h_3 s^3 + h_2 s^2 + h_1 s + h_0\right) \\
&= s^7 + \left(a_2' + f_2\right)s^6 + \left(a_1' + f_2 a_2' + f_1\right)s^5 + \left(a_0' + a_1' f_2 + a_2' f_1 + f_0\right)s^4 \\
&\qquad + \left(a_0' f_2 + a_1' f_1 + a_2' f_0 + b_0 h_3\right)s^3 + \left(a_0' f_1 + a_1' f_0 + b_0 h_2\right)s^2 \\
&\qquad + \left(a_0' f_0 + b_0 h_1\right)s + b_0 h_0 \\
&= s^7 + d_6 s^6 + d_5 s^5 + d_4 s^4 + d_3 s^3 + d_2 s^2 + d_1 s + d_0
\end{aligned} \tag{4.154}$$

where d_i $i = 0,1,\ldots,6$, are the desired polynomial coefficients.

Figure 4.138 shows the structure used to implement the polynomial controller of Figure 4.137 where the controller polynomial coefficients (i.e., the controller gains) are found by first setting the desired characteristic polynomial using equation (4.154).

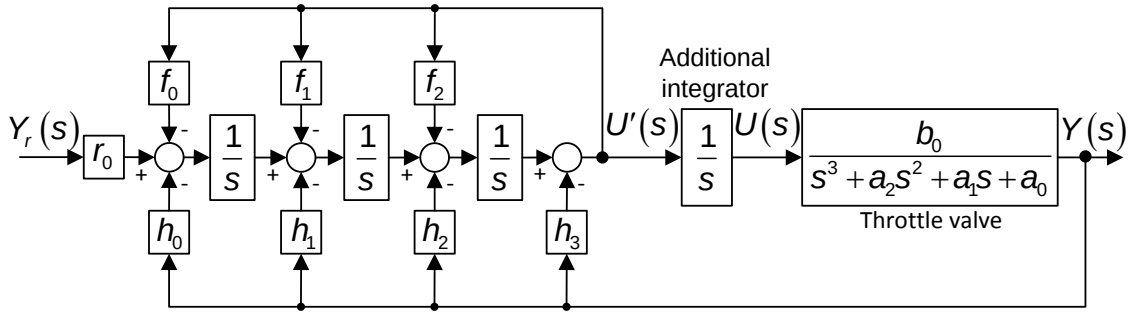

Figure 4.138: Implementation of the Polynomial control with additional integrator

Initially the pole placement was carried out using the settling time formula (5% criterion) with multiple placements of all seven poles. Then

$$\begin{aligned} & s^7 + d_6 s^6 + d_5 s^5 + d_4 s^4 + d_3 s^3 + d_2 s^2 + d_1 s + d_0 \\ & = \left(s + \frac{1.5(1+n)}{T_S} \right)^n \Bigg|_{n=7} = (s+p)^7 \\ & = s^7 + 7ps^6 + 21p^2 s^5 + 35p^3 s^4 + 35p^4 s^3 + 21p^5 s^2 + 7p^6 s + p^7 \end{aligned}$$

where $p = 12/T_s$. The desired polynomial coefficients are then

$$d_6 = 7p,\ d_5 = 21p^2,\ d_4 = 35p^3,\ d_3 = 35p^4,\ d_2 = 21p^5,\ d_1 = 7p^6 \text{ and } d_0 = p^7 \tag{4.155}$$

This worked with the linear throttle valve model in the simulation. Unfortunately, however, the system immediately saturated when substituting the nonlinear model of subsection 2.5. This was attributed to the stick-slip friction combined with the control saturation limiting. In view of the potential of robust control techniques to accommodate plant nonlinearities, the technique of robust pole assignment introduced in subsection 4.4.2.2 was applied. This entailed placing one pole with a relatively large value, implicitly introducing relatively high gains to give the robustness while the remaining poles, which dominate the closed loop dynamics, are placed coincidently using the settling time formula. The desired characteristic polynomial is then

$$D(s) = \left[s + \frac{1.5N}{T_s} \right]^{N-1} \left[s + \frac{3}{T_s / r_{pp}} \right] \tag{4.156}$$

Here, r_{pp} is the pole-to-pole dominance ratio (Dodds, 2013), which ensures that the $N-1$ poles placed using the settling time formula are dominant as well as ensuring that the single dominated pole is sufficiently large to give the system robustness. Again, this did not work correctly with the full nonlinear model of subsection 2.5, even with $r_{pp}=60$. The relevant closed loop step response simulation is shown in Figure 4.139, with $Y_r=1$ [rad]. It is evident that the controller output saturates and throttle valve hits the hard stop.

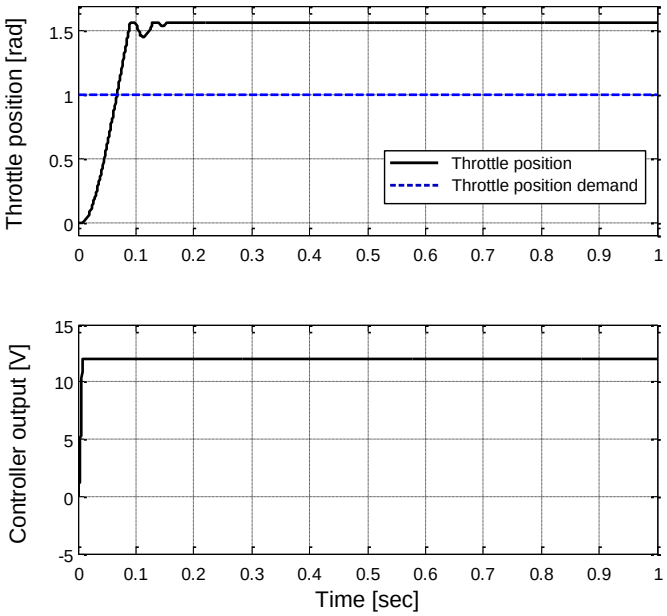

Figure 4.139: Closed loop step response with one fast pole

In a further attempt to solve the problem, the robust pole placement principle was extended to have more than one 'fast' pole, with the idea that this could produce more robustness. Here, the set of N closed loop poles are split into to two groups of n_d dominant poles and n_r robust poles. Then the n_d dominant poles are placed using the settling time formula and the n_r robust poles are linked to the dominant poles by the pole-to-pole dominance ratio r_{pp}. Then the desired closed loop characteristic polynomial is

$$D(s)=\left[s+\frac{1.5(1+n_d)}{T_s}\right]^{n_d}\left[s+\frac{1.5(1+n_r)}{T_s/r_{pp}}\right]^{n_r} \tag{4.157}$$

where $n_d+n_r=N$.

Good simulation results were obtained with $n_d=4$ and $n_r=3$, these are presented in subsection 4.8.5.1. The design equations for this case are as follows. The desired closed loop characteristic polynomial is

$$D(s)=(s+p)^4(s+q)^3 \tag{4.158}$$

where $p=7.5/T_s$ and $q=6r_{pp}/T_s$.

Hence,

$$\begin{aligned}D(s)&=\left(s^4+4ps^3+6p^2s^2+4p^3s+p^4\right)\left(s^3+3qs^2+3q^2s+q^3\right)\\&=s^7+(3q+4p)s^6+\left(6p^2+12qp+3q^2\right)s^5\\&\quad+\left(4p^3+18qp^2+12q^2p+q^3\right)s^4\\&\quad+\left(p^4+12qp^3+18q^2p^2+4q^3p\right)s^3\\&\quad+\left(3qp^4+12q^2p^3+6q^3p^2\right)s^2\\&\quad+\left(3q^2p^4+4q^3p^3\right)s+q^3p^4\end{aligned} \tag{4.159}$$

Substituting $D(s)$ in equation (4.154) using (4.159) yields the following equations for the controller polynomial coefficients.

f_2:

$$a_2+f_2=3q+4p\Rightarrow f_2=3q+4p-a_2 \tag{4.160}$$

f_1:

$$a_1+f_2a_2+f_1=6p^2+12qp+3q^2\Rightarrow f_1=6p^2+12qp+3q-a_1-f_2a_2 \tag{4.161}$$

f_0:

$$\begin{aligned}a_0+a_1f_2+a_2f_1+f_0&=4p^3+18qp^2+12q^2p+q^3\Rightarrow\\f_0&=4p^3+18qp^2+12q^2p+q^3-a_0-a_1f_2-a_2f_1\end{aligned} \tag{4.162}$$

h_3:

$$\begin{aligned} a_0 f_2 + a_1 f_1 + a_2 f_0 + b_0 h_3 &= p^4 + 12qp^3 + 18q^2 p^2 + 4q^3 p \Rightarrow \\ h_3 &= \left(p^4 + 12qp^3 + 18q^2 p^2 + 4q^3 p - a_0 f_2 - a_1 f_1 - a_2 f_0 \right) / b_0 \end{aligned} \tag{4.163}$$

h_2:

$$\begin{aligned} a_0 f_1 + a_1 f_0 + b_0 h_2 &= 3qp^4 + 12q^2 p^3 + 6q^3 p^2 \Rightarrow \\ h_2 &= \left(3qp^4 + 12q^2 p^3 + 6q^3 p^2 - a_0 f_1 - a_1 f_0 \right) / b_0 \end{aligned} \tag{4.164}$$

h_1:

$$a_0 f_0 + b_0 h_1 = 3q^2 p^4 + 4q^3 p^3 \Rightarrow h_1 = \left(3q^2 p^4 + 4q^3 p^3 - a_0 f_0 \right) / b_0 \tag{4.165}$$

h_0:

$$b_0 h_0 = q^3 p^4 \Rightarrow h_0 = \left(q^3 p^4 \right) / b_0 \tag{4.166}$$

r_0:

$$r_0 = h_0 \tag{4.167}$$

4.8.4.2 Reduced Order Polynomial Control with Additional Integrator for Steady State Error Elimination

In this subsection, a polynomial controller is designed using the reduced order throttle valve model from subsection 2.6, equation (2.42). It will be recalled that this was obtained by removing the armature inductance resulting in a second order model. As in subsection 4.8.4.1, an additional integrator is inserted at the plant input for the purpose of avoiding a steady state error in the step response. The complete control system block diagram is shown in Figure 4.140.

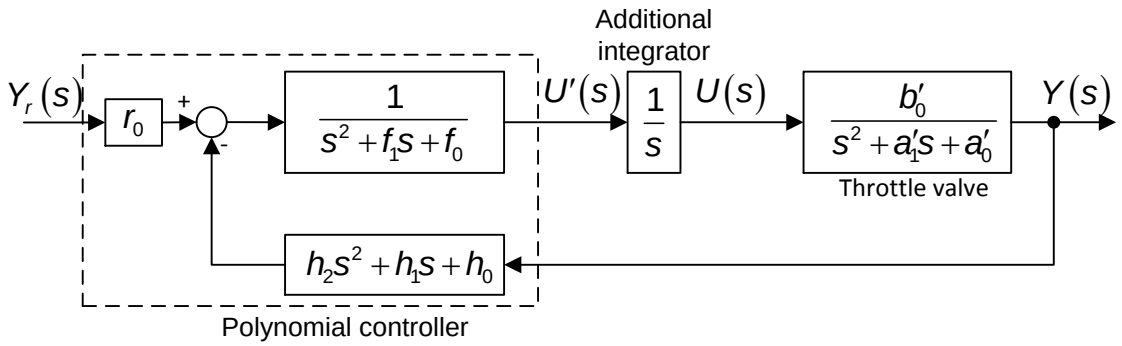

Figure 4.140: Polynomial control with additional integrator and a second order plant model used for the controller design

Following the same procedure as in subsection 4.8.4.1, the closed loop characteristic polynomial, $A(s)F(s)+B(s)H(s)$ is equated to the desired characteristic polynomial, $D(s)$, to yield

$$\begin{aligned}&\left(s^3+a_1's^2+a_0's\right)\left(s^2+f_1s+f_0\right)+\left(b_0\right)\left(h_2s^2+h_1s+h_0\right)\\&=s^5+\left(f_1+a_1'\right)s^4+\left(f_0+a_1'f_1+a_0'\right)s^3+\left(a_1'f_0+a_0'f_1+b_0h_2\right)s^2\\&\qquad+\left(a_0'f_0+b_0h_1\right)s+b_0h_0\\&=s^5+d_4s^4+d_3s^3+d_2s^2+d_1s+d_0\end{aligned}\tag{4.168}$$

where d_i $i=0,1,\ldots,4$, are the desired polynomial coefficients.

Good simulation results were obtained using the desired closed loop characteristic polynomial given by (4.157) for the robust pole placement with $n_d=3$ and $n_r=2$. These are presented in subsection 4.8.5.2. The design equations for this case are as follows. The desired closed loop characteristic polynomial is

$$D(s)=\left(s+p\right)^3\left(s+q\right)^2\tag{4.169}$$

where $p=6/T_s$ and $q=4.5r_{pp}/T_s$.

Hence,

$$\begin{aligned} D(s) &= \left(s^3 + 3ps^2 + 3p^2 s + p^3\right)\left(s^2 + 2qs + q^2\right) \\ &= s^5 + (2q + 3p)s^4 + \left(3p^2 + 6qp + q^2\right)s^3 \\ &\quad + \left(p^3 + 6qp^2 + 3q^2 p\right)s^2 + \left(3p^2 q^2 + 2qp^3\right)s + q^2 p^3 \end{aligned} \tag{4.170}$$

Substituting $D(s)$ in equation (4.168) using (4.170) yields the following equations for the controller polynomial coefficients.

f_1:

$$f_1 + a_1' = 2q + 3p \Rightarrow f_1 = 2q + 3p - a_1' \tag{4.171}$$

f_0:

$$\begin{aligned} f_0 + a_1' f_1 + a_0' &= 3p^2 + 6qp + q^2 \Rightarrow \\ f_0 &= 3p^2 + 6qp + q^2 - a_1' f_1 - a_0' \end{aligned} \tag{4.172}$$

h_2:

$$\begin{aligned} a_1' f_0 + a_0' f_1 + b_0 h_2 &= p^3 + 6qp^2 + 3q^2 p \Rightarrow \\ h_2 &= \left(p^3 + 6qp^2 + 3q^2 p - a_1' f_0 - a_0' f_1\right) / b_0 \end{aligned} \tag{4.173}$$

h_1:

$$a_0' f_0 + b_0 h_1 = 3p^2 q^2 + 2qp^3 \Rightarrow h_1 = \left(3p^2 q^2 + 2qp^3 - a_0' f_0\right) / b_0 \tag{4.174}$$

h_0:

$$b_0 h_0 = q^2 p^3 \Rightarrow h_0 = \left(q^2 p^3\right) / b_0 \tag{4.175}$$

r_0:

$$r_0 = h_0 \tag{4.176}$$

4.8.4.3 Obtaining Larger Settling Times using the Precompensator

Figure 4.141 shows the results of an investigation by simulation of attempting to increase the settling time through values likely to be specified by users of the control system.

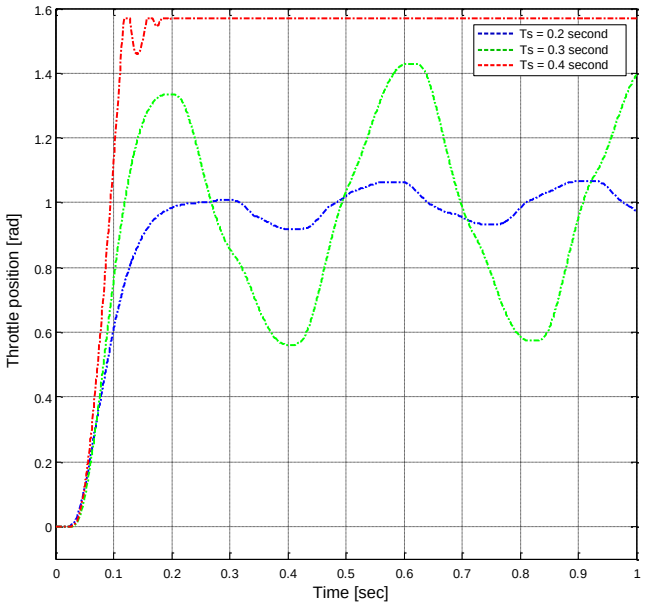

Figure 4.141: Simulated closed loop response step response at $T_s = \{0.2 \quad 0.3 \quad 0.4\}$ [sec]

As is evident, if a settling time longer than 0.1 second is required, the gains of the control loop are insufficient to produce enough actuator torque to overcome the static friction resulting in limit cycle oscillations. These increase in amplitude as T_s is increased because a larger position error is needed to generate the minimum torque needed to produce movement. In the extreme, for $T_s = 0.4$ sec., the theoretical limit cycle amplitude exceeds the end stop limits so no limit cycle can occur, the system instead staying at the limit. This problem can be circumvented by introducing a precompensator with a dominant pole placed to yield the required settling time, having previously designed the polynomial control loop to have a sufficiently short settling time and associated high gains to overcome the static friction.

The polynomial control loop was designed using robust pole placement as described in subsection 4.8.4.1. The specified settling time is now that of the

precompensator which will be denoted by T_{sp}. Then the polynomial control loop settling time (not now realised by the actual system) is set to a value shorter than the minimum needed to overcome the static friction problem. Setting $T_s = T_{sp}/5$ was found to be sufficient.

The precompensator is designed using settling time formula (4.12) with $n = 1$. Thus

$$\frac{R(s)}{Z(s)} = \frac{Y_r'(s)}{Y_r(s)} = \frac{\frac{3}{T_{sp}}}{s + \frac{3}{T_{sp}}} \tag{4.177}$$

Figure 4.142 shows a closed loop step response simulation of the polynomial controller and the nonlinear throttle valve model, using a precompensator with $T_{sp} = \{0.2 \quad 0.3 \quad 0.4\}$, noting that, for comparison purposes, they are the same as the values of T_s set to produce the results of Figure 4.141.

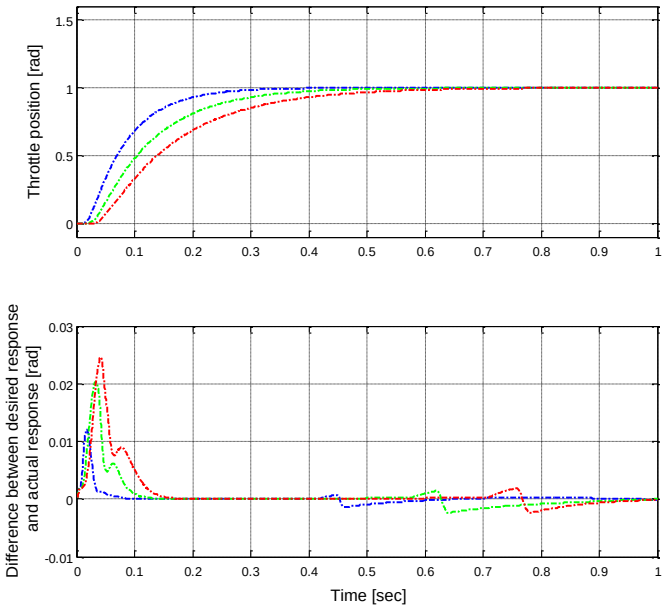

Figure 4.142: Simulated closed loop response step response using a precompensator with the settling time $T_{sp} = \{0.2 \quad 0.3 \quad 0.4\}$ sec

It is evident that satisfactory performance has now been achieved.

4.8.5 Simulation and Experimental results

4.8.5.1 Polynomial Control with Additional Integrator for Steady State Error Elimination

The polynomial controller gains are determined as described in subsection 4.8.4.1, equation (4.160) to (4.167) with $T_s = 0.1$ [sec], two groups of poles, $n_p = 4$ and $n_q = 3$, and a robust pole-to-pole ratio of 40. A dither signal is added to the control signal to reduce the effects of the static friction as described in subsection 4.4.3. The integrator anti-windup strategy is enabled to minimise the saturation during the step reference input. The polynomial controller is tested experimentally with three different reference input functions as described in subsection 4.3.3. The dSPACE system is used for the experiments as explained in subsection 4.3.2.

The simulation results presented in this subsection are obtained with the full nonlinear plant model presented in section 2.5.

First, simulated and experimental responses to a step reference position change within the throttle valve stop limits are presented in Figure 4.143.

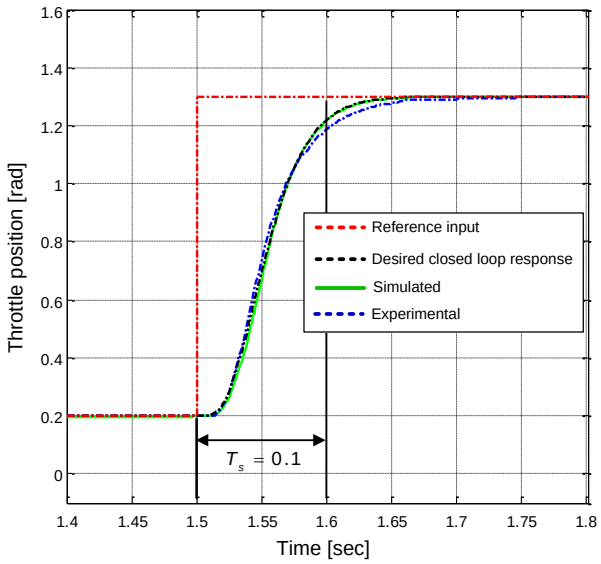

Figure 4.143: Closed loop step response, from 0.2 to 1.3 [rad]

The vertical black lines mark the nominal settling time of $T_s = 0.1\,[\text{sec}]$. It is evident that both the experimental and simulated responses come close to this at ≈ 1.24 [rad].

Figure 4.144 shows the simulated and experimental closed loop responses.

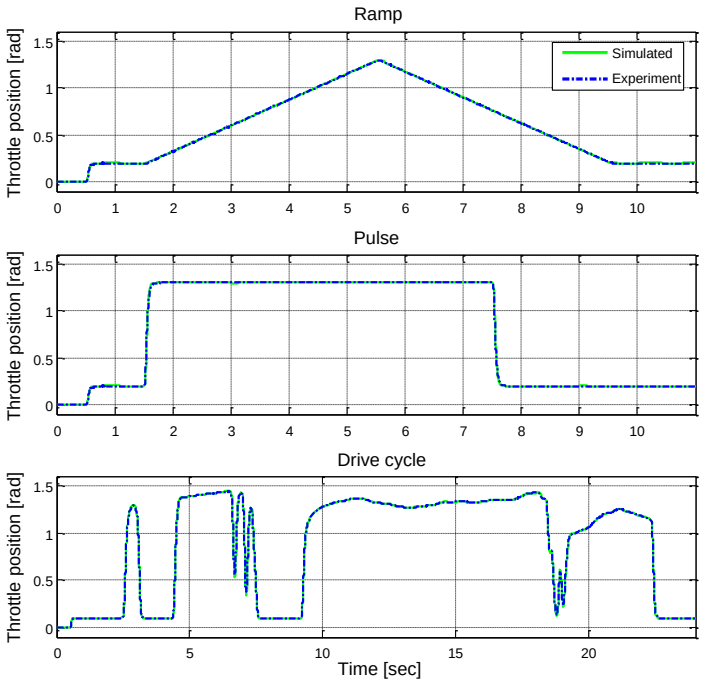

Figure 4.144: Experimental and simulated response of the polynomial controller

Figure 4.145 shows very small differences between the desired and the experimental closed loop responses (Figure 4.144), which is attributed to the robust pole placement.

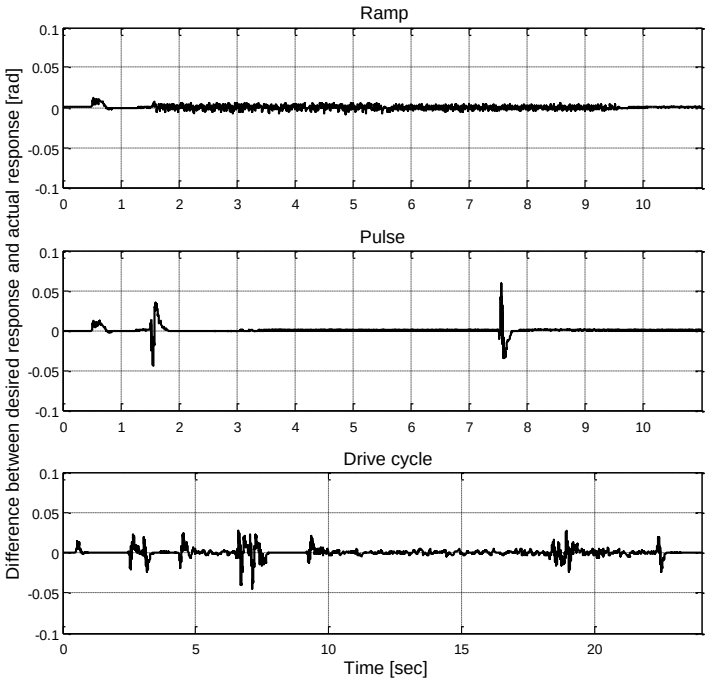

Figure 4.145: The difference between the desired and the experimental closed loop responses

As described in subsection 4.3.4.3 a spring failure can cause the engine to stall due to air starvation. The behaviour of the polynomial controller during a spring break, at $t = 1$ [sec], is simulated using the nonlinear throttle valve model, and the result is shown in Figure 4.146. It shows a good robustness against the disturbance, with little deviation from the throttle position demand.

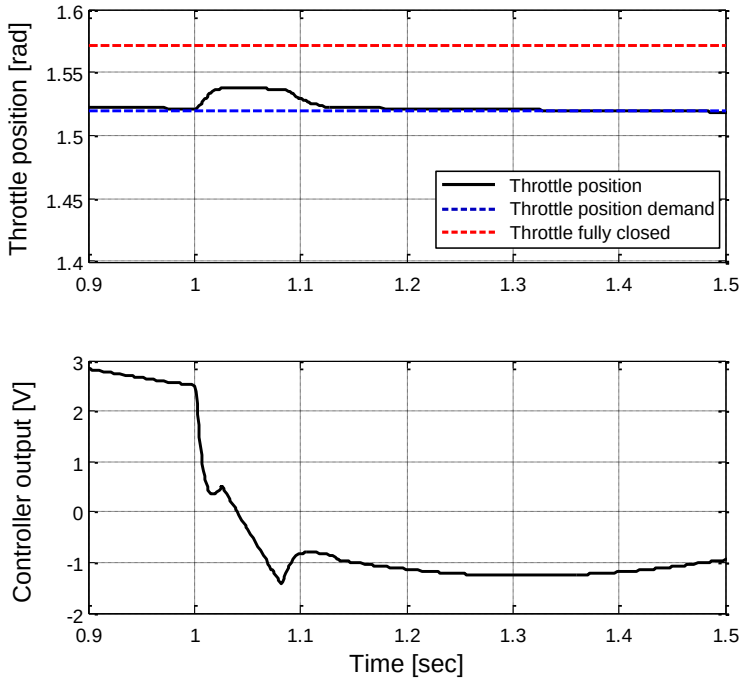

Figure 4.146: Polynomial controller during a spring failure

The robustness against plant parameter variations away from the nominal values is tested using the Monte Carlo method described in subsection 4.3.4.2. The parameter variation simulation uses the nonlinear throttle valve model with the controller output saturation, integrator anti-windup and dither. The polynomial controller's gains are designed using a robust pole-to-pole ration of 40. The result of the parameter variation simulation is shown in Figure 4.147 for the maximum possible standard deviation of $\sigma = 14\%$. The figure shows the operational envelope for 1000 simulation runs, where the blue and red lines are the minimum and maximum values. The nominal parameter closed loop controller response and controller output are shown in black.

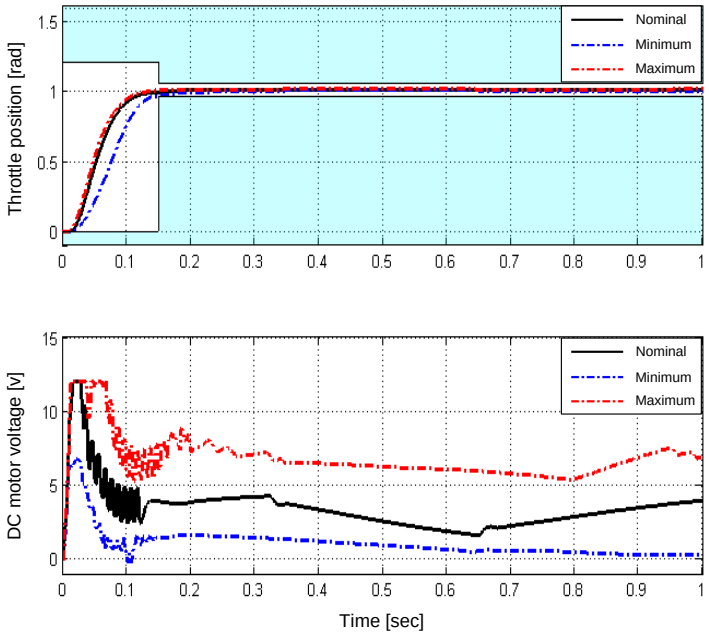

Figure 4.147: Maximum / minimum throttle position and DC motor voltage envelope at a pole group ratio = 40 (Standard deviation: $\sigma = 14\%$)

This indicates that the plant parameters can deviate significantly from the nominal values before having an adverse impact on the performance of the controller.

The sensitivity for the implemented polynomial controller is analysed in the frequency domain by using the relationship of equation (4.3) in subsection 4.3.4.1. This is done with the aid of the Matlab Control System Analysis Toolbox and the block diagram of Figure 4.148 implemented in Simulink with $D(s)$ as the input and $V(s)$ as the output to obtain $S_p^C dB(\omega)$.

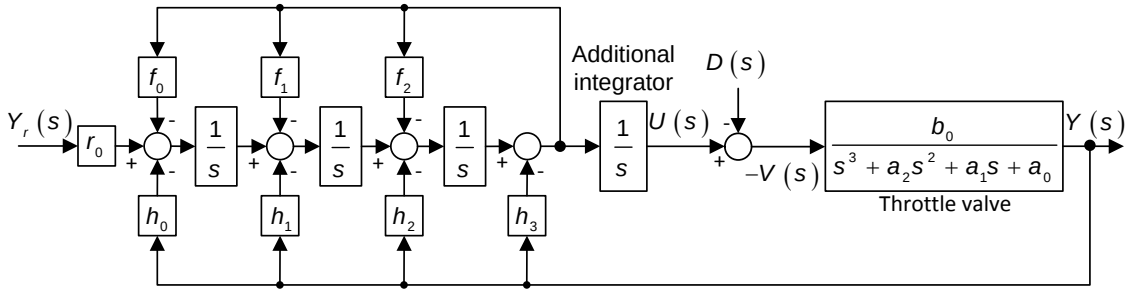

Figure 4.148: Control structure used to analyse the external disturbance sensitivity

The sensitivity result is shown in Figure 4.149.

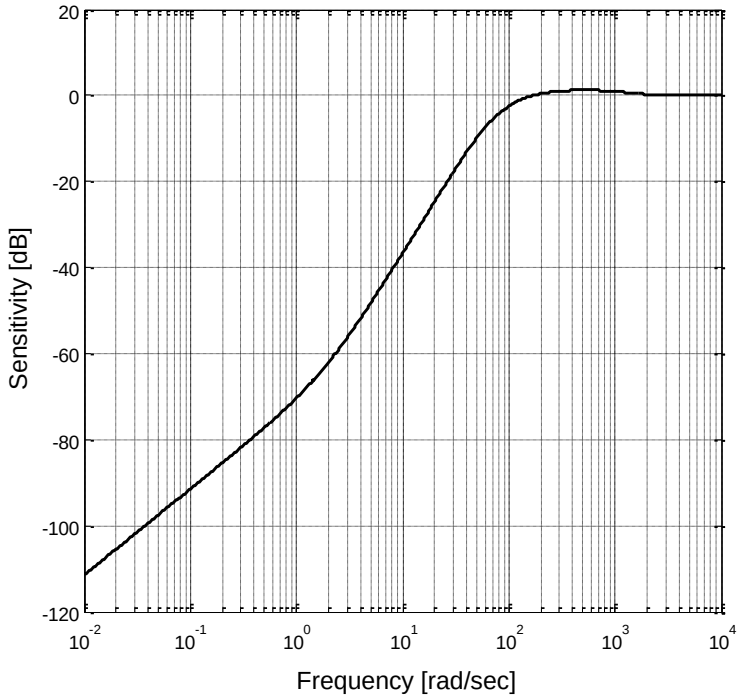

Figure 4.149: Polynomial control sensitivity

This indicates a relatively low sensitivity, equivalent to high robustness. This corresponds well with the time domain result found by the above spring failure analysis and the Monte Carlo parameter variation simulation.

4.8.5.2 Reduced Order Polynomial Control with Additional Integrator for Steady State Error Elimination

Figure 4.150 shows the implementation version of the polynomial controller of Figure 4.140 applied to the non-reduced third order throttle valve model to test the ability of the simpler controller designed using the reduced order model.

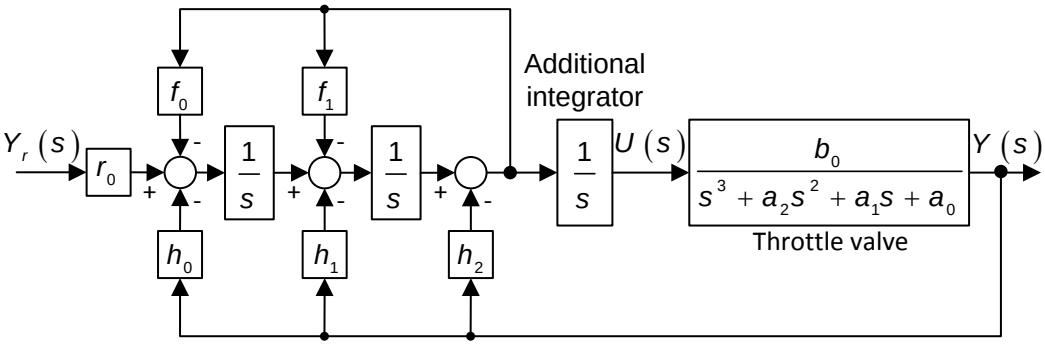

Figure 4.150: Implementation of the Polynomial control with additional integrator

The polynomial controller gains are determined as described in subsection 4.8.4.2, equation (4.171) to (4.176) with $T_s = 0.1$ [sec], two groups of poles, $n_p = 3$ and $n_q = 2$, and a robust pole-to-pole ratio of 60. A dither signal is added to the control signal to reduce the effects of the static friction as described in subsection 4.4.3. The integrator anti-windup strategy is enabled to minimise the saturation during the step reference input. The polynomial controller is tested experimentally with three different reference input functions as described in subsection 4.3.3. The dSPACE system is used for the experiments as explained in subsection 4.3.2.

The simulation results presented in this subsection are obtained with the full nonlinear plant model presented in section 2.5.

First, simulated and experimental responses to a step reference position change within the throttle valve stop limits are presented in Figure 4.151.

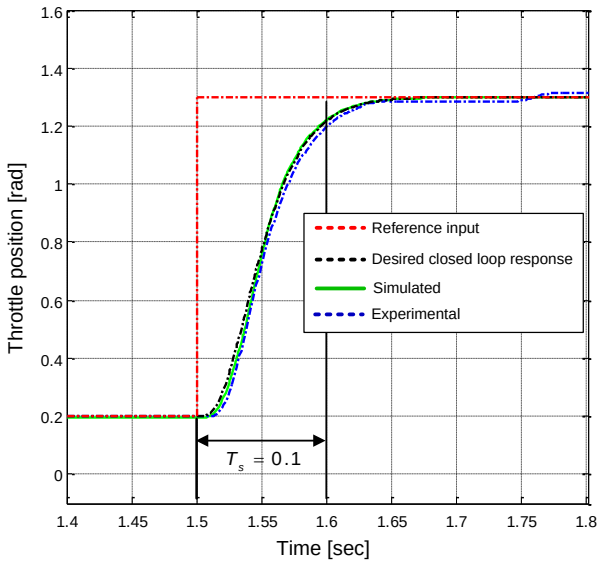

Figure 4.151: Closed loop step response, from 0.2 to 1.3 [rad]

The vertical black lines mark the nominal settling time of $T_s = 0.1\,[\text{sec}]$. It is evident that both the experimental and simulated responses come close to this at ≈ 1.24 [rad].

Figure 4.152 shows the simulated and experimental closed loop responses.

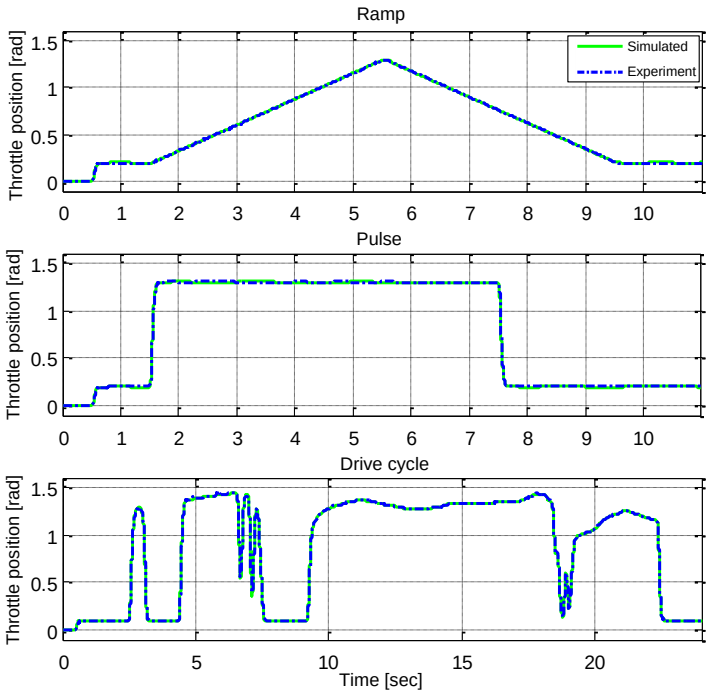

Figure 4.152: Experimental and simulated response of the polynomial controller

Figure 4.153 shows very small differences between the desired and the experimental closed loop responses (Figure 4.152), which is attributed to the robust pole placement.

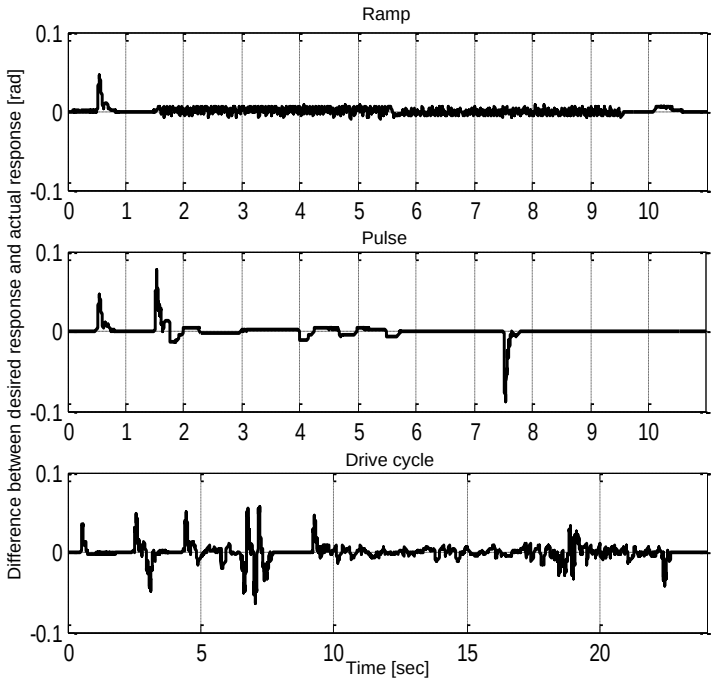

Figure 4.153: The difference between the desired and the experimental closed loop responses

As described in subsection 4.3.4.3 a spring failure can cause the engine to stall due to air starvation. The behaviour of the LSF controller during a spring break, at $t = 1$ [sec], is simulated using the nonlinear throttle valve model, and the result is shown in Figure 4.154. It shows a good robustness against the disturbance, with little deviation from the throttle position demand. The oscillations on the control signal at $t = 1.02$ [sec] are the added dither signal that increases in amplitude when the control error, $y_r - y$, exceeds a preset threshold of 1% of the full scale movement range as described in subsection 4.4.3.

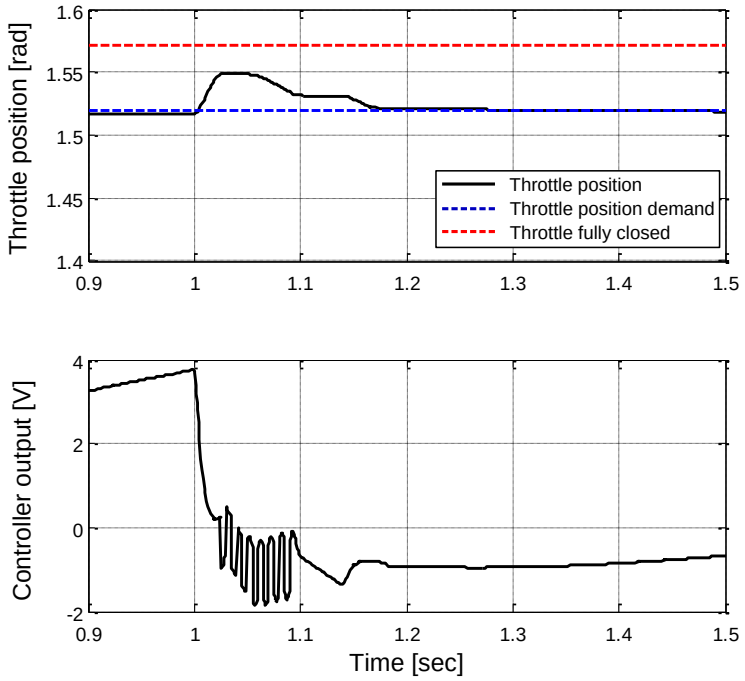

Figure 4.154: Polynomial controller during a spring failure

The robustness against plant parameter variations away from the nominal values is tested using the Monte Carlo method described in subsection 4.3.4.2. The parameter variation simulation uses the nonlinear throttle valve model with the controller output saturation, integrator anti-windup and dither. The polynomial controller's gains are designed using a robust pole-to-pole ration of 60. The result of the parameter variation simulation is shown in Figure 4.155 for the maximum possible standard deviation of $\sigma = 15\%$. The figure shows the operational envelope for 1000 simulation runs, where the blue and red lines are the minimum and maximum values. The nominal parameter closed loop controller response and controller output are shown in black.

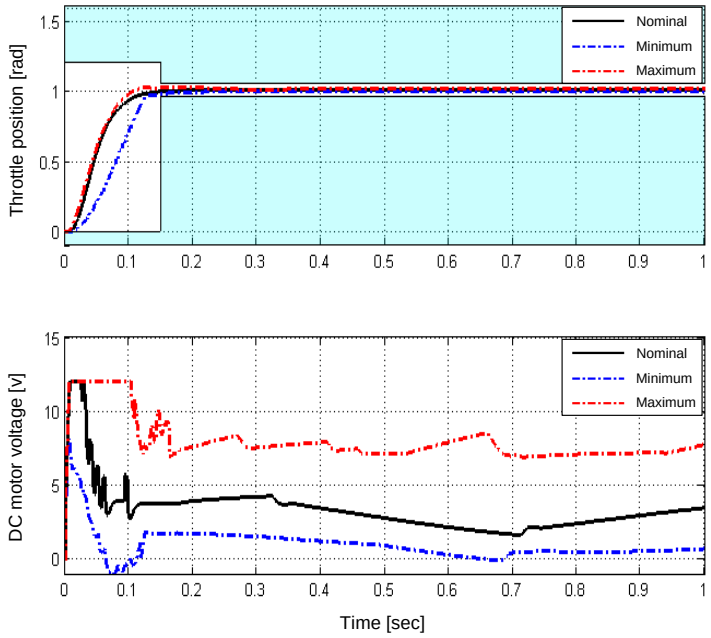

Figure 4.155: Maximum / minimum throttle position and DC motor voltage envelope at a pole group ratio = 60 (Standard deviation: $\sigma = 15\%$)

This indicates that the plant parameters can deviate significantly from the nominal values before having an adverse impact on the performance of the controller.

The sensitivity for the polynomial controller is analysed in the frequency domain by using the relationship of equation (4.3) in subsection 4.3.4.1. This is done with the aid of the Matlab Control System Analysis Toolbox and the block diagram of Figure 4.156 implemented in Simulink with $D(s)$ as the input and $V(s)$ as the output to obtain $S_p^C dB(\omega)$.

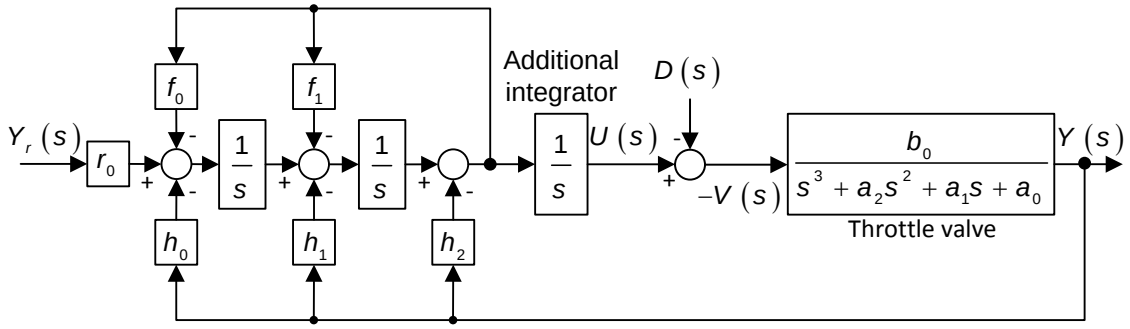

Figure 4.156: Control structure used to analyse the external disturbance sensitivity

The sensitivity result is shown in Figure 4.157

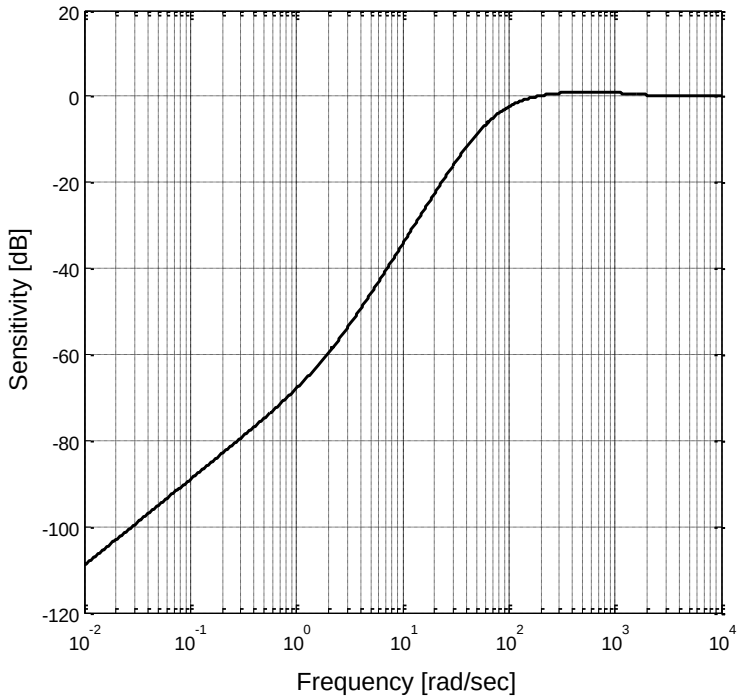

Figure 4.157: Polynomial control sensitivity

This indicates a relatively low sensitivity, equivalent to high robustness. This corresponds well with the time domain result found by the above spring failure analysis and the Monte Carlo parameter variation simulation.

4.8.5.3 Obtaining Larger Settling Times using the Precompensator

The polynomial controller gains are determined as described in subsection 4.8.4.1, equation (4.160) to (4.167) with $T_s = T_{sp}/5$ [sec], two groups of poles, $n_p = 4$ and $n_q = 3$, a robust pole-to-pole ratio of 16 and a precompensator with a settling time $T_{sp} = 0.2$ [sec]. A dither signal is added to the control signal to reduce the effects of the static friction as described in subsection 4.4.3. The integrator anti-windup strategy is enabled to minimise the saturation during the step reference input. The polynomial controller is tested experimentally with three different reference input functions as described in subsection 4.3.3. The dSPACE system is used for the experiments as explained in subsection 4.3.2.

The simulation results presented in this subsection are obtained with the full nonlinear plant model presented in section 2.5.

First, simulated and experimental responses to a step reference position change within the throttle valve stop limits are presented in Figure 4.158.

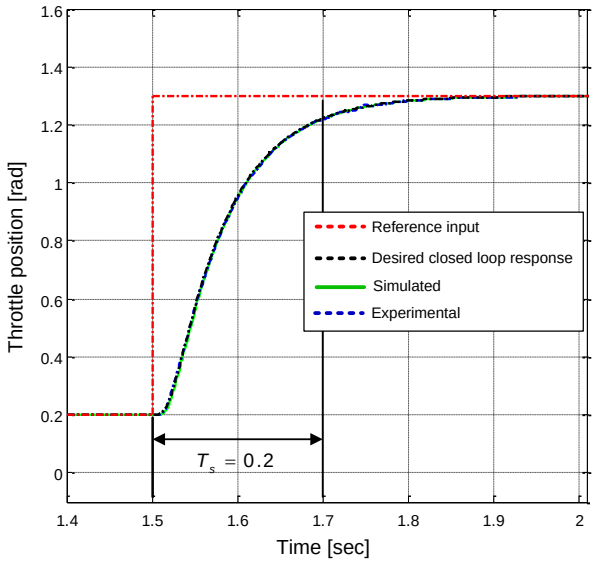

Figure 4.158: Closed loop step response, from 0.2 to 1.3 [rad]

The vertical black lines mark the nominal settling time of $T_s = 0.2$ [sec]. It is evident that both the experimental and simulated responses come close to this at ≈ 1.24 [rad].

Figure 4.159 shows the simulated and experimental closed loop responses.

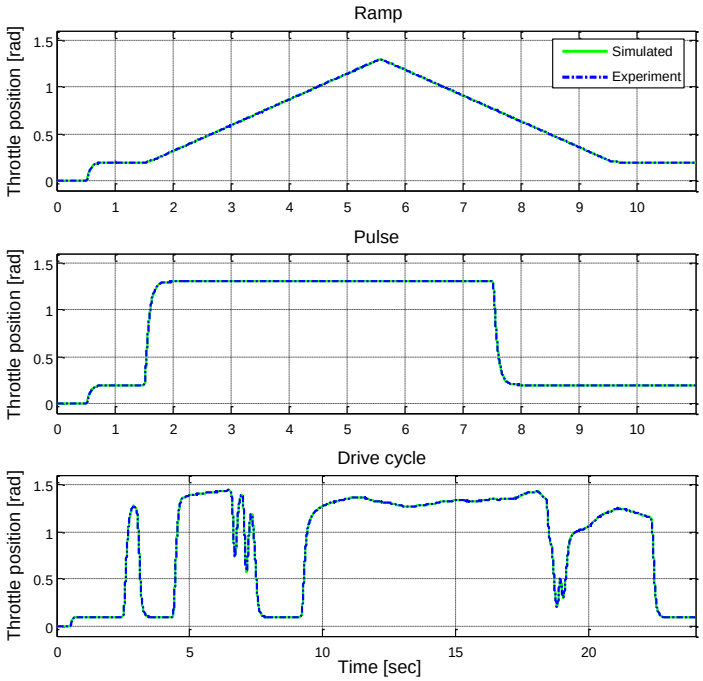

Figure 4.159: Experimental and simulated response of the polynomial controller

Figure 4.160 shows small differences between the desired and the experimental closed loop responses (Figure 4.159), which, again, attributed to the robust pole placement.

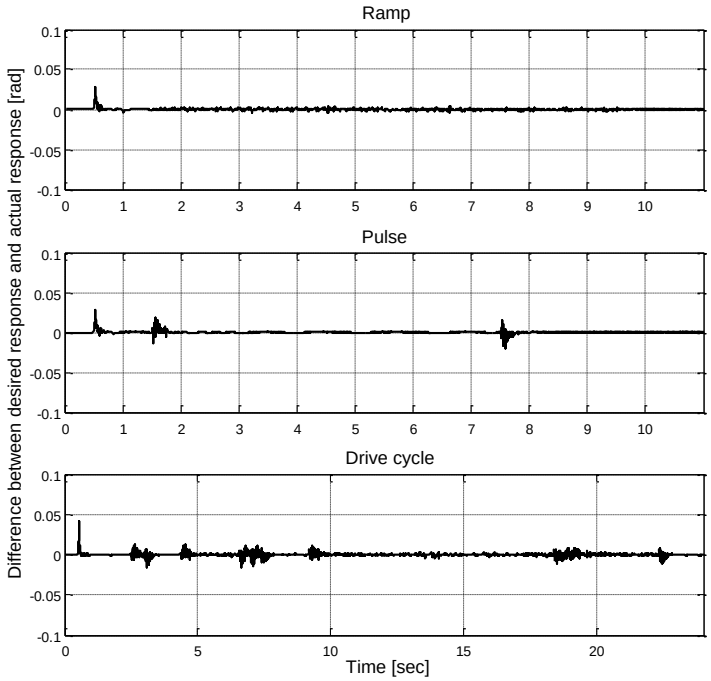

Figure 4.160: The difference between the desired and the experimental closed loop responses

As described in subsection 4.3.4.3 a spring failure can cause the engine to stall due to air starvation. The behaviour of the polynomial controller during a spring break, at $t = 1$ [sec], is simulated using the nonlinear throttle valve model, and the result is shown in Figure 4.161. It shows a good robustness against the disturbance, with little deviation from the throttle position demand.

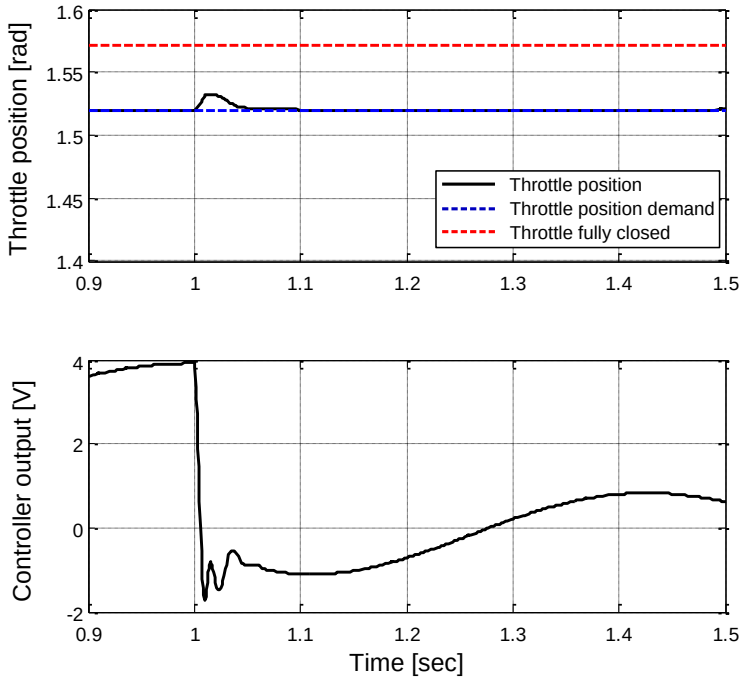

Figure 4.161: Polynomial controller during a spring failure

The robustness against plant parameter variations away from the nominal values is tested using the Monte Carlo method described in subsection 4.3.4.2. The parameter variation simulation uses the nonlinear throttle valve model with the controller output saturation, integrator anti-windup and dither. The polynomial controller's gains are designed using a robust pole-to-pole ration of 16. The result of the parameter variation simulation is shown in Figure 4.162 for the maximum possible standard deviation of $\sigma = 11\%$. The figure shows the operational envelope for 1000 simulation runs, where the blue and red lines are the minimum and maximum values. The nominal parameter closed loop controller response and controller output are shown in black.

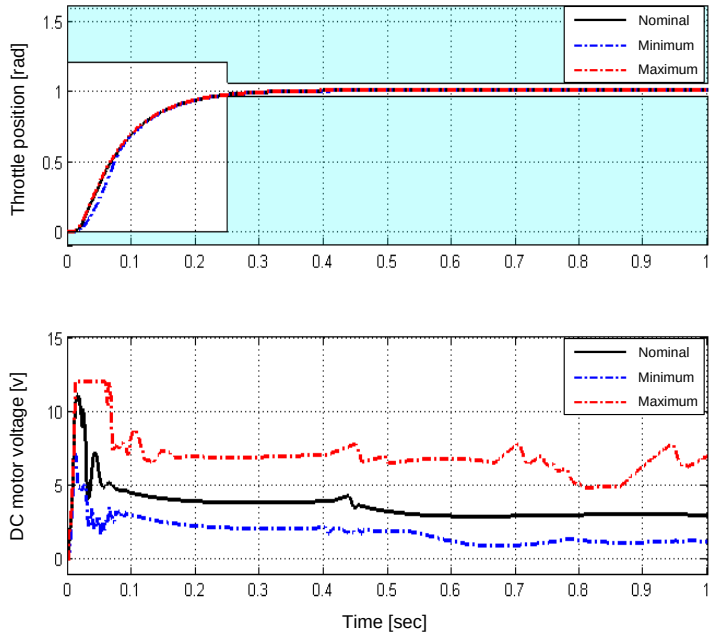

Figure 4.162: Maximum / minimum throttle position and DC motor voltage envelope at a $T_s = 0.2$ sec and a pole group ratio = 16 (Standard deviation: $\sigma = 11\%$)

This indicates that the plant parameters can deviate significantly from the nominal values before having an adverse impact on the performance of the controller.

4.9 Sliding Mode Control and its Relatives

4.9.1 Introduction and Brief History

Variable Structure Control (VSC) systems were introduced by Emelyanov among others in 1960s, but only in Russian. The VSC is a form of a discontinuous nonlinear controller in which, effectively, the control variable of the plant is switched between the outputs of two controllers connected permanently to the plant measurement variables, as shown in Figure 4.163.

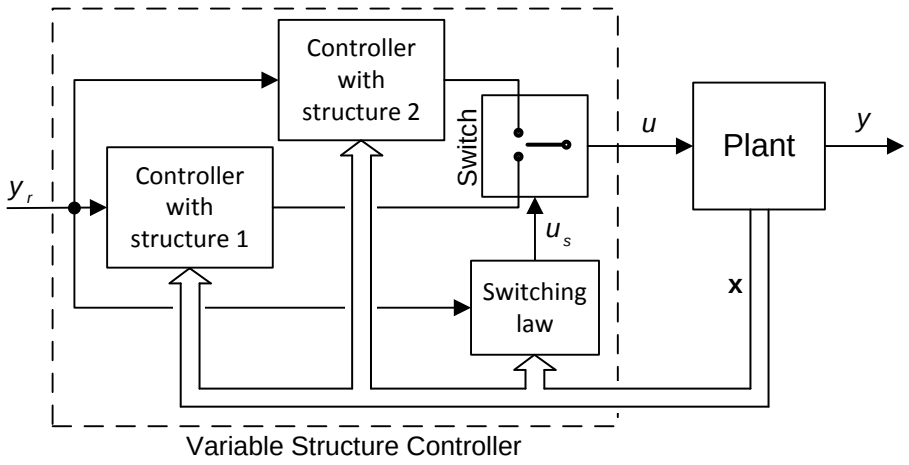

Figure 4.163: A basic variable structure control system

The purpose of such a controller is to achieve robustness with respect to plant parametric uncertainties and external disturbances, i.e., the dynamic response of $y(t)$ to $y_r(t)$ is as intended in the control system design and is not significantly influenced by unknown plant parameter changes and external disturbances. Whether or not this is attained depends upon the state representation, the only suitable one being

$$\mathbf{x}^{\mathrm{T}} = k\left[\, y \quad \dot{y} \quad \ddot{y} \quad \cdots \quad y^{(r-1)} \,\right] \tag{4.178}$$

where r is the relative degree of the plant and k is a known constant. For a linear plant with transfer function, $\frac{y(s)}{u(s)} = \frac{N(s)}{D(s)}$, $r = \deg\left[D(s)\right] - \deg\left[N(s)\right]$. In more general terms, and in the time domain, which applies to nonlinear as well as linear plants, r is the lowest order derivative of $y(t)$ that depends algebraically on $u(t)$, in the sense that a step change in $u(t)$ causes a step change in $y^{(r)}(t)$ at the same instant.

The intended operational mode of the VSC system is the sliding mode. The switching law in Figure 4.163 is of the form

$$u(t) = -\text{sgn}\left[S(\mathbf{x}, y_r)\right] \tag{4.179}$$

The basic control objective is to drive $S(\mathbf{x}, y_r)$ to zero and then maintain this condition. The equation

$$S(\mathbf{x}, y_r) = 0 \tag{4.180}$$

defines a switching boundary of dimension, $n-1$, in the n-dimensional state space for a SISO plant. In the literature (Utkin et al., 1999) the term, *switching manifold*, is frequently used, which refers to several concurrent switching boundaries, one for each control variable of a multivariable plant. Since the research undertaken here is restricted to SISO plants, the term, *switching boundary* will be used. If the state trajectories, $\mathbf{x}^+(t)$ for $u = +u_{\max}$ and $\mathbf{x}^-(t)$ for $u = -u_{\max}$, under switching law equation (4.179) are directed towards the boundary equation (4.180) from both sides in a finite region on the boundary including the point where the state trajectory first meets the switching boundary, then after this event, the control, $u(t)$, will switch at a high frequency and with a varying mark-space ratio so as to hold the state point on the boundary. Generally, the state point is free to move in the boundary. The manner in which it moves depends on the closed loop system differential equation, which is determined by equation (4.180). If $S(\mathbf{x}, y_r)$ is designed correctly, then the state

will converge to a point at which $y = y_r$ and the behaviour of $y(t)$ during this convergence will be as desired. Since during this convergence, the state point appears to slide in the boundary, then the system is defined to be operating in a *sliding mode*. Specifically, if the state representation is according to equation (4.178) then the closed loop differential equation determined by equation (4.180) becomes

$$S\left(y,\dot{y},\ddot{y},\ldots,y^{(r-1)},y_r\right)=0\,. \tag{4.181}$$

In the 1970's a book from Itkis (Referenced in (Spurgeon and Edwards, 1998)) and a paper (Utkin, 1977) was published in English investigating the Sliding Mode Control (SMC). Since then a variety of publications have emerged; Books (Spurgeon and Edwards, 1998), (Sabanovic et al., 2004), (Dodds, 2013), and in particular one paper should be mentioned 'A Control Engineer's Guide to Sliding Mode Control' (Utkin et al., 1999) which contain many good references.

4.9.2 Basic Sliding Mode Control

The classic double integrator plant is used as an example for the introduction to sliding mode control:

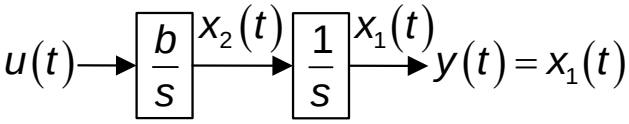

Figure 4.164: Double integrator plant

where $u(t)$ is the input to the plant and x_1, x_2 are the two states.

The dynamics are

$$\dot{x}_1(t)=x_2(t) \tag{4.182}$$

$$\dot{x}_2(t)=b\cdot u(t) \tag{4.183}$$

To visualise the solution for the double integrator plant the two state variables can be plotted against each other in a two dimensional space called the *state plane*, in this case referred to as the *phase plane,* as one state variable is the derivative of the other. The solution can be found by forming the state trajectory differential equation, dividing equation (4.182) by (4.183)

$$\frac{\dot{x}_2(t)}{\dot{x}_1(t)} = \frac{dx_2 / dt}{dx_1 / dt} = \frac{b \cdot u(t)}{x_2(t)} \Rightarrow$$
$$\frac{dx_2}{dx_1} = \frac{b \cdot u(t)}{x_2(t)} \tag{4.184}$$

If $u(t)$ is assumed constant, a solution can be found by integrating equation (4.184)

$$\int x_2 \cdot dx_2 = \int b \cdot u(t) \cdot dx_1 \Rightarrow$$
$$x_2^2(t) = 2 \cdot b \cdot x_1(t) \cdot u(t) + c \tag{4.185}$$

where c is a constant.

The above solution indicates that a parabolic shape will form for different values of c, and dependent on the sign of u the parabola will be open to the right or left.

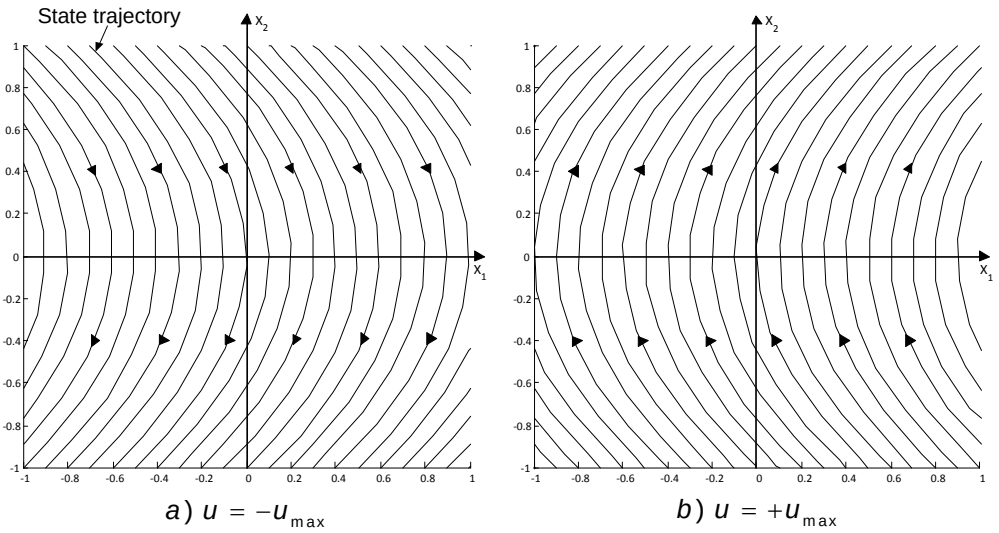

Figure 4.165: Phase portraits for a double integrator plant with $b = 1$

Figure 4.165 shows a simulation of the double integrator plant's differential equations in Matlab for $u = +u_{\max}$ and $u = -u_{\max}$, with different initial values of the state x_1.

To apply a Bang-Bang controller to the double integrator plant the control law has to be designed in such a way that it forces the closed loop system to have an equilibrium at $x_1, x_2 = (0,0)$ for $x_r = x_{1,ref} = 0$. Looking at Figure 4.165 (a) or (b) shows no sign of the plant coming to rest at $x_1, x_2 = (0,0)$ for which $u = \pm u_{\max}$, indicating that closed loop control is needed. In sliding mode control, the first step is to form a bang-bang state control law for which $u = \pm u_{\max}$, as shown in Figure 4.166.

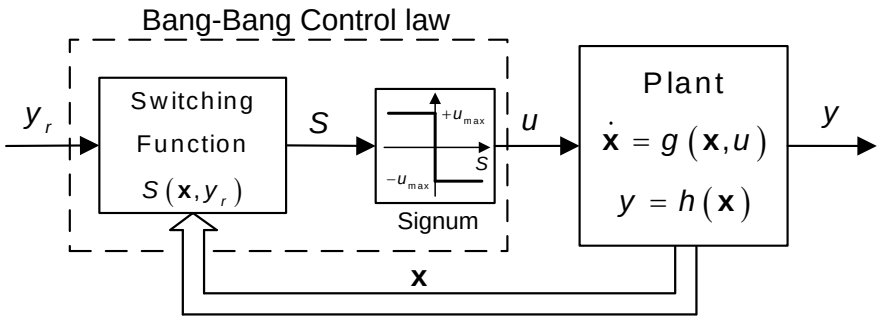

Figure 4.166: Block diagram of a Bang-Bang controller for a SISO plant

The linear switching function for a SISO plant is

$$S(\mathbf{x}, y_r) = w_1(x_1 - y_r) + w_2 \cdot x_2 + \ldots + w_n \cdot x_n \qquad (4.186)$$

where

$\mathbf{x}$: Plant states

w : Constants

n : Number of plant states

In the basic SMC a signum function is used to represent the switching of u. Thus

$$u = -u_{\max} \cdot \operatorname{sgn}\left[S\left(x_1, x_2, y_r\right) \right] \tag{4.187}$$

where

$$\operatorname{sgn}(S) = \begin{cases} +1 & \text{for } S > 0, \\ 0 & \text{for } S = 0, \\ -1 & \text{for } S < 0 \end{cases} \tag{4.188}$$

The signum function can be regarded as a high gain in view of its infinite slope at the origin as shown in Figure 4.166, which will make the control strategy very robust against parameter variations and disturbances, such as the failing spring in a throttle valve.

The switching function for the double integrator plant is

$$S\left(x_1, x_2, y_r\right) = w_1\left(x_1 - y_r\right) + w_2 \cdot x_2 \tag{4.189}$$

Figure 4.167 shows a *closed loop phase portrait* using this switching function with $y_r = x_r = 0$ and a slope of -1. The plot is done with different initial states $\left(x_1, x_2\right)$, to show how they move towards the set point at the origin.

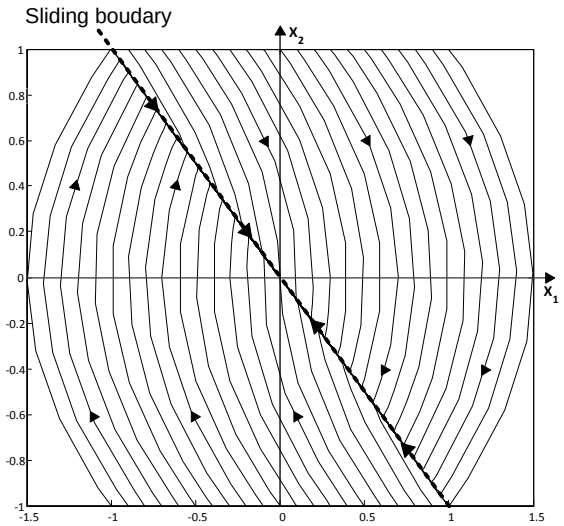

Figure 4.167: Closed loop phase portrait of a double integrator plant for $w_1, w_2 = 1$

Figure 4.168 shows the bang-bang controller output $u(t)$ and the plant's states $x_1(t)$, $x_2(t)$ as a function of time with the initial condition, $x_1(0) = x_2(0) = -1$.

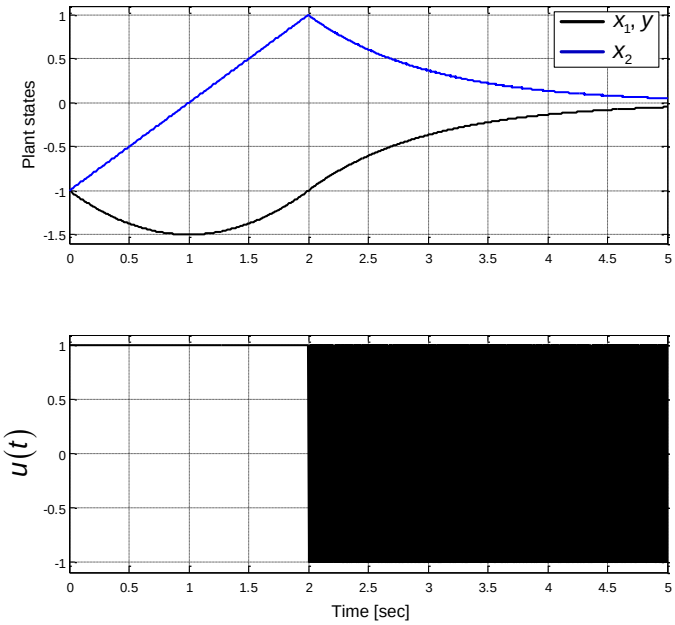

Figure 4.168: Closed loop response and bang-bang controller output of a double integrator plant

In Figure 4.169 one trajectory is shown to visualise the different states the Bang-Bang controller goes through with the same initial conditions as Figure 4.168. The initial condition for the system is at P1 (at time = 0 [sec]) where $u = +u_{\max}$ making the states move towards the positive part of x_2. There will be no change in the controllers output from P1 till P2. When the trajectory reaches the point P2 (at time = 2 [sec]) it enters the boundary layer and the controllers output will switch to $u = -u_{\max}$. After point P2 is reached, the controller will switch u at an infinite frequency, *in theory*, with a continuously varying mark-space ratio to keep the plant states on the switching boundary. This will, in this case, move the states towards the centre of the phase portrait (for $y_r = 0$).

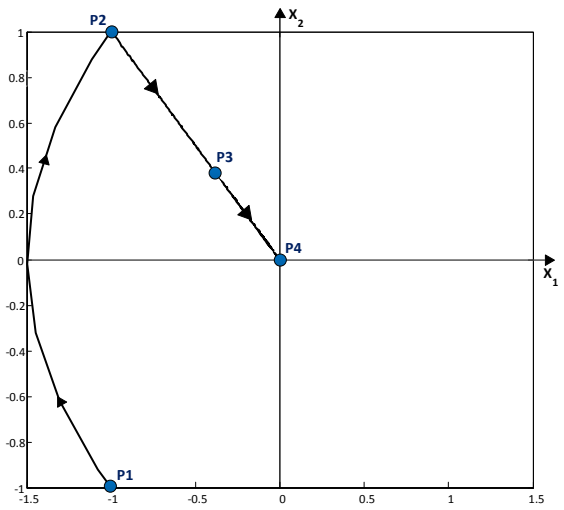

Figure 4.169: An example of a trajectory for the double integrator plant.

When the system states (x_1, x_2) are on switching boundary segment between P2 and P4 (which could be referred to as the sliding boundary in view of the system behaviour), the system will be governed by equation (4.189)

$$w_1\left(x(t) - y_r(t)\right) + w_2 \cdot \dot{x}(t) = 0 \;\Rightarrow\; \dot{x}(t) = \frac{1}{T_c}\left(x(t) - y_r(t)\right) \qquad (4.190)$$

where $T_c = w_2 / w_1$ and y_r is the set point.

The closed loop system is only of order of one while the plant order is two. This is due to the fact that the SMC forces the state to stay on the switching boundary, thereby removing one degree of freedom of motion in the state space. In general, if the plant order is n, the closed loop system will be of order $n-1$.

The general linear switching function is

$$S(y_r, x_n) = w_1(x_1 - y_r) + w_2 \cdot x_2 + w_3 \cdot x_3 + ... + w_n \cdot x_n \qquad (4.191)$$

The basic aim of any controller is to control the output of the plant, $y(t)$, to match the reference input $y_r(t)$. This is not generally hard to achieve but the additional aim here is to attain a prescribed closed loop dynamic response such as specified settling time and zero overshoot. If the state representation of the plant model upon which the controller design is based is such that the output $y(t)$ depends on the states, $x_1, x_2 ..... x_n$, via plant parameters. A change in these plant parameters can cause a difference in the responses to changes in the reference input and possibly violate the control system performance specification. This point is illustrated in Figure 4.170.

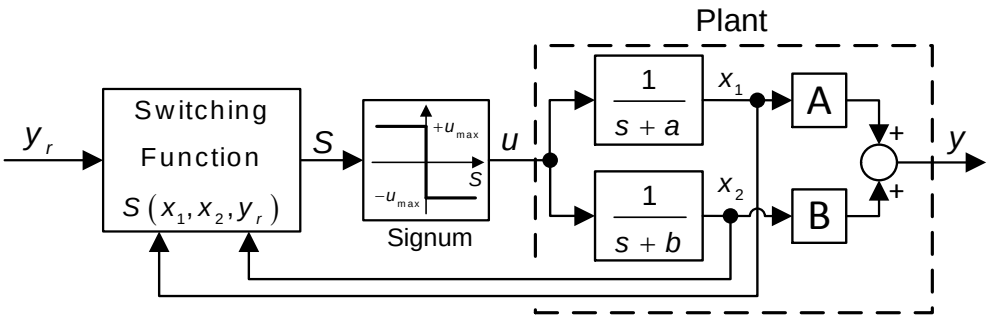

Figure 4.170: Plant output not directly linked to the plant states

Suppose $y_r(t)$ is sufficiently slowly varying for sliding motion to be maintained. Despite this, if the plant parameters, A or B, change, then the response of $y(t)$

to a given $y_r(t)$ will change, thereby defeating the object of achieving robustness. To circumvent this issue the state representation of equation (4.178) can be used, in which the states consist of the plant output, $y(t)$, and its derivatives. Replacing the states in equation (4.191) with these derivatives yields

$$S(y_r, \mathbf{y}) = w_1 \cdot (y - y_r) + w_2 \cdot \dot{y} + w_3 \cdot \ddot{y} + ... + w_n \cdot y^{n-1} \tag{4.192}$$

The order of the sliding boundary is $n-1$ which makes one of the gains in equation (4.192) redundant. Hence dividing equation (4.192) with w_1 yields

$$S(y_r, \mathbf{y}) = (y - y_r) + \frac{w_2}{w_1}\dot{y} + \frac{w_3}{w_1}\ddot{y} + ... + \frac{w_n}{w_1}y^{n-1} \tag{4.193}$$

and therefore the constants are redefined as follows.

$$S(y_r, \mathbf{y}) = (y - y_r) + w_1 \cdot \dot{y} + w_2 \cdot \ddot{y} + ... + w_{n-1} \cdot y^{n-1} \tag{4.194}$$

Note that the order, n, is used in equation (4.194) rather than the relative degree, r, since the plant considered in this research programme. i.e., the throttle valve, has no finite zeros in the transfer function.

The '*Equivalent Control Method*' described in (Spurgeon and Edwards, 1998) (Trivedi and Bandyopadhyay, 2010, Xinghuo et al., 2008), can be used to analyse the behaviour of the system when it is on, or close to the sliding manifold (line segment between P2 and P4 in Figure 4.169). It describes the continuous fictitious control variable, $u_{eq}(t)$, that is equivalent to the rapidly switching actual control output, $u(t)$, in the sense that it would keep the state trajectory in the switching boundary. It is, in fact, the short term average value of

the rapidly switching physical control, whose form is useful in analysing the system behaviour. The algebraic solution for $u_{eq}(t)$ is found by assuming that the states are on the switching boundary by setting the switching function $S = 0$, implying $\dot{S} = 0$. For a linear SISO plant

$$\dot{\mathbf{x}} = A \cdot \mathbf{x} + B \cdot u \tag{4.195}$$

where u is the control input and $\mathbf{x}$ are the states of the plant. For $y_r(t) = 0$ the switching boundary is

$$S(\mathbf{x}) = w_1 \cdot x_1 + w_2 \cdot x_2 + w_3 \cdot x_3 + ... + w_n \cdot x_n = \mathbf{w}^T \cdot \mathbf{x} = 0 \tag{4.196}$$

Hence

$$\begin{aligned} \dot{S} &= 0 \\ \mathbf{w}^T \cdot \dot{\mathbf{x}} &= 0 \\ \mathbf{w}^T \left[A\mathbf{x} + Bu \right] &= 0 \\ u_{eq} &= -\left[\mathbf{w}^T \cdot B \right]^{-1} \mathbf{w}^T A\mathbf{x} \end{aligned} \tag{4.197}$$

Figure 4.171 shows again the simulation of Figure 4.168 but with $u(t)$ replaced by $u_{eq}(t)$. The value $u_{filtered}(t)$ is a low pass filtered version of $u(t)$ which is used to check the correctness of $u_{eq}(t)$.

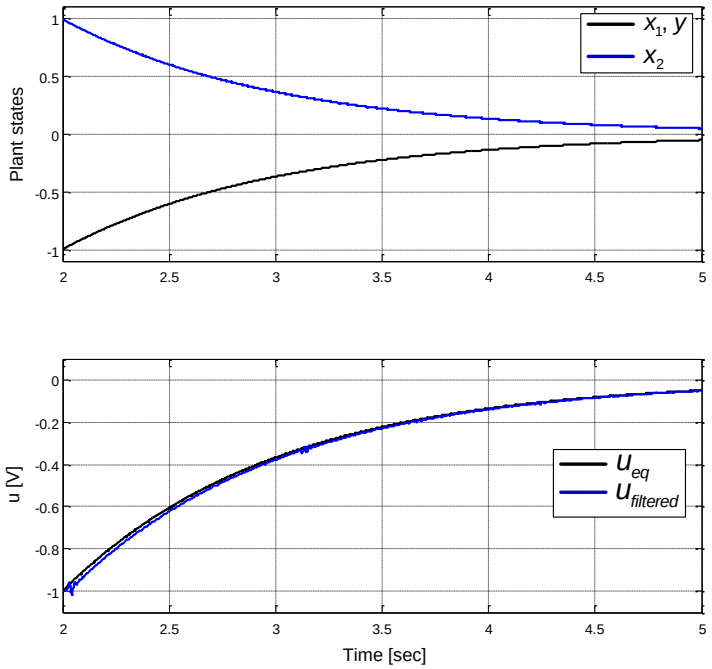

Figure 4.171: Display of equivalent control for simulation of Figure 4.168.

4.9.3 Methods for Eliminating or Reducing the Effects of Control Chatter

Two methods of control chattering elimination are presented here with the throttle valve as the plant. Figure 4.172 shows the basic sliding mode control system as a starting point.

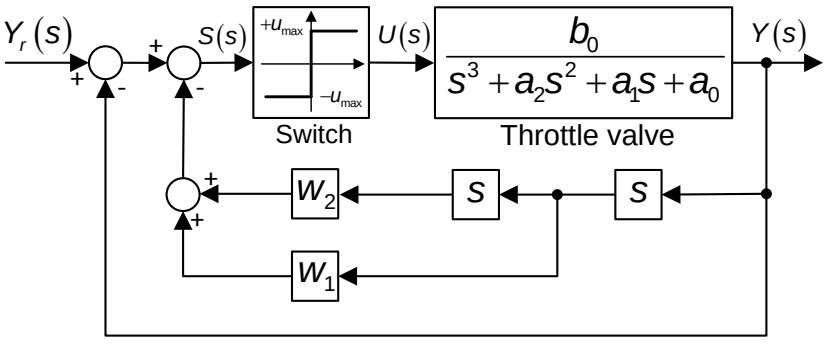

Figure 4.172: An example of a basic SMC for a throttle valve plant

The closed loop system can be designed to yield the desired response using the settling time formula as in the previous sections. The characteristic equation of Figure 4.172, for $S(s)=0$ and $Y_r(s)=0$ using equation (4.194). Thus

$$\begin{aligned} &-Y(s)\left(1+w_1 s+w_2 s^2\right)=0 \quad \Rightarrow \\ &s^2+\frac{w_1}{w_2}s+\frac{1}{w_2}=0 \end{aligned} \tag{4.198}$$

Using the settling time formula for $n=2$,

$$\left(s+\frac{9}{2T_s}\right)^2=s^2+\frac{9}{T_s}s+\frac{81}{4T_s{}^2} \tag{4.199}$$

Comparing equation (4.198) and (4.199) yields $w_2=4T_s{}^2/81$ and $w_1=9/T_s\cdot w_2$.

As already pointed out, the basic SMC will switch at an infinite frequency with variable mark-space ratio to keep the state on the switching boundary. In practice, however, the sampling frequency will be finite which will allow the state trajectory to execute a zig-zag movement about the sliding boundary as shown in Figure 4.173 (b). The associated control switching can be damaging for the actuator or system. This phenomenon is known as *control chatter*.

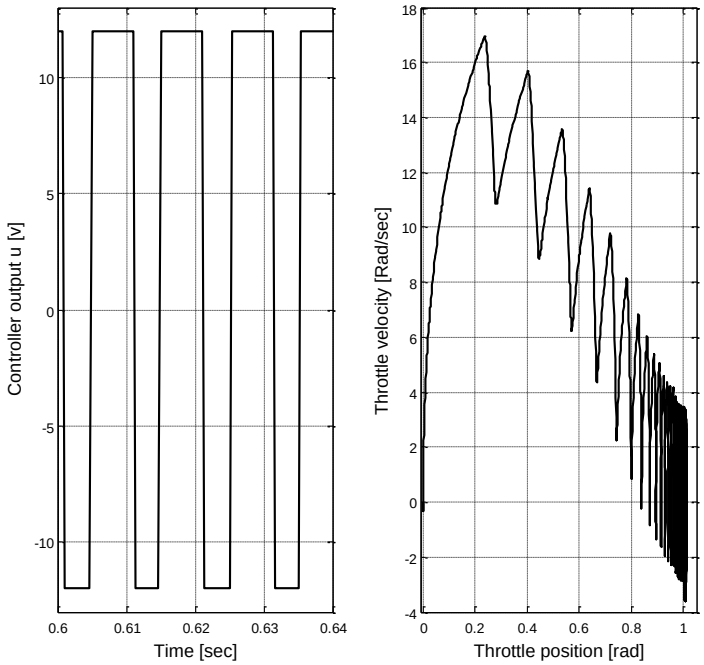

a) Control variable **b)** State trajectory

Figure 4.173: Basic sliding mode controller behaviour

4.9.3.1 Control Smoothing Integrator Method

To avoid the 'control chatter' an integrator can be inserted between the controller output and the plant to smooth out the switching (Dodds and Walker, 1991) (Vittek et al., 2008) (Sira-Ramirez, 1993, Tseng and Chen, 2010). This will be referred to as the *control smoothing integrator method*. Figure 4.174 shows the new controller with the extra integrator between the controller and the plant in which $U(s)$ will be a filtered value of $U'(s)$. The control system design to achieve the closed loop system response is done in two steps.

a) The additional integrator is assumed to be a part of the plant which will increase its order by one.

b) To accommodate for the increase in the plant order, the basic sliding mode controller order has to be increased by one.

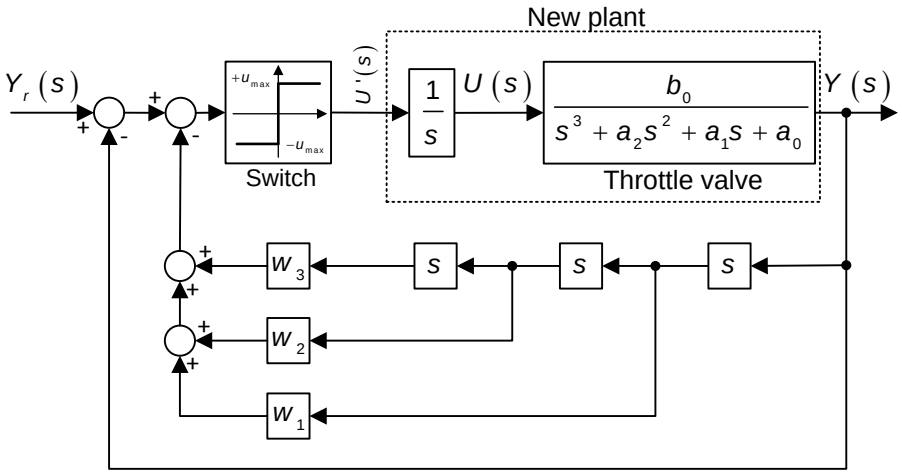

Figure 4.174: Basic SMC with a Control Smoothing Integrator

Figure 4.175 shows a simulation result of a throttle valve system controlled by a basic SMC with and without a *control smoothing integrator*. Plot (a) shows the coil current of the basic SMC without the integrator where the amplitude level of the current > +/- 4 amps. Plot (b) shows that the current amplitude has now decreased by more than a factor of 10, through adding the integrator on the output of the switching function.

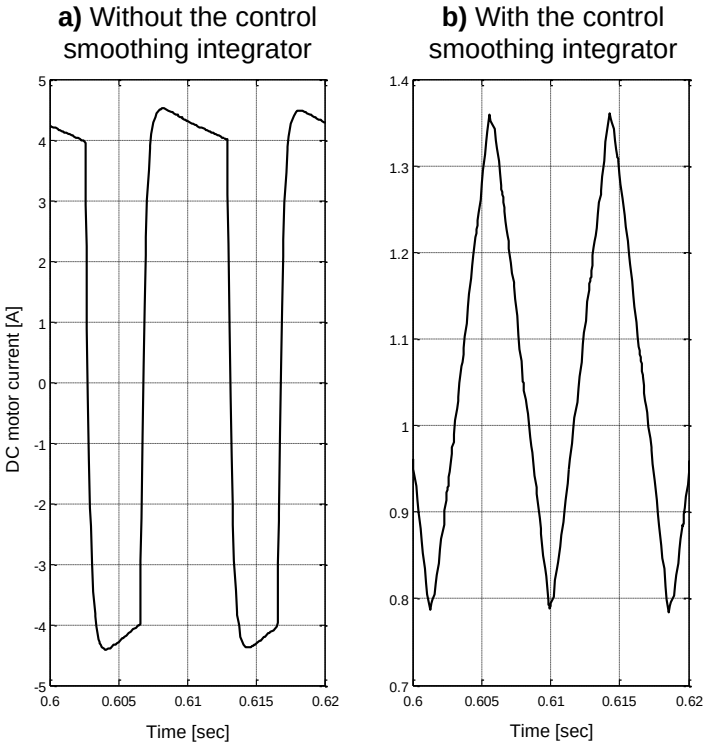

Figure 4.175: DC-Motor current levels. Sample frequency = 3000 Hz.

The desired closed loop response for $T_s = 0.1$ [sec] and a sampling time of 1/3000 [sec] is the same for both plots. In the case with the extra integrator the switch level, $u_{\max}$, is a number in the software that can be made as large as possible to maximise the range of states over which the robustness is retained. This, however, is limited ultimately by the saturation limit of the physical control variable, which is +/- 12 Volt for the throttle valve used.

4.9.3.2 Boundary Layer Method

Another way to avoid the control chatter is to replace the signum switching function in the forward path with a high gain, i.e., high slope, transfer characteristic with saturation (Dodds, 2004) (Dodds and Vittek, 2009). Thus

$$u = -u_{\max} \cdot Saturation\left[K \cdot S\left(y_r, y\right)\right] \tag{4.200}$$

where u will be saturated at $\pm u_{\max}$ when $|S| < u_{\max} / K$. This introduces a region straddling the original switching boundary, between two saturation boundaries. This will make the state move continuously towards the set point on the sliding surface while the control also behaves smoothly, approximating the equivalent control described in subsection 4.9.2. The global behaviour of this high gain controller is similar to the basic SMC. In theory, with $K \to \infty$ the boundary layer shrinks to infinitesimal proportions and makes the state trajectory identical to that of the basic ideal SMC but with the equivalent control replacing the original control switching at infinite frequency. Figure 4.176 shows this high gain SMC which will be called the *boundary layer* SMC.

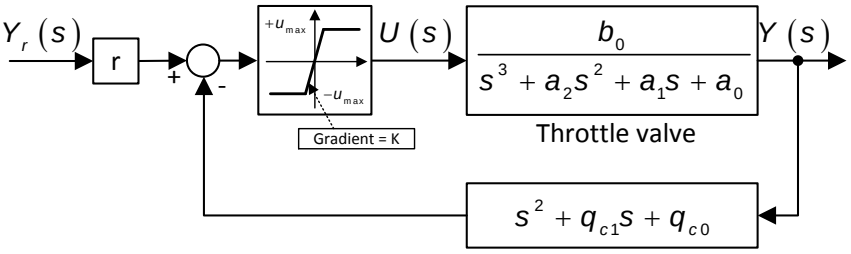

Figure 4.176: Boundary Layer Sliding Mode Control

In this case there are three controller parameters, q_{c1}, q_{c0} and K, determined using the settling time formula and pole placement as in the previous chapters. The gain, K, is finite which results in a steady state error, as in the basic LSF, but this is generally much smaller than that of the LSF if the latter is designed with a multiple closed loop pole to achieve the same settling time. r is found by letting $s \to 0$ in the transfer function for $Y(s)/Y_r(s)$.

4.9.4 Controller Design

4.9.4.1 Control Smoothing Integrator Method

It is well known that measurement noise will make it impractical to implement differentiators without noise filtering. The differentiators are combined with simple low pass filters, as shown in Figure 4.177.

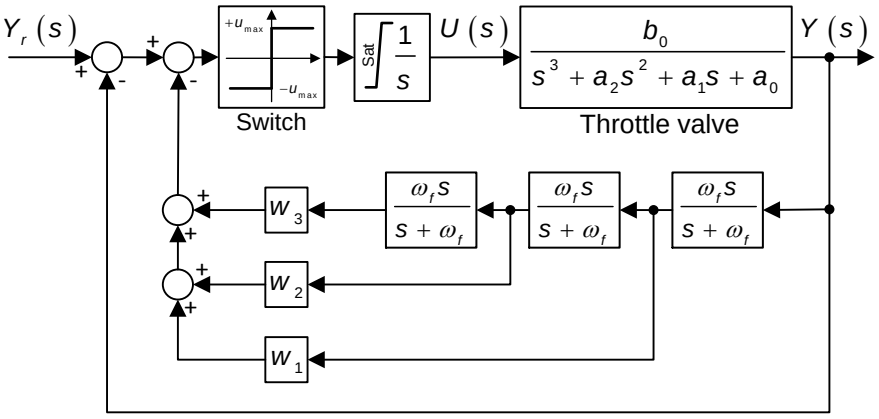

Figure 4.177: Switching boundary SMC with measurement noise filtering and integrator with saturation

The filter frequency, ω_f, is chosen to be higher than the bandwidth of the closed loop system, in this case 500 [rad/sec]. An integrator anti windup scheme is needed to prevent large error excursions that would otherwise occur due to the hardware imposed saturation limits. In this instance the integrator is connected directly to the plant of which the voltage limits are known. A simple integrator with saturation could be used to perform this function.

As can be seen in Figure 4.175 (b) the method reduces but does not entirely eliminate the control chatter. To minimise the control chatter even more, therefore, a variable switching level could be used on the input of the integrator as shown in Figure 4.178. The idea is that the integrator output should ideally be constant in steady state conditions. By making the switching level smaller as

the steady state is approached, i.e., as $|e(t)|$ reduces, the oscillation limits of the triangular integrator output, $u(t)$, will be made sufficiently small for the application in hand. For the test with the throttle valve the variable switch level A is chosen linear as a function of the $e(t)$, as follows.

$$A = \begin{cases} 100, & |e(t)| < 0.01 \\ 15000 \cdot (|e(t)| - 0.01) + 100, & 0.01 \le |e(t)| \le 0.05 \\ 700, & |e(t)| > 0.05 \end{cases} \qquad (4.201)$$

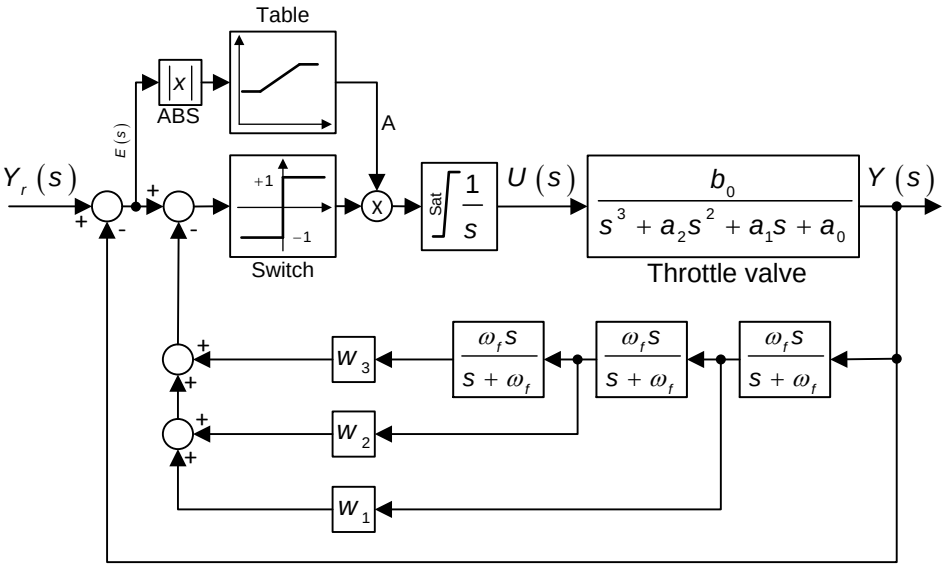

Figure 4.178: Practicable SMC with control smoothing integrator and variable gain to minimise control chatter for small position errors

The minimum and maximum switch levels depend on the application and have been chosen to suite the throttle valve. The influence here is a relatively high level of static friction which causes a significant limit cycle of the closed loop system if the minimum level is too low. If the maximum level is chosen too high, the closed loop system could be unstable. The levels have to be found

empirically, but a simulation can be used for determining preliminary settings that can be applied in the initial experiments with reasonable confidence.

The characteristic equation for the system of Figure 4.178 in the sliding mode for which $S(s)=0$ and $Y_r(s)=0$ is given by

$$\begin{aligned} &-Y(s)\left(1+w_1 s+w_2 s^2+w_3 s^3\right)=0 \quad \Rightarrow \\ &s^3+\frac{w_2}{w_3}s^2+\frac{w_1}{w_3}s+\frac{1}{w_3}=0 \end{aligned} \tag{4.202}$$

The settling time formula for $n=3$ yields the desired characteristic equation,

$$\left(s+\frac{18}{T_s}\right)^3=s^3+\frac{18}{T_s}s^2+\frac{108}{T_s^{\,2}}s+\frac{216}{T_s^{\,3}}=0 \tag{4.203}$$

Equating the left hand side of polynomial (4.202) and (4.203) yields

$$\begin{aligned} w_3 &= T_s^{\,3}/216 \\ w_2 &= 108/T_s^{\,2}\cdot w_3 \\ w_1 &= 18/T_s\cdot w_3 \end{aligned} \tag{4.204}$$

4.9.4.2 Boundary Layer Method

As stated before, noise filtering is needed with the output differentiators, as shown in Figure 4.179.

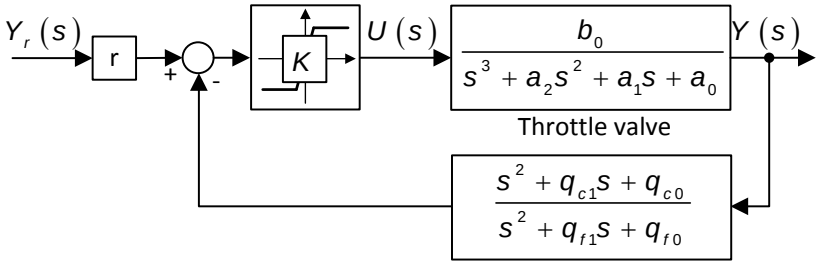

Figure 4.179: Boundary layer method SMC with measurement noise filtering

By replacing the polynomial with a transfer function it is possible to choose a suitable filter characteristic via q_{f1} and q_{f0}. All the gains can be designed using the settling time formula and pole placement or robust pole placement described in subsection 4.4.2.2. The steady state error that would be caused by finite gain, K, in the system of Figure 4.179 can be eliminated by an integrator added in the forward path as shown in Figure 4.180.

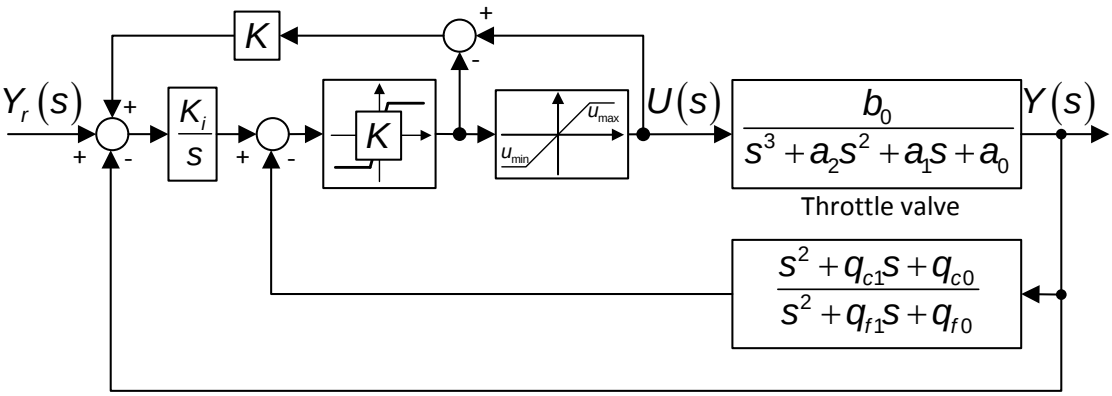

Figure 4.180: Boundary layer method SMC with integrator in the forward path and measurement noise filtering

Note that integrator anti-windup has been added as in the system of Figure 4.178.

Using Mason's formula on Figure 4.180, without saturation, yields

$$\frac{Y(s)}{Y_r(s)} = \frac{K_i K b_0 \left(s^2 + q_{f1}s + q_{f0}\right)}{\begin{aligned} &s^6 + (q_{f1} + a_2)s^5 + (q_{f0} + a_2 q_{f1} + a_1)s^4 + (a_2 q_{f0} + a_1 q_{f1} + a_0 + Kb_0)s^3 \\ &+ \left(a_1 q_{f0} + a_0 q_{f1} + Kb_0 (q_{c1} + K_i)\right)s^2 \\ &+ \left(a_0 q_{f0} + Kb_0 (q_{c0} + K_i q_{f1})\right)s + Kb_0 K_i q_{f0} \end{aligned}} \quad (4.205)$$

To enhance robustness the desired closed loop characteristic equation is designed by robust pole placement using two groups of poles, one for the desired settling time and a faster one for the filter: $p_c = T_s / 6$ and $p_f = r_{pp\,\min} \cdot p_c$ where $r_{pp\,\min} = 16.2$, which is the minimum pole-to-pole ratio for dominance in a sixth order system with 3 dominant poles. Thus

$$\begin{aligned} (s + p_f)^3 (s + p_c)^3 &= s^6 + 3(p_f + p_c)s^5 + \left[3\left(p_f^2 + p_c^2\right) + 9p_f p_c\right]s^4 \\ &+ \left[p_f^3 + p_c^3 + 9p_f p_c (p_f + p_c)\right]s^3 + \left[3p_f p_c \left(p_f^2 + p_c^2\right) + 9p_f^2 p_c^2\right]s^2 \\ &+ 3p_f^2 p_c^2 (p_f + p_c)s + p_f^3 p_c^3 = 0 \end{aligned} \quad (4.206)$$

Equating the denominator of equation (4.205) with the left hand side of equation (4.206), to determine the three control parameters yields

q_{f1}:

$$q_{f1} + a_2 = 3(p_f + p_c) \Rightarrow q_{f1} = 3(p_f + p_c) - a_2$$

q_{f0}:

$$\begin{aligned} q_{f0} + a_2 q_{f1} + a_1 &= 3\left(p_f^2 + p_c^2\right) + 9p_f p_c \Rightarrow \\ q_{f0} &= 3\left(p_f^2 + p_c^2\right) + 9p_f p_c - \left(a_2 q_{f1} + a_1\right) \end{aligned}$$

K:

$$\begin{aligned} a_2 q_{f0} + a_1 q_{f1} + a_0 + Kb_0 &= p_f^3 + p_c^3 + 9p_f p_c (p_f + p_c) \Rightarrow \\ K &= \left[p_f^3 + p_c^3 + 9p_f p_c (p_f + p_c) - \left(a_2 q_{f0} + a_1 q_{f1} + a_0\right)\right] / b_0 \end{aligned}$$

q_{c1} :

$$a_1 q_{f0} + a_0 q_{f1} + K b_0 \left(q_{c1} + K_i \right) = 3 p_f p_c \left(p_f^2 + p_c^2 \right) + 9 p_f^2 p_c^2 \Rightarrow$$
$$q_{c1} = \left[3 p_f p_c \left(p_f^2 + p_c^2 \right) + 9 p_f^2 p_c^2 - \left(a_1 q_{f0} + a_0 q_{f1} \right) \right] \Big/ \left(K b_0 \right) - K_I$$

q_{c0} :

$$a_0 q_{f0} + K b_0 \left(q_{c0} + K_i q_{f1} \right) = 3 p_f^2 p_c^2 \left(p_f + p_c \right) \Rightarrow$$
$$q_{c0} = \left[3 p_f^2 p_c^2 \left(p_f + p_c \right) - a_0 q_{f0} \right] \Big/ \left(K b_0 \right) - K_I q_{f1}$$

K_i :

$$K b_0 K_i q_{f0} = p_f^3 p_c^3 \Rightarrow K_i = p_f^3 p_c^3 \Big/ \left(b_0 K q_{f0} \right)$$

4.9.5 Simulation and Experimental results

4.9.5.1 Control Smoothing Integrator Method

The sliding mode controller's gains, w_1, w_2 and w_3, are determined as described in subsection 4.9.4.1, equation (4.204) with $T_s = 0.1$ [sec], $\omega_f = 500$ [rad/sec] and a maximum gain of $A = 700$. A dither signal is added to the control signal to reduce the effects of the static friction as described in subsection 4.4.3. The integrator saturation limits are enabled during the step reference input. The SMC is tested experimentally with three different reference input functions as described in subsection 4.3.3. The dSPACE system is used for the experiments as explained in subsection 4.3.2.

The simulation results presented in this subsection are obtained with the full nonlinear plant model presented in section 2.5.

First, simulated and experimental responses to a step reference position change within the throttle valve stop limits are presented in Figure 4.181.

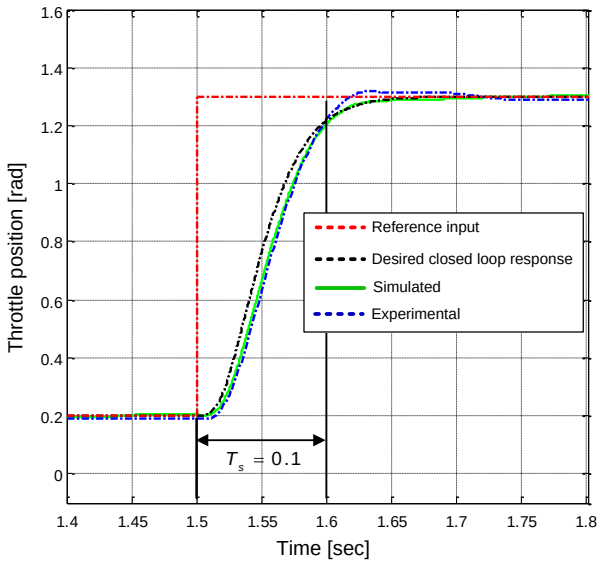

Figure 4.181: Closed loop step response, from 0.2 to 1.3 [rad]

The vertical black lines mark the nominal settling time of $T_s = 0.1\,[\text{sec}]$. It is evident that both the experimental and simulated responses come close to this at ≈ 1.24 [rad].

Figure 4.182 shows the simulated and experimental closed loop responses.

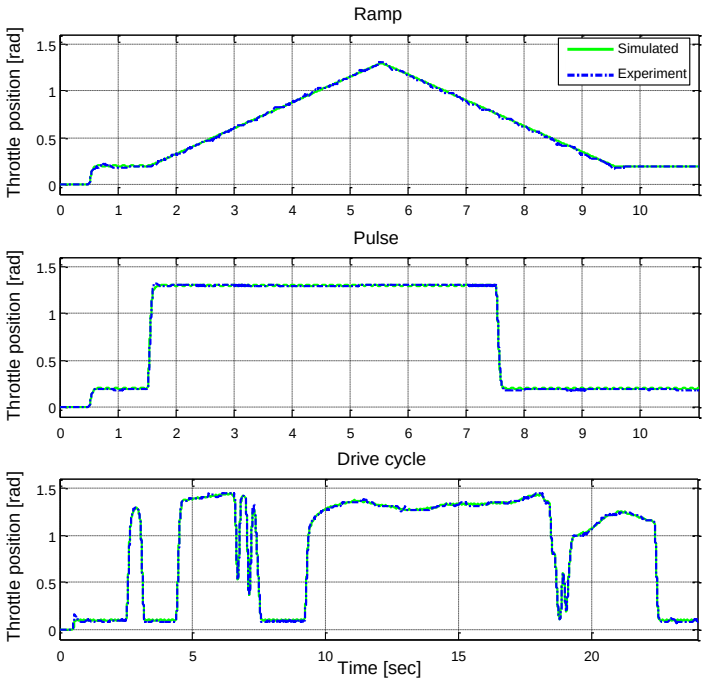

Figure 4.182: Experimental and simulated response of the SMC - control smoothing integrator method

The experiments, Figure 4.182, were repeated without control dither added. The results showed very little difference between the two sets of experiments. This is due to the switching element in the control strategy, shown in Figure 4.178, which will generate control chatter, even with the smoothing integrator in loop.

Figure 4.183 shows the difference between the desired and the experimental closed loop response (Figure 4.182), indicating that the tracking is adequate but not as good as would be expected using a robust control technique.

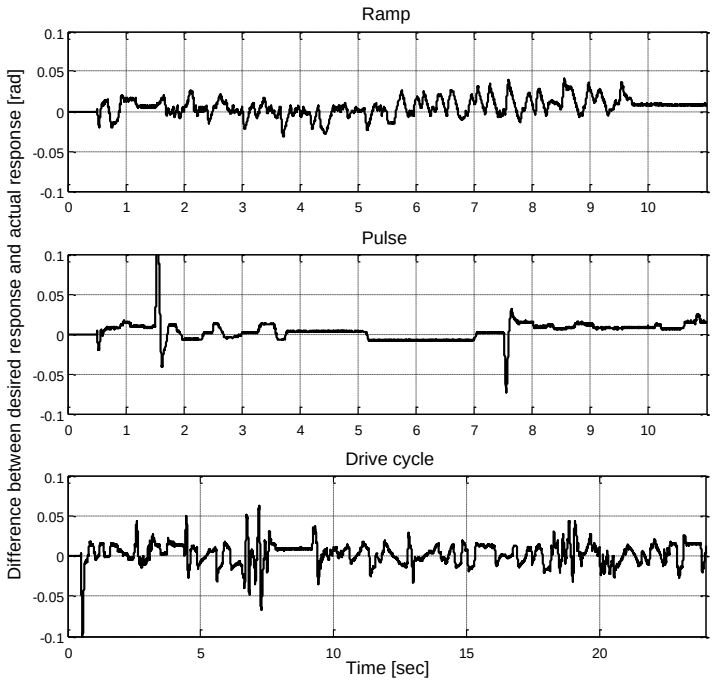

Figure 4.183: The difference between the desired and the experimental closed loop responses with a maximum gain of 700

The experiment, Figure 4.182, was repeated with a fixed gain of 300. The difference between the desired and the experimental closed loop response is seen to increase in Figure 4.184.

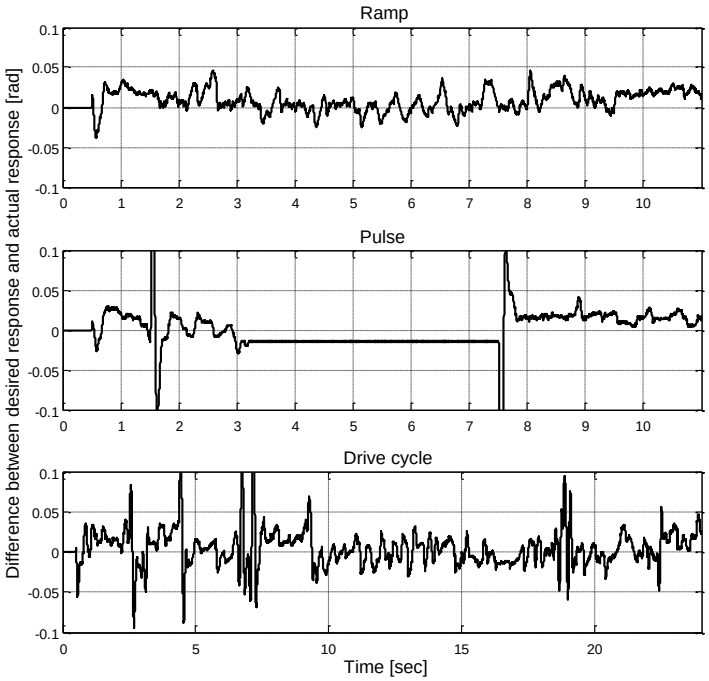

Figure 4.184: The difference between the desired and the experimental closed loop responses with a fixed gain of 300

As described in subsection 4.3.4.3 a spring failure can cause the engine to stall due to air starvation. The behaviour of the SMC controller during a spring break, at $t = 1$ [sec], is simulated using the nonlinear throttle valve model, and the result is shown in Figure 4.185. It shows a poor robustness against the disturbance and the throttle closes for about 0.2 [sec]. The oscillations on the control signal at $t = 1.02$ [sec] are the added dither signal that increases in amplitude when the control error, $y_r - y$, exceeds a preset threshold of 1% of the full scale movement range as described in subsection 4.4.3.

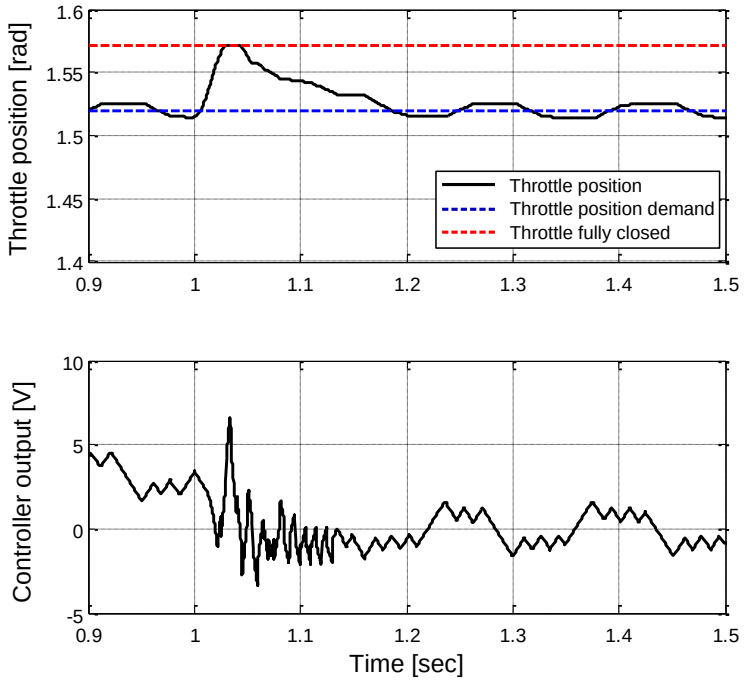

Figure 4.185: SMC - Control smoothing integrator method during a spring failure

The robustness against plant parameter deviations away from the nominal values is tested using the Monte Carlo method described in subsection 4.3.4.2. The parameter variation simulation uses the nonlinear throttle valve model with the controller output saturation, integrator saturation (smoothing integrator) and dither. The result of the parameter variation simulation is shown in Figure 4.186 for the maximum possible standard deviation of $\sigma = 8\%$. The figure shows the operational envelope for 1000 simulation runs, where the blue and red lines are the minimum and maximum values. The nominal parameter closed loop controller response and controller output are shown in black.

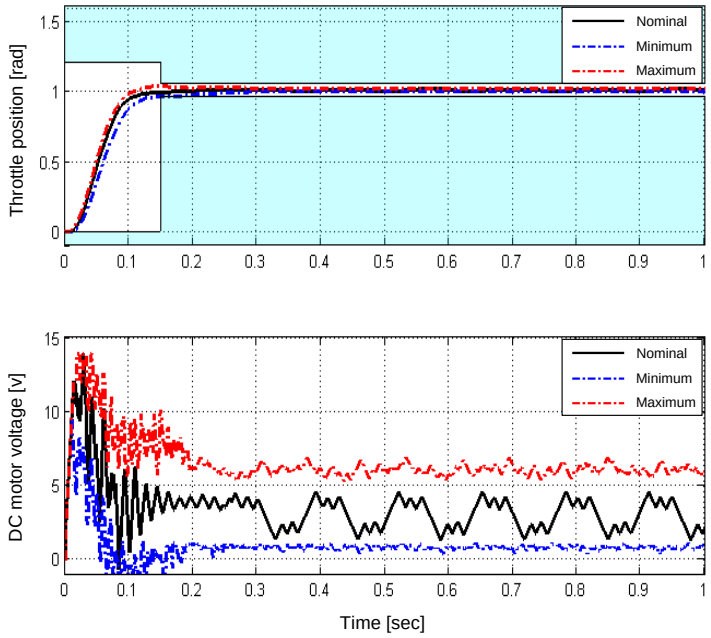

Figure 4.186: Maximum / minimum throttle position and DC motor voltage envelope (Standard deviation: $\sigma = 8\%$)

A standard deviation of $\sigma = 8\%$, Figure 4.186, indicates that the estimated parameters used for the control gain design can vary slightly before having an impact on the performance of the controller.

The sensitivity for the sliding mode controller is analysed in the frequency domain by using the relationships of equation (4.3) in subsection 4.3.4.1. Before this can be done, the switching element has to be replaced by a high gain, k, as in the boundary layer method, to render the closed loop system linear, as shown in Figure 4.187.

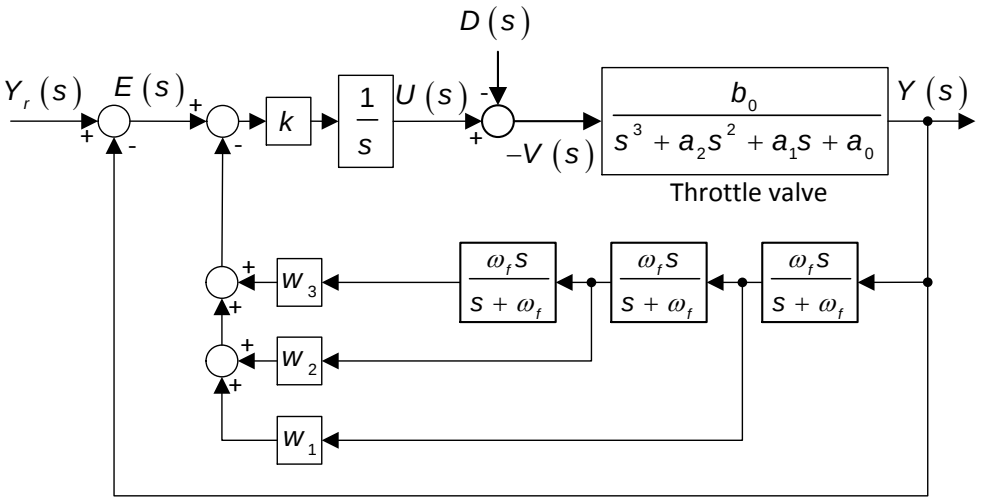

Figure 4.187: Structure used for analysing sensitivity

The sensitivity is then done with the aid of the Matlab Control System Analysis Toolbox and the block diagram of Figure 4.187 implemented in Simulink with $D(s)$ as the input and $V(s)$ as the output to obtain $S_p^C dB(\omega)$.

The sensitivity of the sliding mode controller is shown in Figure 4.188. The figure indicates a relatively low sensitivity, equivalent to high robustness. This corresponds well with the time domain result found by the Monte Carlo parameter variation simulation, but not so well with time domain spring failure analysis, shown in Figure 4.185. This can partial be explained by the fixed gain = 700 used for the sensitivity analyses, if the gain value is reduced to 300, shown in Figure 4.189, the sensitivity rises by +10dB.

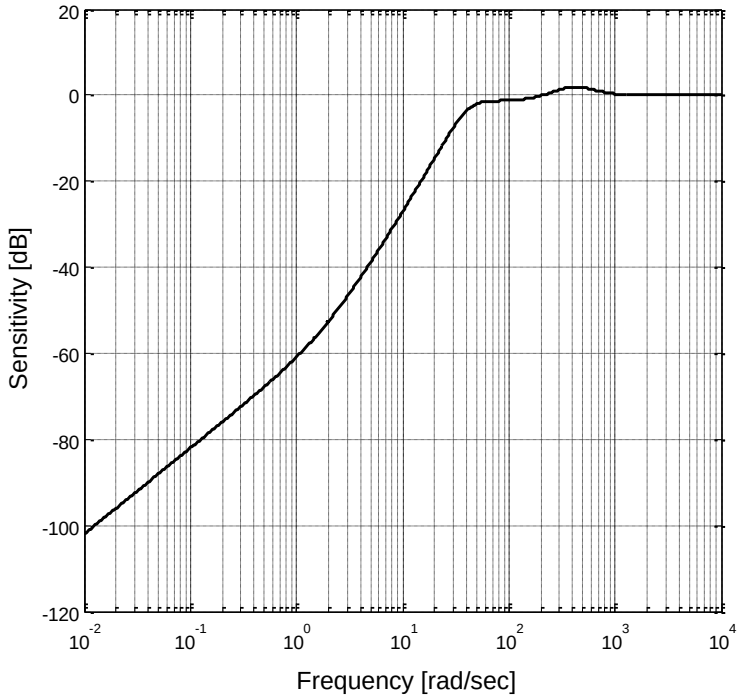

Figure 4.188: SMC - Control smoothing integrator method sensitivity with a fixed gain = 700

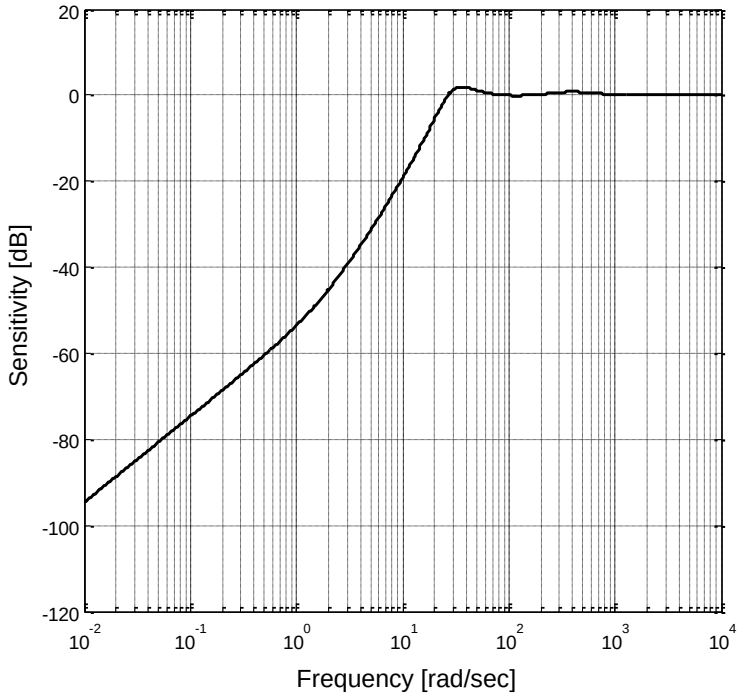

Figure 4.189: SMC - Control smoothing integrator method sensitivity with a fixed gain = 300

4.9.5.2 Boundary Layer Method

The sliding mode controller's gains are determined as described in subsection 4.9.4.2, with $T_s = 0.1$ [sec], two groups of poles, $n_p = 3$ and $n_f = 3$, and a robust pole-to-pole ratio of 40. A dither signal is added to the control signal to reduce the effects of the static friction as described in subsection 4.4.3. The integrator anti-windup strategy is enabled to minimise the saturation during the step reference input. The SMC is tested experimentally with three different reference input functions as described in subsection 4.3.3. The dSPACE system is used for the experiments as explained in subsection 4.3.2.

The simulation results presented in this subsection are obtained with the full nonlinear plant model presented in section 2.5.

First, simulated and experimental responses to a step reference position change within the throttle valve stop limits are presented in Figure 4.190.

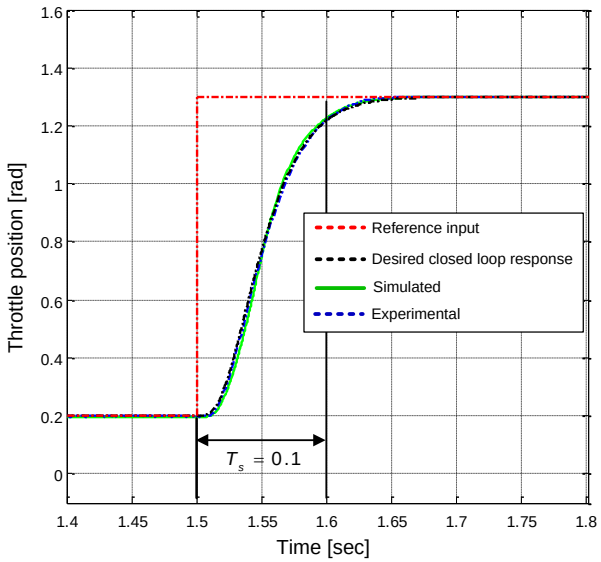

Figure 4.190: Closed loop step response, from 0.2 to 1.3 [rad]

The vertical black lines mark the nominal settling time of $T_s = 0.1\,[\text{sec}]$. It is evident that both the experimental and simulated responses come close to this at ≈ 1.24 [rad].

Figure 4.191 shows the simulated and experimental closed loop responses.

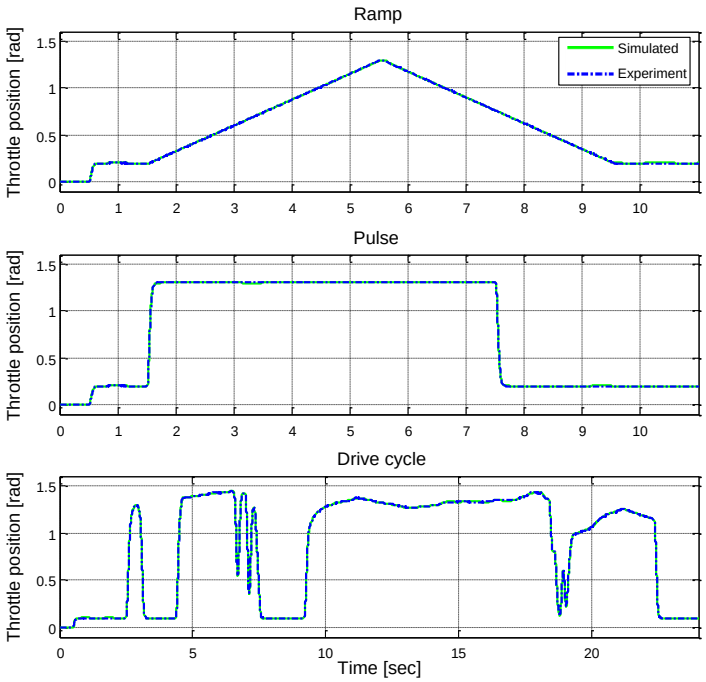

Figure 4.191: Experimental and simulated response of the SMC - Boundary layer method

Figure 4.192 shows small differences between the desired and the experimental closed loop responses (Figure 4.191), which, in contrast to the results with the control smoothing integrator in subsection 4.9.5.1, which is what would be expected using a robust control technique.

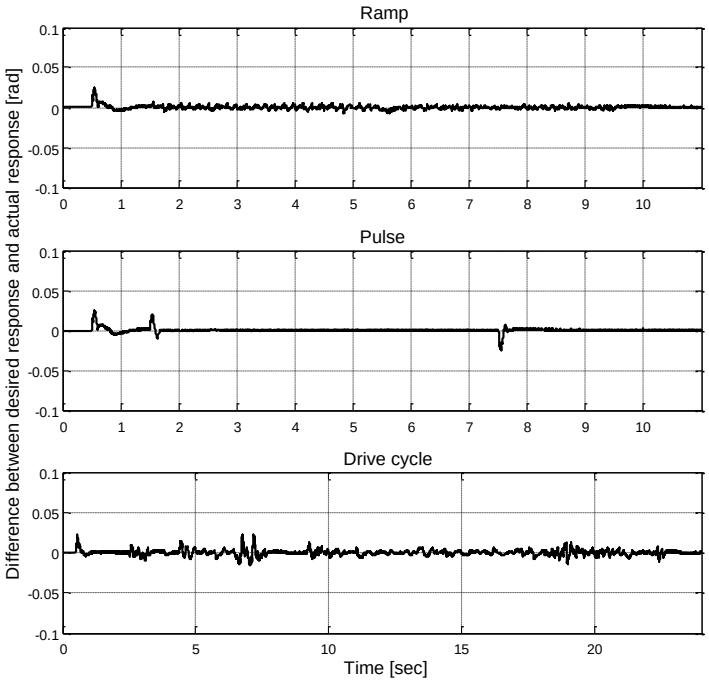

Figure 4.192: The difference between the desired and the experimental closed loop responses

As described in subsection 4.3.4.3 a spring failure can cause the engine to stall due to air starvation. The behaviour of the SMC during a spring break, at $t = 1$ [sec], is simulated using the nonlinear throttle valve model, and the result is shown in Figure 4.193. It shows a good robustness against the disturbance, with little deviation from the throttle position demand. The oscillations on the control signal at $t = 1.02$ [sec] are the added dither signal that increases in amplitude when the control error, $y_r - y$, exceeds a preset threshold of 1% of the full scale movement range as described in subsection 4.4.3.

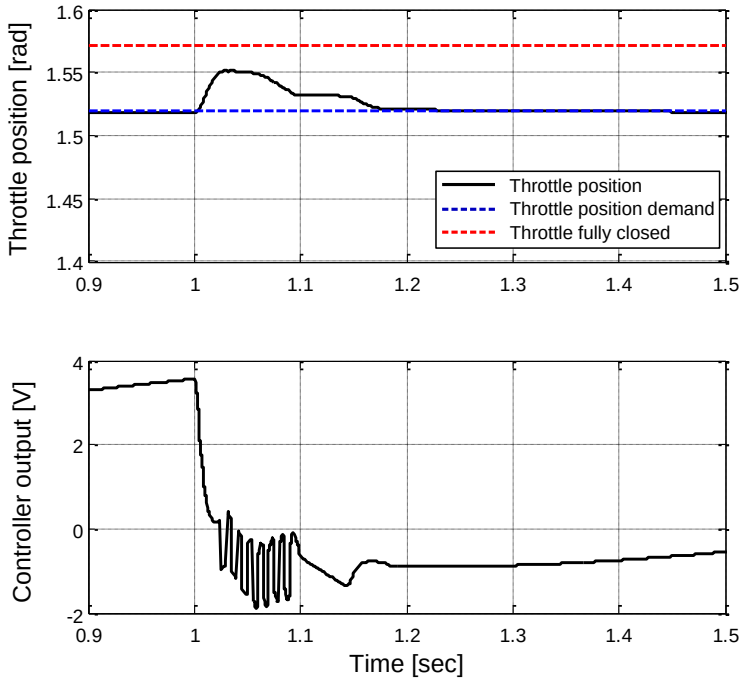

Figure 4.193: SMC - Boundary layer method during a spring failure

The robustness against plant parameter variations away from the nominal values is tested using the Monte Carlo method described in subsection 4.3.4.2. The parameter variation simulation uses the nonlinear throttle valve model with the controller output saturation, integrator anti-windup and dither. The result of the parameter variation simulation is shown in Figure 4.194 for the maximum possible standard deviation of $\sigma = 15\%$. The figure shows the operational envelope for 1000 simulation runs, where the blue and red lines are the minimum and maximum values. The nominal parameter closed loop controller response and controller output are shown in black.

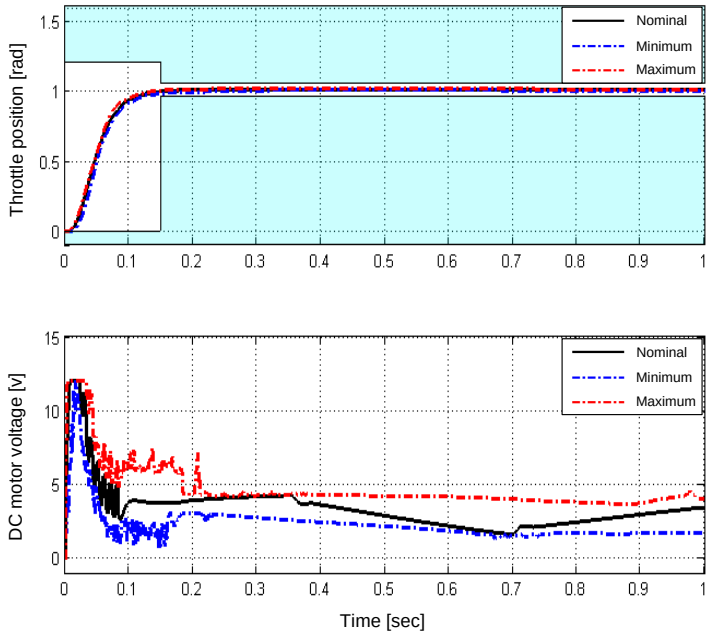

Figure 4.194: Maximum / minimum throttle position and DC motor voltage envelope (Standard deviation: $\sigma = 15\%$)

This indicates that the plant parameters can deviate significantly from the nominal values before having an adverse impact on the performance of the controller.

The sensitivity for the sliding mode controller is analysed in the frequency domain by using the relationship of equation (4.3) in subsection 4.3.4.1. This is done with the aid of the Matlab Control System Analysis Toolbox and the block diagram of Figure 4.195 implemented in Simulink with $D(s)$ as the input and $V(s)$ as the output to obtain $S_p^C dB(\omega)$.

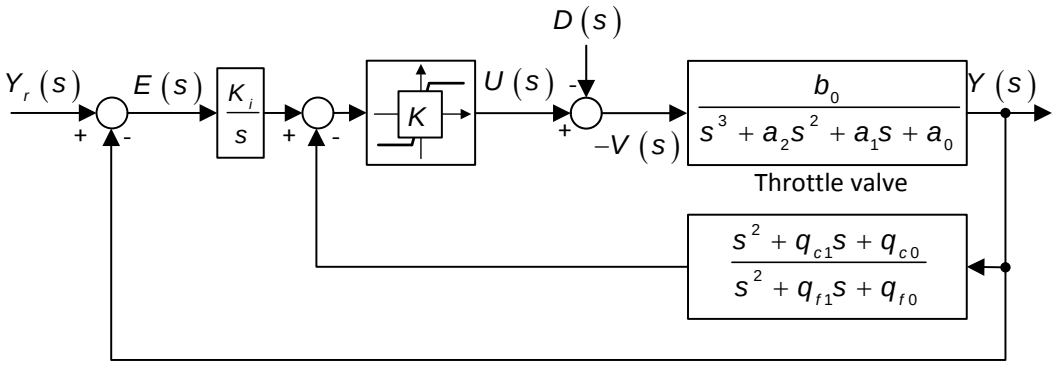

Figure 4.195: Structure used for analysing sensitivity

The sensitivity of the sliding mode controller is shown in Figure 4.196 for a robust pole-to-pole ratio of 40. The figure indicates a relatively low sensitivity, equivalent to high robustness. This corresponds well with the time domain result found by the above spring failure analysis and the Monte Carlo parameter variation simulations.

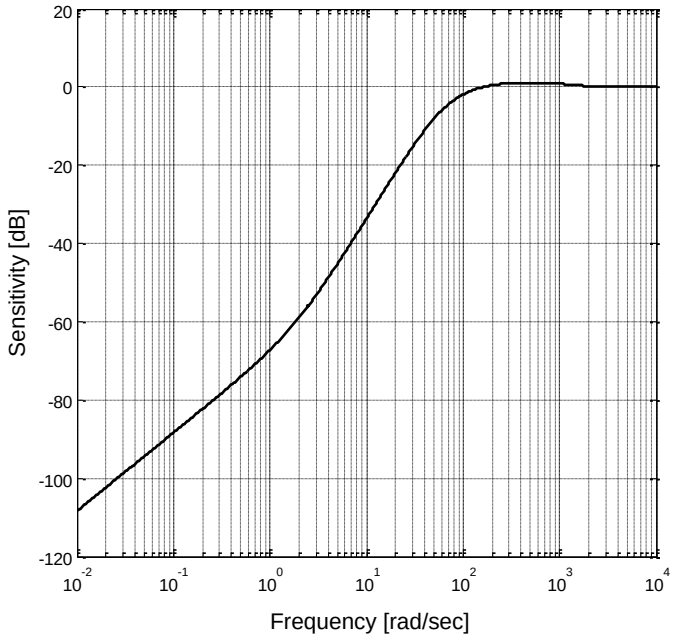

Figure 4.196: SMC - Boundary layer method sensitivity

5 Performance Comparisons

The information gained from the simulation and experimental result sections for each controller above is condensed here into a form that enables recommendations to be made for future throttle valve controllers.

Only the linear state feedback plus integral controller with coincident pole placement, in subsection 4.6.4.1, could definitely be rejected on the basis of a poor step response. First preliminary comparisons of the remaining controllers are made by assembling graphs showing a) the difference between the experimental step response and the simulated step response with the nonlinear plant model, and b) the difference between the experimental step response and the ideal step response (i.e., the simulated step response with the linear plant model). These are presented in Figure 5.1 and Figure 5.2.

Arguably, the most robust controllers are those that exhibit the smallest differences between the simulated and experimental step responses, as the true plant parameters will always be different from those assumed in the controller design, which are common for all the controllers (except the DPI controller with feed forward and manual tuning). On the other hand, the controllers will all have been designed using the linear plant model for which the ideal step response is the one obtained by simulating the control system with this linear model using the nominal parameters. To avoid awarding ‘high marks’ to controllers that have small differences between poor experimental and simulated step responses, the difference between the ideal step response and the experimental step response is included in Figure 5.1 and Figure 5.2.

An initial ranking has been made by visual inspection of these figures, the first being the best:

1) SMC with boundary layer
2) Restructured observer aided LSF+I control with robust pole placement
3) Observer based robust control
4) Polynomial controller with additional integrator
5) LSF+I control with robust pole placement
6) IPD, DPI and PID controllers
7) Observer aided LSF+I control with robust pole placement
8) Reduced order polynomial controller with additional integrator
9) DPI controller with feed forward and manual tuning
10) SMC with control smoothing integrator

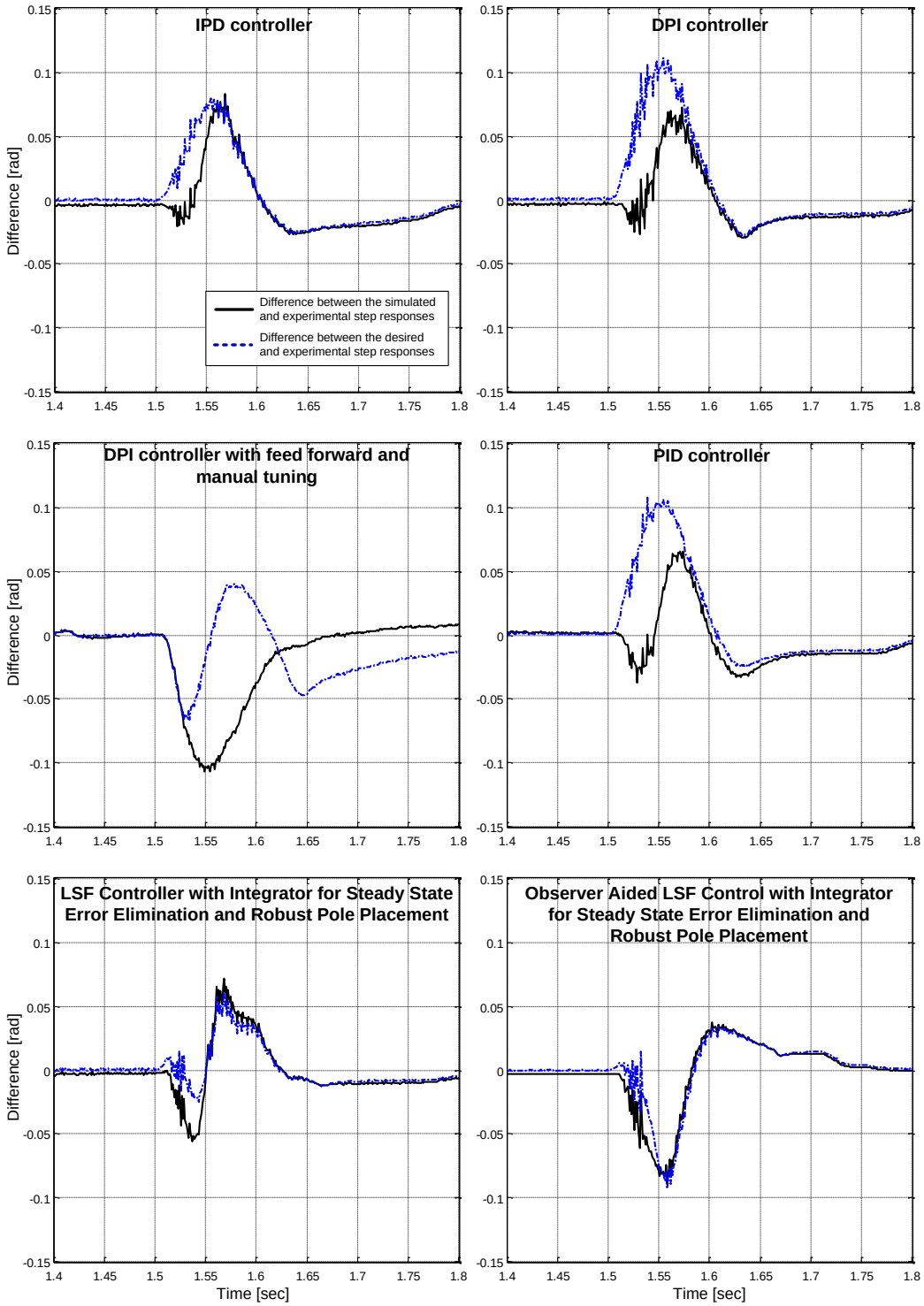

Figure 5.1: Step response differences for comparison #1

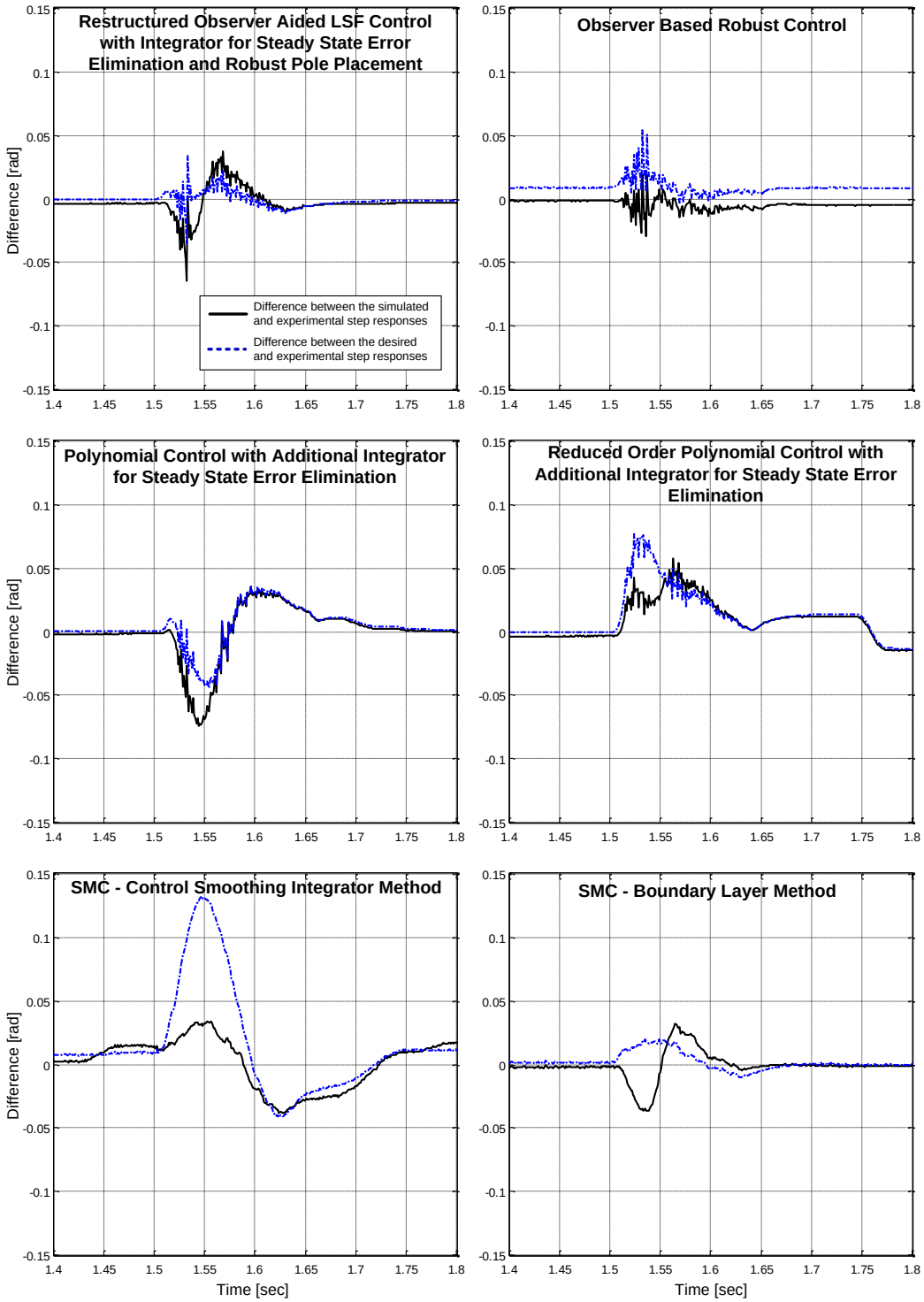

Figure 5.2: Step response differences for comparison #2

The results are summarised in Table 5.1 to give an overview of the different control techniques investigated and their individual performances using the following, mainly qualitative, criteria:

1	Overall performance regarding reference tracking, transient response and steady state error	G: Good, A: Acceptable, P: Poor
2	Anti-friction needed (Dither signal)	Y: Yes, N: No
3	External disturbance tolerance (Spring failure)	G: Good, A: Acceptable, P: Poor
4	Robustness against plant parameter variations	Maximum possible standard deviation [%]
5	Sensitivity indication	L: Low, M: Moderate, H: High
6	Complexity of the design procedure	L: Low, M: Moderate, H: High
7	Practicability including sample rate and extra inputs (DC motor current)	G: Good, A: Acceptable, P: Poor

Table 5.1: Overall performance comparison data

Controller	1) Overall performance	2) Anti-friction needed	3) External disturbance tolerance	4) Robustness against plant parameter variations	5) Sensitivity indication	6) Complexity of the design procedure	7) Practicability
IPD	G	Y	A	15%	L	L	G
DPI	G	Y	A	14%	L	L	G
DPI with Feed Forward and Manual Tuning	A	Y	P	2%	M	L	G
PID	G	Y	A	14%	L	L	G
Linear State Feedback plus Integrator	P	Y	-[4]	-[4]	-[4]	L	P[2]
Linear State Feedback plus Integrator with robust pole placement	G	Y	A	10 to 16%	L	L	P[2]
Observer Aided LSF with Integrator with robust pole placement	G	Y	A	15%	L	M	G
Restructured Observer Aided LSF plus Integrator with robust pole placement	G	Y	A	15%	L	M	G
Observer Based Robust Control	A	Y	G	10%	M	H	G
Polynomial Control with Additional Integrator	G	Y	A	14%	L	L	G
Reduced Order Polynomial Control with Additional Integrator	G	Y	A	15%	L	L	G
Polynomial Control with Precompensator	G	Y	A	11%	L	L	G
SMC with Control Smoothing Integrator	A	N	P	8%	L[1]	L	A[3]
SMC with Boundary Layer	G	Y	A	15%	L	L	G

Notes for Table 5.1:

[1] With $k = 700$

[2] A DC motor current measurement is needed

[3] Tests indicated that a higher sample rate would give the controller better performance.

[4] Not tested due to poor performance.

For the purpose of obtaining a ranking from Table 5.1, the following numerical scoring will be attached to the ratings

$$\mathrm{P}=0;\ \mathrm{A}=1;\ \mathrm{G}=2;\ \mathrm{H}=1;\ \mathrm{M}=2;\ \mathrm{L}=3;\ \mathrm{Y}=0;\ \mathrm{N}=1. \qquad (5.1)$$

In addition, the standard deviation rating, $\sigma_{\%}$, is needed but it would be appropriate to introduce a weighting factor of less than unity for the following reason: with reference to all the figures of sections 4.5, 4.6, 4.7, 3.8 and 4.9, showing the set of step responses of the Monte Carlo run for each controller, although the step responses are very closely grouped in many cases they all, including the ideal step response, come very close to the upper left corner of the lower rectangular 'no go' area. It therefore requires very little deviation from the nominal ideal response for the system to fail. The controllers whose nominal step response come the closest to this 'no go' corner therefore stand at a disadvantage. Two examples of this are the OBRC and the polynomial controller with the precompensator. These, respectively, score only 10% and 11% on the maximum standard deviation while other controllers score much higher with a larger spread of step responses (indicating poorer robustness) due to the ideal one being well clear of the 'no go' corner. The test, though an industry standard one is therefore harsh and arguably a little unfair. In view of this, the standard deviation assessment will be downscaled so that the maximum contribution is 3, which is no more than the maximum contribution from the qualitative assessments. Hence $\frac{3}{16}\sigma_{\%}$ is added to the qualitative ratings, the results being presented in Table 5.2.

Table 5.2 Numerical ratings and rankings

Controller	Rating	Ranking	
SMC with Boundary Layer	13.8	1st	(1st)
IPD	13.8		(6th)
Reduced Order Polynomial Control with Additional Integrator	13.8		(8th)
Polynomial Control with Additional Integrator	13.6	2nd	(4th)
DPI	13.6		(6th)
PID	13.6		(6th)
Restructured Observer Aided LSF plus Integrator with robust pole placement	12.8	3rd	(2nd)
Observer Aided LSF with Integrator & robust pole placement	12.8		(7th)
Linear State Feedback plus Integrator with robust pole placement	12.0	4th	(5th)
SMC with Control Smoothing Integrator	10.5	5th	(10th)
Observer Based Robust Control	9.9	6th	(3rd)
DPI with Feed Forward and Manual Tuning	8.4	7th	(9th)

The rankings in parenthesis on the right are the preliminary rankings obtained by visual inspection of Figure 5.1 and Figure 5.2. Unfortunately these present some anomalies but it must be realised that most of the qualitative aspects of the assessment are independent of the appearance of the step response errors. It can be concluded, however, that manual tuning, which is currently practiced, is not recommended. The sliding mode control with the control smoothing integrator produced disappointing results but further work on this is encouraged since not all avenues of this technique have been explored. As far as the model based control system design is concerned, linear state feedback with coincident pole placement is also not recommended but robust pole placement with the same control technique is worth considering further. The traditional controllers (PID, DPI and IPD) score high, but with model based design. It is clear that the polynomial controller and the boundary layer based sliding mode controller perform well and should be considered seriously.

6 Conclusions and Recommendations for Further Research

6.1 Overall Conclusions

6.1.1 Modelling

A generic third order nonlinear throttle valve plant model has been developed including hard stops and friction. The nonlinear friction model, which is an original contribution, includes static friction, and has been developed to be realistic without inordinately slowing down simulations around the zero velocity range. A practical observation, however, has been that the friction transfer characteristic between the relative velocity and the friction force varies from day-to-day, particularly with the temperature rise following the system turn on, making it difficult to compensate for this in model based control strategies.

The parameters of the plant model were identified by grey box methodology, i.e., by means of a combination of physical measurements and mathematical model determination from experimental data, aided by the Simulink® Design Optimization toolbox from Mathworks®. The model was validated in both the time domain, shown in subsection 3.3, and in the frequency domain, shown in subsection 3.4, showing good correlation with the physical plant. This was further verified in the ‘Simulation and Experimental results’ of the individual control strategies under investigation.

6.1.2 Control techniques

This work focuses on the angular position control of the plate of a throttle valve used for controlling the air flow to a Diesel engine.

A comprehensive range of different control strategies have been considered, including the orthodox ones, with a view to exploring the possibilities of taking advantage of modern digital implementation to achieve performance levels unattainable by the traditional methods, from the point of view of ease of design and commissioning as well as accuracy and robustness. The three traditional PID, DPI and IPD controllers are included but model based gain determination has been exhaustively explored for them (as well as the traditional manual tuning approach). The non-orthodox controllers fall into two categories: a) those based on the robust control strategies of sliding mode control and observer based robust control and b) those based on the linear control strategies of linear state feedback control (with and without observers) and polynomial control (often recognised as the RST controller in the linear discrete *z*-domain). The complete set of controllers have been assessed and compared regarding their performance for positioning accuracy, parametric uncertainty sensitivity and disturbance rejection, as well as the design effort and commissioning effort entailed.

It is important to recall that any linear controller can be expressed by the basic transfer function relationship,

$$U(s) = G_{\mathrm{r}}(s)Y_{\mathrm{r}}(s) - G_{\mathrm{y}}(s)Y(s) \tag{6.1}$$

Each controller, however, will have specific orders and relative degrees of the transfer functions, $G_{\mathrm{r}}(s)$ and $G_{\mathrm{y}}(s)$. Some of the controllers may be based on different control strategies but have the same orders and relative degrees of these transfer functions. Furthermore, it may be possible to adjust their parameters to make the transfer functions identical. In this case, although the two controllers may have an entirely different structure, in theory they may be designed to have precisely the same performance regarding parametric uncertainty, sensitivity, disturbance rejection and control accuracy. This would explain the closeness of performance of some of the controllers examined in

Chapter 3. This would also explain the polynomial controller with robust pole placement and sliding mode controller with boundary layer performing similarly, as both have separated closed loop poles that give robustness.

Taking an overview of the work reported in Chapter 3, it is evident that for the throttle valve application the difference in performance between the best and worst of the top ten (out of fourteen) controllers identified in Table 5.2 is relatively small so that none of these can really be rejected for future throttle valve control systems. All these, however, were designed using model based techniques. Notably, the second worst performer of the complete set was a traditional controller tuned manually. A strong recommendation to the industry, at least for the throttle valve application, is therefore to adopt the more scientific approach of determining a mathematical model of the plant and designing a controller on the basis of this model.

It is evident from subsection 4.8.4 that coincident pole placement using the polynomial controller yielded unsatisfactory results and even conventional robust pole placement with one closed loop pole of large magnitude did not produce sufficient improvement. This result is attributed to the nonlinear static friction as simulations with linear kinetic friction predicted satisfactory performance. This problem, however, did not occur with the other controllers. The explanation is the higher order, i.e., seven, of the polynomial control loop, when designed on the basis of the third order throttle valve model. In contrast, the sliding mode controller with boundary layer gives a control loop order of only three and worked well with only one closed loop pole of large magnitude. On the other hand, modifying the pole split using the polynomial controller to give four coincident dominant closed loop poles and three closed loop poles of large magnitude for robustness yielded even better results than obtained with the lower order control loops, albeit by only a small margin. These were similar to the results obtained with the observer aided linear state feedback (LSF) plus

integral control. This system is also of seventh order. In this case, the design of the main fourth order LSF loop was based on conventional robust pole placement, with only one closed loop pole of large magnitude. The three observer poles, however, were also larger in magnitude than all the main LSF loop poles, which is standard practice, resulting in three dominant poles and four large poles. This is not quite the same split as used for the polynomial controller but would explain the similarly good performance.

Finally, it will be recalled from subsection 4.8.4.3 that a special system was introduced that enabled an extended settling time, often requested in the industry, to be attained despite the static friction. This was achieved by 'tightening up' the feedback loop by significantly reducing its specified settling, in this case from 0.1 [sec] to 0.04 [sec] (no problems with measurement noise being observed) and then inserting a precompensator in the reference input that reduces the acceleration of the step response to levels avoiding initial control saturation by introducing a dominant pole that sets the real settling time, in this case to 0.2 [sec]. This system performed better than all of the systems compared in section 5 but is not included in this comparison because it is a special case. It is important to mention, however, as it would be a practicable approach. The same basic idea could be used with all the other controllers but then the differences in the controller performances would probably become even smaller than observed in section 5. For the purpose of finding the best controllers, the comparison made is considered better.

6.2 Recommendations for Further Research

At the outset of the research programme, the approach was to obtain the most accurate model of the throttle valve within practical constraints and then design controllers based on this model, which is of third order. Consequently it was relatively late in the research programme that the potential of greatly simplifying

the polynomial controller by using a reduced order throttle valve model was recognised. The model order reduction is carried out by ignoring the time constant of the plant mainly influenced by the inductance and resistance of the actuator coil since it is at least an order of magnitude less than the time constant associated with the moment of inertia and kinetic friction of the mechanical assembly. This simplified controller, in fact, produced the best result. It is therefore strongly recommended to redesign all the other nine controllers (taken from the ten best in Table 5.2) and assess these. This also enables the traditional controllers all to be designed by complete pole assignment, rather than partial pole assignment, which was necessary using the third order model.

In view of the good performance obtained using the polynomial controller with the three-four robust multiple pole split, it is recommended to undertake further research to find an optimal robust pole placement pattern, i.e., not necessarily with multiple poles, and establish how much further improvement in the robustness is attainable. Once an optimal pole pattern has been established, in which the ratios between the pole magnitudes are fixed, then a specified settling time could be realised by simply scaling the pole magnitudes. In fact, the inverse scaling law between pole patterns and step response time scale could be used to establish a new settling time formula for a specific pole pattern that would render the control system design straightforward.

Since the throttle valve characteristics are known to slowly change during the lifetime of a vehicle, the performance of a controller with fixed parameters may deteriorate significantly given that ideal robustness is unattainable. Due to this problem, periodic vehicle maintenance includes time consuming in-situ controller retuning. This could be avoided if an on-line plant parameter estimation algorithm could be used to continually update the model based controller parameters, thereby realising a form of adaptive control. Since the

plant model is fairly simple, it is recommended to carry out further research to arrive at a practicable on-line parameter estimation model. As problems are known to occur when attempting to estimate the parameters of a plant having widely differing pole magnitudes with significant measurement noise, it is strongly recommended to base the parameter estimation on the second order throttle valve model in which the electrical time constant of the actuator coil is ignored. This is another reason for re-designing the controllers using this reduced order plant model. Some challenges would be expected, however, due to the variable static friction characteristic.

Another integrator anti-windup strategy that has been successfully employed in the industry with traditional controllers could be investigated to establish whether an improvement in performance over the high gain control loop method is possible: The proposed strategy avoids the high gain control loop and is as follows.

All controllers containing an integral term produce a demanded control output given by

$$u' = u_{\mathrm{I}} + u_{\mathrm{c}} \tag{6.2}$$

where u_{I} is the output of the integral term and u_{c} is the net contribution from all the other terms in the controller. The physical control input, u, is subject to saturation and given by

$$u = \begin{cases} u_{\max} & \text{if} \quad u' > u_{\max} \\ u' & \text{if} \quad |u'| < u_{\max} \\ -u_{\max} & \text{if} \quad u' < -u_{\max} \end{cases} \tag{6.3}$$

For example, in a linear state feedback plus integral controller applied to a third order plant such as the throttle valve,

$$u_I = K_{\mathrm{I}} \int (y_{\mathrm{r}} - y)\, dt \tag{6.4}$$

and

$$u_c = -\left(g_1 \cdot \hat{x}_1 + g_2 \cdot \hat{x}_2 + g_3 \cdot \hat{x}_3\right) \tag{6.5}$$

Whenever saturation occurs, the integrator is reinitialised to

$$\frac{1}{K_I}\left(u - u_c\right) \tag{6.6}$$

Finally, it was realised that the go/no-go test used to determine the maximum allowed parametric variance during the Monte Carlo runs, though at the moment an industry standard, is less than ideal. It is proposed instead to carry out some tests using another criterion, which is the RMS control error of the step response relative to the ideal step response, $y_{\text{ideal}}(t)$, taken as a proportion of the step reference input level, Y_r, taken over a duration equal to the settling time. Thus

$$e_{\text{rms}} = \frac{1}{|Y_r|}\sqrt{\int_0^{T_s}\left[y(t) - y_{\text{ideal}}(t)\right]^2 dt}\,, \tag{6.7}$$

A maximum threshold, $e_{\text{rms}}^{\max}$, would be decided in advance. Then the variance, $\sigma_{\%}$, would be stepped up and the Monte Carlo runs continued until $e_{\text{rms}} > e_{\text{rms}}^{\max}$ whereupon the corresponding maximum variance, $\sigma_{\%}^{\max}$, would be noted as a figure of merit for the controller under test, as previously.

References

ARMSTRONG-HELOUVRY, B. & AMIN, B. (1994) PID control in the presence of static friction: exact and describing function analysis. *American Control Conference.*

ASTRÖM, K. J. & HÄGGLUND, I. (1995) *PID controllers theory design and tuning*.

ASTROM, K. J. & RUNDQWIST, L. (1989) Integrator Windup and How to Avoid It. *American Control Conference, 1989.*

BANKS, A., NIVEN, M. & ANDERSSON, P. (2010) Boosting technology for Euro VI and Tier 4 final heavy duty diesel engines without NOx aftertreatment. *Ricardo Consulting Engineers Ltd*.

DODDS, S. J. (2004) A novel approach to robust motion control of electric drives with model uncertainty. *Advances in Electrical and Electronic Engineering,* 3.

DODDS, S. J. (2007) Observer based robust control. *Advances in Computing and Technology Conference (AC&T) , University of East London.*

DODDS, S. J. (2008) Settling time formulae for the design of control systems with linear closed loop dynamics. *Advances in Computing and Technology Conference (AC&T) , University of East London.*

DODDS, S. J. (2013) *Feedback Control: Techniques, Design and Industrial applications* Springer (Planed for publication by the end of the year).

DODDS, S. J. & VITTEK, J. (2009) Sliding mode vector control of PMSM drives with flexible couplings in motion control. *Advances in Computing and Technology Conference (AC&T) , University of East London.*

DODDS, S. J. & WALKER, A. B. (1991) Three axis Sliding Mode Attitude Control of Rigid body Spacecraft with Unknown Dynamic Parameters. *International Journal of Control,* 54.

FALLAHI, A. (2013) Robust Control of Diesel Drivelines. *ACE (Thesis).* University of East London.

FRANKLIN, G. F., POWELL, D. P. & EMAMI-NAEINI, A. (2002) *Feedback Control Of Dynamic Systems (Fourth Edition)*.

HAESSIG, D. A. & FRIEDLAND, B. (1990) On the Modeling and Simulation of Friction. *American Control Conference, 1990.*

HENSEN, R. H. A. (2002) Controlled Mechanical Systems with Friction. *DISC Thesis (ISBN 90-386-2693-2).* Technische Universiteit Eindhoven.

HEYWOOD, J. B. (1988) *Internal Combustion Engine Fundamentals*.

IANNELLIA, L., JOHANSSONB, K. H., JÖNSSONC, U. T. & VASCAA, F. (2005) Averaging of nonsmooth systems using dither. *Automatica*.

KALMAN, R. E. (1960) On the General Theory of Control Systems. *First IFAC Moscow Congress.*

LANDAU, L. D. & ZITO, G. (2006) *Digital Control Systems - Design Identification and Implementation*, Springer.

LEONARD, N. E. & KRISHNAPRASAD, P. S. (1992) Adaptive friction compensation for bi-directional low-velocity position tracking. *Proceedings of the 31st IEEE Conference on Decision and Control.*

LJUNG, L. (1998) *System Identification - Theory for the User*, Pearson Education.

LUENBERGER, D. (1971) An introduction to observers. *IEEE Transactions on Automatic Control,* 16**,** 596-602.

LUENBERGER, D. G. (1964) Observing the State of a Linear System. *IEEE Transactions on Military Electronics,* 8**,** 74-80.

MAJD, V. J. & SIMAAN, M. A. (1995) A continuous friction model for servo systems with stiction. *Proceedings of the 4th IEEE Conference on Control Applications.*

MESHRAM, P. M. & KANOJIYA, R. G. (2012) Tuning of PID controller using Ziegler-Nichols method for speed control of DC motor. *Advances in Engineering, Science and Management (ICAESM),.*

MOHAN, N., UNDERLAND, T. M. & ROBBINS, W. P. (1995) *Power Electronics Converters, Applications ans Design (Second Edition)*.

PAPADOPOULOS, E. G. & CHASPARIS, G. C. (2002) Analysis and model-based control of servomechanisms with friction. *IEEE/RSJ International Conference on Intelligent Robots and Systems.*

PEDERSEN, J. L. & DODDS, S. J. (2011) A comparison of two robust control techniques for throttle valve control subject to nonlinear friction. *Advances in Computing and Technology Conference (AC&T) , University of East London.*

PINTELON, R. & SCHOUKENS, J. (2004) *System Identification - A Frequency Domain Approach*, John Wiley & Sons.

POPOV, V. L. (2010) *Contact Mechanics and Friction*, Springer.

RADCLIFFE, C. J. & SOUTHWARD, S. C. (1990) A Property of Stick-Slip Friction Models which Promotes Limit Cycle Generation. *American Control Conference, 1990.*

SABANOVIC, A., FRIDMAN, L. & SPURGEON, S. K. (2004) *Variable Structure Systems: from Principles to Implementation* Institution of Electrical Engineers.

SANJUAN, M. & HESS, D. P. (1999) Understanding dynamic of machinery with friction through computer simulation. *ASEE Southeastern Section Conference.*

SCATTOLINI, R., SIVIERO, C., MAZZUCCO, M., RICCI, S., POGGIO, L. & ROSSI, C. (1997) Modeling and identification of an electromechanical internal combustion engine throttle body. *Control Engineering Practice,* 5**,** 1253-1259.

SCHÖPPE, D., GEURTS, D., BALLAND, J. & SCHREURS, B. (2005) Integrated Strategies for Boost and EGR Sys-tems for Diesel Engines to achieve most stringent Emission Legislation. *10. Aufladetechnischen Konferenz in Dresden.*

SHAHROKHI, M. & ZOMORRODI, A. (2003) Comparison of PID Controller Tuning Methods. *8th National Iranian Chemical Engineering Congress*

SIRA-RAMIREZ, H. (1993) On the dynamical sliding mode control of nonlinear systems. *International Journal of Control, Special Issue on Variable Structure Control,* 57.

SPURGEON, S. K. & EDWARDS, C. (1998) *Sliding Mode Control: Theory and Applications*, Taylor & Francis.

STADLER, P. A. (2008) Modelling and Control of a Vacuum Air Bearing Linear Drive in the Nanometer Range. *SCOT Thesis.* University of East London.

STADLER, P. A., DODDS, S. J. & WILD, H. G. (2007) Observer based robust control of a linear motor actuated vacuum air bearing. *Advances in Computing and Technology Conference (AC&T) , University of East London.*

TOWNSEND, W. & SALISBURY, J., JR. (1987) The Effect of coulomb friction and stiction on force control. *IEEE International Conference on Robotics and Automation.*

TRIVEDI, P. K. & BANDYOPADHYAY, B. (2010) Non unique equivalent control in sliding mode with linear surfaces. *International Conference on Power, Control and Embedded Systems (ICPCES).*

TSENG, M.-L. & CHEN, M.-S. (2010) Chattering reduction of sliding mode control by low-pass filtering the control signal. *Asian Journal of Control,* 12.

UTKIN, V. (1977) Variable structure systems with sliding modes. *IEEE Transactions on Automatic Control,* 22**,** 212-222.

UTKIN, V. I., YOUNG, K. D. & OZGUNER, U. (1999) A control engineer's guide to sliding mode control. *IEEE Transactions on Control Systems Technology,* 7**,** 328-342.

VITTEK, J., BRIS, P., STULRAJTER, M., MAKYS, P., COMNAC, V. & CERNAT, M. (2008) Chattering free sliding mode control law for the drive employing PMSM position control. *Optimization of Electrical and Electronic Equipment, 2008. OPTIM 2008. 11th International Conference on.*

WALLANCE, F., WATSON, N., FRENCH, C. J., JOYCE, A. & REITZ, R. (1999) *Diesel Engine Reference Book (Second edition), Chapter 1, 2, 5, 6 & 7*.

XINGHUO, Y., QINGLONG, H., XIANGJUN, L. & CHANGHONG, W. (2008) Time-delay effect on equivalent control based single-input sliding mode control systems. *International Workshop on Variable Structure Systems, 2008. VSS '08. .*

ZAMES, G. & SHNEYDOR, N. (1976) Dither in nonlinear systems. *Automatic Control, IEEE Transactions on,* 21**,** 660-667.

ZAMES, G. & SHNEYDOR, N. (1977) Structural stabilization and quenching by dither in nonlinear systems. *Automatic Control, IEEE Transactions on,* 22**,** 352-361.

Appendix

A.1 Engine Systems Overview

A.1.1 The Natural Aspirated Diesel Engine

With reference to Figure A, the fresh atmospheric air enters the system through the air filter which removes particle like dirt and sand which would otherwise damage the engine system. The air enters the four-stroke engine through the inlet valves into a cylinder (one at the time) during the intake stroke. Once the intake valves are closed, the compression stroke commences in which the engine piston moves towards the top of the cylinder. The trapped air in the cylinder increases in temperature to several hundred degrees Celsius. Just before the piston reaches top dead centre, the fuel is injected. This starts to combust due to the high air temperature inside the cylinder. The pressure force from the combustion pushes the piston down on the power stroke, to drive the crank shaft. The crank shaft is connected to the wheels of the vehicle through the drive train (gearbox, drive shaft etc.).

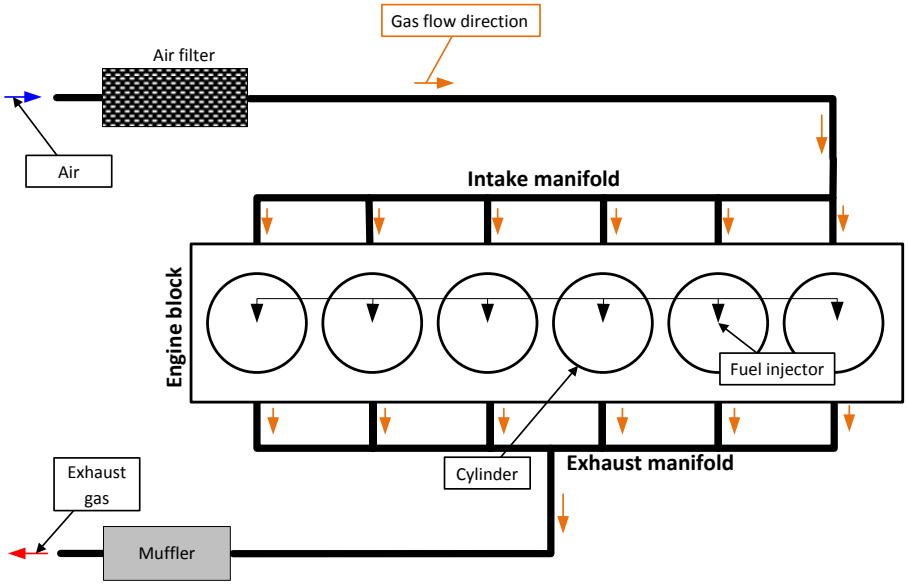

Figure A: Basic schematic of a natural aspirated Diesel engine

At a certain point the exhaust valve is opened and the hot gas exits the cylinder through the exhaust manifold into the muffler/silencer which removes the noise due to pressure alternations from the combustion.

The air-to-fuel ratio inside the cylinder is very important for the combustion process. The stoichiometric air-to-fuel ratio (Heywood, 1988)

$$AF_{ratio} = \frac{Air\ mass}{Fuel\ mass} \tag{A.1}$$

for a Diesel engine is 14.6, meaning that to burn 1 kg of fuel, 14.6 kg of air is needed to burn all the fuel. Compared to the petrol engine process where it is important to maintain a specified stoichiometric air-to-fuel ratio, the Diesel engine process can run with a wider range of air-to-fuel ratios. In practice, the Diesel engine runs with air-to-fuel ratios between 19 and 60. Too low an A/F ratio, however, will suffocate the combustion resulting in a decrease in torque and an increase in the smoke / particulate matter level. Some of the *particulate matter* (PM) is fine particles which can cause serious health issues.

The natural aspirated Diesel engine has a tendency to run with a low A/F ratio caused by the air restrictions like the air filter, air duct etc. To circumvent this problem the air pressure in the intake manifold can be increased letting more air into the cylinder making the A/F ratio higher. This can be done by adding a mechanical compressor (driven by the crank shaft) or a turbo charger (driven by the exhaust gas flow) to the engine system. The turbo charger has two components comprising a compressor and a turbine which are linked together with a rotating mechanical shaft as shown in Figure B. The turbine is located on the exhaust side where the hot gas passes through it. The gas expands through the turbine, which converts the energy from the gas into mechanical energy making the mechanical shaft rotate.

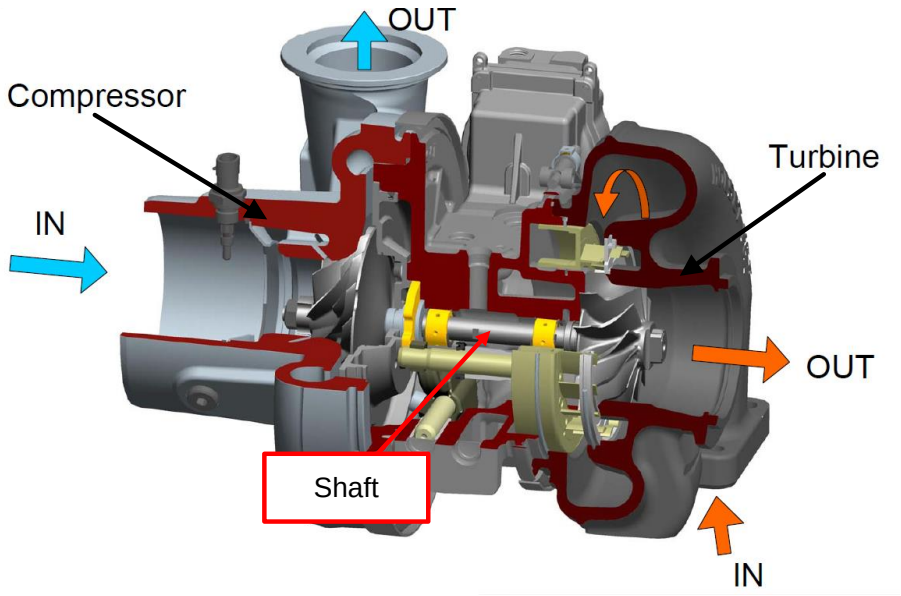

Figure B: Turbo charger from Cummins Turbo Technologies

The shaft drives the compressor which will increase the air pressure on the output. The compressor is located between the air filter and the intake manifold as shown in Figure C.

A.1.2 The Turbo Charged Diesel Engine

In a turbo charged engine system (Figure C) the fresh atmospheric air enters the system through the air filter as in the natural aspirated engine. The air is boosted to a higher pressure by the compressor, this increases the air density but also its temperature. This is taken advantage of to increase the air density further by passing this heated air through an air-to-air cooler called the intercooler. The cooled air enters the engine through the inlet valves and from this point the events that take place are the same as in the naturally aspirated engine described in subsection 0.

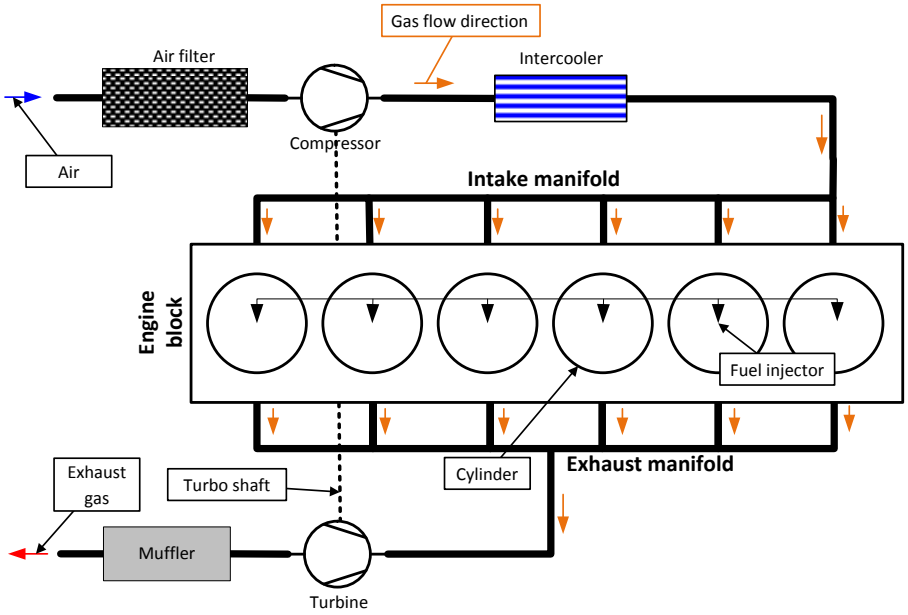

Figure C: Basic schematic of a turbo charged Diesel engine

The exhaust gas expands through the turbine, which spins typically in a range between 90,000 to 200,000 [rpm], and the air, which is cooled by this process, leaves the engine system through a muffler/silencer as it was described in subsection 0.

Increasing the A/F ratio will, however, also increase the combustion temperature leading to an increase in the production of *nitrogen oxides* (NO_x) in the exhaust gases. The NO_x has a damaging effect on the environment, forming a) particulates by reacting with ammonia and b) ozone by reacting with volatile organic compounds. The ozone can have a damaging effect on the respiratory system. These considerations have led to enhanced emission standards around the world, in particular Japan, US, Europe, mostly concerned with CO, NO_x, HC and PM. Different regions have, at present, different maximum emission thresholds, but a world harmonised standard is being developed. In Europe there are different emission standards for cars, off road vehicles and HD Diesel engines, entailing different maximum thresholds and

test specifications. Today there are two emission tests for HD Diesel engines, a steady-state (Table A.1) and a transient test cycle (not shown). The emission standard for HD Diesel engines is somewhat different from that of cars, because the engine is tested in isolation from the vehicle. This implies that if more than one vehicle uses the same engine model, the test only has to be carried out just one time.

Table A.1: EU Emission Standards for HD Diesel Engines: Steady-State Testing

Standard	**Date**	**CO [g/kWh]**	**NO_x [g/kWh]**	**HC [g/kWh]**	**PM [g/kWh]**
EURO 0	1988-1992	12.3	15.8	2.60	none
EURO I	1992-1995	4.9	9.0	1.23	0.40
EURO II	1995-1999	4.0	7.0	1.10	0.15
EURO III	1999-2005	2.1	5.0	0.66	0.10
EURO IV	2005-2008	1.5	3.5	0.46	0.02
EURO V	2008-2012	1.5	2.0	0.46	0.02
EURO VI	2013-	1.5	0.4	0.13	0.01

Source: The Internet (Dieselnet.com & Delphi.com)

In the steady-state test the engine is tested at different speeds and load points in which the emission is measured and tested against the thresholds in Table A.1. In the transient test, the engine is again tested at different speeds and loads but including engine stops and starts. In this case, the emission levels are monitored continually during the test and their peak values are not allowed to exceed a certain value.

The first emission standard EURO 0 for HD Diesel engines came into place in the late 1980's. Through the years emission levels have decreased dramatically, as it is evident in Table A.1, a pertinent example being the NO_x

levels dropping from 15.8 [g/kWh] in 1988 to 0.4 in 2012 (-3850%). These decreasing emission thresholds have forced the automotive industry to find new technologies to meet the lower emission thresholds. There are different ways of achieving lower emission outlets such as piston and cylinder design, Diesel injector design, fuel properties, exhaust gas after-treatment and exhaust gas recirculation (EGR).

EGR helps to reduce NO_x by reducing the peak combustion temperature. The idea is to mix inert gas (i.e., gas that cannot take part in the combustion process) with fresh air to reduce the peak combustion temperature. This inert gas is contained in the exhaust gas, which is re-circulated to the intake side of the engine (Figure D). For this, the exhaust gas recirculation rate is defined as

$$EGR_{rate} = \dot{m}_{egr} / \left(\dot{m}_{egr} + \dot{m}_{air} \right) \quad \text{(A.2)}$$

where $\dot{m}_{air}$ is the air mass flow rate and $\dot{m}_{egr}$ is the EGR mass flow rate. The EGR_{rate} will moderate the NO_x concentration in the exhaust gases, a higher EGR_{rate} giving less NO_x.

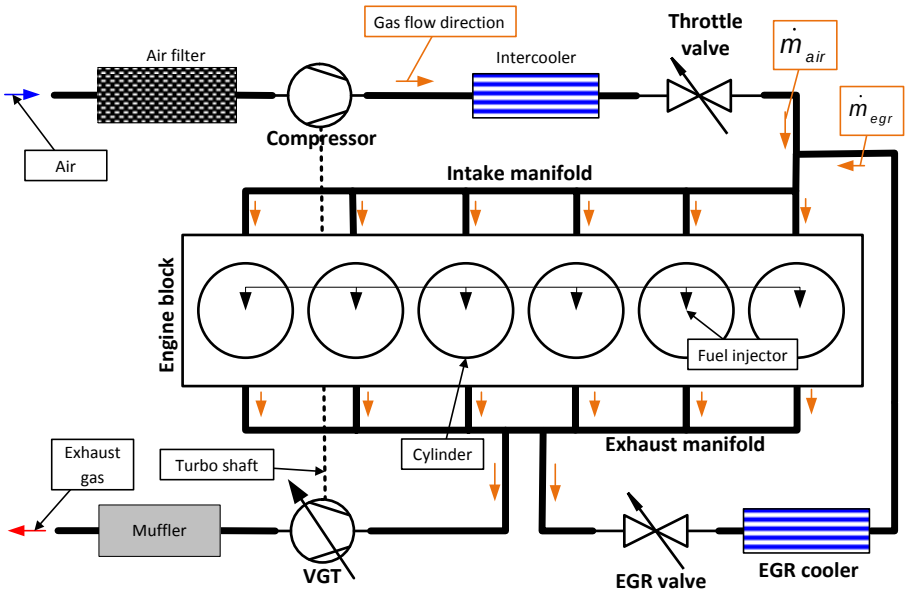

Figure D: Schematic of a turbo charged Diesel engine with EGR

The EGR path (EGR valve and EGR cooler) in Figure D, is often referred to as a high pressure EGR due to the high pressure in the exhaust / intake manifold. This high pressure is a result of the operating range for the turbine and compressor.

The EGR flow can be adjusted by the valve in the EGR path, but the maximum flow rate which can be achieved depends on the differential pressure across the EGR path (EGR valve, EGR cooler and pipe work). The differential pressure is a function of factors such as the turbo system operating point, inlet and outlet valve design and the combustion characteristics.

In Figure D, the turbine has been replaced by a *variable geometry turbine* (VGT). The operating point of the VGT can be adjusted by opening and closing its vanes. This varies the turbine speed, making it possible to adjust the compressor output pressure. The pressure can only be adjusted in a limited range which is a function of the engines operation point, such as the exhaust flow and temperature. The pressure in the intake manifold determines how much gas/air can go into the cylinder per intake stroke. More engine torque, requires more air which again requires a higher intake manifold pressure. If the EGR_{rate} of equation A.2 has to be kept constant, then $\dot{m}_{egr}$ has to increase as well making the pressure even higher.
One of the problems of using EGR is that the re-circulated exhaust gas contains particulate matter from the combustion which clogs up the EGR cooler in time.

As mentioned before more air in the cylinder gives a cleaner combustion which again lowers the PM output, but it also leads to an increase in the NO_x formation. A higher EGR_{rate}, however, decreases the NO_x formation but increases the particulate output, caused by the increased inert gas in the

combustion chamber. This conflict between the EGR and air results in a compromise for the set points of the AF_{ratio} and the EGR_{rate}.

The low levels of emission in the standards have forced engine manufacturers to add more emission decreasing devices to the engine system to meet these (Banks et al., 2010). A schematic example of a EURO VI engine configuration can be seen in Figure E. There are two major differences between this and the previous figure which are the low/high pressure EGR loops and the exhaust gas after treatment.

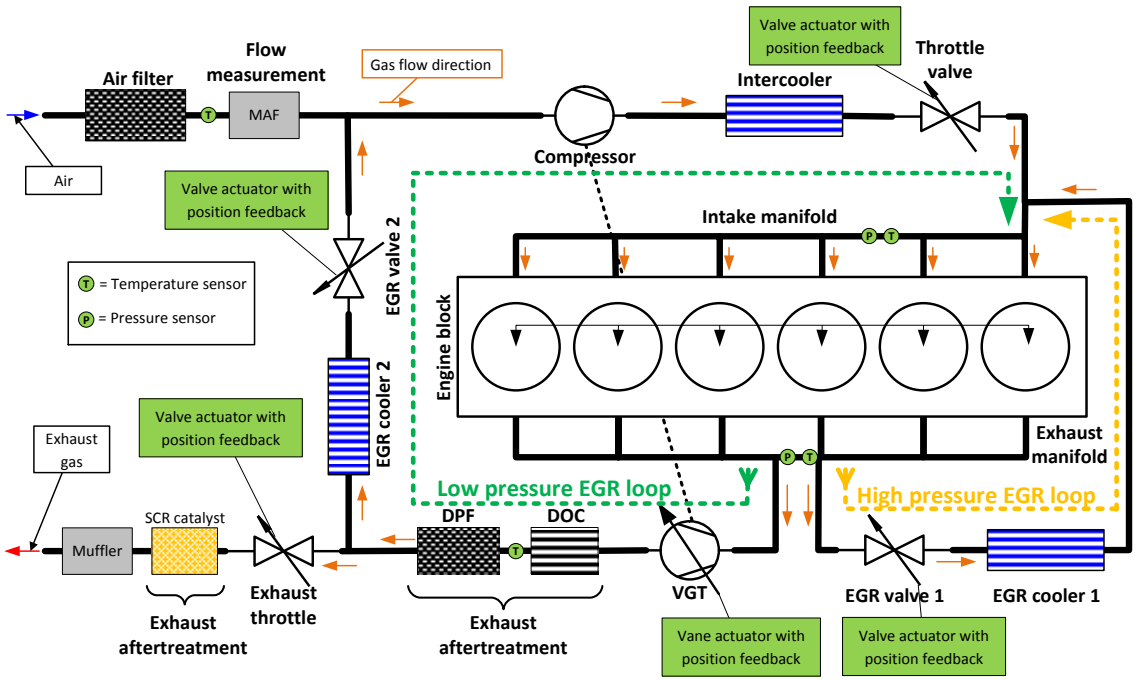

Figure E: An example of a schematic for Euro VI engine configuration with high and low pressure EGR

The after treatment is a necessity for most modern engine systems to meet the strict emission regulations. There are different after treatment systems available on the market and still more are coming. They can be split into the following two groups:

a) The NO_x reduction system, which is usually based on *selective catalytic reduction* (SCR), which converts nitrogen oxides into N_2 and water. For this system, either ammonia (NH_3) or urea (NH_2) has to be added to the exhaust gas before the catalyst. For most SCR systems on HGVs, a water diluted urea solution is used called *AdBlue,* stored in a separate tank. This solution is dosed (pumped) into the hot exhaust gas before the SCR unit for it to evaporate into gas form. The amount of AdBlue is determined by how much the engine NO_x level has to be reduced.

b) The particulate reduction system, which requires a *Diesel oxidation catalyst* (DOC) and a *Diesel particulate filter* (DPF) inserted in the exhaust system as close as possible to the engine outlet manifold, to maximise the temperature and hence the reaction rate. The DPF catches the particles from the exhaust gas in a ceramic filter structure. When the engine runs the DPF will slowly clog up with particulate matter, thereby impeding the exhaust gas. The DPFs used on HGVs are of the regenerative type. During the regeneration, the trapped particulate matter is burned away in the DPF, creating ash. The ash leaves the ceramic filter and into the surrounding environment through the exhaust system. The regeneration burn of the DPF starts when a minimum temperature of several hundred °C is reached and enough oxygen is available. The DOC is an oxidation catalyst which can create heat by oxidising/burning the non-burned fuel and oxygen in the exhaust gas. The heat from the DOC can start the regeneration process in the DPF. Too high a temperature in the DPF can damage the filter structure, and too low a temperature will stop the regeneration. It is therefore important to keep the correct exhaust Air-to-fuel ratio during the regeneration of the DPF.

The function of the low pressure EGR is the same as the high pressure EGR, which is to lower the exhaust NO_x level. The low pressure EGR takes the gas after it has been filtered through after-treatment which it leaves with less

particulate matter. The low pressure EGR path also benefits from a higher level of cooling making the density higher. The low pressure EGR is sometimes used to save money on the exhaust after-treatment system and can in some cases remove the need for after-treatment. To control the flow through the low pressure EGR path, two valves are sometimes needed, as shown in Figure E. The EGR valve, in the low pressure EGR path, is used to control the flow through the low pressure EGR cooler and the exhaust throttle valve to create a differential pressure over the low pressure EGR system.

With reference to Figure E, there are five position control loops indicated, required for four valves and the VGT. The throttle valve, described in more detail in Chapter 1, is the focus of this research programme but this will be equally useful for the other applications as each of these has similar characteristics.

A.2 Parameters used for the Simulation

Parameters used throttle valve for the simulations:

1. DC motor wheel diameter [-]
   - N_m = 1
2. Throttle plate wheel diameter [-]
   - N_{pl} = 11.5
3. DC motor torque constant [Nm/A]
   - k_t = 0.0257
4. DC motor speed constant [V sec/rad]
   - k_e = 0.0257
5. DC motor resistance [ohm]
   - R_a = 2.795
6. Inductance [H]
   - $L_a = 8.372 \cdot 10^{-4}$
7. Total system pure time delay (Electrical & mechanical) [sec]
   - System_delay = 0.0016
8. Coil spring constant [Nm/rad]
   - k_{spring} = 0.0581
9. Throttle system moment of inertia (plate, DC motor and spindle) [kg*m^2]
   - $J_x = 8.521 \cdot 10^{-4}$
10. Initial spring position (Simulates the initial spring torque) [Rad]
    - $\theta_{Initial\ spring}$ = 4.427
11. Hard stop gain [Nm/rad]
    - $k_{hard\ stop}$ = 100
12. Maximum position hard stop [Rad]
    - $\theta_{pl_{max}}$ = 90/360*2*pi

13. Minimum position hard stop [Rad]
    - $\theta_{pl_{\min}}$ = -0.1/360*2*pi
14. Kinetic friction constant [Nm sec/rad]
    - $k_{kinetic}$ = 0.0022
15. Coulomb friction constant [Nm]
    - $k_{coulomb}$ = 0.0836
16. Static friction model speed constant [rad/sec]
    - ω_1 = 0.01
17. Static friction model torque constant [Nm sec/rad]
    - Γ_1 = 0.0539
18. Static friction model speed constant [rad/sec]
    - ω_2 = 0.0470
19. Static friction model torque constant [Nm sec/rad]
    - Γ_2 = 0.001

A.3 Calculations for Linear State Feedback with Integrator for Steady State Error Elimination

This section contains a detailed calculation for the 'Linear State Feedback with Integrator for Steady State Error Elimination' in subsection 4.6.3.1.

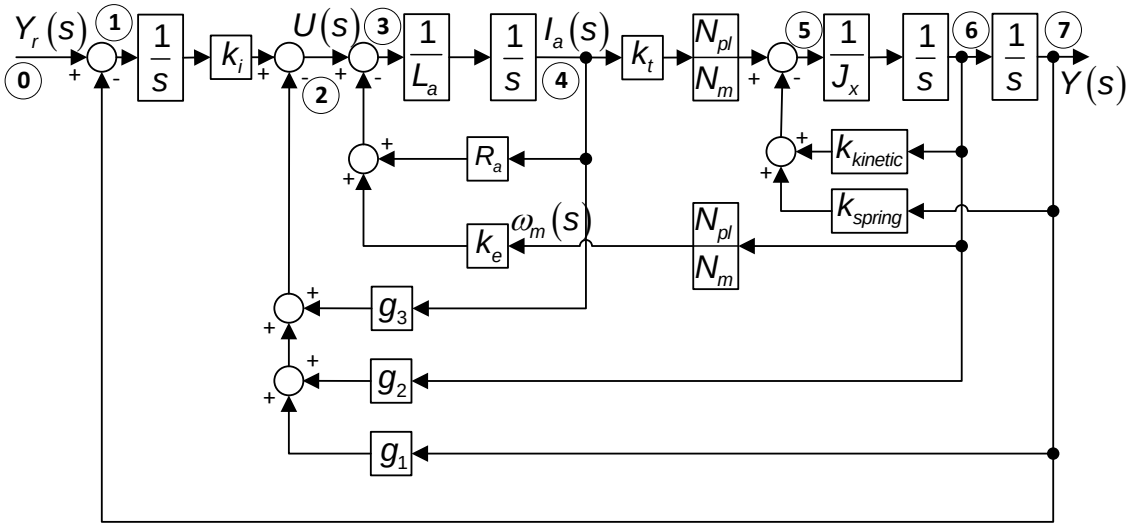

Figure F: LSF with integrator and plant model

Using Mason's rule to calculate the closed loop transfer function of Figure F (numbers refers to encircled numbers)

L1: [3,4,3]

L2: [5,6,5]

L3: [5,6,7,5]

L4: [3,4,5,6,3]

L5: [2,3,4,2]

L6: [2,3,4,5,6,2]

L7: [2,3,4,5,6,7,2]

L8: [1,2,3,4,5,6,7,1]

Forward path gain (from y_r to y) [0,1,2,3,4,5,6,7]

$$\frac{k_t}{L_a}\frac{N_{pl}}{N_m}\frac{1}{J_x}\frac{1}{s^4}k_i \tag{G.1}$$

Loop path gain

L1: $-\frac{R_a}{L_a}\frac{1}{s}$, L2: $-\frac{k_{kinetic}}{J_x}\frac{1}{s}$, L3: $-\frac{k_{spring}}{J_x}\frac{1}{s^2}$, L4: $-\frac{k_t}{L_a}\frac{k_e}{J_x}\left(\frac{N_{pl}}{N_m}\right)^2\frac{1}{s^2}$,

L5: $-\frac{g_3}{L_a}\frac{1}{s}$, L6: $-g_2\frac{k_t}{L_a}\frac{N_{pl}}{N_m}\frac{1}{J_x}\frac{1}{s^2}$

L7: $-g_1\frac{k_t}{L_a}\frac{N_{pl}}{N_m}\frac{1}{J_x}\frac{1}{s^3}$, L8: $-\frac{k_t}{L_a}\frac{N_{pl}}{N_m}\frac{1}{J_x}\frac{1}{s^4}k_i$

None touching loops

(L1,L2): $\frac{R_a}{L_a}\frac{k_{kinetic}}{J_x}\frac{1}{s^2}$, (L1,L3): $\frac{R_a}{L_a}\frac{k_{spring}}{J_x}\frac{1}{s^3}$, (L2,L5): $\frac{g_3}{L_a}\frac{k_{kinetic}}{J_x}\frac{1}{s^2}$,

(L3,L5): $\frac{g_3}{L_a}\frac{k_{spring}}{J_x}\frac{1}{s^3}$

$$G(s)=\frac{\frac{k_t}{L_a}\frac{N_{pl}}{N_m}\frac{k_i}{J_x}\frac{1}{s^4}}{1-(L1+L2+L3+L4+L5+L6+L7+L8)+L1\cdot L2+L1\cdot L3+L2\cdot L5+L3\cdot L5} \tag{G.2}$$

$$G(s)=\frac{\frac{k_t}{L_a}\frac{N_{pl}}{N_m}\frac{k_i}{J_x}}{s^4+s^3\left(\frac{R_a}{L_a}+\frac{k_{kinetic}}{J_x}+\frac{g_3}{L_a}\right)+s^2\left(\frac{k_{spring}}{J_x}+\frac{k_t}{L_a}\frac{k_e}{J_x}\left(\frac{N_{pl}}{N_m}\right)^2+\frac{R_a}{L_a}\frac{k_{kinetic}}{J_x}+\frac{k_t}{L_a}\frac{N_{pl}}{N_m}\frac{g_2}{J_x}+\frac{g_3}{L_a}\frac{k_{kinetic}}{J_x}\right)+s\left(\frac{R_a}{L_a}\frac{k_{spring}}{J_x}+\frac{k_t}{L_a}\frac{N_{pl}}{N_m}\frac{g_1}{J_x}+\frac{g_3}{L_a}\frac{k_{spring}}{J_x}\right)+\frac{k_t}{L_a}\frac{N_{pl}}{N_m}\frac{k_i}{J_x}}$$

(G.3)

Using equation (G.3), and after some manipulation

$$\frac{Y(s)}{Y_r(s)}=G(s)=\frac{b_0}{s^4+a_3s^3+a_2s^2+a_1s+a_0} \qquad \text{(G.4)}$$

where

$$b_0=\frac{k_t}{L_a}\frac{N_{pl}}{N_m}\frac{k_i}{J_x}$$

$$a_0=\frac{k_t}{L_a}\frac{N_{pl}}{N_m}\frac{k_i}{J_x}$$

$$a_1=\frac{R_a}{L_a}\frac{k_{spring}}{J_x}+\frac{k_t}{L_a}\frac{N_{pl}}{N_m}\frac{g_1}{J_x}+\frac{g_3}{L_a}\frac{k_{spring}}{J_x}$$

$$a_2=\frac{k_{spring}}{J_x}+\frac{k_t}{L_a}\frac{k_e}{J_x}\left(\frac{N_{pl}}{N_m}\right)^2+\frac{R_a}{L_a}\frac{k_{kinetic}}{J_x}+\frac{k_t}{L_a}\frac{N_{pl}}{N_m}\frac{g_2}{J_x}+\frac{g_3}{L_a}\frac{k_{kinetic}}{J_x}$$

$$a_3=\frac{R_a}{L_a}+\frac{k_{kinetic}}{J_x}+\frac{g_3}{L_a}$$

A.4 H-bridge with Output Current Measurement

The DC motor is driven by an H-bridge circuit acting like a power amplifier, shown in Figure G. The demand is converted by the dSPACE system into a *pulse width modulation* (PWM) signal with fixed switch frequency and a mark-space ratio (duty cycle) which dependents on the voltage demand. The H-bridge driver converts the PWM and direction signals, into pulses which drives the four transistors dependent on the direction. To drive the DC motor in the clockwise direction the transistor T1 and T4 have to be on, and for the anticlockwise direction transistor T2 and T3 have to activated.

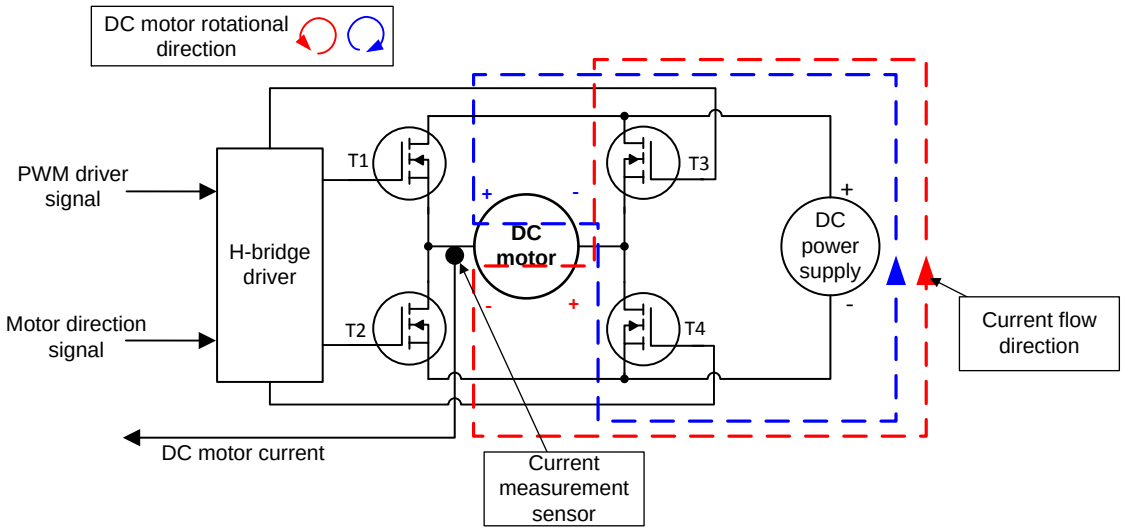

Figure G: H-bridge schematic

The output current from the H-bridge is measured by a current sensor. The current sensor is a closed loop Hall–effect type with a high frequency bandwidth. Throughout the industry the norm is to sample a PWM driven current synchronous to the switching to eliminate the aliasing effect. Unfortunately the dSPACE cannot sample the signals synchronous due to limitations in the hardware. The output from the current sensor is low pass filter by a passive filter acting as a high frequency antialiasing filter. To circumvent

the problem with asynchronous sampling the current signal is oversampled (= 20 kHz) and a periodical average signal is generated every time the control strategy runs.

The H-Bridge and current measurement circuit are done on separate boards to keep the switching noise to a minimum. The switching noise is generated when the H-Bridge transistors are rapidly turn on and off (switch frequency = 10 kHz). The H-Bridge and current measurement circuit boards are made by the author, shown in Figure H.

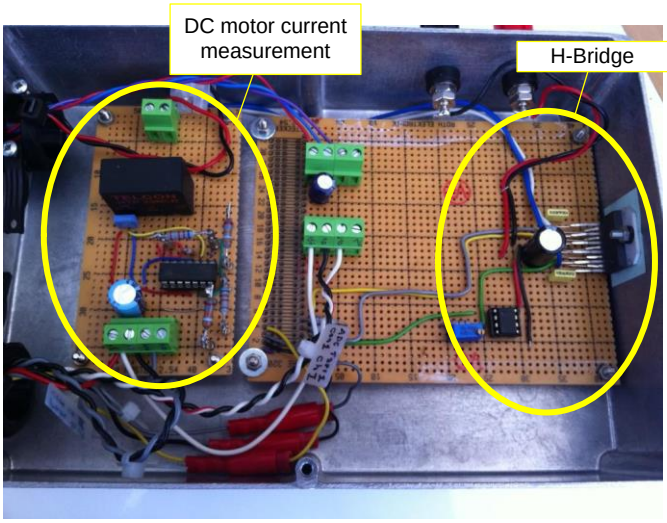

Figure H: H-bridge and current measurement boards

A.5 Throttle Valve Exploded View

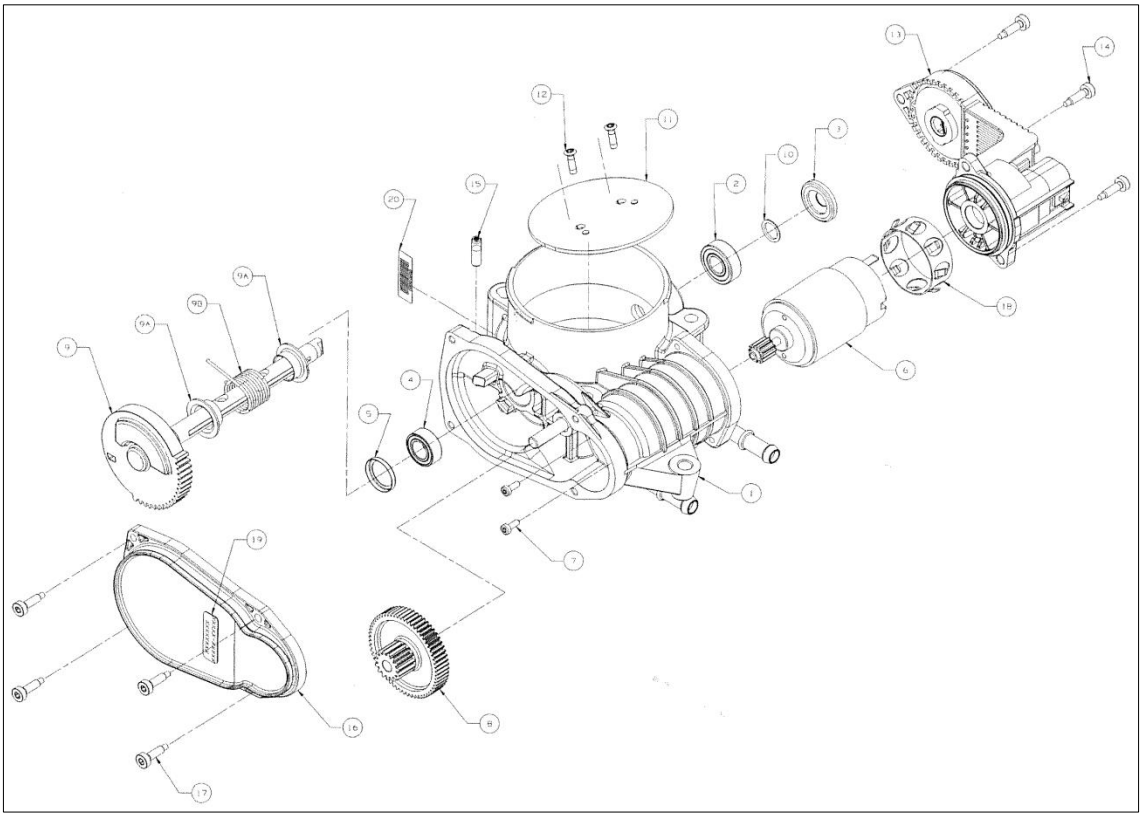

Figure I: Throttle valve exploded view

Published Work

A comparison of two robust control techniques for throttle valve control subject to nonlinear friction

A COMPARISON OF TWO ROBUST CONTROL TECHNIQUES FOR THROTTLE VALVE CONTROL SUBJECT TO NONLINEAR FRICTION

Jacob L. Pedersen†, Stephen J. Dodds‡
†Delphi Diesel Systems Ltd, Park Royal, London, United Kingdom
‡CITE, University of East London, United Kingdom
Jacob.pedersen@delphi.com, stephen.dodds@spacecon.co.uk

Abstract: Throttle valves for internal combustion engines suffer from considerable nonlinear friction in their mechanisms that is difficult to model and subject to significant variations due to changes in temperature and wear over the lifetime. The stick slip friction component is particularly troublesome. This presents a challenge to control system designers when it is important to obtain a prescribed dynamic response to reference input position changes. The contributions of this paper are a) the comparison of two different robust control techniques (sliding mode control and observer based robust control) aimed at overcoming this difficulty and b) a new simple but accurate nonlinear friction model for simulation. The control system performances using these techniques are compared with one another and with the performance attainable with a conventional PI controller.

1. Introduction:

The throttle valve, an example of which is shown in Figure 1, is an essential component on both petrol and Diesel internal combustion engines. They are used mainly for controlling the air-to-fuel ratio by applying a variable constraint to the air path.

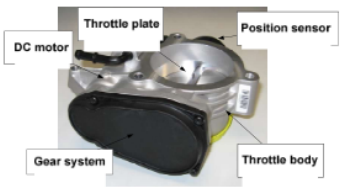

Figure 1: Throttle valve

This is achieved by opening and closing the throttle plate which is driven by a DC motor through a gear system. The position is measured by a position sensor attached to the plate.

Throttle valves suffer from considerable nonlinear friction in their mechanisms that is considered difficult to model and is subject to significant variations due to changes in temperature and wear over the lifetime. The stick slip friction component is particularly troublesome and causes controller limit cycling (Armstrong-Helouvry and Amin, 1994). This presents a challenge to control system designers when it is important to obtain a prescribed dynamic response to reference input position changes.

The state of the art controller is a PI governor with measures to overcome the static friction. This can be achieved, for example, by injecting an additional oscillatory signal to the control variable that produces a corresponding torque just sufficient to overcome the static friction, known as dither. The amplitude and frequency of this signal depends on the mechanical components and their wear. This makes the task of commissioning the controller time consuming. The robust control methods presented in this paper are intended to overcome this limitation.

2. Throttle valve modelling:

2.1. Linear throttle valve model:

The DC motor drives a gear train that is connected to the throttle plate and a position sensor, as modelled in Figure 2.

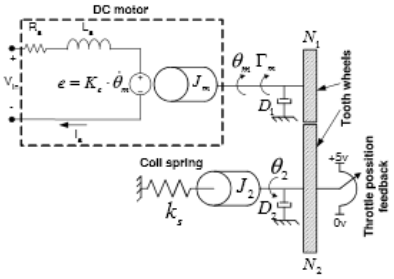

Figure 2: Throttle system model.

On both sides of the gear there are moments of inertia, J_m and J_2, and kinetic friction (i.e., viscose friction) coefficients, D_1 and D_2. The DC motor is modelled in the standard form:

$$v_{in}(t) = L_a \frac{di_a}{dt} + R_a \cdot i_a(t) + K_e \cdot \omega_m(t) \quad (1)$$

where i_a, R_a, L_a and K_e are, respectively, the armature current, resistance, inductance and back EMF constant. Rearranging (1):

$$\frac{di_a}{dt} = \frac{1}{L_a}\left(v_{in} - i_a \cdot R_a - K_e \cdot \dot{\theta}_m\right) \quad (2)$$

The torque produced by the DC motor is

$$\Gamma_m = i_a(t) \cdot K_t \quad [Nm] \quad (3)$$

where $K_t \cong K_e$ is the motor torque constant. To simplify the model, J_m and D_1 are referred to the right hand side of the gear using

$$\boxed{\frac{\Gamma_2}{\Gamma_m} = \frac{\theta_m}{\theta_2} = \frac{N_2}{N_1}} \quad (4)$$

where N_1 and N_2 are, respectively, the numbers of teeth on the input and output gearwheels. This results in the simplified mechanical subsystem model of Figure 3.

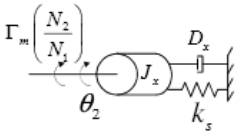

Figure 3: Simplified mechanical system model

The corresponding torque balance equation is

$$\Gamma_m(N_2/N_1) = J_x \cdot \ddot{\theta}_2 + D_x \cdot \dot{\theta}_2 + \theta_2 \cdot k_s \quad (5)$$

where the system inertia and kinetic friction are $J_x = J_m(N_2/N_1)^2 + J_2 \quad \left[kg \cdot m^2\right]$ and $D_x = D_1(N_2/N_1)^2 + D_2 \quad \left[Nm \cdot \sec/rad\right]$, the coil spring constant is k_s [Nm/rad], the gear ratio is N_2/N_1 and the DC motor torque is Γ_m [Nm].

Rearranging (5) yields

$$\ddot{\theta}_2 = \frac{1}{J_x}\left(\Gamma_m \frac{N_2}{N_1} - D_x \cdot \dot{\theta}_2 - \theta_2 \cdot k_s\right) \quad (6)$$

The states for the throttle valve model are chosen as $x_1 = i_a$, $x_2 = \dot{\theta}_2$ and $x_3 = \theta_2$. The measurements are $y_1 = i_a$ and $y_2 = \theta_2$.

The state differential equation can be formed from (2), (3) and (6):

$$\dot{\mathbf{x}} = \mathbf{A}.\mathbf{x} + \mathbf{B}.u \Rightarrow$$

$$\begin{bmatrix} \dot{x}_1 \\ \dot{x}_2 \\ \dot{x}_3 \end{bmatrix} = \begin{bmatrix} a_0 & a_1 & 0 \\ a_2 & a_3 & a_4 \\ 0 & 1 & 0 \end{bmatrix} \cdot \begin{bmatrix} x_1 \\ x_2 \\ x_3 \end{bmatrix} + \begin{bmatrix} b_0 \\ 0 \\ 0 \end{bmatrix} \cdot V_{in} \quad (7)$$

where $a_0 = -R_a / L_a$, $a_1 = -K_e \cdot N_2 / (L_a \cdot N_1)$, $a_2 = K_t \cdot N_2 / (J_x \cdot N_1)$, $a_3 = -D_x / J_x$ $a_4 = -k_s / J_x$ and $b_0 = 1 / L_a$.

The measurement equation is

$$y = C \cdot x \Rightarrow \begin{bmatrix} y_1 \\ y_2 \end{bmatrix} = \begin{bmatrix} 1 & 0 & 0 \\ 0 & 0 & 1 \end{bmatrix} \cdot \begin{bmatrix} x_1 \\ x_2 \\ x_3 \end{bmatrix} \quad (8)$$

The corresponding block diagram is shown in Figure 4.

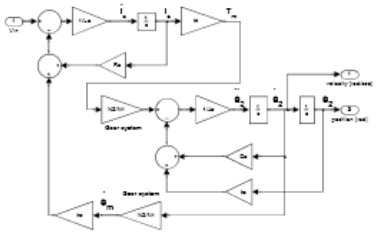

Figure 4: Linear throttle valve model

2.2. Additional nonlinear friction and hard stop models:

Additional refinements to the model of section 2.1 are presented here. They are 1) hard stops, 2) initial coil spring torque and 3) a nonlinear friction model.

2.2.1. Hard stops. The throttle plate has a limited range of angles, usually from 0 to about 90°. These mechanical position constrains are called hard stops. These are modelled by applying a restraining torque proportional to the distance by which the angular limits are exceeded, using a relatively large constant of proportionality, as shown in Figure 5.

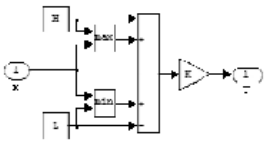

Figure 5 Hard stop model (MathWorks Inc.)

Hence, when x > H the restraining torque is $\Gamma = (H - x) \cdot K$ and when x < L it is $\Gamma = (x - L) \cdot K$.

2.2.2. Initial coil spring torque. The coil spring is pre-stressed in the factory to keep the throttle open in the case of an electrical failure. To model this, a constant torque is added, equal to $\theta_{Initial\ spring} \cdot k_s$

2.2.3. Nonlinear friction model. Through time, the throttle valve on a vehicle will be exposed to moisture and dirt that infiltrates the mechanical system. This will result in an increase in the friction between relatively moving components.

The classical friction model of a bi-directional mechanical system, such as the throttle valve under study, illustrated in Figure 6, comprises three components:

i) Kinetic friction which is a function of velocity: $\Gamma_{kinetic} = \omega \cdot k_{kinetic}$ (9)

ii) Steady (Coulomb) friction:
$$\Gamma_{steady} = sign(\omega) \cdot k_{steady} \quad (10)$$

iii) Static (stick-slip) friction (Papadopoulos and Chasparis, 2002):
$$\Gamma_{stick} = \begin{cases} \Gamma_e, & |\Gamma_e| < \Gamma_s,\ \dot{\theta} = 0,\ \ddot{\theta} = 0 \\ \Gamma_s \cdot sign(\Gamma_e), & |\Gamma_e| > \Gamma_s,\ \dot{\theta} = 0,\ \ddot{\theta} \neq 0 \end{cases} \quad (11)$$

where Γ_e is the externally applied torque, and Γ_s is the breakaway torque.

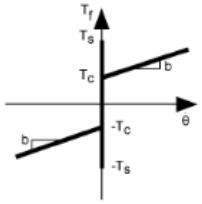

Figure 6: Classic friction model (Papadopoulos and Chasparis, 2002)

This, however, has the drawback of inaccuracy around zero velocity and therefore an improved version will be used.
A generic friction model was proposed by (Majd and Simaan, 1995) which includes a more realistic continuous transition between the breakaway torque and the sum of the kinetic and steady torque components of (9) and (10). The nonlinear function used, however, is relatively complicated but the authors have produced a simpler version imposing a lesser computational demand, as follows:

$$\Gamma_{total} = \left(\Gamma_{kinetic} + \Gamma_{steady} + \Gamma_{static}\right) \cdot y_t \quad (12)$$

where Γ_{steady}, $\Gamma_{kinetic}$ are define by (9) and (10),

$$y_t = \begin{cases} |\omega|/\omega_1, \{\omega | -\omega_1 \le \omega \le \omega_1\} \\ 1, \quad \{\omega | \omega_1 \le |\omega|\} \end{cases} \quad (13)$$

and

$$\Gamma_{static} = \frac{A}{\omega + |B| sign(\omega)} \quad (14)$$

where $A = \Gamma_1 (B + \omega_1)$, $B = \frac{\Gamma_1 \omega_1 - \Gamma_2 \omega_2}{\Gamma_2 - \Gamma_1}$ and ω_1 together with ω_2 are defined in Figure 7.

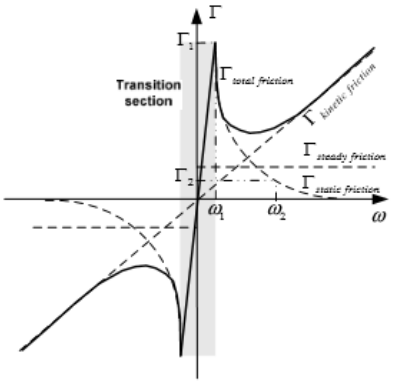

Figure 7: Friction model and its components.

The following constant parameters are used: $\omega_1 = 0.01$ and $\Gamma_2 = 0.001$. $\Gamma_1 = k_{static}$ and ω_2, $\{\omega_2 | \omega_2 > \omega_1\}$ were found using the Simulink Parameter Estimation tool.
Finally, Figure 8 shows a simulation of the friction model to be incorporated in the subsequent simulations.

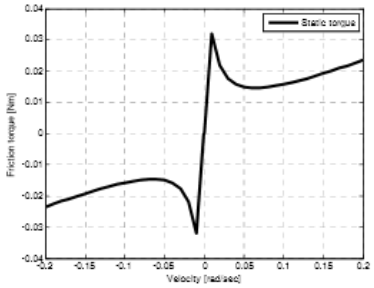

Figure 8: Friction model simulation - Γ_{total}

3. Throttle valve control:

3.1. Standard PI control

Figure 9 shows the standard PI control loop including control dither to avoid the limit cycling errors that would otherwise be caused by the stick-slip friction component.

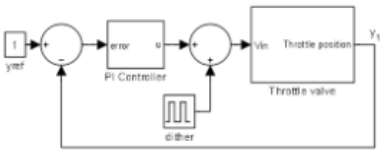

Figure 9: Standard PI control loop

3.2. Observer Based Robust Control

OBRC is a control technique that can be applied to linear and nonlinear plants with disturbances (Dodds, 2007) & (Stadler et al.,

2007). Figure 10 shows the general block diagram of this scheme.

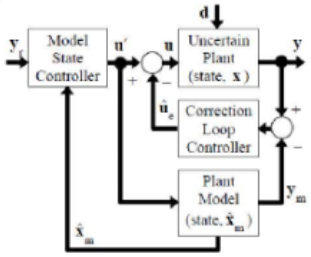

Figure 10: OBRC block diagram (Dodds, 2007).

Here, **x**, **y**, **d** and **u** are, respectively, the plant state, measurement, disturbance and control vectors. This block diagram structure results from the following. First an observer is formed with model state, $\hat{\mathbf{x}}_m$, and an estimate, $\hat{\mathbf{u}}_e$, of the disturbance referred to the control input that is *equivalent* to the combination of **d** with the theoretical disturbance equivalent to parametric mismatches between the model and the plant. Then $\hat{\mathbf{u}}_e$ is subtracted from both the plant and the model inputs. This converts the problem of controlling the uncertain plant to that of controlling the known model. Hence the model state controller shown in Figure 10, that responds to the reference input vector, $\mathbf{y}_r$, is designed like any other state space controller. A wide range of plant models is possible with a rank at least equal to that of the real plant but in the system under study, the linear throttle valve model of Figure 4 is used.

Applying the model state control law

$$u = r.y_{2r} - \left(k_1\hat{x}_{m1} + k_2\hat{x}_{m2} + k_3\hat{x}_{m3}\right) \quad (15)$$

where r is the reference input scaling coefficient and $k_i, i = 1,2,3$ are the state feedback gains, and adding its equivalent block diagram to Figure 4 enables the closed loop transfer function to be derived with the aid of Mason's rule, yielding:

$$\frac{Y(s)}{Y_r(s)} = \frac{b_1}{s^3 + a_1 s^2 + a_2 s + a_3} \quad (16)$$

where: $b_1 = r \cdot k_t N_2 / \left(L_a N_1 J_x\right)$

$$a_1 = R_a / L_a + D_x / J_x + k_3 / L_a$$

$$a_2 = \frac{k_s}{J_x} + \frac{k_t}{L_a}\frac{k_a}{J_x}\left(\frac{N_2}{N_1}\right)^2 + k_2\frac{k_t}{L_a}\frac{N_2}{N_1}\frac{1}{J_x} + \frac{R_a}{L_a}\frac{D_x}{J_x} + k_3\frac{1}{L_a}\frac{D_x}{J_x}$$

$$a_3 = k_1\frac{k_t}{L_a}\frac{N_2}{N_1}\frac{1}{J_x} + \frac{R_a}{L_a}\frac{k_s}{J_x} + k_3\frac{1}{L_a}\frac{k_s}{J_x}$$

The Dodds 5% settling time formula (Dodds, 2008) is used to obtain a non overshooting closed loop response with settling time, T_s, by choosing the closed loop characteristic polynomial as

$$\left(s + \frac{6}{T_s}\right)^3 = s^3 + \frac{18}{T_s}s^2 + \frac{108}{T_s^2}s + \frac{216}{T_s^3} \quad (17)$$

The gains can be found by equating (17) with the denominator of (16).

The observer is also designed using the model of Figure 4 but with additional disturbance estimation (referred to the control input), as shown in Figure 11.

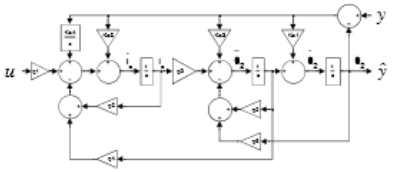

Figure 11: The observer.

Equating the determinant of Masons rule to zero then yields the observer correction loop characteristic polynomial as follows:

$$\Delta = s^4 + s^3\left(q_3 + q_5 + Ko_1\right) + s^2\begin{pmatrix} q_6 + q_4 \cdot q_2 + Ko_2 + q_3 \cdot q_5 + \\ Ko_1 \cdot q_3 + Ko_1 \cdot q_5 \end{pmatrix} + s\begin{pmatrix} Ko_3 \cdot q_2 + q_3 \cdot q_6 + Ko_2 \cdot q_3 + \\ Ko_1 \cdot q_4 \cdot q_2 + Ko_1 \cdot q_3 \cdot q_5 \end{pmatrix} + Ko_4 \cdot q_2 \quad (18)$$

where: $q_1 = 1/L_a$, $q_2 = k_t N_2/(J_x N_1)$, $q_3 = R_a/L_a$, $q_4 = k_e N_2/(L_a N_1)$, $q_5 = D_x/J_x$ and $q_6 = k_s/J_x$

Again the Dodds 5% settling time formula is used to design the observer to have a correction loop settling time of T_{so}:

$$\left(s + 15/(2T_{so})\right)^4 = s^4 + \frac{30}{T_{so}}s^3 + \frac{1350}{4T_{so}^2}s^2 + \frac{13500}{8T_{so}^3}s + \frac{50625}{16T_{so}^4} \quad (19)$$

Equating (18) and (19) then yields

$$Ko_1 = 30/T_{so} - q_3 - q_5$$

$$Ko_2 = 1350/4T_{so}^2 - q_6 - q_4 \cdot q_2 - q_3 \cdot q_5 - Ko_1 \cdot q_3 - Ko_1 \cdot q_5$$

$$Ko_3 = \begin{pmatrix} 13500/8T_s^3 - q_3 \cdot q_6 - Ko_2 \cdot q_3 \\ -Ko_1 \cdot q_4 \cdot q_2 - Ko_1 \cdot q_3 \cdot q_5 \end{pmatrix}\frac{1}{q_2}$$

$$Ko_4 = \left(\frac{50625}{16T_s^4}\right)\frac{1}{q_2}$$

3.3. Sliding Mode Control (SMC):

It is a well documented that sliding mode control (SMC) can achieve robustness in linear and nonlinear systems (Utkin et al., 1999), (Dodds and Vittek, 2009). There are many variations on this theme, some of which are designed to eliminate the control chatter of the basic version. In this investigation, the boundary layer method is employed, equivalent to a high gain output derivative feedback control system. Since the high gain is finite, an outer integral control loop can be added, resulting in the closed loop system of Figure 12.

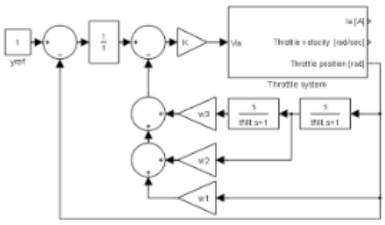

Figure 12: Boundary layer based SMC with an integrator to remove the steady state error.

The low pass filtering with time constant, T_{filter}, is introduced to avoid amplification of measurement noise at high frequencies.

Again, the Dodds 5% settling time formula is used to determine the three output derivative weights, w_1, w_2 and w_3, assuming the aforementioned filtering has a negligible effect on the closed loop dynamics, yielding a settling time of T_s as follows:

$$\frac{Y(s)}{Y_r(s)} = \frac{1}{1 + w_1 s + w_2 s^2 + w_3 s^3} = \left[\frac{1}{1 + s \cdot a}\right]^3 \quad (20)$$

where $a = T_s/6$. Then $w_1 = 3a$, $w_2 = 3a^2$, $w_3 = a^3$.

4. Simulations:

4.1. Parameters:

4.1.1. Throttle valve. The following parameters are found by laboratory tests and the Simulink Parameter Estimation Tool:

$K_t = 0.0261$; $K_e = 0.027$; $R_a = 1.25$; $L_a = 0.02$; $J_x = 0.003$; $k_s = 0.0932$; $\theta_{Initial\ spring} = 2.73$; $t_{system\ delay} = 0.0011$; $k_{kinetic} = 8.6119e-05$; $\omega_n = 0.251$; $k_{static} = 0.1353$; $k_{steady} = 0.1524$.

4.1.2. Conventional PI control loop. The controller gains were adjusted to yield $T_s = 0.3[s]$ without overshooting: $K_p = 3.8$ and $K_I = 1.7$. The square wave dither

amplitude and frequency are, respectively, $u_{dither} = \pm 1\ [V]$ and $f_{dither} = 10\ [Hz]$.

4.1.3. Observer based robust controller. A settling time of $T_s = 0.3[s]$ was used to calculate the state feedback gains: $k_1 = 1.05$, $k_2 = -0.165$ and $k_3 = -0.047$. To maximise the robustness, the minimum observer correction loop settling time was found to be $T_{so} = 0.015$. Attempting to reduce this further resulted in undesirable oscillatory behaviour. Observer gains: $Ko_1 = 1937$, $Ko_2 = 1497761$, $Ko_3 = 4257095$ and $Ko_4 = 532141336$.

4.1.4. Sliding mode controller. The output derivative filtering time constant, $T_{filt} = 0.0005$, was set to a relatively small value to avoid limiting the high gain. A settling time $T_s = 0.3[s]$ was selected to determine the derivative feedback weightings: $w_1 = 0.15$, $w_2 = 0.0075$ and $w_3 = 0.000125$. To maximise the robustness, the system gain was set to K= 500. Beyond this, the system response became oscillatory.

4.2. Step response comparison

In all three Simulink simulations, a stiff numerical integration algorithm was employed to cater for the two robust control techniques.
The PI control loop was tuned to achieve a non-overshooting step response with the specified settling time but this entailed much time and effort, in comparison with the SMC and OBRC.
Figure 13 shows the superimposed responses using all three controllers with a reference input commencing at zero, stepping to 1 rad. at $t = 2[s]$ and returning to zero at $t = 7[s]$.
Since they appear very close together on this amplitude scale, differences in performance are made more visible by plotting the position control errors (Figure 14), defined as $y(t) - y_{ideal}(t)$, where $y_{ideal}(t)$ is the step response that the system is designed to achieve ideally.

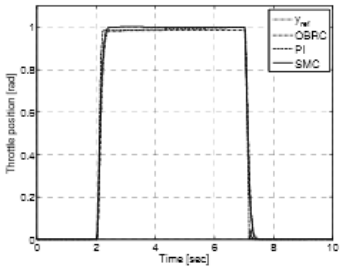

Figure 13: Step responses.

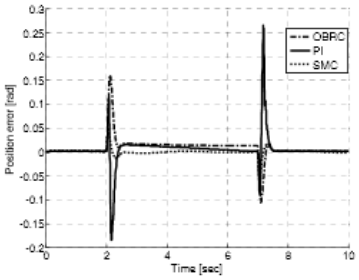

Figure 14: Step response errors

It is evident that the PI control yielded the worst errors. As expected the robust control methods yielded better responses but the SMC has a smaller error than the OBRC.

4.3. Ramp response control comparison

Since the throttle position demand is continuous during the normal operation of an engine management system, the second reference input used for performance comparisons ramps up at $+1\ [rad/s]$ from zero at $t = 2[s]$ and at $t = 5[s]$ ramps down at $-1\ [rad/s]$ to zero at

$t = 7[s]$, remaining zero thereafter. The results are shown in Figures 15 and 16.

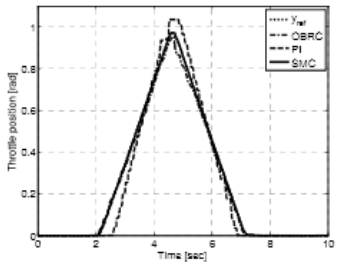

Figure 15: Ramp responses.

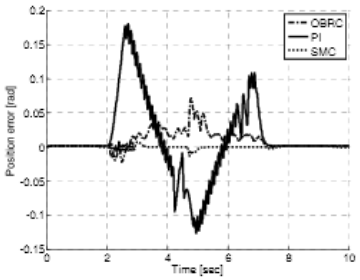

Figure 16: Ramp response errors.

Despite the control dither, the PI control loop is adversely affected by the stick-slip friction. As for the step responses, both the robust controllers improve on this but the SMC performs better than the OBRC.

5. Conclusions and Recommendations:

It is remarkable that even without control dither, the robust controllers performed better that the PI controller *with* the control dither. Furthermore, it is recommended that a fairer comparison be carried out by applying control dither with all three controllers.

The different plant models such as the multiple integrators (Dodds, 2007) should be considered in case this permits a smaller value of T_{so} and therefore higher robustness.

Finally, experimental work currently in progress will be published later.

6. References

ARMSTRONG-HELOUVRY, B. & AMIN, B. (1994) PID control in the presence of static friction: exact and describing function analysis. *American Control Conference.*

DODDS, S. J. (2007) Observer based robust control. *AC&T.*

DODDS, S. J. (2008) Settling time formulae for the design of control systems with linear closed loop dynamics. *AC&T.*

DODDS, S. J. & VITTEK, J. (2009) Sliding mode vector control of PMSM drives with flexible couplings in motion control. *AC&T.*

MAJD, V. J. & SIMAAN, M. A. (1995) A continuous friction model for servo systems with stiction. *Proceedings of the 4th IEEE Conference on Control Applications.*

PAPADOPOULOS, E. G. & CHASPARIS, G. C. (2002) Analysis and model-based control of servomechanisms with friction. *IEEE/RSJ International Conference on Intelligent Robots and Systems.*

STADLER, P. A., DODDS, S. J. & WILD, H. G. (2007) Observer based robust control of a linear motor actuated vacuum air bearing. *AC&T.*

UTKIN, V. I., YOUNG, K. D. & OZGUNER, U. (1999) A control engineer's guide to sliding mode control. *IEEE Transactions on Control Systems Technology,* 7, 328-342.

Forced dynamic control of non-minimum-phase plants via study of the classical inverted pendulum

FORCED DYNAMIC CONTROL OF NON-MINIMUM-PHASE PLANTS VIA STUDY OF THE CLASSICAL INVERTED PENDULUM

Jacob L. Pedersen†, Stephen J. Dodds‡
†Delphi Diesel Systems Ltd, Park Royal, London, United Kingdom
‡CITE, University of East London, United Kingdom
Jacob.pedersen@delphi.com, stephen.dodds@spacecon.co.uk

Abstract: The general problem of controlling a non-minimum-phase plant is tackled via study of the classical inverted pendulum (IP). A full nonlinear model of the IP is used for simulation and a linearised version is used for the controller design. The trolley position is controlled while keeping the pendulum inverted by use of an input/output feedback linearisation method called Forced Dynamic Control (FDC). This is generally more straightforward to apply than conventional techniques such as linear state feedback with pole assignment but in its basic form yields right half plane zero cancellation which creates an unstable closed loop mode. This is circumvented in this paper by creating an artificial controlled output that is a weighted sum of the state variables such that the right half plane zeros do not exist in the transfer function. Furthermore a non-oscillatory response with a specified settling time is achieved with the aid of the Dodds settling time formula (Dodds, 2008). The computational delay introduced to eliminate the algebraic loop in the nonlinear model is shown to have a negligible effect. Simulations are presented that demonstrate the correct operation of the control system and determine differences between the ideal and actual step responses due to the nonlinearities, parametric errors and external disturbances.

1. Introduction:

It is well known that linear state feedback control (LSFC) laws for linear non-minimum phase plants, can be designed by pole assignment, an acceptable transient response being attainable by balancing the right half plane zeros by mirror image poles (Franklin et al., 2002). This is applicable, for example, to the inverted pendulum when its motion is restricted to small perturbations about an operating point. The motivation for applying forced dynamic control (FDC), however, is that it is also applicable to nonlinear plants and is quicker to apply than conventional LSFC. Since FDC is a time domain method, a different approach to deal with non-minimum phase plants is needed. It should be noted here that the term 'non-minimum phase', strictly applies to linear plants and that the equivalent term covering nonlinear plants in addition is 'unstable zero dynamics' (Stadler, 2008).

The direct application of FDC to a plant of rank $r < n$ where n is the plant order will leave the zero dynamics of order $n-r$ uncontrolled in the closed loop system. The purpose of this paper is to investigate the solution of this problem by appending the plant state space model with an artificial output equation such that the 'new plant' created is of full rank and the application of FDC to this achieves full state control and therefore avoids the closed loop instability. The paper addresses the choice of the closed loop dynamics using the Dodds settling time formula (Dodds, 2008).

In this paper, the FDC design is based on a linearised model of the IP but the performance of this design is assessed for the true nonlinear IP as well as the linearised model by simulation. It is intended that the work presented here should pave the way to generally applicable FDC of plants with unstable zero dynamics.

2. Inverted pendulum modelling:

2.1 Nonlinear model:

The input force, F, is used for controlling the movement of the IP, as shown in Figure 1.

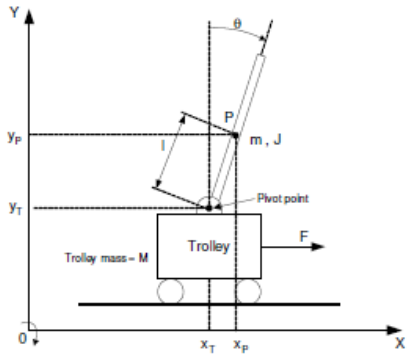

Figure 1 Inverted pendulum system

The coordinates, θ (angle of the pendulum) and x_T (position of the trolley), are outputs from the single input, multiple output (SIMO) plant.

Lagrange's method is used to derive the following equations of motion:

$$\ddot{x}_T = \frac{F - b\dot{x}_T - ml\ddot{\theta}\cos\theta + ml\dot{\theta}^2\sin\theta}{M+m} \quad (1)$$

$$\ddot{\theta} = \frac{mgl\sin\theta - ml\ddot{x}_T\cos\theta}{m\cdot l^2 + J} \quad (2)$$

2.2 Linear IP model:

Linearising (1) and (2) about the operating point, $\theta = \dot{\theta} = 0$ yields:

$$\ddot{x}_T = -\frac{b}{M+m}\dot{x}_T - \frac{m\cdot l}{M+m}\ddot{\theta} + \frac{1}{M+m}F \quad (3)$$

$$\ddot{\theta} = \frac{mgl}{J+l^2m}\theta - \frac{ml}{J+l^2m}\ddot{x}_T \quad (4)$$

The states of the IP are chosen as $x_1 = \theta$, $x_2 = \dot{\theta}$, $x_3 = x_T$ and $x_4 = \dot{x}_T$. Equations (3) and (4) may then be replaced by the following state differential equation:

$$\dot{x} = A\cdot x + B\cdot u \Rightarrow$$

$$\begin{bmatrix}\dot{x}_1\\ \dot{x}_2\\ \dot{x}_3\\ \dot{x}_4\end{bmatrix} = \begin{bmatrix}0 & 1 & 0 & 0\\ a_0 & 0 & 0 & a_1\\ 0 & 0 & 0 & 1\\ a_2 & 0 & 0 & a_3\end{bmatrix}\cdot\begin{bmatrix}x_1\\ x_2\\ x_3\\ x_4\end{bmatrix} + \begin{bmatrix}0\\ b_0\\ 0\\ b_1\end{bmatrix}\cdot F \quad (5)$$

The measurement equation is

$$y = C\cdot x \Rightarrow$$

$$\begin{bmatrix}\theta\\ x_T\end{bmatrix} = \begin{bmatrix}1 & 0 & 0 & 0\\ 0 & 0 & 1 & 0\end{bmatrix}\cdot\begin{bmatrix}x_1\\ x_2\\ x_3\\ x_4\end{bmatrix} \quad (6)$$

where

$a_0 = \left[(M+m)\cdot m\cdot g\cdot l\right]/q_1$, $a_1 = (m\cdot l\cdot b)/q_1$,

$a_2 = \left(m^2\cdot g\cdot l^2\right)/q_2$, $a_3 = \left(J + l^2\cdot m\right)\cdot b/q_2$,

$b_0 = -(m\cdot l)/q_1$, $b_1 = -\left(J + l^2\cdot m\right)/q_2$ and

$q_1 = J(M+m) + l^2\cdot M\cdot m$,

$q_2 = -J(M+m) - l^2\cdot m\cdot M$

The corresponding state variable block diagram used for the linear Matlab-Simulink simulation is shown in Figure 2.

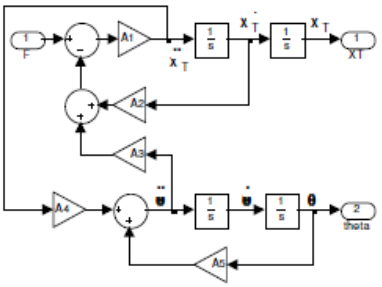

Figure 2: Linear IP Simulink model

3. Forced Dynamic Control (FDC):

The general FDC method is fully described by (Vittek and Dodds, 2003). Here, the goal is to control the trolley position while

keeping deviations of the pendulum position about the vertical within acceptable bounds. It is evident by inspection of (1) and (2) that this plant is of order, 4. The rank w.r.t. the controlled output, x_T, is 2 due to the direct dependence of $\ddot{x}_T$ on the control force, F. Direct application of FDC would therefore yield a closed loop system of order 2 and therefore only two of the plant state variables, i.e., x_T and $\dot{x}_T$, would be controlled. The other two state variables, θ and $\dot{\theta}$, are associated with the zero dynamic subsystem (2). The input of this subsystem is $\ddot{x}_T$ but this is not used to control the pendulum angle, θ, which will vary as a 'side effect'. In the linearised model, the zero dynamics is described by (4) and the natural motion of the unforced system, obtained by setting $\ddot{x}_T = 0$, is *unstable* since the roots of the characteristic equation, $s^2 - mgl/(J+l^2m) = 0$ are $s_{1,2} = \pm\sqrt{mgl/(J+l^2m)}$.

To circumvent this problem, the approach taken is to augment the plant model by creating an artificial controlled output

$$z = C_1 x_T + C_2 \dot{x}_T + C_3 \theta + C_4 \dot{\theta} \qquad (7)$$

where the constant coefficients are chosen such that a) the plant is of full rank, i.e., the rank with respect to z is 4, and b) controlling z to reach a constant demanded value results in x_T reaching the same value. Figure 3 shows a block diagram of this augmented plant. For conciseness, the coefficients are defined as $A_1 = 1/(M+m)$, $A_2 = b$, $A_3 = ml$, $A_4 = -ml/(J+l^2m)$ and $A_5 = mgl/(J+l^2m)$.

The standard FDC method will now be applied to the augmented plant of Figure 3. Since the plant has to be of full rank, C_1, C_2, C_3 and C_4 are chosen so that z, $\dot{z}$, $\ddot{z}$ and $\dddot{z}$ are state variables, which is achieved by

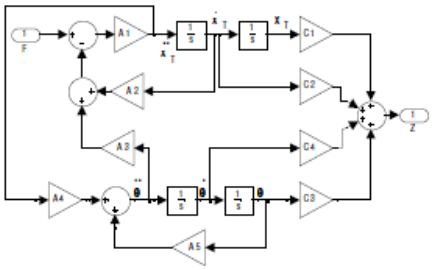

Figure 3: Linear IP with artificial output z.

ensuring that none of these variables has direct algebraic dependence on the control variablrale, F. Differentiating (7) yields

$$\dot{z} = C_1 \dot{x}_T + C_2 \ddot{x}_T + C_3 \dot{\theta} + C_4 \ddot{\theta} \qquad (8)$$

Substituting for the derivatives of the state variables appearing on the right hand side of (8) using (5) and (6) yields:

$$\dot{z} = C_1 \dot{x}_T + C_2 \dot{\theta} + C_2 \left[A_1 \left(F - A_2 \dot{x}_T - A_3 \ddot{\theta} \right) \right] + C_4 \ddot{\theta} \qquad (9)$$

From Figure 3, $\ddot{\theta} = A_5 \theta + A_4 A_1 \left(F - A_2 x_T - A_3 \ddot{\theta} \right)$

$$\Rightarrow \left(1 - A_4 A_1 A_3\right) \ddot{\theta} = A_5 \theta + A_4 A_1 F - A_4 A_1 A_2 x_T$$

$$\ddot{\theta} = \left(A_5 \theta + A_4 A_1 F - A_4 A_1 A_2 x_T\right) / \left(1 - A_4 A_1 A_3\right) \qquad (10)$$

Substituting for $\ddot{\theta}$ in (9) using (10) yields

$$\dot{z} = C_1 \dot{x}_T + C_3 \dot{\theta} + C_2 A_1 F - C_2 A_1 A_2 \ddot{x}_T - \left(C_4 - C_2 A_1 A_3\right) \left[\frac{A_5 \theta + A_4 A_1 F - A_4 A_1 A_2 \dot{x}_T}{1 - A_4 A_1 A_3} \right] \qquad (11)$$

The F term in (11) must vanish in order for $\dot{z}$ to be a state variable. Hence $C_4 = C_2 A_1 A_3$ and $C_2 = 0 \Rightarrow C_4 = 0$ which yields

$$\dot{z} = C_1 \dot{x}_T + C_3 \dot{\theta} \Rightarrow \ddot{z} = C_1 \ddot{x}_T + C_3 \ddot{\theta}. \qquad (12)$$

Repeated substitution for $\ddot{x}_T$ and $\ddot{\theta}$ using the equations implied by Figure 3 yields

$$\ddot{z} = C_1 A_1 \left(F - A_2 \dot{x}_T - A_3 \ddot{\theta} \right) + C_3 \left[A_5 \theta + A_4 A_1 \left(F - A_2 \dot{x}_T - A_3 \ddot{\theta} \right) \right] \Rightarrow$$

$$\ddot{z} = \left(C_1 + C_3 A_4\right) A_1 \left(F - A_2 \dot{x}_T - A_3 \ddot{\theta} \right) + C_3 A_5 \theta$$

$$\Rightarrow \ddot{z}=C_3A_5\theta$$
$$+(C_1+C_3A_4)A_1\left[\begin{array}{c}F-A_2\dot{x}_T\\ -A_3\left(\dfrac{A_5\theta+A_4A_1F-A_4A_1A_2\dot{x}_T}{1-A_4A_1A_3}\right)\end{array}\right] \quad (13)$$

For F to vanish, $C_1=-C_3A_4$, yielding $\ddot{z}=C_3A_5\theta$ and differentiating again yields

$$\dddot{z}=C_3A_5\dot{\theta}. \quad (14)$$

C_3 has be chosen such that $z=x_T$ in the steady state assuming closed loop stability. Then, $x_T=const$, $\dot{x}_T=0$, $\theta=0$ and $\dot{\theta}=0$ and therefore the steady state outputs satisfy

$$z_{ss}=C_1x_{T_{ss}}\Rightarrow C_1=1\Rightarrow C_3=-1/A_4.$$

Summarising, the required constants are $C_1=1$, $C_2=0$, $C_3=-1/A_4$ and $C_4=0$. Then (7) yields

$$z=C_1x_T+C_3\theta=x_T-(1/A_4)\theta \quad (15)$$

$$\dot{z}=\dot{x}_T-(1/A_4)\dot{\theta} \quad (16)$$

$$\ddot{z}=-(A_5/A_4)\theta \quad (17)$$

$$\dddot{z}=-(A_5/A_4)\dot{\theta} \quad (18)$$

The output derivative equation for FDC is then obtained by a further differentiation:

$$\ddddot{z}=C_3A_5\ddot{\theta}$$

Substituting for $\ddot{\theta}$ using (10) yields

$$\ddddot{z}=C_3A_5\left(\frac{A_5\theta+A_4A_1F-A_4A_1A_2\dot{x}_T}{1-A_4A_1A_3}\right)\Rightarrow$$

$$\ddddot{z}=-\frac{A_5}{A_4}\left(\frac{A_5\theta+A_4A_1F-A_4A_1A_2\dot{x}_T}{1-A_4A_1A_3}\right)$$

Solving for F then yields the general FDC law in which $\ddddot{z}$ has to be chosen to achieve the required closed loop dynamics:

$$\boxed{F=\frac{1}{A_4A_1}\left[-\frac{A_4}{A_5}(1+A_4A_1A_3)\right]\ddddot{z}-A_5\theta+A_4A_1A_2\dot{x}_T} \quad (19)$$

The Dodds 5% settling time formula, $T_s=1.5(1+n)T_c$ (Dodds, 2008), will now be used to obtain the desired non-overshooting closed loop step response, $z(t)$. Thus

$$\frac{z(s)}{z_r(s)}=\left[\frac{\frac{1}{T_C}}{s+\frac{1}{T_C}}\right]^n=\left[\frac{\frac{1.5(1+n)}{T_S}}{s+\frac{1.5(1+n)}{T_S}}\right]^n \quad (20)$$

Where z_r is the reference input and T_c is closed-loop time constant for the n-order system. For n = 4, (20) becomes

$$\frac{z(s)}{z_r(s)}=\left(\frac{a}{s+a}\right)^4 \text{ where } a=\frac{15}{2T_S}$$

from which

$$\left(s^4+4as^3+6a^2s^2+4a^3s+a^4\right)z(s)=a^4z_r(s)$$

so in the time domain:

$$\ddddot{z}+4a\dddot{z}+6a^2\ddot{z}+4a^3\dot{z}+a^4=a^4z_r\Rightarrow$$
$$\ddddot{z}=a^4(z_r-z)-4a^3\dot{z}-6a^2\ddot{z}-4a\dddot{z}$$

Using (15) to (18) and setting $z_r=x_{T_r}$ gives

$$\ddddot{z}=a^4\left(x_{Tr}-x_T+\frac{1}{A_4}\theta\right)-4a^3\left(\dot{x}_T-\frac{1}{A_4}\dot{\theta}\right)+6a^2\frac{A_5}{A_4}\theta+4a\frac{A_5}{A_4}\dot{\theta} \quad (21)$$

Substituting for $\ddddot{z}$ in (21) using (19) yields the required FDC law:

$$\boxed{\begin{array}{l}F=\dfrac{1}{A_4A_1}\left(-\dfrac{A_4}{A_5}(1+A_4A_1A_3)\right)\cdot\\ \left(\begin{array}{c}a^4\left(x_{Tr}-x_T+\dfrac{1}{A_4}\theta\right)-4a^3\left(\dot{x}_T-\dfrac{1}{A_4}\dot{\theta}\right)\\ +6a^2\dfrac{A_5}{A_4}\theta+4a\dfrac{A_5}{A_4}\dot{\theta}\\ -A_5\theta+A_4A_1A_2\dot{x}_T\end{array}\right)\end{array}} \quad (22)$$

To summarise, an overall block diagram of the control system is shown in Figure 4.

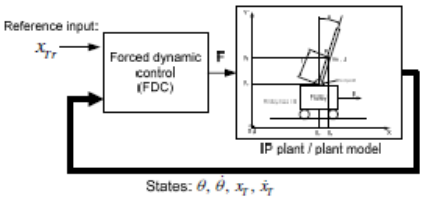

Figure 4: FDC and IP plant

Regarding future practical implementation, a rapid prototyping system such as dSPACE could be used. All the plant states are required but in the real world only the trolley position x_T and the pendulum angle θ would be measured. The other states, $\dot{x}_T$ and $\dot{\theta}$ could be calculated using software differentiation. As formulated above, the control variable is the force F [Nm] but in the real system this would be implemented as a control signal equivalent to the force from the processor. For example, if the actuator is a DC motor, the torque would be $\Gamma_m = K_m i_a / R = F.r$ where i_a is the armature current, K_m is the motor torque constant, R is the gearbox ratio and r is the truck wheel radius from which $i_a = (R.r/K_m)F$. This would then be the current demand of a relatively high bandwidth current control loop as shown in Figure 5.

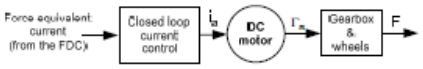

Figure 5: Control force implementation.

4. Simulations:

4.1. Parameters:

The parameters used are as follows unless otherwise specified: Gravitational acceleration: $g = 9.8\left[m/\sec^2\right]$; Trolley mass: $M = 0.4\left[kg\right]$; Pendulum mass: $m = 0.1\left[kg\right]$; Pendulum length: $l = 0.5\left[m\right]$; Moment of inertia about the pendulums pivot point: $J = ml^2/3\left[kg\,m^2\right]$.

4.2. Simulations with linear plant model:

In all the simulations presented below, all the state variables start at zero, the 5% settling time is set to $T_s = 2\,\mathrm{s}$, a positive step truck position reference, $x_{T_r}(t)$ is applied at $t = 2\,\mathrm{s}$ and an equal and opposite step reference input is applied at $t = 7\,\mathrm{s}$.

Inspection of Figure 2 reveals an algebraic loop, $A_1 \rightarrow A_4 \rightarrow A_3 \rightarrow A_1$. It is well known that Matlab/Simulink does not accept this. A simple solution of this problem is to insert a time delay of one numerical integration step, h, in the loop to render the simulation a causal system. But this does introduce a modelling inaccuracy. The authors therefore considered it necessary to have a linear IP model without such a delay to validate the FDCs performance and accuracy. This is derived in the appendix (7.1). Figure 6 shows the response to two consecutive oppositely signed steps of 1m magnitude of the FDC applied to the aforementioned model superimposed on the step response of the nominal closed loop system with transfer function (20) for $n = 4$, which is used as a benchmark. These responses are not distinguishable from one another and pass through the $0.95x_{T_r}$ line at $t = T_s = 2\,\mathrm{s}$, confirming their correctness.

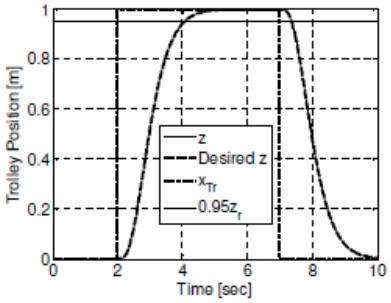

Figure 6: Validation of FDC

As no error between the two responses is visible in Figure 6, Figure 7 shows this error on a visible scale, proving that it is negligible. The pseudo random behaviour is due to the numerical integration operating at a finite word-length.

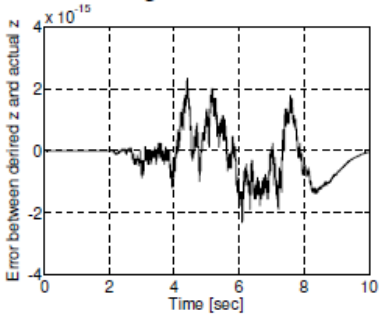

Figure 7: Error between z of simulated FDC without the plant delay and nominal z.

Figure 8 shows the corresponding trolley position, indicating the undershoot following the step changes in x_{T_r} that are typical with non-minimum-phase plants.

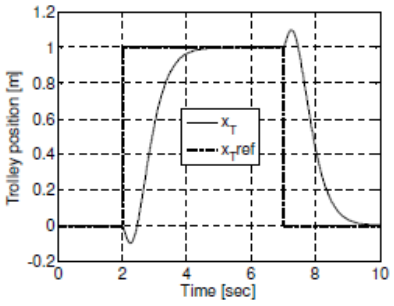

Figure 8 Trolley position

At less than 10%, of the step reference input magnitude, this undershoot is considered to be acceptable. The corresponding pendulum angle plotted in Figure 9 is kept within ±11deg. of the vertical position, confirming the effective control of all the plant states.

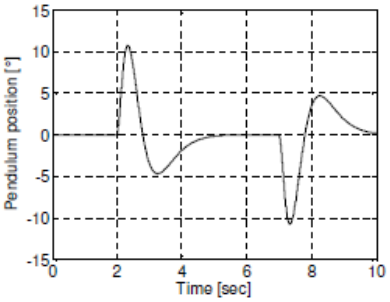

Figure 9: Pendulum position (Vertical = 0)

Figure 10 shows the error corresponding to Figure 9 when the plant model without the algebraic loop (Figure A1 in the Appendix to this paper) is replaced by the basic one of Figure 2 but with a time delay of $h = 1\,\text{ms}$ introduced between $\ddot{\theta}$ and the gain, A_3. Although this has increased the error magnitude by a factor of approximately 10^{11}, the peak error is less than $10^{-4}\,\text{m}$ in magnitude, which can be considered acceptable when compared with the position change of 1 m.

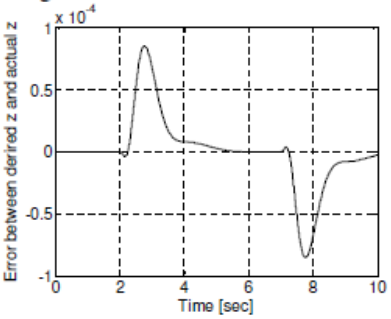

Figure 10 Error between z of simulated FDC with the plant delay and nominal z.

4.3. Simulations with nonlinear plant model:

Figure 11 shows a step response error corresponding to Figure 10 but with the nonlinear plant model using the same FDC

control law as applied above to the linear plant model.

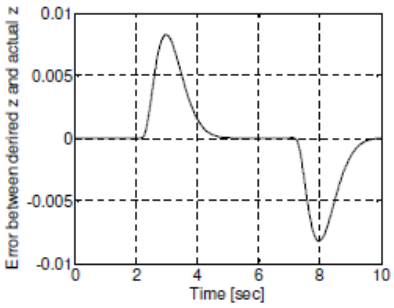

Figure 11: Error between nominal z and z of FDC with nonlinear plant model and delay.

As can be seen, the error increases further in magnitude by a factor of approximately 100 but it still only peaks at approximately 0.8% of the 1 m step reference magnitude, which is considered acceptable.

Variation of the step responses with increasing reference input magnitude is shown in Figure 12. Despite the plant nonlinearity, the step response shape does not vary visibly with the reference input magnitude.

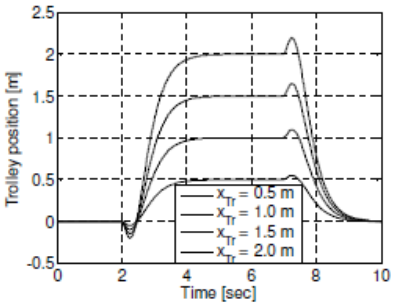

Figure 12: Step responses with nonlinear plant model and increasing reference input magnitude.

Next the robustness of the system to plant parameter variations from the nominal values has been investigated with +/- 10 % mismatches of the pendulum length, pendulum mass, trolley mass and the wheel bearing friction, in all combinations. Figure 13 shows the nominal error with no plant parameter mismatches, identical to that of Figure 11, together with the errors with the maximum positive and maximum negative peaks taken from the complete set of simulations to show the worst cases.

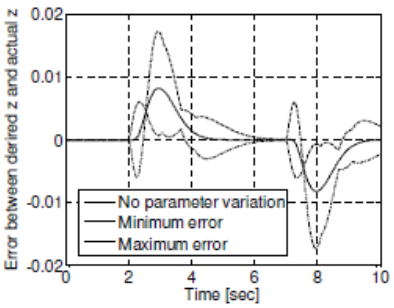

Figure 13: Nominal error and worst case error envelope for +/- 10% plant parameter variations.

The peak worst case errors of ±0.0166 m is acceptable. Figure 14 shows the corresponding worst case pendulum angle, $\theta(t)$, taken from the complete set of simulations superimposed on the pendulum angle with no parameter mismatching. It is evident that the parameter mismatching has a negligible influence on θ.

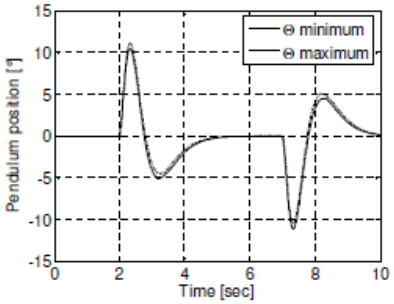

Figure 14: Worst case pendulum angle excursions for +/- 10% plant parameter variations.

5. Conclusions and Recommendations:

The investigations show that FDC is very effective in controlling the non-minimum phase plant consisting of a trolley supporting an IP when the technique of creating a fictitious plant output with full rank is applied. This technique may prove effective for many other non-minimum-phase plants and therefore further investigations in this direction are recommended. Regarding the IP, application of FDC using the full nonlinear plant model is recommended as this would be a useful preliminary study for control of other nonlinear non-minimum-phase plants for which the control system performance may more critically depend on use of the nonlinear model. The main problem to be solved for the IP is the formulation of the full rank fictitious output equation for the nonlinear case. Also, a preliminary study of FDC of the IP with the trolley on an inclined slope has been carried out by the authors and this indicates a steady state trolley position error. A modification of the FDC method to eliminate this error would be a worthwhile further investigation as the general method could be applied to other plants with significant constant or slowly varying external disturbances.

6. References

Dimarogonas A. D., Haddad S., *Vibration for Engineers*, Prentice Hall, Englewood Cliffs, NJ, 1992.

Dodds S. J., "Settling Time Formulae for the Design of Control Systems with Linear Closed Loop Dynamics, *Proceedings of AC&T,* University of East London, 2008.

Franklin G. F., Powell D. P. Emami-Naeini A., *Feedback Control of Dynamic Systems (Fourth Edition),* Prentice Hall, Upper Saddle River, NJ, 2002.

Stadler P. A., Dodds S. J., "Modelling and Control of a Vacuum Air Bearing Linear Drive in the Nanometer Range", *Proceedings of AC&T*, University of East London, 2008.

Vittek J., Dodds, S. J., *Forced Dynamic Control of Electric Drives*, Zilina University Press, Slovakia, 2003.

Woods R. L., Lawrence, K. L., *Modeling and Simulation of Dynamic Systems*, Prentice Hall, Englewood Cliffs, NJ, 1997.

7. Appendix

7.1. Plant model without algebraic loop

Using Masons rule on Figure 2:

$$\frac{\dot{x}_T(s)}{F(s)} = \frac{A_1(s-A_5)}{s^3 + A_1A_2\,s^2 A_1A_3A_4\,s^3 + A_5\,s - A_1A_2A_5}$$

$$\Rightarrow \frac{\dot{x}_T(s)}{F(s)} = \frac{b_0(s-A5)}{s^3 + a_2\,s^2 + a_1\,s - a_0} \quad (23)$$

where $b_0 = A_1/(1+A_1A_3A_4)$,

$a_2 = A_1A_2/(1+A_1A_3A_4)$, $a_1 = A_5/1+A_1A_3A_4$

and $a_0 = A_1A_2A_5/(1+A_1A_3A_4)$.

For the output θ:

$$\frac{\theta(s)}{F(s)} = \frac{\dfrac{A_1A_4\,s}{1+A_1A_3A_4}}{s^3 + a_2\,s^2 + a_1\,s - a_0} \Rightarrow$$

$$\frac{\theta(s)}{F(s)} = \frac{b_1\,s}{s^3 + a_2\,s^2 + a_1\,s - a_0} \quad (24)$$

where: $b_1 = A_1A_4/(1+A_1A_3A_4)$. Figure A1 shows the corresponding Simulink block diagram which is the state variable block diagram in the control canonical form realising transfer functions (23) and (24).

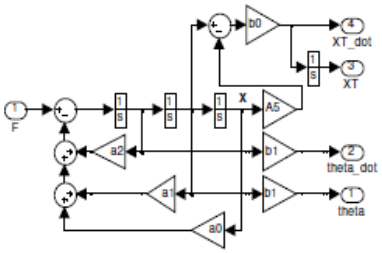

Figure A1: Linear IP model without algebraic loop